

AN INFRARED VIEW OF THE COEVOLUTION OF MASSIVE
BLACKHOLES AND GALAXIES

by

Yong Shi

A Dissertation Submitted to the Faculty of the

DEPARTMENT OF ASTRONOMY

In Partial Fulfillment of the Requirements
For the Degree of

DOCTOR OF PHILOSOPHY

In the Graduate College

THE UNIVERSITY OF ARIZONA

2 0 0 8

THE UNIVERSITY OF ARIZONA
GRADUATE COLLEGE

As members of the Final Examination Committee, we certify that we have read the dissertation prepared by Yong Shi entitled “AN INFRARED VIEW OF THE CO-EVOLUTION OF MASSIVE BLACKHOLES AND GALAXIES” and recommend that it be accepted as fulfilling the dissertation requirement for the Degree of Doctor of Philosophy.

George Rieke

Date: 2 May 2008

Daniel Eisenstein

Date: 2 May 2008

Xiaohui Fan

Date: 2 May 2008

Richard Green

Date: 2 May 2008

Chris Impey

Date: 2 May 2008

Final approval and acceptance of this dissertation is contingent upon the candidate's submission of the final copies of the dissertation to the Graduate College.

I hereby certify that I have read this dissertation prepared under my direction and recommend that it be accepted as fulfilling the dissertation requirement.

Dissertation Director: George Rieke

Date: 2 May 2008

STATEMENT BY AUTHOR

This dissertation has been submitted in partial fulfillment of requirements for an advanced degree at The University of Arizona and is deposited in the University Library to be made available to borrowers under rules of the Library.

Brief quotations from this dissertation are allowable without special permission, provided that accurate acknowledgment of source is made. Requests for permission for extended quotation from or reproduction of this manuscript in whole or in part may be granted by the head of the major department or the Dean of the Graduate College when in his or her judgment the proposed use of the material is in the interests of scholarship. In all other instances, however, permission must be obtained from the author.

SIGNED: _____ Yong Shi

ACKNOWLEDGEMENTS

I am deeply indebted to my Ph.D. advisor, George Rieke. Without your unremitting efforts to bring me to the US, my graduate study would not have been possible. Your scientific inspiration, consistent encouragement and support helped me in all the time of research and life for the past five years. Your great examples of doing science and enjoying life will benefit my whole future life.

Many thanks to those who have assisted my research: Robert Antonucci, Lei Bai, Myra Blaylock, Jeroen Bouwman, Kieran Cleary, Aleksandar Diamond-Stanic, Jennifer Donley, Jun Cui, Eiichi Egami, Xiaohui Fan, Karl D. Gordon, Varoujan Gorjian, Dean C. Hines, Linhua Jiang, Emeric Le Floch, Jennifer Lotz, John Moustakas, Frank J. Low, Patrick Ogle, Casey Papovich, Pablo G. Prez-Gonzalez, Jane Rigby, Paul S. Smith, Amy Stutz, Michael Werner and Christopher Willmer.

Special thanks to my previous and current officemates: Lei Bai, Aleksandar Diamond-Stanic, John Moustakas, Jeremiah Murphy, Amy Stutz, for all happy things you have shared with me and for all efforts you have put into my research and life.

Thanks to Daniel Eisenstein, Xiaohui Fan, Richard Green, Chris Impey to improve the final writing of this thesis.

Thanks to Michelle Cournoyer for consistent help. Thanks to the full support of graduate study provided by Steward Observatory.

DEDICATION

I dedicate this dissertation to my wife, Songqing Xu.

TABLE OF CONTENTS

LIST OF FIGURES	10
LIST OF TABLES	17
ABSTRACT	19
CHAPTER 1 INTRODUCTION	20
1.1 Coevolution of MBHs and Galaxies	20
1.2 Active Galactic Nuclei (AGN) – Manifestation of MBH Growth	20
1.3 LIRGs – an Intense Star Formation Phase of Galaxy Evolution	22
1.4 Major Mergers – A Possible Driving Mechanism of MBH-Galaxy Co- evolution	22
1.5 Infrared View of the Interplay between MBH and Galaxy	23
1.5.1 AGN Classification and Unification Models	23
1.5.2 The Dusty Tori	25
1.5.3 AGN Feedback: the Case Study of M87	26
1.5.4 Star Formation Rate in AGN Host Galaxies	27
1.5.5 Morphologies of LIRGs	29
CHAPTER 2 Far Infrared Observations of Radio Quasars and FR II Radio Galaxies	31
2.1 Introduction	31
2.2 Observations	31
2.2.1 The Sample and Extended Sample	31
2.2.2 Infrared Data	38
2.2.3 HST Images	39
2.2.4 Chandra Data	39
2.3 Analysis	40
2.3.1 Division of the sample into quasars and galaxies	40
2.3.2 Spectral Energy Distribution	41
2.4 Discussion	44
2.4.1 Energy Source for IR Emission	44
2.4.1.1 Extension of the IR Emission Region	45
2.4.1.2 Emission Line Ratio and IR Color	45
2.4.1.3 Relation of IR emission to the Central Hard X-ray Emission	48

TABLE OF CONTENTS – *Continued*

2.4.2	Tests of Unification Models	50
2.4.2.1	IR Color vs. R Parameter	50
2.4.2.2	An Indication of the Torus Opening Angle	53
2.4.2.3	The Relation of IR emission and 178 MHz radio emission	54
2.4.3	Compact Steep Spectrum Sources	56
2.5	Conclusions	58
CHAPTER 3 9.7 μm Silicate Features in AGNs: New Insights into Unification Models		
3.1	Introduction	60
3.2	Sample and Data Reduction	60
3.3	Results	68
3.4	Discussion	80
3.5	Conclusions	83
CHAPTER 4 Thermal and Non-Thermal Infrared Emission from M87 . . .		
4.1	Introduction	84
4.2	Data Reduction and Analysis	84
4.2.1	HST image	84
4.2.2	<i>SPITZER</i> DATA	85
4.2.3	Radio Data	89
4.2.4	Image Convolution	91
4.3	RESULTS	91
4.3.1	Infrared Image	91
4.3.2	Infrared Emission from the Host Galaxy	93
4.3.3	Behavior of the Nonthermal Sources	98
4.3.3.1	SEDs of the Nonthermal Sources	98
4.3.3.2	Minimum Pressure Analysis	101
4.3.3.3	Model of the Synchrotron Emission	102
4.3.3.4	<i>In Situ</i> Reacceleration in the Lobe	104
4.4	Conclusions	105
CHAPTER 5 Aromatic Features in AGN: Star-Forming Infrared Luminosity Function of AGN Host Galaxies		
5.1	Introduction	106
5.2	DATA AND ANALYSIS	107
5.2.1	Sample	107
5.2.2	Data Reduction	117
5.2.3	The Extraction of Aromatic Features	119

TABLE OF CONTENTS – *Continued*

5.2.4	Uncertainty of the Aromatic Flux	127
5.3	EXCITATION MECHANISM OF AROMATIC FEATURES IN AGNS	128
5.3.1	The Profile of Aromatic Features in AGN	128
5.3.1.1	The Composite Spectra	128
5.3.1.2	The Distribution of the Aromatic Feature Ratio . . .	132
5.3.2	The Global IR SED	134
5.3.3	Molecular Gas	136
5.4	The Conversion Factor from Aromatic Flux to the SFR	138
5.5	Origin of the Far-IR emission of AGN	141
5.6	STAR-FORMING IR LUMINOSITY FUNCTION OF QUASAR HOST GALAXIES	145
5.6.1	Methodology	145
5.6.2	Star-forming IR Luminosity Function of Active Galaxies . . .	148
5.6.2.1	Comparison to Field Galaxies	148
5.6.2.2	Dependence on AGN Luminosity	152
5.6.2.3	Comparison Between Different Subsamples	155
5.6.3	Implications for Nuclear Activity	156
5.7	CONCLUSIONS	159
CHAPTER 6 Morphology of <i>Spitzer</i> 24 μ m-Detected Galaxies in the UDF: the Links between the Star Formation and Galaxy Morphology		
6.1	Introduction	161
6.2	The Data	161
6.2.1	<i>Spitzer</i> Data	161
6.2.2	<i>HST</i> Data	162
6.2.3	Results and Band Merging	164
6.3	Methodology	167
6.3.1	Sample Definition	167
6.3.2	Quantitative Morphology Classification: Concentration and Asymmetry	168
6.4	RESULTS	172
6.4.1	Morphologies of a Representative Sample of LIRGs at $0.3 < z < 1.4$	172
6.4.2	Comparison of LIRG Morphologies to those of MIPS-non- detected Galaxies	174
6.4.2.1	Distributions of the Asymmetry and Concentration Parameters	174
6.4.2.2	Merging Galaxies	178
6.5	Discussion	179

TABLE OF CONTENTS – *Continued*

6.5.1	Continuous Morphological Transformation plus Episodic Star-	
	bursts	179
6.5.2	Comparisons to the Local LIRGs	182
6.6	Conclusions	183
CHAPTER 7 CONCLUSIONS AND FUTURE WORK		185
7.1	CONCLUSION	185
7.1.1	Testing the Unification Model	185
7.1.2	Case Study of AGN Feedback in M87	186
7.1.3	Star Formation of AGN Host Galaxies	186
7.1.4	Understanding Cosmic SFR Evolution	187
7.2	FUTURE WORK	187
7.2.1	Revisiting the Role of Major Mergers In Galaxy Evolution . .	187
7.2.2	AGN in Dwarf Host Galaxies	189
7.2.3	Cosmic Evolution of Star Formation in Quasar Hosts	189
7.2.4	Test the Unification Model with Unusual AGN	190
7.2.5	Prospectives for Future Facilities	190
REFERENCES		192

LIST OF FIGURES

2.1	The distributions of sources in the plane of the 178 MHz flux versus redshift (top panel) and 178 MHz flux versus spectral index α (bottom panel).	32
2.2	The spectral energy distributions of all sources. The 1-sigma error is used in the plot. The crosses are the radio and millimeter photometry data from NED. The solid line is the parabola model for the synchrotron emission. The open circle, open triangle, and filled triangle denote MIPS, <i>IRAS</i> and <i>ISO</i> data, respectively. The dotted line for radio galaxies is the template of stellar light for a normal elliptical galaxy, normalized to the apparent B magnitude. 'Quasar', 'BLRG', 'NLRG' and 'WLRG' indicate Quasar, broad line radio galaxies, narrow line radio galaxies and weak line radio galaxies, respectively. . . .	42
2.2	Continued	43
2.3	IR color versus emission-line ratio. The dashed line is a hypothetical mixing line on which the AGN fraction is labelled. This figure is from Kewley et al. (2001), with our sources added. The open triangles denote our sources. Filled circles, unfilled circles and crosses denote AGNs, ambiguous classification and starbursts, respectively in Kewley et al. (2001). Note that Section 2.4.2.1 shows that the torus may have significant optical depth at 24 μm and thus the IR color underestimates the fraction of AGN contributions for Type II AGN.	47
2.4	The correlation of K-corrected 70 μm flux density with 1-sigma error, K-corrected 24 μm flux density with 1-sigma error and central K-corrected hard X-ray flux corrected for absorption.	48
2.5	The correlation between IR color with 1-sigma error and R parameter. The IR color is defined as the ratio of 70 μm flux to 24 μm flux. The R parameter is defined as the ratio of the core radio flux to the total radio flux at 5 GHz. The solid line shows the least square fit. . . .	51
2.6	The relation of the K-corrected 70 μm emission with 1-sigma error and K-corrected radio emission at 178 MHz. The solid line is the least square fit to the radio quasars, excluding 3C 380 with substantial contribution by non-thermal core output (See Section 3.2), unlike those of the other quasars. The two dashed lines are the 3-sigma scatter of the relation indicated by the solid line.	55

LIST OF FIGURES – *Continued*

2.7	The plot of linear radio size vs. K-corrected FIR luminosity with 1-sigma error.	59
3.1	IRS spectra of 3 objects with fits. The dashed line is the fitted continuum and the dotted line is the estimated uncertainty in the continuum fitting. The scaling factors for (a) MCG-2-58-22, (b) Fairall9 and (c) NGC4388, are 30, 5 and 1.5, respectively.	67
3.2	The IRS spectra for objects with available X-ray data in order of the HI column density. Narrow emission lines have been removed from the spectra (see text). The dashed lines are the fitted continua and the dotted lines show the estimated uncertainties in the continuum fitting. The scaling factor to normalize the spectra at $5\ \mu\text{m}$ and the logarithm of the HI column density in units of cm^{-2} are given for each object.	69
3.2	Continued	70
3.2	Continued	71
3.2	Continued	72
3.2	Continued	73
3.3	The strength of the silicate feature as a function of HI column density. The strength of the silicate feature is defined as $(F_f - F_c)/F_c$, where F_f and F_c are the observed flux density and underlying continuum flux density, respectively, at the peak (for emission) or the minimum (for absorption) of the silicate feature. The black line is the linear fit to all objects while the red line is the fit to Seyfert galaxies. 'PG': PG quasar; 'RLQ': radio-loud quasar; 'Sy1': Seyfert 1 galaxies; 'Sy2': Seyfert 2 galaxies; 'BALQ': broad absorption-line quasar; 'FRII': FR II radio galaxies; 'LINER': low-ionization nuclear emission-line region; '2MQ': 2MASS Quasar.	74
3.4	The composite spectra of AGNs in different HI column bins. The number in parenthesis is the number of objects used for the composite spectrum in each bin.	75

LIST OF FIGURES – *Continued*

3.5	The structure of the material surrounding the central blackhole in the first quarter section. The whole structure is symmetric about the disk axis and the equatorial plane. From inside to outside: 1.) the inner accretion disk (AD), which produces X-ray and UV radiation ionizing the narrow-emission-line (NEL) and broad-emission-line clouds, and heating the dust; 2.) the middle disk (MD) with a diffuse component (grey) and with denser embedded clouds – the diffuse component produces the silicate emission while the embedded clouds heavily obscure the central X-ray emission when the line of sight intercepts them; and 3.) the outer disk (OD) with clouds that obscure the silicate and X-ray emission, and are responsible for the far-IR emission. Four lines of sight indicate: 1.) silicate emission with low HI column; 2.) silicate emission with high HI column; 3.) silicate absorption with low HI column; 4.) silicate absorption with high HI column.	81
4.1	Original <i>HST</i> images of M87 in the left column and galaxy-light subtracted image in the right column.	86
4.2	Original MIPS images of M87 in the left column. MIPS images of M87 after subtracting the nucleus in the middle column. The radial profile of surface brightness is shown in the right column where the solid line is the profile of the original image and the dotted line is the profile of the PSF at the corresponding wavelength. The subplot at $24\mu\text{m}$ shows the surface brightness of the emission after masking the central lobe region defined by the lowest level contour in Figure 4 of Hines et al. (1989).	87
4.3	Original <i>IRAC</i> images in the left column and galaxy-light subtracted images in the right column.	90
4.4	The radio, MIPS $24\mu\text{m}$, <i>IRAC</i> $8\mu\text{m}$ and <i>HST</i> optical image of M87 after subtracting the nucleus at the resolution of the MIPS $24\mu\text{m}$ image. The galaxy light is also subtracted for the <i>IRAC</i> and <i>HST</i> images. The contours (thin solid lines) are superposed to illustrate two local maxima in the Sf lobe at the infrared wavelength while only one maximum is present in the radio and optical.	92
4.5	The map of the spectral index $\alpha_{5\text{GHz}}^{24\mu\text{m}}$. The measurements of flux density at 5GHz and $24\mu\text{m}$ were made on the image with nuclear subtraction at the resolution of MIPS at $24\mu\text{m}$. The solid contour is the intensity distribution of the original 6 cm image. Contour intervals are [0.11, 0.43, 0.53, 0.64, 1.06, 5.32, 10.64, 173.86] mJy. . .	94

LIST OF FIGURES – *Continued*

4.6	Comparison of large aperture photometry with models of the stellar and nonthermal SEDs. The light lines show the models of the power law nonthermal emission and the stellar output, and the heavy line is the sum of the two components. The open circles are the 60 arcsec diameter aperture photometry. The filled boxes show the flux densities for the nucleus, jet, and lobes from this work at 70 and 24 μ m, and from Perlman et al. (2001b) (with a correction for low surface brightness components) at 10.8 μ m. The diamonds show the residual fluxes after subtracting the model from the totals measured. At 70 μ m, we label the points for total, nonthermal, and residual flux density. . . .	97
4.7	SEDs of individual regions in the MIPS 24 μ m image (see Figure 4.2). The photometry of the nonthermal features is shown as diamonds, with downward pointing arrows for the upper limits. The lines are the fits of the KP synchrotron emission models.	99
5.1	The redshift distribution of the three subsamples in this study (shaded area) compared to the corresponding parent samples for the PG, 2MASS and 3CR objects. The insert plots show the flux distribution of the subsample (shaded area) and the corresponding parent sample for the 3CR and 2MASS objects.	118
5.2	Examples of the extraction of the 7.7 and 11.3 μ m aromatic features in the spectra with silicate emission, no silicate feature and silicate absorption, respectively. The dotted lines are the IRS spectra while the solid lines are the continua. The subplots show the Drude profiles of the two features where the 11.3 μ m feature is fitted with two Drude profiles (dotted lines).	120
5.3	IRS spectra of AGN with detected aromatic features. The solid line is the derived continuum for the 7.7 μ m and/or 11.3 μ m aromatic features. The subplots show the Drude profiles of the two features. .	121
5.3	Continued.	122
5.3	Continued.	123
5.3	Continued.	124
5.3	Continued.	125

LIST OF FIGURES – *Continued*

5.4	(a) The number of objects in each wavelength bin of the composite spectrum. (b) The arithmetic mean spectrum (the heavy solid line) of AGN with one of the 7.7 and 11.3 μm aromatic features detected and the fitted continuum (the light solid line). (c) The continuum-subtracted spectrum (the heavy solid line) superposed with the composite spectrum (the dotted line) of the HII-like galaxies from Smith et al. (2007).	129
5.5	(a) The number of objects in each wavelength bin of the composite spectra of PG, 2MASS and 3CR AGN, respectively. (b) The arithmetic mean spectra and the fitted continua (the light solid lines). (c) The continuum-subtracted spectra of PG and 2MASS AGN, superposed with the composite spectra (the dotted lines) of the HII-like galaxies from Smith et al. (2007).	130
5.6	The ratio of the 11.3 μm aromatic flux to the 7.7 μm flux. The upper plot is the ratio for normal spiral galaxies from Lu et al. (2003) and Smith et al. (2007) while the lower plot is for active galaxies in this paper.	133
5.7	(a) The number of objects in each wavelength bin of the composite spectra of the high- $L(\text{PAH})/L(\text{MIR})$ subsample (solid line plus filled circles) and the low- $L(\text{PAH})/L(\text{MIR})$ subsample (dotted line plus open circles), where $L(\text{MIR})$ is the total mid-IR luminosity between 5.0 and 6.0 μm and $L(\text{PAH})$ is the 11.3 μm aromatic luminosity or the 7.7 μm aromatic luminosity multiplied by a factor of 0.27 for objects with only the 7.7 μm feature detected. (b) The geometric mean spectra of the two subsamples. (c) The spectrum of high- $L(\text{PAH})/L(\text{MIR})$ minus low- $L(\text{PAH})/L(\text{MIR})$ objects superposed on the starburst template with $L_{8-1000\mu\text{m}}=2.0\times 10^{11} L_{\odot}$ from Dale et al. (2001) and Dale & Helou (2002).	135
5.8	The plot of the mass of CO-derived molecular hydrogen gas versus the aromatic-based total IR luminosity (triangles) for AGN. Open and filled circles indicate weakly-interacting normal galaxies and strongly interacting normal galaxies from Solomon & Sage (1988), respectively.	137
5.9	The star-formation fraction at 24, 70 and 160 μm versus the mid-IR (5-6 μm) luminosity for the PG, 3C and 2MASS objects, respectively.	142
5.10	The star-formation fraction at 24, 70 and 160 μm versus the ratio of mid-IR (5-6 μm) luminosity and the Eddington luminosity for PG quasars. The solid line is the regression line and the two dotted lines are 2σ confidence bounds.	143

LIST OF FIGURES – *Continued*

5.11	Star-forming infrared luminosity functions for the PG, 2MASS and 3CR AGN. The dotted line is the re-normalized luminosity function of local field galaxies from Le Floc'h et al. (2005).	149
5.12	Star-forming infrared luminosity functions of PG quasars as a function of quasar brightness. The dashed line is the re-normalized luminosity function of star formation in CfA Seyfert 1 galaxies from Maiolino et al. (1995). The dotted line is the re-normalized luminosity function of local field galaxies from Le Floc'h et al. (2005). The solid lines are Schechter-function fits to the two PG subsamples. . .	153
5.13	Cumulative fraction luminosity functions $F(>L) = \sum_{L=L_0}^{\infty} f(L)$ for the PG objects versus 2MASS objects (upper plot) and the PG objects versus 3CR objects (lower plot), where $f(L)$ is the fractional luminosity function (See text).	157
6.1	The redshift distributions of LIRG ($L_{IR}(8-1000\mu\text{m}) > 10^{11}L_{\odot}$), non-LIRG ($L_{IR}(8-1000\mu\text{m}) < 10^{11}L_{\odot}$) and MIPS-non-detected control samples. The dot-dashed histogram indicates the control sample, the dotted histogram indicates the LIRGs and the solid histogram indicates the non-LIRGs. The control and LIRG samples have almost the same redshift distributions, while non-LIRGs are mainly at low redshift due to the detection limit. The inserted plot shows the IR luminosity at the $24\mu\text{m}$ detection limit (0.06 mJy) as a function of the redshift.	170
6.2	The rest-frame B-band images ($5\times 5\text{ arcsec}$) of non-X-ray LIRGs in the UDF along with the redshifts, structural parameters and the galaxy types based on the <i>CA</i> classification scheme. The center of the image is the position of the MIPS source. The light solid and dashed curves show contours at 20% and 50% enclosing flux for IRAC and MIPS, respectively. The heavy solid and dashed circles show the position accuracy for IRAC sources (0.1 arcsec) and MIPS sources (0.5 arcsec).	175
6.3	The distributions of LIRGs (triangles), non-LIRGs (open circles) and MIPS-non-detected control sample galaxies (stars) in the plane of concentration and asymmetry. The two solid curves divide the plane into three regions populated by early-, intermediate- and late-type galaxies. The dotted line indicates $A = 0.35$, to the right of which galaxies are identified as merging systems. The cross shows typical errors of concentration (0.3) and asymmetry (0.04).	176

LIST OF FIGURES – *Continued*

7.1	Upper panel: The merging fraction of LIRGs in different studies. Lower panel: the difference in asymmetry between UDF and GOODS images for 46 galaxies.	188
-----	---	-----

LIST OF TABLES

2.1	MIPS Measurements of Steep Spectrum Radio Sources	34
2.2	Other Properties of the MIPS Sample	35
2.3	The Extended Sample of Radio Galaxies and Quasars	36
2.3	The Extended Sample of Radio Galaxies and Quasars	37
2.4	Kendall Tau test	46
3.1	Source Characteristics	63
3.1	Source Characteristics	64
3.1	Source Characteristics	65
3.2	The linear fits to objects with different AGN types	76
3.3	Tests of the correlation	77
4.1	Photometry within the central 60'' diameter region	95
4.2	Photometry at 70 μm of the nucleus, jet and lobes	95
4.3	Spectral properties of the nucleus, jet and lobes at the resolution of MIPS at 24 μm	100
4.4	The physical parameters from the spectrum fit	102
5.1	AGN with associated physical parameters	108
5.1	AGN with associated physical parameters	109
5.1	AGN with associated physical parameters	110
5.1	AGN with associated physical parameters	111
5.1	AGN with associated physical parameters	112
5.1	AGN with associated physical parameters	113
5.1	AGN with associated physical parameters	114
5.1	AGN with associated physical parameters	115
5.1	AGN with associated physical parameters	116
5.2	The Star Formation Fraction at Three MIPS Bands as a Function of the mid-IR Luminosity	145
5.3	The Star Formation Fraction at Three MIPS Bands as a Function of the Eddington ratio	146
5.4	Fractional Bivariate Luminosity Function for PG quasars	147
5.5	Fractional Bivariate Luminosity Function for 2MASS quasars	147
5.6	Fractional Bivariate Luminosity Function for 3CR radio galaxies and quasars	148
5.7	Best-fitting parameters to star-forming IR LF of PG quasars	155

LIST OF TABLES – *Continued*

6.1	LIRGs in the UDF with unambiguous optical counterpart	163
6.2	The statistics of morphologies of $M_B < -18.5$ galaxies in the UDF and local LIRGs	169

ABSTRACT

Massive blackhole (MBH) growth is now recognized as a critical ingredient of galaxy formation and evolution. To investigate the interplay between MBH growth and galaxy evolution, we have used the capabilities of the Spitzer Space Telescope to study active galactic nuclei (AGN) and luminous infrared galaxies. We have tested the unification model for radio-loud AGN by finding that radio quasars and some FRII radio galaxies follow a correlation between low-frequency radio and the $70\ \mu\text{m}$ emission, two presumably isotropic indicators of nuclear radiation. We have found that mid-IR obscuration (characterized by the strength of the silicate feature) correlates with the X-ray obscuration (characterized by the HI column density), such that low HI columns correspond to silicate emission while high columns correspond to silicate absorption, for various types of AGN. We have demonstrated that *in situ* electron acceleration is required for both jet and lobe emission in M87. We have measured aromatic features in local AGN, demonstrated the diverse nature (star formation vs. AGN) of the far-IR emission mechanism, and constructed the star formation luminosity functions of the AGN hosts. These luminosity functions are flatter than that of field galaxies, implying that the interplay between star formation and nuclear activity enhances both processes. For luminous infrared galaxies (LIRGs), we have characterized galaxy morphologies of a complete sample of LIRGs at $z \sim 1$ and found that LIRGs at $z \sim 1$ are as asymmetric as local ones, implying similar conditions within galaxies lead to a LIRG level of star formation.

CHAPTER 1

INTRODUCTION

1.1 Coevolution of MBHs and Galaxies

Massive blackhole (MBH) growth is now recognized as a critical ingredient of galaxy formation and evolution. The demography of local galaxies suggests that most – perhaps all – massive galaxies host MBHs at their centers (e.g. Magorrian et al., 1998). MBHs have also been identified in less massive galaxies (Verolme et al., 2002; Filippenko & Ho, 2003), although such galaxies may not harbor MBHs as often as do massive galaxies (Merritt et al., 2001; Valluri et al., 2005). Following the discoveries of the MBHs at galaxy centers, it was realized that MBH masses are correlated with various properties of host galaxies – such as the bulge luminosity (Kormendy & Richstone, 1995), bulge masses (Magorrian et al., 1998), velocity dispersion (Gebhardt et al., 2000; Ferrarese & Merritt, 2000) and halo circular velocity (Ferrarese, 2002). The wide existence of MBHs in galaxies and the relations between MBH and galaxy properties strongly imply the coeval evolution of galaxies and MBHs.

1.2 Active Galactic Nuclei (AGN) – Manifestation of MBH Growth

The most accurate and direct way to find MBHs is using the dynamical signatures of gas and stars whose motions are affected by the gravitational potential of MBHs at galaxy centers. The measurement of MBH masses in about 30 galaxies through this method has been used to calibrate other techniques and has formed the basis of the studies of MBH masses, such as the local MBH mass function and the correlations between MBH mass and various galaxy properties as discussed above. However, due to the small sphere of influence of MBH gravity, the dynamical method is limited to the local massive galaxies. The active galactic nuclei, the manifestation of MBH

accretion and thus MBH growth, are probably the most efficient way to find MBHs and study their interplay with galaxy evolution.

MBH gravitational potential powers the radiation and kinetic energy associated with AGN. The enormous radiations usually arise over the whole range of the electromagnetic spectrum. Therefore, the selection of AGN can be conducted through various methods, such as radio emission, optical/UV color, X-ray emission, emission line identification and etc, leading to discovery of a large number of MBHs including a handful of very distant MBHs (e.g. Fan et al., 2004) and low mass ones (e.g. Greene & Ho, 2004). MBH properties can be deduced from the AGN observations. For example, the gravitationally redshifted X-ray iron lines provide additional evidence for the existence of MBHs (e.g. Nandra et al., 1997). By assuming that the broad line regions (BLR) are virialized, the black hole mass can be estimated by reverberation mapping techniques (Peterson, 1993) or the BLR size-luminosity relations (Kaspi et al., 2000).

The local correlations between MBH masses and galaxy properties (see the last section) suggest that MBH growth is correlated with galaxy evolution. It is the AGN phase, instead of the low accretion rate phase or BH merging processes, where MBHs grow predominantly. This is demonstrated by the match between the local BH mass function and the predicted mass function from integration of the cosmic evolution of AGN luminosity functions (Soltan, 1982; Yu & Tremaine, 2002; Shankar et al., 2004). As a result, any feedback from MBHs to their host galaxies most likely occurs in the AGN phase. Examples of energy feedback from AGN have been witnessed in different aspects of galaxy evolution. AGN may serve as the heating sources for cooling flows in clusters (e.g. McNamara & Nulsen, 2007). They may suppress star formation in their host galaxies and cause them to migrate from blue cloud to red-sequence in the color-magnitude plot (Nandra et al., 2007; Georgakakis et al., 2008) and they may account for “down-sizing” galaxy evolution (e.g. Cowie et al., 1996).

1.3 LIRGs – an Intense Star Formation Phase of Galaxy Evolution

(Ultra)luminous infrared galaxies ((U)LIRG; $L_{\text{infrared}} > 10^{(12)11} L_{\odot}$) (Rieke & Low, 1972) have been demonstrated to be a critical phase of galaxy stellar mass assembly over cosmic history. Although LIRGs are rare in the local universe, they show dramatic cosmic evolution and start to dominate the cosmic star formation density around $z = 1$ (Le Floch et al., 2005; Pérez-González et al., 2005).

Indications of possible relations between ULIRGs and high luminosity AGN were focused even before the discoveries of the relationships between MBH masses and galaxy properties. In the local universe, ULIRGs show enormous radiation outputs comparable to high-luminosity AGN and have an even higher spatial number density (Sanders & Mirabel, 1996). A large fraction of ULIRGs harbor AGN at their centers (e.g. Genzel et al., 1998).

1.4 Major Mergers – A Possible Driving Mechanism of MBH-Galaxy Coevolution

Major mergers may play a critical role in the coevolution of MBH and galaxy. The study of high-luminosity AGN shows elevated counts of companion galaxies (e.g. Bahcall et al., 1997). Morphological studies reveal interacting features in AGN host galaxies, even in those with apparently normal elliptical hosts (Canalizo et al., 2007). The study of the galaxy morphologies of LIRGs indicates that a significant fraction of LIRGs are currently experiencing major mergers and this fraction increases with infrared luminosity (Sanders & Mirabel, 1996).

To explain the correlations between MBH masses and galaxy properties, models involve the galaxy merging process to feed central MBHs and to trigger intense star formation in their host galaxies (e.g. Granato et al., 2004; Springel et al., 2005; Hopkins et al., 2006). The theoretical picture of the “cosmic cycle” of galaxy evolution (e.g. Hopkins et al., 2006) connects galaxy mergers, starbursts and nuclear accretion. Galaxy mergers induce gas inflow producing starbursts and obscured nuclear activity. As the feedback from the MBH starts to heat and expel the circumnuclear medium, the nuclear activity becomes visible as an optically bright AGN. Even-

tually, the nuclear activity and starbursts are terminated as the gas and dust are thoroughly expelled.

1.5 Infrared View of the Interplay between MBH and Galaxy

With the the overall goal to understand the interplay between MBH accretion and galaxy evolution, this dissertation presents a study of AGN and LIRGs mainly based on data obtained by the *Spitzer* Infrared Space Telescope.

For AGN, we have tested the unification model (§ 1.5.1 and Chapter 2), constrained the structure of the dusty torus (§ 1.5.2 and Chapter 3), presented the case study of AGN feedback in the radio galaxy M87 (§ 1.5.3 and Chapter 4) and discussed the general behavior of star formation in AGN host galaxies (§ 1.5.4 and Chapter 5). We have studied galaxy morphologies of a complete sample of LIRGs at $z \sim 1$ (§ 1.5.5 and Chapter 6). The conclusions and future works are presented in Chapter 7. Throughout this dissertation, we assume $H_0=70 \text{ km s}^{-1} \text{ Mpc}^{-1}$, $\Omega_0=0.3$ and $\Omega_\Lambda=0.7$.

1.5.1 AGN Classification and Unification Models

AGN produce strong continua over the whole electromagnetic spectrum. They are classified into radio-loud and radio-quiet types based on the strength of radio emission, with radio-loud AGN showing stronger radio-to-optical emission. Based on the bolometric luminosity, radio-loud AGN can be further divided into radio galaxies and radio quasars with quasars showing higher luminosity. The classification using radio morphologies produces two types of radio-loud AGN, FR I versus FR II. FR II objects have bright radio hot spots at the edge of extended radio lobes while FR I ones show the brightest emission near the galaxy centers. FR I/II classifications are correlated with the radio luminosity. For radio-quiet AGN, the high luminosity sources are called radio-quiet quasars and the low luminosity ones are called Seyfert galaxies. Based on the width of the permitted emission lines, AGN are divided into broad-line AGN and narrow-line AGN. Blazars are one special AGN type with a

very compact morphology and highly variable radiation. Note that there are no strict dividing lines between different types.

The AGN unification model tries to encompass all the types of AGN as described above. It proposes that the material surrounding the MBH is arranged in several different structures. At the very center, the MBH is fed by an accretion disk where soft-Xray/UV/optical emission arises. A hot corona lies above the accretion disk and couples to the accretion disk to produce the hard X-ray emission. In radio-loud AGN, the jet is launched in the vicinity of the MBH, probably within tens of Schwarzschild radii and produces strong radio emission. Radiation from the accretion-disk/corona ionizes the so-called broad line regions (BLR) which emit the broad emission lines. All the above structures are surrounded by a dusty torus with inner radius determined by the sublimation radius of dust. The dusty torus has a large covering factor and obscures the direct emission from inner structures along many lines of sight. Above the dusty torus are the narrow emission line regions (NEL), which are presumably free of obscuration by the torus. Although the details are not clear, the above arrangements of material surrounding MBHs are most likely the result of physical mechanisms transporting mass inward and angular momentum outward. Understanding their properties is crucial to our knowledge of MBH accretion and feedback from MBHs to host galaxies.

With the above structures, the AGN unification model hypothesizes that apparently distinct types of AGN harbor intrinsically similar nuclear engines that may be described by a small number of fundamental physical parameters. For example, it is proposed that orientation-dependent obscuration by a torus surrounding the central MBH, along with beamed emission of a radio jet, is responsible for the large diversity in the appearance of radio-loud AGN (as reviewed by e.g. Urry & Padovani 1995). For radio-quiet AGN, the jet is assumed to be absent. In the purest form of the model, the torus is always of the same geometry, so differences among sources arise only due to different inclinations relative to the observer and different AGN luminosities. To test this simple unification model for radio-loud AGN, we have carried out a test to compare far-IR and low frequency radio emission, two presumably

isotropic tracers of nuclear radiation (Shi et al., 2005, Chapter 2).

1.5.2 The Dusty Tori

As a crucial component of the unification model, the dusty torus plays a critical role in the AGN physics and the interplay between MBHs and host galaxies. A significant fraction of radiation from the accretion disk is absorbed by the dusty torus and reemits at infrared wavelengths. About 10-20% of the cosmic infrared background is contributed by infrared emission from AGN (Fadda et al., 2002). The obscuration by a dusty torus is also invoked in the X-ray background synthesis model to fit the X-ray background spectrum, which predicts that 75% of the X-ray background is contributed by obscured accretion (Fabian, 2004). The dusty torus also collimates feedback (i.e. outflow) from the central MBH, as evident from the ionization cones seen in local edge-on AGN (Pogge, 1988). With the inner radius about tenth of a pc and outer radius of tens or probably hundreds of pc, the dusty torus acts as a bridge connecting host galaxy and accretion disk and transporting material from galaxy down to the central accretion disks (Wada, 2004).

Although spatially resolved imaging may be the most direct way to study the structure of the dusty torus, it is limited to a few nearby Seyfert galaxies (Jaffe et al., 2004; Tristram et al., 2007). As a form of direct emission by the dusty torus, infrared radiation provides a powerful way to understand the properties of these structures. The shape of the infrared (IR) spectral energy distribution (SED) can be used to indicate how the material in the torus is organized. Based on IR SED fitting, there are at least three different possibilities: compact (Pier & Krolik, 1992, 1993), extended (Granato & Danese, 1994; Granato et al., 1997) and cloudy (Krolik & Begelman, 1986; Rowan-Robinson, 1995; Nenkova et al., 2002) structure models all fit the data well (assuming an extra component of star formation in the compact model). In the unification model, the silicate feature is predicted to be in absorption for type 2 AGN and in emission for type 1 AGN. Although the presence of the silicate absorption feature in type 2 AGN has long been confirmed by observations (Roche et al., 1991), the silicate emission feature in type 1 AGN was not clearly detected

until the *Spitzer* observations (Siebenmorgen et al., 2005; Hao et al., 2005). To probe the structure of the dusty torus further, we have carried a study of the behavior of the silicate features in various types of AGN (Shi et al., 2006b, Chapter 3).

1.5.3 AGN Feedback: the Case Study of M87

The powerful jets in radio-loud AGN play critical feedback roles in their host galaxies and environments. In galaxy clusters, the kinetic energy carried by a jet is thought to be deposited into the intracluster medium to reheat the cooling flow.

Because it is relatively nearby ($d=16\text{Mpc}$, 78 pc arcsec^{-1} ; Tonry, 1991), M87 is one of the most readily studied examples of feedback by radio jets. Radio observations have revealed multiple structures in M87 possibly related to the mechanism of interaction between MBHs and the surrounding media. The radio jet is launched close to the MBH within 30 Schwarzschild radii (Junor et al., 1999). The powerful jet is disrupted in a so-called inner region ($1'.5\times2'.0$), which forms the radio lobe composed of the North-preceding (Np) lobe and South-following (Sf) lobe (Turland, 1975; Forster, 1980). High resolution radio images of this region have revealed complex structure, with knots, filaments, edges and rings (e.g. Owen et al., 1980; Hines et al., 1989), probably the manifestation of the interaction between the jet and the surrounding medium. This inner region is embedded in a halo with a diameter up to $\sim15'.0$ (e.g. Mills, 1952; Baade & Minkowski, 1954; Rottmann et al., 1996). Two spectacular outflows originating from the inner region terminate at the boundary of the radio halo (Owen et al., 2000). In the subarcsecond *Chandra* X-ray image, two outflow-like structures extend from the nucleus east and southwest, respectively, possibly created by buoyant bubbles (e.g. Young et al., 2002; Forman et al., 2006).

The spectrum of the synchrotron emission contains important physical information about the emitting regions, such as the age, the minimum kinetic energy and the magnetic field, which give significant insights into the interplay between jet and intracluster medium. IR photometry is critical to constrain the synchrotron emission model for extragalactic jets. This is not only because it fills the gap in the SED between radio and optical wavelengths, but also because in many circumstances,

the break frequency of the synchrotron model resides in the IR regime. Ground-based mid-IR observations have only detected the emission from the nucleus and the brightest knots of the jet in M87, and are consistent with synchrotron emission models (Perlman et al., 2001b; Whysong & Antonucci, 2004). The *Infrared Space Observatory* (*ISO*) mid-IR images have marginally detected the lobe (Xilouris et al., 2004). Other features, such as the individual filaments in the lobe, are only detected weakly in the near-IR, but not yet in the mid-IR (Stocke et al., 1981; Smith et al., 1983; Neumann et al., 1995; Perlman et al., 2001a). *ISO* and the *Infrared Astronomical Satellite* (*IRAS*) observations of M87 reveal excess far-infrared emission above the synchrotron interpolation from the radio (Haas et al., 2004; Xilouris et al., 2004). However, the available information in the infrared has lagged far behind the exquisite and very deep images available in the radio, optical, ultraviolet, and X-ray. To help remedy this situation, we present and analyze infrared images of M87 obtained with the Infrared Array Camera (IRAC; Fazio et al., 2004) and the Multiband Imaging Photometer (MIPS; Rieke et al., 2004) on *Spitzer* (Shi et al., 2007a, Chapter 4).

1.5.4 Star Formation Rate in AGN Host Galaxies

The interplay between MBHs and star formation is now recognized as a critical ingredient in galaxy evolution, as demonstrated by the correlations between the blackhole masses and the bulge properties of their host galaxies (M - σ relation) (Kormendy & Richstone, 1995; Magorrian et al., 1998; Gebhardt et al., 2000; Ferrarese & Merritt, 2000). However, because the star formation rate (SFR) is difficult to measure around active galactic nuclei (AGN), we are unable to answer basic questions about the interrelations between the two processes: in what star-forming environments does AGN activity tend to be triggered? Does feedback from one process trigger or quench another?

The current understanding of the interplay between MBH and star formation comes mainly from several theoretical hypotheses, such as: 1.) intense SF in the host galaxy drives the inward mass flow that activates a MBH into an active galactic

nucleus (AGN) (e.g. Granato et al., 2004); 2.) AGN feedback enhances the host galaxy SF, leading to an ultraluminous stage (e.g. Silk, 2005); 3.) negative feedback from an AGN quenches SF and regulates the bulge mass (Di Matteo et al., 2005); and 4.) both SF and MBH accretion are triggered by the inflowing gas driven by a merging process (Springel et al., 2005). These possibilities are not necessarily mutually exclusive but may occur in a time sequence. They are difficult to explore in depth with observations because of the difficulty in determining the level of star formation around the bright glare of a central quasar.

The mid-IR aromatic features are prominent at 3.3, 6.2, 7.7, 8.6, 11.3 and 12.7 μm (Gillett et al., 1973). They are seen in various Galactic environments including HII regions, diffuse interstellar clouds, planetary nebulae, reflection nebulae and photodissociation regions (PDRs) and in extragalactic objects (for a review, see Tielens et al., 1999). The aromatic emission in normal star-forming galaxies is similar to that in Galactic star-forming regions (e.g. Genzel et al., 1998; Clavel et al., 2000), with a well understood correlation to the SFR (e.g. Roussel et al., 2001; Dale & Helou, 2002). The aromatic features in active galaxies have much lower equivalent width (EW) than in star-forming galaxies (e.g. Roche et al., 1991; Clavel et al., 2000), implying the destruction of the aromatic carriers by the harsh nuclear radiation or the inability of the nuclear radiation to excite the aromatic features. Evidence for excitation of the aromatic features by star formation in active galaxies comes from spatially resolved mid-IR spectra of nearby examples, where the observed aromatic emission is mainly from the disk (e.g. Cutri et al., 1984; Desert & Dennefeld, 1988; Voit, 1992; Laurent et al., 2000; Le Floch et al., 2001). Various infrared diagnostics have been developed based on a correlation of aromatic feature strength with star forming activity to discriminate the power sources (star formation versus nuclear activity) for luminous infrared galaxies (LIRGs; $L_{\text{IR}} > 10^{11} L_{\odot}$) (e.g. Genzel et al., 1998; Laurent et al., 2000; Tran et al., 2001; Peeters et al., 2004). To understand the general behavior of star formation in AGN host galaxies, we have presented a study of 7.7 and 11.3 μm aromatic features in a large sample of local AGN, including 3CR radio-loud AGN, PG quasars and 2MASS red quasars (Shi et

al., 2007b, Chapter 5).

1.5.5 Morphologies of LIRGs

Two fundamental aspects of galaxy formation and evolution are mass assembly and morphology transformation. While mass assembly is often accompanied by strong episodes of star formation, the morphology of a galaxy reflects its dynamical history and evolution. For example, different Hubble types are associated with different motion patterns of stars and gas and different histories of star formation. The interplay between these two processes may play a crucial role in galaxy formation and evolution: the dynamics, indicated by the morphology, drives the star formation, while the depletion of gas from star formation as well as feedback from young stars through supernovae and stellar winds may re-shape the galaxy morphology. Thus, in the local Universe, later-type galaxies are gas-rich and the sites of elevated star formation (for a review, see Kennicutt, 1998), while the more extreme star-forming galaxies often show peculiar morphologies, resulting from collisions and mergers (e.g. Soifer et al., 1984; Cutri & McAlary, 1985; Sanders et al., 1988; Armus et al., 1987; Kleinmann et al., 1988; Barton et al., 2000).

The comoving star formation density rises by an order of magnitude from $z = 0$ to $z \sim 1$ (Lilly et al., 1995; Ellis et al., 1996; Steidel et al., 1999; Hopkins, 2004). In the high-redshift universe, the high rate of star formation seems to be associated with a large fraction of peculiar and morphologically disturbed galaxies. Deep surveys, especially those carried out by the Hubble Space Telescope (*HST*), reveal that the fraction of irregular and interacting galaxies increases dramatically toward high redshift, from around 4% (Marzke et al., 1998) in the local universe to more than 80% at $z \geq 2$ (Conselice et al., 2005). Even the high-redshift galaxies classified as traditional Hubble types still show many peculiar features, with tidal or disturbed structures and distorted disks.

The Hubble (1926, 1936) galaxy classification as modified by Sandage (1961), Sandage & Tammann (1987), Sandage & Bedke (1994), van den Bergh (1960a,b) and de Vaucouleurs (1959), has achieved remarkable success in categorizing local

galaxies with normal morphology (for a review, see Roberts & Haynes, 1994). However, the Hubble scheme is unable to characterize the level of irregularity that is much more common in the high redshift Universe (Driver et al., 1995, 1998; Abraham et al., 1996a,b; Brinchmann et al., 1998; Cassata et al., 2005). To understand how morphologies and star formation are coupled to drive galaxy evolution at high redshift, we have used a quantitative classification method, called the *CA* system, to measure the galaxy morphologies of a complete sample of LIRGs at $z \sim 1$ in the Ultra Deep Field (UDF). The success in distinguishing between different Hubble types; the robust measurements of parameters over a large range of redshift range of galaxy types especially quantifying the irregularity of peculiar galaxies; and the strong relations between the parameters and physical properties such as color, all make the *CA* system useful for classifying galaxies found in deep fields. The extremely deep *HST* images in the UDF allow us to apply the *CA* system to analyze the optical morphologies of the $z \sim 1$ LIRGs down to a limiting surface brightness comparable to those of local LIRGs. This work is discussed in Shi et al. (2006a, Chapter 6).

CHAPTER 2

Far Infrared Observations of Radio Quasars and FR II Radio Galaxies

2.1 Introduction

In this Chapter, we combine IR measurements of radio-loud AGN obtained with the Multiband Imaging Photometer for *Spitzer* (MIPS) (Rieke et al. 2004) and previous data from the *Infrared Astronomical Satellite* (*IRAS*) and *Infrared Space Observatory* (*ISO*). We use these observations to show that the IR emission is usually dominated by radiation from dust heated by the AGN. Thus we can use the far infrared properties of these sources to gain new insights to unification models for radio-loud AGN.

This chapter is organized as follows. Chapter 2.2 describes the sample selection, observation and data reduction. The AGN classification of the sample is given in Chapter 2.3.1 while Chapter 2.3.2 determines the non-thermal contribution to the IR emission. Chapter 2.4 discusses the energy source (star formation vs. AGN) for thermal IR emission and tests of the unification model. The final conclusions are included in Chapter 2.5.

2.2 Observations

2.2.1 The Sample and Extended Sample

We have used MIPS to observe twenty FR II radio galaxies and steep spectrum radio quasars listed in Tables 2.1 and 2.2. The sample is drawn from Neugebauer et al. (1986) and Golombek et al. (1988), with priority on objects at $z < 0.4$ and with good *Hubble Space Telescope* (*HST*) images. To complement these measurements, we defined an extended sample, consisting of the 27 additional 3CR sources listed in Table 2.3, all of which are detected by *IRAS* or *ISO* at least at two wavelengths

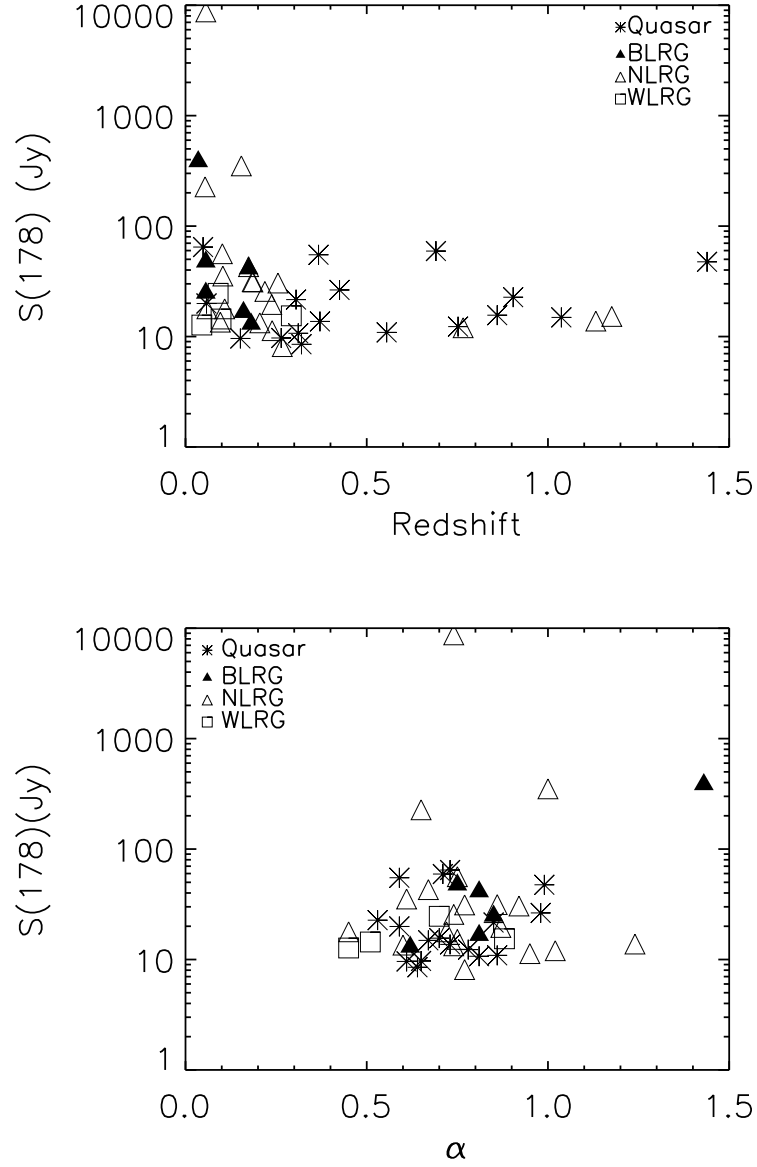


Figure 2.1 The distributions of sources in the plane of the 178 MHz flux versus redshift (top panel) and 178 MHz flux versus spectral index α (bottom panel).

between $10\ \mu\text{m}$ and $200\ \mu\text{m}$. The *IRAS* data are from the NASA/IPAC Extragalactic Database (NED) and the *ISO* data are from Haas et al. (2004), van Bemmelen et al. (2001) and NED. The uncertainties in the *ISO* data from Haas et al. (2004) are quoted as 10-30%; in this paper we adopt 30% uniformly. Except for Pic A and 3C 218 the sources belong to the parent 3CR sample. For this study, we divide the sample into two subsamples as described in Section 2.3.1: Type I sources including radio quasars and broad line radio galaxies (BLRG) and Type II sources composed of narrow line radio galaxies (NLRG) and weak line radio galaxies (WLRG).

To investigate possible selection biases for our sample, in Figure 2.1 we plot the distribution of all the sources in the plane of 178 MHz flux density versus redshift (top box) and 178 MHz flux density versus spectral index α (bottom box; α is defined as $f_\nu \propto \nu^{-\alpha}$ between 38 MHz and 750 MHz). The top box indicates for our sample that the 178 MHz flux density spans a range from 6 Jy to 10^4 Jy and the redshift a range from 0.03 to 1.4. From this figure, we see that the flux density distributions of Type I and II sources are similar. The Kolmogorov-Smirnov (K-S) test indicates a probability of 82% that the two subsamples have the same distributions. However, the sample contains many more high redshift ($z > 0.3$) Type I sources, mainly radio quasars, than high-redshift type II sources. The bottom box indicates that the spectral indices of the two sub-samples are mainly in the range between 0.5 and 1.2. The K-S test gives a probability of 89% that both types have the same distributions of spectral index. Based on Figure 2.1, we find that our sample is not biased in AGN characteristics except that there are relatively more Type I sources at high redshift and thus high luminosity.

Table 2.1. MIPS Measurements of Steep Spectrum Radio Sources

source	Integ. time(sec)	24 μ m(mJy)	Integ. time(sec)	70 μ m(mJy)
(1)	(2)	(3)	(4)	(5)
3C48	48.2	131.0 ± 0.09	37.7	696 ± 8
3C61.1	48.2	5.0 ± 0.07	125.8	30 ± 4
PicA	165.7	130 ± 0.04	125.8	171 ± 5
3C171	165.7	7.5 ± 0.05	125.8	19 ± 3
3C173.1	165.7	0.51 ± 0.06	125.8	1.7 ± 2
3C218	165.7	8.6 ± 0.06	125.8	118 ± 5
3C219	165.7	12.7 ± 0.07	125.8	29 ± 5
3C236	165.7	17.4 ± 0.07	125.8	50 ± 3
3C249.1	48.2	45.0 ± 0.07	125.8	57 ± 2
3C277.1	48.2	19.8 ± 0.07	125.8	20 ± 2
3C284	165.7	24.6 ± 0.07	125.8	80 ± 2
3C303.1	165.7	7.6 ± 0.05	125.8	27 ± 15
3C315	165.7	1.9 ± 0.05	125.8	28 ± 4
3C323.1	48.2	33.0 ± 0.08	125.8	30 ± 2
3C327	165.7	245 ± 0.07	125.8	468 ± 7
3C348	165.7	0.25 ± 0.07	125.8	28 ± 5
3C349	165.7	≤ 0.15	125.8	7 ± 3
3C351	48.2	103 ± 0.07	125.8	182 ± 3
3C381	165.7	46 ± 0.05	125.8	40 ± 3
3C388	165.7	2.34 ± 0.05	125.8	16 ± 3

Note. — Nominal photon-noise errors are given to show the intrinsic signal to noise ratio for the measurements. Systematic calibration uncertainties are discussed in the text. The upper limit is at 3σ significance. The integration time at 160μ m was 84 seconds per source. Sources detected at this wavelength are: 3C48, 1147 ± 93 ; PicA, 475 ± 40 mJy; 3C218, 211 ± 31 mJy; 3C327, 425 ± 38 mJy; 3C351, 182 ± 21 mJy

Table 2.2. Other Properties of the MIPS Sample

source	M_B	Type	z	F_{5t} (mJy)	F_{5c} (mJy)	Ref	Size (kpc)	Γ_X	X-ray	Line ratio	Ref
(1)	(2)	(3)	(4)	(5)	(6)	(7)	(8)	(9)	(10)	(11)	(12)
3C48	-26.5	Q	0.367	$5,330 \pm 70$	896	A91	2.4	2.12	2.39	-0.013	GW94
3C61.1	-21.3	NLRG	0.186	$1,900 \pm 90$	2.64	ZB95	535			0.47	La96
PicA	-19.5	BLRG	0.035	$15,500 \pm 470$	1004	ZB95	281	1.69	8.66	0.62	Ta93
3C171	-22.0	NLRG	0.238	$1,210 \pm 60$	1.68	ZB95	31			0.79	ST03
3C173.1	-22.4	WLRG	0.292	770 ± 120	7.21	ZB95	244				
3C218	-22.4	NLRG	0.054	13,100	245	ZB95		1.79	0.224	-0.125	Sm96
3C219	-22.5	BLRG	0.174	$2,270 \pm 110$	49.2	ZB95	441	1.58	1.62	0.32	La96
3C236	-21.6	WLRG	0.098	$1,330 \pm 130$	141	ZB95	3956			0.57	La96
3C249.1	-26.8	Q	0.311	780 ± 40	76	K89	89	1.77	1.49	0.97	BO84
3C277.1	-24.7	Q	0.320	$1,040 \pm 50$			6.5	1.63	0.691	0.20	GW94
3C284	-21.5	NLRG	0.239	685 ± 60	3.2	Gi88	635				
3C303.1	-22.0	NLRG	0.267	457 ± 50	<4.7	ZB95	9.6				
3C315	-21.4	NLRG	0.108	$1,260 \pm 60$	<150	Gi88	257				
3C323.1	-24.3	Q	0.264	880	32	K89	267			0.71	BO84
3C327	-21.9	NLRG	0.103	$2,740 \pm 140$	30.4	ZB95	369			1.22	de92
3C348	-22.2	NLRG	0.154	$11,800 \pm 590$	10.2	ZB95	286				
3C349	-21.1	NLRG	0.205	$1,130 \pm 60$	25.0	ZB95	257				
3C351	-27.7	Q	0.371	$1,200 \pm 60$	8.0	K89	277	1.69	1.36	-0.016	CB96
3C381	-22.0	BLRG	0.160	$1,280 \pm 50$	5.12	ZB95	177			1.26	GO78
3C388	-23.1	WLRG	0.090	$1,760 \pm 40$	59.0	ZB95	48			0.49	La96

Note. — Column (3): The emission-line type, 'NLRG'=Narrow line radio galaxy, 'BLRG'=Broad line radio galaxy, 'WLRG'=weak line radio galaxy, 'Q'=Quasar. Column (5): The 5 GHz flux density in units of mJy. Column(6): The radio core flux at 5 GHz in the units of mJy. Column (7): References for Column (6): A91 - Akujor et al. (1991); Gi88 - Giovannini et al. (1988); K89 - Kellermann et al. (1989); ZB95- Zirbel & Baum (1995). Column (8): The linear radio size in units of kpc. The references for radio sizes are Akujor et al. (1995), Allington-Smith (1984), Gavazzi et al. (1978) and Nilsson et al. (1993). Column (9): The spectral index of hard X-ray emission over 2-10 keV in the rest frame, assuming a power law SED. Column (10): The rest-frame 2-10 keV absorption-corrected X-ray flux in the central $2.5''$ region. Units are $10^{-12} \text{ ergs s}^{-1} \text{ cm}^{-2}$. Column (11): The logarithm of the ratio of the intensity of $[\text{O III}]\lambda 5007$ to $\text{H}\beta$. Column (12): References for the Column (11): BO84 - Boroson & Oke (1984); CB96 - Corbin & Boroson (1996); de92 - de Grijs et al. (1992); Fa89 - Fanti et al. (1989); Fe97 - Fernini et al. (1997); GO78 - Grandi & Osterbrock (1978); GW94 - Gelderman & Whittle (1994); H89 - Hough et al. (1989); La96 - Lawrence et al. (1996); S87 - Saikia et al. (1987); Sm96 - Simpson et al. 1996; ST03 - Solórzano-Iñárrrea & Tadhunter (2003); Ta93 - Tadhunter et al. (1993); V98 - van Bemmelen et al. (1998)

Table 2.3. The Extended Sample of Radio Galaxies and Quasars

source	M_B	Type	z	F_{5t} (mJy)	F_{5c} (mJy)	Ref	F_{24} (mJy)	F_{70} (mJy)	F_{160} (mJy)	Size (kpc)	Γ_X	X-ray	Line ratio	Ref
(1)	(2)	(3)	(4)	(5)	(6)	(7)	(8)	(9)	(10)	(11)	(12)	(13)	(14)	(15)
3C2	-27.8	Q	1.037	$1,400 \pm 70$	50	S87		91 ± 30		37				
3C20	-21.9	NLRG	0.174	$4,150 \pm 210$	2.6	Fe97		107 ± 35	162 ± 140	146				
3C33.1	-22.2	BLRG	0.181	860 ± 40	14.02	ZB95	42 ± 18	45 ± 15		614				
3C47	-25.6	Q	0.425	$1,090 \pm 50$	77.9	V98	42 ± 30	117 ± 37	165 ± 71	353	1.28	1.55	-0.18	CB96
3C65	-24.9	NLRG	1.176	770 ± 120	0.50	ZB95	24±193	110 ± 20	42 ± 34	134				
3C79	-23.9	NLRG	0.255	$1,300 \pm 70$	10.00	ZB95	59 ± 15	141 ± 26		322			0.40	Sc65
3C109	-25.7	Q	0.305	$1,630 \pm 160$	305.85	ZB95	165 ± 41	208 ± 34		403	1.69	8.66		
3C111	-23.8	Q	0.049	$7,870 \pm 393$			213 ± 54	342 ± 100		244				
3C234	-22.3	NLRG	0.184	$1,530 \pm 50$	95.79	ZB95	259 ± 75	269 ± 54		317			0.48	Sc65
3C277.2	-23.9	NLRG	0.766	480	<15.04	ZB95		122 ± 42		379				
3C293	-21.5	WLRG	0.045	$1,857 \pm 40$	100	Gi88	42 ± 6	305 ± 31		70				
3C298	-32.2	Q	1.439	$1,450 \pm 70$			37 ± 12	191 ± 27	238 ± 74	15	1.75	2.25		
3C309.1	-29.5	Q	0.904	$3,730 \pm 190$	2350	H89	36±133	114 ± 13	251 ± 84	15	1.40	1.44	0.14	La96
3C318	-25.1	Q	0.752	750	<44.43	ZB95		197 ± 64	379 ± 114	6.8				
3C321	-22.3	NLRG	0.0961	$1,210 \pm 120$	30	Gi88	326 ± 6	1006 ± 46		482				
3C325	-24.9	Q	0.860	830 ± 120	2.4	Fe97	27±63	154 ± 52	35±46	114				
3C332	-23.2	Q	0.1515	830 ± 42			18 ± 5	52 ± 30		224				
3C334	-28.2	Q	0.555	620	159.5	V98		75 ± 21	55 ± 24	276	1.59	0.935		
3C368	-26.5	NLRG	1.132	210 ± 30	<0.72	ZB95	39±77	87 ± 28	79 ±82	60				
3C380	-28.2	Q	0.691	$7,450 \pm 370$	7447	H89	13 ± 7.5	55 ± 17	78 ± 33	49	1.32	2.48	0.15	GW94
3C382	-23.1	Q	0.058	$2,220 \pm 111$	188	Gi88	93 ± 23	107 ± 31		188				
3C390.3	-20.8	BLRG	0.056	$4,450 \pm 79$	344.37	ZB95	320 ± 7.6	237 ± 6		208			-0.24	La96
3C403	-21.7	NLRG	0.059	$2,060 \pm 100$			220 ± 30	503 ± 52		103				

Table 2.3 (cont'd)

source	M_B	Type	z	F_{5t} (mJy)	F_{5c} (mJy)	Ref	F_{24} (mJy)	F_{70} (mJy)	F_{160} (mJy)	Size (kpc)	Γ_X	X-ray	Line ratio	Ref
(1)	(2)	(3)	(4)	(5)	(6)	(7)	(8)	(9)	(10)	(11)	(12)	(13)	(14)	(15)
3C405	-21.7	NLRG	0.056	371,000 \pm 18,500	314.07	ZB95	834 \pm 113	2771 \pm 56	430 \pm 230	123	0.89	18.5	1.11	Ta94
3C433	-21.7	NLRG	0.102	3,710 \pm 190	5	Gi88	193 \pm 48	319 \pm 93		87				
3C445	-20.6	BLRG	0.056	2,030 \pm 100	88.52	ZB95	315 \pm 47			730			1.11	Ta93
3C459	-23.0	NLRG	0.219	1,350 \pm 70	1138.26	ZB95		962 \pm 176	947 \pm 351	27				

Note. — Column (3): The emission-line type, 'NLRG'=Narrow line radio galaxy, 'BLRG'=Broad line radio galaxy, 'WLRG'=weak line radio galaxy, 'Q'=Quasar. Column (5): The 5 GHz flux density in units of mJy. Column(6): The radio core flux at 5 GHz in units of mJy. Column (7): References for the Column (6): Fe97 - Fernini et al. (1997); Gi88 - Giovannini et al. (1988); H89 - Hough et al. (1989); S87 - Saikia et al. (1987); ZB95- Zirbel & Baum (1995); V98 - van Bemmle et al. (1998). Column (8), (9) and (10): The flux with uncertainty at 24 μ m, 70 μ m, 160 μ m, respectively. Bold indicates the sources are not detected to a 3-sigma level. Column (11): The linear radio size in units of kpc. The references for radio sizes are Akujor et al. (1995), Allington-Smith (1984), Gavazzi et al. (1978) and Nilsson et al. (1993). Column (12): The spectral index of the hard X-ray emission at 2-10 keV in the rest frame, assuming a power law SED. Column (13): The rest-frame 2-10 keV absorption-corrected X-ray flux in the central 2.5 '' region. Units are 10^{-12} ergs s $^{-1}$ cm $^{-2}$. Column (14): The logarithm of the ratio of the intensity of [O III] λ 5007 to H β . Column (15): References for Column (14): CB96 - Corbin & Boroson (1996); Fa89 - Fanti et al. (1989); GW94 - Gelderman & Whittle (1994); La96 - Lawrence et al. (1996); Sc65 - Schmidt (1965); Ta93 - Tadhunter et al. (1993); Ta94 - Tadhunter et al. (1994).

2.2.2 Infrared Data

Our observations were made with the standard MIPS small field photometry mode. The effective integration time for each source is listed in Table 2.1. The data were reduced with the MIPS instrument team Data Analysis Tool (DAT) version 2.73 (Gordon et al. 2004a, b).

To obtain the 24 μm fluxes, we performed aperture photometry using the IDL-based image processing package IDP3 (Schneider & Stobie 2002). We set the radius of the object aperture to 6 pixels (15.0'') and we measured the background to be the median flux in a 5 pixel (12.5'') wide annulus, at a central radius 11 pixels (27.4'') from the centroid of the target. Contamination from other sources within the sky annulus was masked by hand. We multiplied by a factor of 1.146 to correct the measured values for the portion of the point spread function lying outside the source aperture. The pixel-to-pixel fluctuations in the background region were used to calculate the 1-sigma uncertainties. The results are listed in Table 2.1. Most of the sources are detected at nominally very high signal-to-noise ratios. In addition, there is a calibration uncertainty of up to 10%.

The 70 and 160 μm photometry was reduced in a similar manner. Additional processing steps, such as bad column removal and time filtering, were performed for 70 μm data. The radius of the object aperture at both wavelengths was 3.0 pixels (30'' at 70 μm and 48'' at 160 μm) and the inner and outer radii of the background region were 4 pixels and 8 pixels (40'' and 80'' at 70 μm ; 64'' and 128'' at 160 μm), respectively. Aperture correction factors of 1.3 and 1.5 were applied to the 70 and 160 μm measurements respectively. The results of the 70 μm photometry are also listed in Table 2.1. The five sources detected (in a 3-pixel aperture) at 160 μm are listed in the footnotes to Table 2.1. There is a calibration uncertainty of up to 20% at both 70 and 160 μm .

To combine the extended sample with the MIPS sample, we need to interpolate the *IRAS* and *ISO* data to calculate the fluxes at the MIPS bands. We use the data points at the two wavelengths closest to the MIPS band for interpolation.

Multiple observations at one wavelength are averaged. We assume power law SEDs to interpolate to the MIPS band and also to propagate the errors. The resulting fluxes are listed in Table 2.3. Additional errors can arise from the difference between the power law and the real SEDs. By comparing interpolations using a suite of blackbody ($T \geq 40$ K) and power law SEDs, we estimate that such errors should be $< 30\%$.

2.2.3 HST Images

We retrieved archived *HST* data for all sources in our sample, except for 3C 218 which has not been observed. The images were taken with the Wide Field and Planetary Camera 2 (WFPC2), generally with the F555W or F702W filters. The data were processed through the PODPS (Post Observation Data Processing System) pipeline to remove bias and flat-field artifacts (Biretta et al. 1995). Individual exposures in an observation were combined to remove cosmic ray events. For observations with only one exposure, the cosmic rays were masked by interpolating over them.

2.2.4 Chandra Data

We retrieved data from the Chandra archive for 19 sources observed with the Advanced CCD Imaging Spectrometer (ACIS). Data reduction and analysis were performed using CIAO 3.0.2. The level 2 event file was made from the level 1 event file after correction for gain, aspect and charge transfer inefficiency, and also after PHA randomization and destreaking. We used the light curve to remove solar flares. Inspection of the images showed that there was severe pileup in the central region of 3C 390.3 where a hole without counts was present. The nuclei of 3C 348 and 3C 173.1 had too few counts for our analysis and they were dropped from the X-ray sample. For the remaining sources, we extracted the spectra of the nuclear region with an aperture diameter of $2.5''$ around the peak pixel and then fitted the rest-frame 2-10 keV spectra using an absorbed power law. Finally we computed the

absorption-corrected hard-X-ray fluxes, which are listed in Column (10) of Table 2.2 and Column (13) of Table 2.3. The photon spectral indices are listed in Column (9) of Table 2.2 and Column (12) of Table 2.3.

2.3 Analysis

2.3.1 Division of the sample into quasars and galaxies

We classified the sources as Type I (radio quasar or BLRG) or Type II (NLRG or WLRG) on a consistent basis. Emission line types were obtained from the literature. The division between radio quasars and BLRG was based on absolute B magnitude. We retrieved the apparent Johnson B magnitude from NED, originally from Sandage et al. (1965), Smith & Heckman (1989) and de Vaucouleurs et al. (1991). For those sources without available blue magnitudes, we took V magnitudes from Spinrad et al. (1985) and assumed $\langle B-V \rangle = 0.3$ mag. The conversion formula from the apparent magnitude to absolute magnitude is:

$$M = m - 5\log(D_L) + 5 - K(z) - A_m \quad (2.1)$$

where M , m are absolute magnitude and apparent magnitude, D_L is the luminosity distance, $K(z)$ is the K-correction at the redshift z and A is the Galactic extinction. A_m is computed using NED. The majority of our sample are in luminous elliptical galaxies; we obtained K-corrections for such galaxies from Pence (1976). We assumed $H_0 = 75 \text{ km s}^{-1} \text{ Mpc}^{-1}$, $\Omega_M = 0.3$ and $\Omega_\Lambda = 0.7$. The resultant absolute blue magnitudes are listed in Column (2) of Table 2.2 and 2.3. Radio quasars have power law SEDs, typically with a spectral index of 0.5. Therefore, we also calculated the absolute B magnitude for all sources using the K-correction based on a power law SED with a spectral index of 0.5

We defined as quasars those broad line sources with an absolute B magnitude < -23 mag and as BLRGs those with fainter absolute B magnitudes. Only four sources have ambiguous classifications. 3C 318, 3C 325, 3C 332 and 3C 382 were classified as radio quasars using the K-correction based on the SED of normal elliptical galaxies,

while they were radio galaxies if we assumed their optical SEDs were power laws. The remaining galaxies without broad lines were classified as NLRG or WLRG according to the strength of their emission lines. Column (3) of Table 2.2 and 2.3 list the results. There are 17 radio quasars, 6 BLRG, 20 NLRG and 4 WLRG. We emphasize that the ambiguous classifications of a few sources do not affect the results of this paper.

2.3.2 Spectral Energy Distribution

For each source, we used NED to compile the SED from radio to millimeter, as presented in Figure 2.2. The radio and millimeter-wave SEDs of these sources are smoothly steepening power laws associated with synchrotron emission. This behavior provides the basis for us to extrapolate to determine the non-thermal contribution to the IR emission. This process requires a synchrotron radiation model and good high-frequency data, since the break frequency of the synchrotron emission occurs at ~ 1 GHz (Polletta et al. 2000). We used a parabola approximation (Andreani et al. 2002) to fit the synchrotron emission. The spectrum in this model is given by

$$\log F_\nu = C + \frac{1}{2A}(\log \nu - \log \nu_t)^2 \quad (2.2)$$

where C is a constant, ν_t characterizes the spectral break (i.e., where the nominal optical depth is unity) and $\frac{1}{A} = 2\alpha_1 - \alpha_2$, where α_1 and α_2 are the spectral indices above and below the break, respectively. For each source, we adjusted C , A and ν_t to fit all data at wavelengths longer than 1 mm. Figure 2.2 shows the results; the extrapolation is well constrained since most sources have high-frequency data and the model can usually fit the data well. The IR emission is generally well above the non-thermal extrapolation. Five sources, 3C 218, 3C 315, 3C 348, 3C 349 and 3C 380, seem to be exceptions: they have IR fluxes below the non-thermal extrapolation at one or more bands. Except for 3C 380, the remaining sources have no sub-millimeter observations and thus their IR emission can be thermal emission by dust if the radio spectrum turns over at very high frequencies. Since their 24 μ m to 70 μ m IR color is redder than the non-thermal continuum, we argue for the thermal

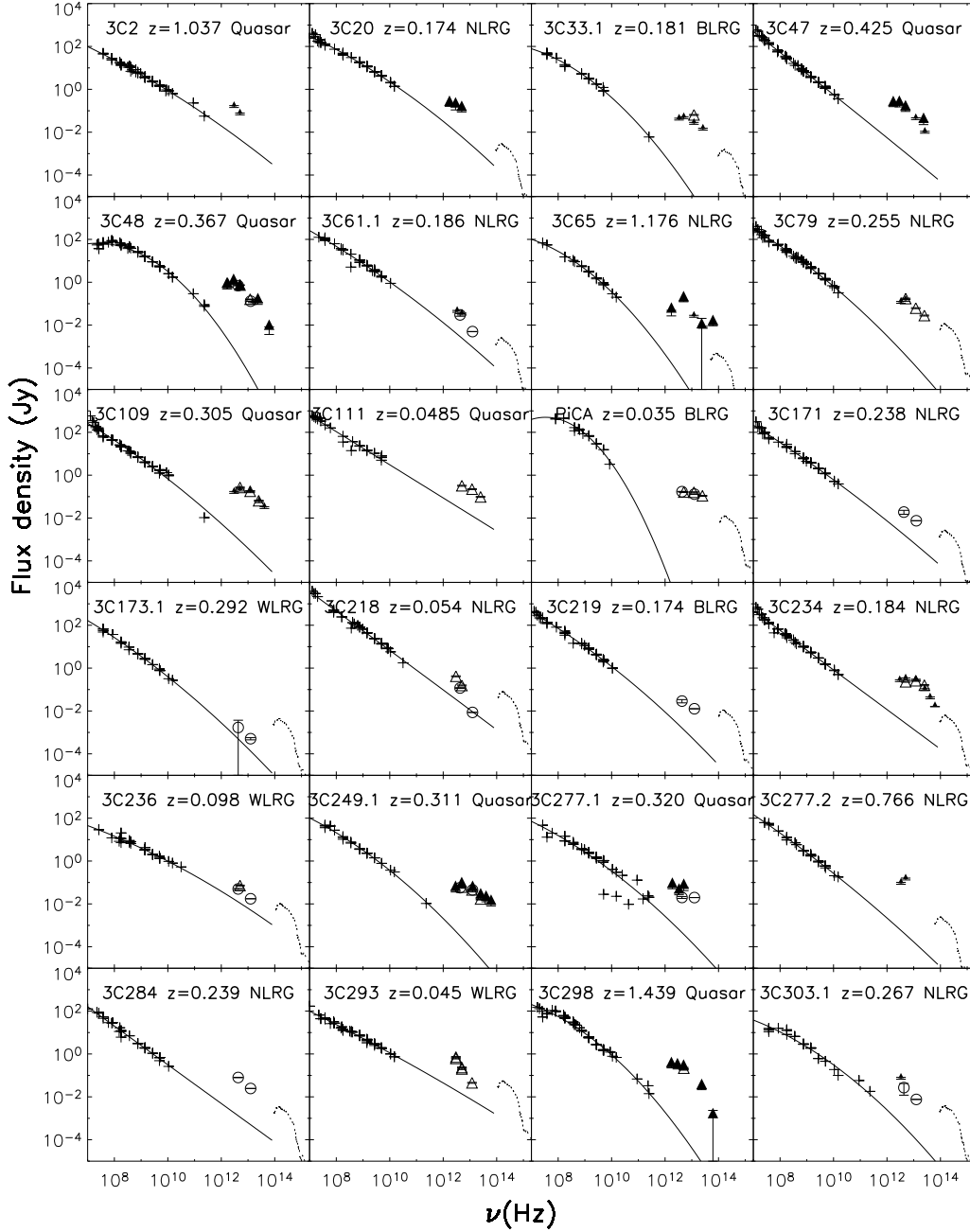


Figure 2.2 The spectral energy distributions of all sources. The 1-sigma error is used in the plot. The crosses are the radio and millimeter photometry data from NED. The solid line is the parabola model for the synchrotron emission. The open circle, open triangle, and filled triangle denote MIPS, *IRAS* and *ISO* data, respectively. The dotted line for radio galaxies is the template of stellar light for a normal elliptical galaxy, normalized to the apparent B magnitude. 'Quasar', 'BLRG', 'NLRG' and 'WLRG' indicate Quasar, broad line radio galaxies, narrow line radio galaxies and weak line radio galaxies, respectively.

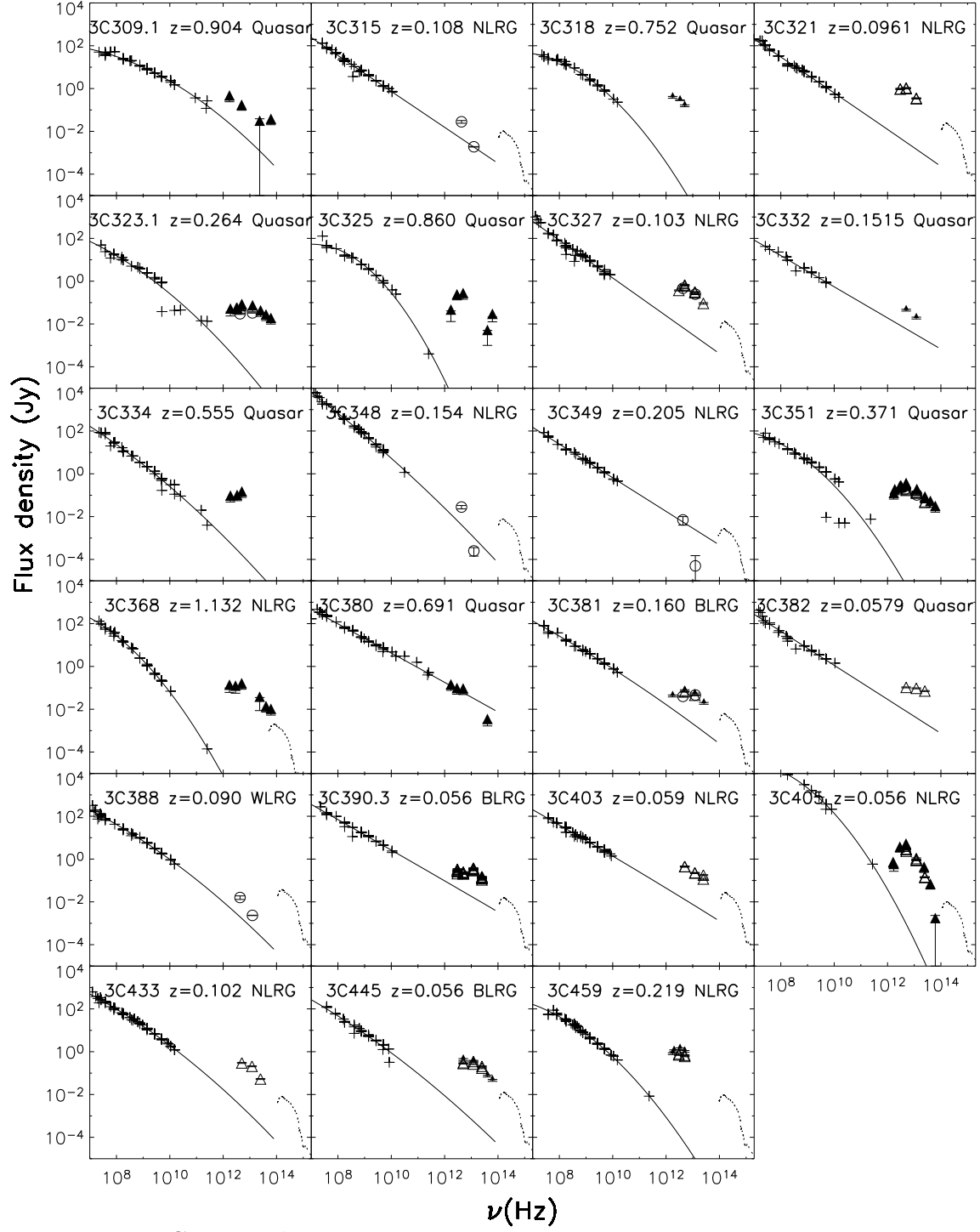


Figure 2.2 Continued

nature of the IR emission for these four sources. This hypothesis is confirmed by a mid-IR spectrum of 3C 218 that shows PAH emission (our unpublished data). The IR flux of 3C 380 is along the non-thermal extrapolation as shown in the Figure 2.2; Bloom et al. (1994) find that the radio spectrum is flat from around 1 cm up to 1100 μm , implying that the non-thermal contribution is significant at infrared wavelengths. The 5 GHz radio emission mainly comes from a region less than 2 arcsec across, as shown by comparing $F_{5\text{t}}$ and $F_{5\text{c}}$ in Table 2.3. VLBI observations of the milliarcsecond-scale structure of this compact core reveal a one-sided core-jet (Wilkinson et al. 1990; Polatidis & Wilkinson 1998). The total flux of all compact components of the core-jet is 2-5 Jy at 5 GHz, contributing 30-60% of the total flux. This radio core with flat spectrum may make a substantial non-thermal contribution to the infrared emission of 3C 380. Given the ambiguities in the origin of the infrared emission, we do not use this source in the following analysis.

We also evaluated contamination from stellar light in the host galaxy. The stellar light in radio quasars should be negligible. To estimate the stellar contribution from the other host galaxies, we used the spectral template for a normal elliptical galaxy over the spectral range from 1400 \AA to 2.75 μm (M. Rieke, private communication). The template was shifted by $(1+z)$ and then normalized at 4405 \AA to the apparent B magnitude. The dotted line in Figure 2.2 shows the stellar emission of the host galaxy; the contribution in the mid-IR (MIR) and FIR wavelength ranges will be negligible.

We conclude that the IR emission of most of our sample of radio-loud galaxies and quasars is mainly thermal IR emission by dust, except for 3C 380.

2.4 Discussion

2.4.1 Energy Source for IR Emission

We will use several methods to assess the relative contributions of forming stars and the AGN in heating the dust in our sample of radio-loud AGNs. We find that star formation provides less than 50% of the IR luminosity in most sources.

2.4.1.1 Extension of the IR Emission Region

The MIPS 24 μm images do not resolve the sources. The beam diameter of $\sim 6''$ corresponds to ~ 10 kpc at a redshift of 0.1. We convolved the HST image with the PSF of MIPS at 24 μm created by STINYTIM and found that the 24 μm image should show some structure for low-redshift ($z < 0.3$) sources if the IR emission is from the entire host galaxy. Thus, the IR emission is constrained to the central region.

2.4.1.2 Emission Line Ratio and IR Color

Baldwin, Phillips, & Terlevich (1981), Osterbrock & de Robertis (1985) and Veilleux & Osterbrock (1987) have developed spectral diagnostics to classify emission-line galaxies and determine the dominant energy source, star formation or an active nucleus. They compare two emission-line ratios combining high and low excitation lines, such as [O III] $\lambda 5007/\text{H}\beta$, [N II] $\lambda 6583/\text{H}\alpha$, or [S II] ($\lambda 6716 + \lambda 6731$)/ $\text{H}\alpha$, in a two dimensional classification diagram.

The dust heated by an AGN is usually warmer than that heated by star formation and thus the IR color can be used instead of one emission line ratio for classification diagnostics (Kewley et al. 2001). We use [O III] $\lambda 5007/\text{H}\beta$ and IR color to diagnose the dominant source of energy for the IR emission. The data for the ratio [O III] $\lambda 5007/\text{H}\beta$ are collected from the literature and the extinction corrections follow Veilleux & Osterbrock (1987). Our extinction estimates assume an intrinsic $I(\text{H}\alpha)/I(\text{H}\beta) = 3.1$ (Kewley et al. 2001). For several sources, we use the ratio of equivalent widths of the emission lines because the flux ratio is not available. The extinction corrections are small in virtually all cases. Some sources could not be corrected for extinction because there are no measurements of $\text{H}\alpha$. The errors introduced by uncorrected line strengths should be negligible, given the small corrections for the other sources.

Figure 2.3 shows the distribution of 22 sources in the emission-line-ratio versus IR-color plot. The IR colors are defined as the ratios of 60 μm flux densities to

Table 2.4. Kendall Tau test

relation	r_{lum}	S_{lum}	r_{flux}	S_{flux}
X-ray vs 70 μm	—	—	0.32	0.09
X-ray vs 24 μm	—	—	0.37	0.05
X-ray vs radio core	—	—	0.30	0.14
IR color vs R parameter	—	—	-0.37	0.04
178MHz vs 70 μm (all)	—	—	0.25	0.02
178MHz vs 70 μm (quasars)	—	—	0.68	0.0002
Radio size vs 24 μm	-0.01	0.96	—	—
Radio size vs 70 μm	-0.11	0.52	—	—

Note. — The r value indicates the rank correlation coefficient and the S value indicates the two-sided significance of the deviation from zero.

24 or 25 μm ones. For sources without 60 μm measurements, the flux densities were obtained by interpolation as in Section 2.2.2. A large [O III] $\lambda 5007/\text{H}\beta$ ratio and warm IR color indicate significant AGN activity, i.e., the upper left region of Figure 2.3e. The lower right part of the figure is the locus of star formation. We use the hypothetical mixing line (Kewley et al. 2001) in Figure 2.3 to estimate the percentage contribution of star formation. Most of our sources lie close to the region delineated by confirmed AGNs (filled dots), and for them we conclude that the AGN contributes $>50\%$ of the total power. However, for a few sources, it appears that the contribution from star formation can be dominant, much higher than the estimation made by IR color alone (Polletta et al. 2000).

In Section 2.4.2.1, we show that the circumnuclear torus may have significant optical depth at 24 μm and so the IR color of Type II AGN may be reddened through obscuration by the torus. Thus, Figure 2.3 may underestimate the fraction of the AGN contribution for Type II AGN.

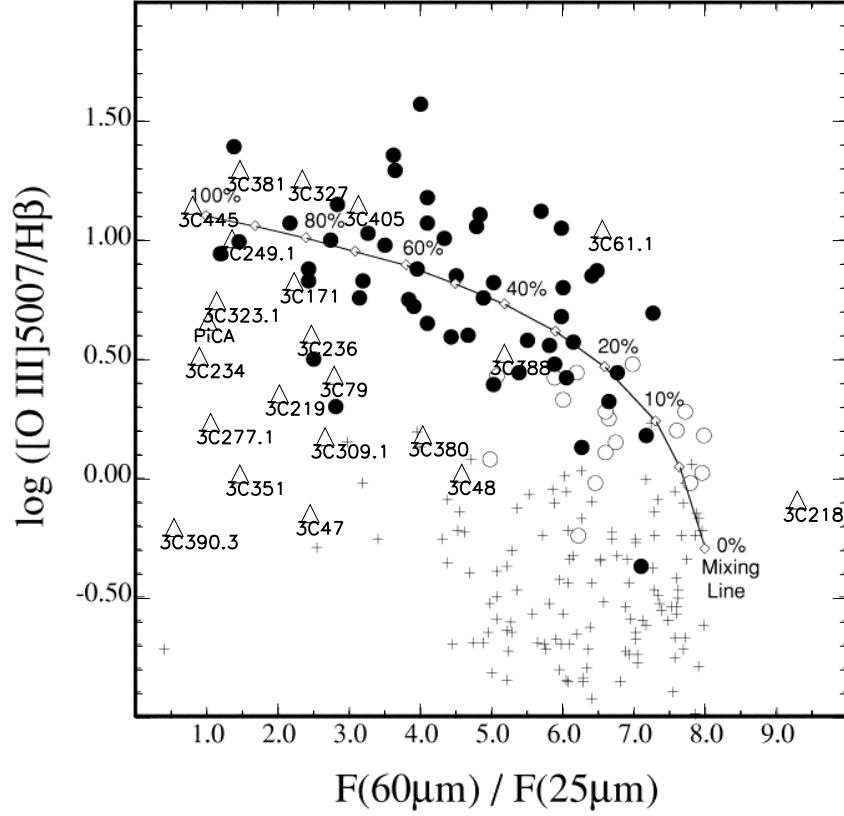


Figure 2.3 IR color versus emission-line ratio. The dashed line is a hypothetical mixing line on which the AGN fraction is labelled. This figure is from Kewley et al. (2001), with our sources added. The open triangles denote our sources. Filled circles, unfilled circles and crosses denote AGNs, ambiguous classification and starbursts, respectively in Kewley et al. (2001). Note that Section 2.4.2.1 shows that the torus may have significant optical depth at $24\ \mu\text{m}$ and thus the IR color underestimates the fraction of AGN contributions for Type II AGN.

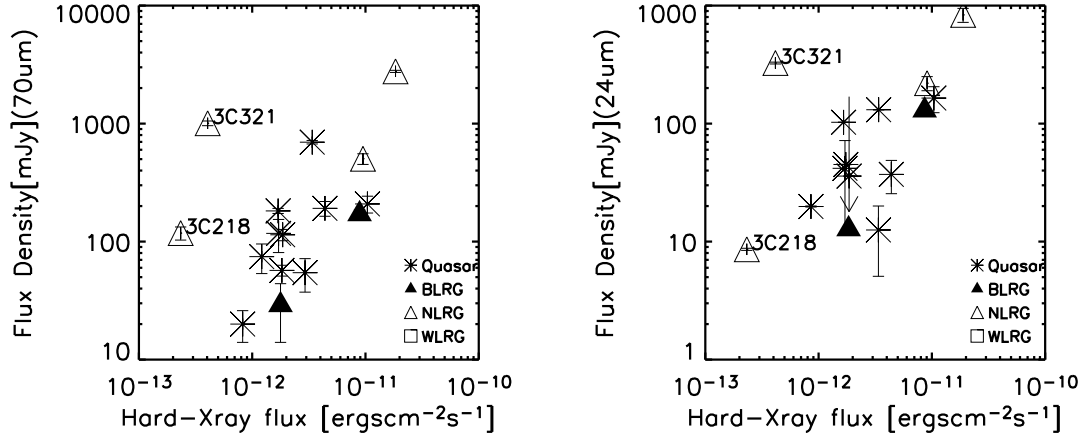


Figure 2.4 The correlation of K-corrected 70 μm flux density with 1-sigma error, K-corrected 24 μm flux density with 1-sigma error and central K-corrected hard X-ray flux corrected for absorption.

2.4.1.3 Relation of IR emission to the Central Hard X-ray Emission

Since the thermal IR emission appears usually to be powered by the nuclear engine, under the unified model we might expect a relation between IR luminosity and nuclear luminosity at other wavelengths. Such a relation might be hidden at wavelengths with strong obscuration by the circumnuclear torus. Hard X-rays are largely immune from such effects. The weakness of the correlation between hard-X-ray flux and core radio flux at 5 GHz as shown in Table 2.4 indicates that the hard X-ray emission for our sources is mainly from the accretion disk and other processes around the central engine, not from the beamed emission. Hard X-rays from the accretion disk are believed to provide a reasonably isotropic estimation of the nuclear luminosity.

Figure 2.4 compares the rest-frame 2-10 keV absorption- and K-corrected X-ray flux in the central 2.5'' region and the 70 μm and 24 μm K-corrected flux densities.

Because of the inhomogeneity of our sample, we compare K-corrected flux densities rather than luminosities. The spectral indices of the power laws assumed for the K-corrections of the X-ray measurements are listed in Column (9) of Table 2.2 and Column (12) of Table 2.3. The K-corrections for the IR bands were calculated assuming a power law SED with spectral index of 1. The Kendall Tau test on these data (see Table 2.4) yields S values of 0.05 and 0.09 respectively at 24 and $70\mu\text{m}$, showing only 5% and 9% probabilities respectively that the measurements are uncorrelated.

Except for 3C 380, all sources in Figure 2.4 have negligible non-thermal IR emission. 3C 321 is well above the correlation in Figure 2.4 and may have significant star formation activity. Additional evidence for active star formation in 3C 321 includes: 3C 321 contains two close nuclei (Roche & Eales 2000) and large amounts of star formation may be triggered by mergers (Sanders et al. 1988); Tadhunter, Dickson, & Shaw (1996) find that the AGN fraction can be as low as 26% of the UV continuum by fitting the observed spectra of 3C 321.

The correlation indicates that the thermal IR emission is associated primarily with the nuclear output, not with processes such as star formation that would operate independently of nuclear power. Thus, the IR emission is largely the emission of dust heated by the central engine. Because of the lack of suitable X-ray detections, the radio galaxies are relatively poorly represented in Figure 2.4, but there is no reason to expect them to behave differently from the other sources.

For the following discussion, we fit the IR/X-ray correlation in luminosity rather than flux density, since converting to this form and fitting the slope reduces the uncertainties due to our rather crude K-corrections. Excluding 3C 380 and 3C 321, the fits are given by $\text{Log}(L_{70}) = 1.68 + 0.89\text{Log}(L_x)$ and $\text{Log}(L_{24}) = 1.21 + 0.93\text{Log}(L_x)$. The dispersion of the relation is given by the relative standard deviation defined by $< ((L_{\text{obs}} - L_{\text{theo}})/L_{\text{theo}})^2 >^{0.5}$, where L_{obs} is the observed IR luminosity and L_{theo} is the theoretical IR luminosity heated by the central black hole, estimated from the fits discussed above. The result is 1.4 and 0.7 for the $70\mu\text{m}$ and $24\mu\text{m}$ relation respectively. We can derive a rough upper limit to the contribution of star formation

by assuming that all of the scatter arises from this process. The dispersion values imply that the contribution from star formation is smaller than 60% and 40% at 70 and 24 μm rest-frame wavelengths, respectively. This result is consistent with the conclusion from our emission-line-ratio vs. IR color analysis.

2.4.2 Tests of Unification Models

Since most of the IR emission from these sources seems to be associated with the AGN, we can use the IR data to probe unification models. We will describe two types of test: 1.) to see if the distribution of physical parameters is consistent with an obscuring circumnuclear torus and beamed emission by a jet, observed over a range of viewing angles; and 2.) to check if the relations between selected physical parameters are the same for the radio quasars and galaxies.

2.4.2.1 IR Color vs. R Parameter

Because of beaming, the emission of the radio core should be orientation-dependent. Thus, the radio compactness, the R parameter, can be used to indicate the viewing angle with respect to the orientation of the radio jet (Orr & Browne 1982). Here we define $R = F_{5c}/F_{5t}$, where F_{5c} and F_{5t} are the core and total radio fluxes at 5 GHz, respectively. $R = 1$ corresponds to the direction along the radio jet and the smaller R , the larger the viewing angle (we assume the torus is perpendicular to the jet, so R is taken as an indication of the viewing angle relative to the torus as well as the jet). We obtained from NED the total 5 GHz radio emission listed in Column (5) of Table 2.2 and Table 2.3, and from the literature the radio core emission listed in Column (6) of Table 2.2 and Table 2.3. We plot the IR color defined by F_{70}/F_{24} as a function of the R parameter in Figure 2.5. In this figure, we do not include sources with upper limits to their IR fluxes, nor the sources with possibly significant non-thermal components or large star formation contributions ($\sim 80\%$ in Figure 2.3).

We find a trend that redder IR color corresponds to a smaller R parameter

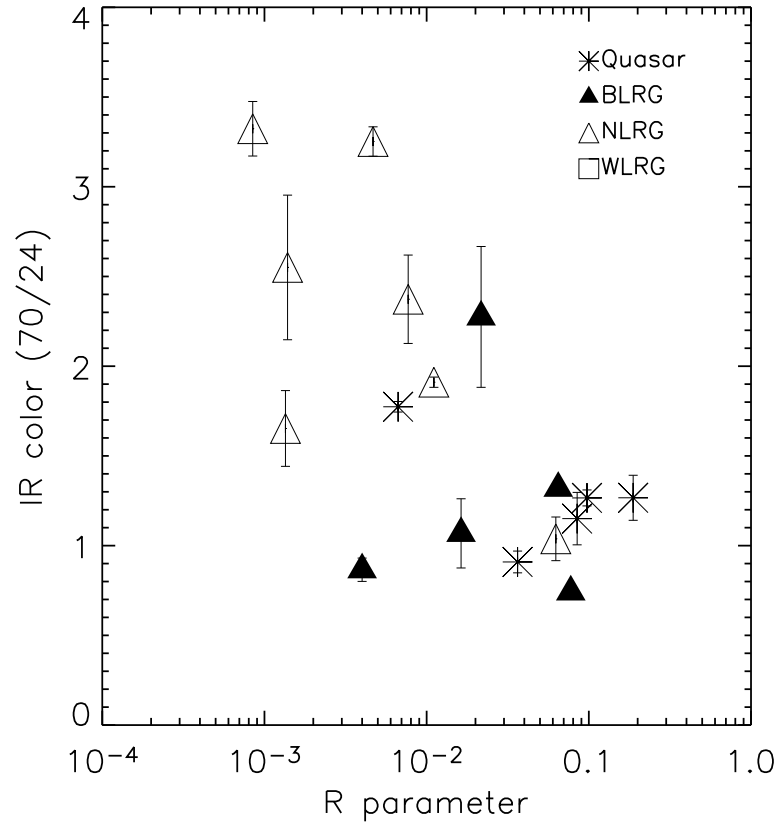


Figure 2.5 The correlation between IR color with 1-sigma error and R parameter. The IR color is defined as the ratio of $70\ \mu\text{m}$ flux to $24\ \mu\text{m}$ flux. The R parameter is defined as the ratio of the core radio flux to the total radio flux at 5 GHz. The solid line shows the least square fit.

and different emission-line types fall in different regions in the plot, qualitatively consistent with the prediction of the unification model. The overlapping between different emission-line types of source in the plot is possibly because the R parameter depends on other characteristics beside the viewing angle (Orr & Browne 1982), such as the core Lorentz factor, and because intrinsic dispersion in the radio core and lobe emission causes dispersion in the R parameter (Lonsdale & Barthel 1987). The least square fit to the relation in Figure 2.5 is given by $F_{70}/F_{24} = 0.35 - 0.74 \text{Log}(R)$. The corresponding Kendall-Tau test result given in Table 2.4 indicates a 96% probability of a significant correlation. The observed range of IR color of a factor of ~ 2.5 indicates that optical depth effects are still significant at $24 \mu\text{m}$ in the typical torus in an FR II radio galaxy. In contrast, Heckman et al. (1994) compare $60 \mu\text{m}$ fluxes between narrow line AGN and broad line AGN and found that they were almost the same, suggesting the torus is optically thin at $60 \mu\text{m}$.

For 3C 405, with the smallest R parameter in our sample, the absorbed power law fit to the hard X-ray spectrum shows the hydrogen column density is $N_{HI} = 10^{23} \text{cm}^{-2}$. Using $A_V = 0.62 * 10^{-21} N_{HI}$ (Savage & Mathis 1979) where A_V is the visual extinction, we have $A_V = 62$. Taking $A_V/A_{70} = 364$, $A_{70} = 0.17$, indicating the extinction is small at $70 \mu\text{m}$ even when we view the AGN through the torus, in agreement with our conclusion from the color behavior.

However, the extinctions at $24 \mu\text{m}$ and $70 \mu\text{m}$ should not be very different; A_{24}/A_{70} is expected to be around 7. Therefore, to explain the systematic change in optical depth between these two wavelengths may require a specific type of torus model. We hypothesize that there is a temperature gradient along the radial direction of the torus; the inner part of the toroidal disk is closer to the central heating source and hence is hotter than the outer region. To maintain a gradient may require that the outer parts of the disk are heated by energy reradiated from the inner parts, that the disk is warped or flared, or that it has a porous (or cloudy) structure. Such a temperature gradient may explain the non-single-blackbody IR SED of the AGN as shown in Figure 2.2. As a result, the $24 \mu\text{m}$ flux is predominately emitted by the dust in the inner torus, while $70 \mu\text{m}$ emission is mainly from the outer region.

If the density of the toroidal disk drops with distance from the central region, then the optical depth to the $24\mu\text{m}$ emission from the inner region could be large while it is still small to a significant portion of the $70\mu\text{m}$ emission from the outer region.

As can be seen in the diagnostic diagram in Figure 2.3, the reddening due to an edge-on accretion torus could drive a pure AGN spectrum toward the star-forming region. These results indicate that the FIR color is not a completely reliable indicator of star formation activity; an AGN with a large torus inclination angle can also have a red FIR color. Two-dimensional diagrams, such as IR color vs. emission-line-ratio may be useful to indicate the level of star formation activity, though they are still not infallible.

Recently, Whysong & Antonucci (2004) argue that the lack of $12\mu\text{m}$ emission from some FR I AGNs indicates that they lack a torus. However, if the torus has significant optical depth at $24\mu\text{m}$, the $12\mu\text{m}$ emission will be strongly suppressed and thus cannot be used to estimate the intrinsic torus emission.

2.4.2.2 An Indication of the Torus Opening Angle

We return to Figure 2.4 to compare the IR and X-ray emission for quasars and radio galaxies. Although the data points in Figure 2.4 are mainly for radio quasars, the various kinds of radio galaxy follow the relation well. Since the IR emission is the reprocessing of the emission from the accretion disk, especially optical and UV photons, the IR emission is determined under the unified model by the central intrinsic emission and the torus structure. The torus structure must be very complicated. However, for simplicity, we assume it is described only by the opening angle and that the light blocked by the torus is reprocessed completely to IR emission, otherwise it can escape completely. Moreover, we assume the emission of the torus is isotropic at $70\mu\text{m}$ (we also show the behavior at $24\mu\text{m}$ for comparison). If the torus opening angle is constant, then the IR emission should be proportional to the X-ray emission. The least square fit indicates the slope is 0.89 and 0.94 for $70\mu\text{m}$ and $24\mu\text{m}$, respectively. Neither value is significantly different from unity. Based on the above simple model, such a slope suggests that the torus opening angle does not

change with the activity level of the central engine. The radio power of our sources is greater than $10^{26.5} \text{ W Hz}^{-1}$ at 178 MHz, so this result is consistent with the invariance of the opening angle based on the quasar fraction (Willott et al. 2000). The result also indicates that most radio galaxies and radio quasars possess a torus with similar structure, supporting the unification model.

2.4.2.3 The Relation of IR emission and 178 MHz radio emission

The 70 μm emission and 178 MHz radio emission should also both be isotropic, so we can use them to probe unification models for different types of radio source. The relation of the K-corrected 70 μm flux density with the K-corrected 178 MHz flux density is shown in Figure 2.6. For the radio, we base K-corrections on a power law SED with spectral index of 0.8, while we used a spectral index of 1 at 70 μm . The relation between 24 μm and 178 MHz emission is not shown because of the many upper limits to the 24 μm flux. Because the 178 MHz flux density is a defining parameter for the sample, Figure 2.6 includes all the radio galaxy members (in comparison, for example, with Figure 2.4 which includes only a fraction). The figure shows the distributions of radio quasars and radio galaxies are different. Radio quasars except for 3C 380 are constrained in a tight correlation with an S value of 3×10^{-3} by the Kendall Tau test. The solid line is the least square fit to the radio quasars excluding 3C 380 (See Section 2.3.2); the dashed lines are the 3-sigma bounds to the relation indicated by the solid line.

Again, 3C 321 is above the 3-sigma bounds. Its behavior may be due to powerful star formation activity triggered by a merger (see Section 2.4.1.3). Three additional galaxies close to the 3-sigma high limit (3C 293, 3C 403 and 3C 459) may also have excess IR emission powered by star formation. Nearly one-third of the radio galaxies are below the region between the two dashed lines. Except for 3C 405, PicA, 3C 218 and 3C 348, the FIR underluminous sources do not show larger radio fluxes compared with radio quasars, so we cannot attribute the behavior in Figure 2.6 to selection bias. Since these galaxies are underluminous at 70 μm , we cannot account for their behavior by an additional FIR source such as star formation. We conclude

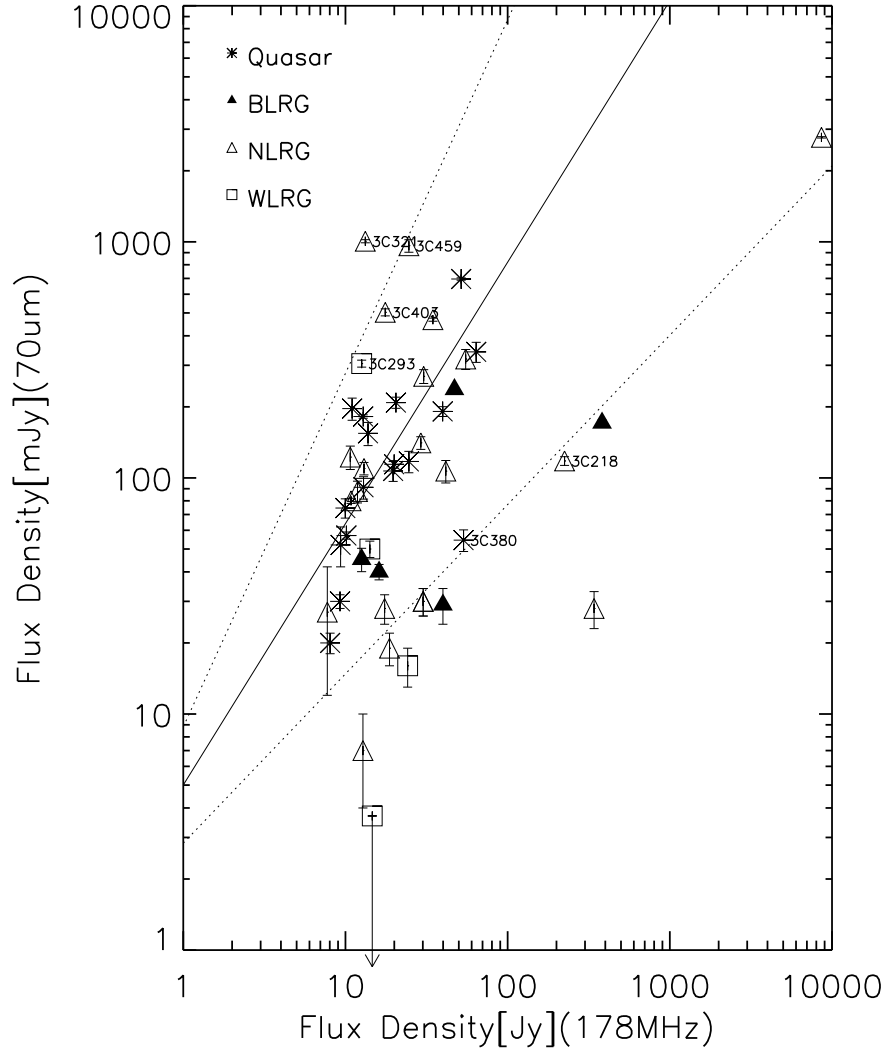


Figure 2.6 The relation of the K-corrected $70\ \mu\text{m}$ emission with 1-sigma error and K-corrected radio emission at 178 MHz. The solid line is the least square fit to the radio quasars, excluding 3C 380 with substantial contribution by non-thermal core output (See Section 3.2), unlike those of the other quasars. The two dashed lines are the 3-sigma scatter of the relation indicated by the solid line.

that the simple unification model works less well for the galaxies in the sample than for the quasars; it appears to predict the properties of some galaxies but not others.

We have examined the FIR underluminous galaxies individually to see if we can understand why they depart from the simple unification model prediction. We look for explanations in terms of their having a weaker nuclear engine, since the FIR emission is a good indicator of the nuclear accretion power, or of their having higher radio emission because of a special environment where radio emission is easily generated (Barthel et al. 1996; Haas et al. 2004).

3C 388: Based on the relation of the optical core luminosity and radio core emission, Chiaberge et al. (2000) argue that 3C 388 has a FR I nucleus, i.e., weaker than for classic FR II galaxies.

3C 348: The radio morphology of 3C 348 is neither like FR I nor FR II. It is better classified as an intermediate type radio source. Thus, we may speculate 3C 348 has a relatively weaker nucleus with respect to normal FR II galaxies.

We have not found a good explanation for the behavior of the remaining galaxies. Their environments are not different from the normal FIR luminous sources. Barthel et al. (1996) find that sources in X-ray clusters show higher radio-to-infrared ratios than non-cluster galaxies. This may be due to the upper-limit measurements of IR fluxes by IRAS, for example, 3C 61.1 and 3C 315 are now detected by MIPS and their ratios can reach 2.9 and 2.75 respectively and therefore only one source in the sample of cluster galaxies shows a significantly higher ratio than for field galaxies. No direct evidence indicates that the remaining FIR underluminous sources have weaker nuclei. It may be necessary to modify the simple unification model to explain them. For example, there may be a large range of optical depths at $70\mu\text{m}$; the weakly emitting galaxies could then be significantly obscured.

2.4.3 Compact Steep Spectrum Sources

Compact Steep Spectrum (CSS) and Gigahertz-Peaked Spectrum (GPS) radio sources have similar radio outputs to other radio sources, but are substantially more compact, 1 to 20kpc. As discussed by O’Dea (1998), IR observations can dis-

tinguish a number of hypotheses regarding these objects, most notably whether they are *frustrated* large-scale sources due to a dense interstellar medium that absorbs the energy of the radio-emitting jets. This absorbed energy would be expected to emerge in the FIR. A number of searches have failed to find any effect of the type predicted by the frustrated source model (Heckman 1994; Fanti et al. 2000). Because the FIR detection limits available to these studies were generally inadequate for measurement of single galaxies, they co-added signals from many galaxies to achieve an average emission level. The levels from the CSS/GPS and control samples are similar, although the significance level of the comparisons is only modest. The comparisons are also subject to uncertainty due to the necessity of stacking detections for higher statistical significance: a few extreme sources can dominate the results. Another probe of these sources is to determine the absorption and hence the density of the surrounding interstellar medium. Pihlström et al. (2003) report HI observations that show an increase in ISM density with decreasing radio size. This behavior is qualitatively consistent with the frustrated source model, but Pihlström et al. (2003) show that the ISM density is probably inadequate to confine the jets, unless the H_2/HI ratio is much higher than normal. Fanti et al. (2000) give additional arguments against the frustrated source model. Our data permit another test of the frustrated source model, based on IR data with enough sensitivity to detect individual galaxies.

We identify six CSS sources whose radio sizes are smaller than 20 kpc in our sample. The comparison sample consists of large scale sources in the redshift range of the CSS sample, from 0.27 to 1.4. Figure 2.7 plots the linear radio size and IR luminosity. The radio size ranges from 2 kpc to 400 kpc and IR luminosity is from $10^{10} L_{\odot}$ to $10^{14} L_{\odot}$. No correlation is indicated. We conclude that the CSS sources do not show significantly different FIR output from the large scale radio sources, consistent with the result of *IRAS* (Heckman et al. 1994) and *ISO* (Fanti et al. 2000). Hes, Barthel, & Hoekstra (1995) find that CSS sources are IR-brighter. Their result may be caused by the selection bias that CSS sources in their sample are at high-redshift and thus high luminosity. In addition, the lack of an additional

IR luminosity component argues against the proposal that these galaxies might be sites of strong star formation induced by the interaction between a jet and ambient matter (Baker et al. 2002).

2.5 Conclusions

In this paper, we present MIPS observations of steep spectrum radio quasars and FR II radio galaxies, and combine them with the sample detected by *IRAS* and *ISO*. We discuss the nature of the IR emission in this combined sample and its implications for the unification model. The main results are:

- (1) The IR emission of most sources is thermal. The thermal IR emission of most sources is dominated by dust heated by the AGN.
- (2) The simple unification model predicts the properties of the radio quasars and some radio galaxies well. However the properties of some FIR underluminous galaxies may be inconsistent with a pure unification model in which there are no orientation-independent intrinsic differences among these sources.
- (3) The behavior of the $70\mu\text{m}/24\mu\text{m}$ color with radio compactness is consistent with the suggestion that a torus that has significant optical depth at $24\mu\text{m}$ surrounds the nuclei of the FR II radio galaxies.
- (4) The CSS sources do not show additional IR emission, arguing against the proposals that these sources reside in extremely dense regions or that they are associated with strong star-forming activity.

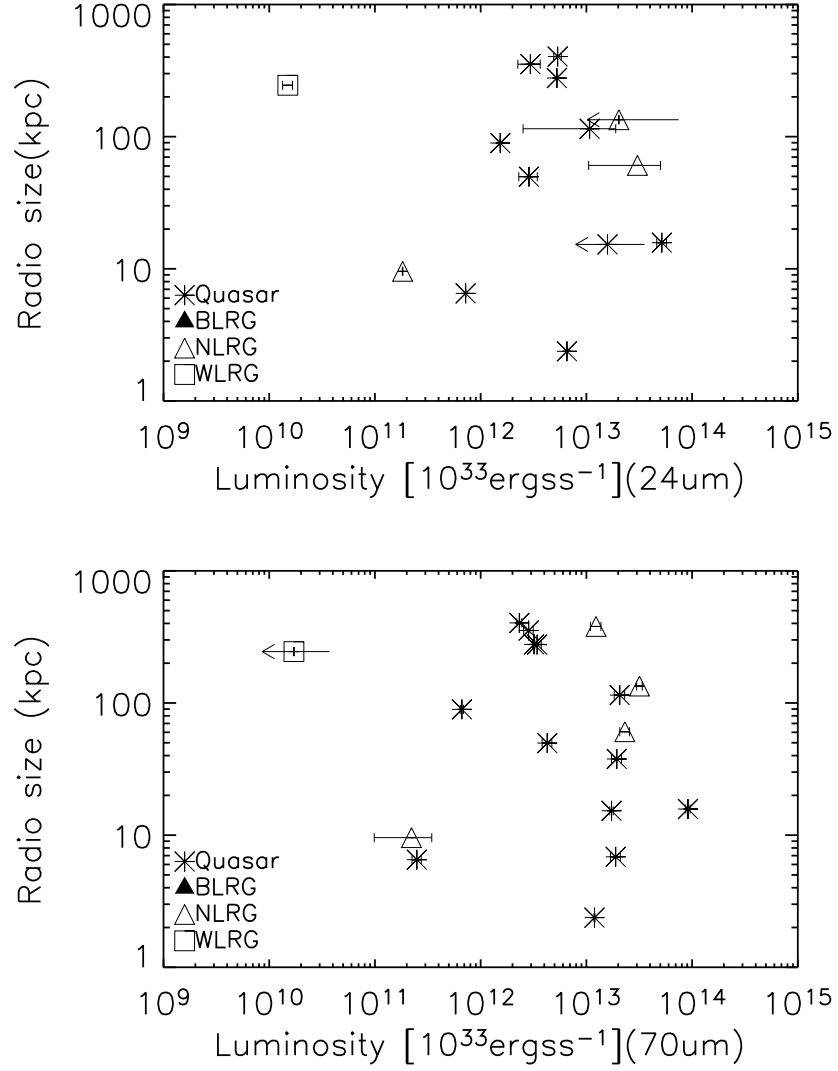


Figure 2.7 The plot of linear radio size vs. K-corrected FIR luminosity with 1-sigma error.

CHAPTER 3

9.7 μm Silicate Features in AGNs: New Insights into Unification Models

3.1 Introduction

In the last chapter, we have tested the unification model for radio-loud AGN using infrared broad-band photometry. In this chapter, we will further test the unification scheme and study the structure of the dusty torus for a variety of AGN types using 9.7 μm silicate features. In Chapter 3.2, we present *Spitzer* Infrared Spectrograph (IRS; Houck et al., 2004) observations of 9.7 μm silicate features in 93 AGNs, including examples from the literature (Siebenmorgen et al., 2005; Hao et al., 2005; Sturm et al., 2005; Ogle et al., 2006). In Chapter 3.3, we describe the correlation between the silicate feature and HI column density inferred from X-ray spectra fits. In Chapter 3.4, a conceptual model is proposed to explain the above correlation. The final conclusions are presented in Chapter 3.5.

3.2 Sample and Data Reduction

Our sample (see Table 3.1) includes a variety of types of AGN: radio-loud quasars, FR II radio galaxies, Seyfert 1 and Seyfert 2 galaxies, broad absorption-line quasars (BALQs), low-ionization nuclear emission-line region (LINER) galaxies, and non-BAL radio-quiet quasars including optically selected Palomar-Green (PG) quasars and IR quasars as selected by the Two-Micron All Sky Survey (2MASS) from Smith et al. (2002). Except for the objects from the literature, quasars of all types and FR II radio galaxies are the most luminous objects in their parent samples (which include upper limits in redshift in their definitions) while Seyfert 1 and Seyfert 2 galaxies are derived to have high brightness and a broad range in HI column density from Turner & Pounds (1989) and Risaliti et al. (1999), respectively. The whole

sample spans a range of HI column density from 10^{20} cm^{-2} up to 10^{25} cm^{-2} . We focus on the sample of 85 objects with available HI column densities in this study, although all 97 objects have available silicate data. X-ray spectra were retrieved from the Chandra data archive for 8 sources. The data reduction and the measurement of column densities through power-law fits are as described in Shi et al. (2005). The column densities of most of the 2MASS QSOs are based on the X-ray hardness ratio from Wilkes et al. (2002) assuming an intrinsic power law X-ray spectrum with a photon index of 1.7. The associated uncertainty is estimated as a factor of 3 corresponding to a change of ~ 1 in the photon index. The column density for the remaining sources is obtained from the literature as shown in the Table 3.1.

The IRS spectra presented for the first time in this paper, except for those of the Seyfert galaxies, were obtained using the standard staring mode. The intermediate products of the *Spitzer* Science Center (SSC) pipeline S11.0.2 were processed within the SMART software package (Higdon et al., 2004). The background was subtracted using associated spectra from the two noded, off-source positions. This also subtracts stray light contamination from the peak-up apertures, and adjusts pixels with anomalous dark current. Pixels flagged by the SSC pipeline as “bad” were replaced with a value interpolated from an 8-pixel perimeter surrounding the suspect pixel. The spectra were extracted using a 6.0 pixel fixed-width aperture for the short low module (SL), and 5.0 pixels for the long low module (LL). The spectra were calibrated using a spectral response function derived from IRS spectra and Kurucz stellar models for a set of 16 Sun-like stars that exhibit: 1) high signal-to-noise observations, 2) no residual instrumental artifacts, and 3) no signs of IR excess. The absolute flux density scale is tied to calibrator stars observed by the IRS instrument team and referenced to calibrated stellar models provided by the SSC (see also Bouwman et al. , 2006). The uncertainties in the final calibration are dominated by random noise. The relative flux calibration across the spectrum is accurate to $\sim 1 - 2\%$ (Hines et al., 2006; Bouwman et al. , 2006).

The data reduction was slightly different for the Seyfert galaxies first presented in this paper. The whole Seyfert sample consists of a mixture of point-like and extended

sources. They are at relatively low redshift ($z \sim 0.01$) and are lower luminosity AGNs, so care was taken to minimize the contribution of the host galaxies. For the extended sources, a fixed-width column extraction that is narrow enough to exclude most of the extended source would be most appropriate. However, narrow fixed-width extraction windows introduced artifacts into the extracted spectra. Instead, a narrow expanding-aperture extraction was performed on all sources, point-like or extended. This was deemed to be an acceptable compromise between rejecting the extended source component and introducing artifacts into the spectrum. The spectra were extracted using an expanding extraction aperture defined to be 4 pixels wide at the wavelengths of 6 μm and 12 μm for the second and the first order of SL, respectively, and of 16 μm and 27 μm for the second and the first order of LL, respectively. At the wavelength of 10 μm , the extraction aperture is around 3.3 pixels. A detailed description of the data reduction is given by Gorjian et al. (2006).

Table 3.1. Source Characteristics

Sources	z	Type	Strength	Reference	N_H^X	Reference
(1)	(2)	(3)	(4)	(5)	(6)	(7)
PG0050+124	0.058	PG	0.38	2	$0.03^{+0.01}_{-0.016}$	10
PG0052+251	0.155	PG	$0.33^{+0.06}_{-0.06}$	0	$0.04^{+0.01}_{-0.01}$	8
PG0804+761	0.100	PG	0.60	2	$0.03^{+0.00}_{-0.005}$	18
PG0953+414	0.234	PG	$0.40^{+0.08}_{-0.08}$	0	< 0.006	9
PG1116+215	0.176	PG	$0.22^{+0.05}_{-0.05}$	0	< 0.019	9
PG1151+117	0.176	PG	$0.36^{+0.13}_{-0.13}$	0		
PG1211+143	0.085	PG	0.55	2	< 0.039	10
PG1309+355	0.184	PG	$0.41^{+0.07}_{-0.07}$	0	< 0.034	9
PG1351+640	0.087	PG	1.25	2	$0.02^{+0.01}_{-0.018}$	18
PG1402+261	0.164	PG	$0.25^{+0.05}_{-0.05}$	0	< 0.028	9
PICA	0.034	FRII	$0.50^{+0.05}_{-0.05}$	0	$0.08^{+0.01}_{-0.01}$	6
HYAA	0.054	FRII	$-0.23^{+0.26}_{-0.25}$	0	$2.09^{+0.48}_{-0.40}$	6
3C220.1	0.610	FRII	0.0	5	0.7	22
3C265	0.811	FRII	0.0	5	$16.8^{+10.5}_{-7.2}$	23
3C280	0.996	FRII	-0.21	5	$9.7^{+6.2}_{-4.7}$	23
3C330	0.550	FRII	-0.22	5	$23.6^{+16.3}_{-13.4}$	23
3C390.3	0.056	FRII	$0.20^{+0.04}_{-0.04}$	0	$0.11^{+0.01}_{-0.01}$	11
CYGA	0.056	FRII	$-0.45^{+0.03}_{-0.03}$	0	$10.78^{+1.45}_{-1.45}$	6
3C445	0.056	FRII	$0.41^{+0.08}_{-0.08}$	0	$5.30^{+0.61}_{-0.37}$	15
3C452	0.738	FRII	-0.11	5	$56.0^{+9.0}_{-9.0}$	24
3C48	0.367	RLQ	$0.12^{+0.05}_{-0.05}$	0	$0.43^{+0.06}_{-0.06}$	6
3C249.1	0.312	RLQ	0.50	1	$1.06^{+0.08}_{-0.081}$	6
3C273	0.158	RLQ	0.12	2	$0.03^{+0.00}_{-0.003}$	10
3C351	0.372	RLQ	0.51	1	$0.85^{+0.04}_{-0.047}$	6
3C371	0.051	RLQ	$0.08^{+0.04}_{-0.04}$	0	$0.50^{+0.23}_{-0.22}$	6
0226-104	2.256	BALQ	$0.28^{+0.16}_{-0.12}$	0		
PG0946+301	1.216	BALQ	$0.16^{+0.06}_{-0.06}$	0	>100	13
1246-057	2.236	BALQ	$0.48^{+0.49}_{-0.32}$	0		
CSO203	2.150	BALQ	$0.25^{+0.17}_{-0.14}$	0		
1556+335	1.646	BALQ	$0.27^{+0.13}_{-0.11}$	0		
PG1700+518	0.292	BALQ	$0.14^{+0.06}_{-0.06}$	0	> 40	20
2233+134	0.326	BALQ	$0.20^{+0.08}_{-0.08}$	0		
PHL5200	1.981	BALQ	$0.35^{+0.20}_{-0.17}$	0	40^{+26}_{-20}	12
IIIZW2	0.090	Sy1	$0.05^{+0.03}_{-0.03}$	0	$0.05^{+0.078}_{-0.021}$	15
Fairall9	0.046	Sy1	$0.21^{+0.07}_{-0.07}$	0	< 0.01	15
NGC3783	0.010	Sy1	$-0.01^{+0.03}_{-0.03}$	0	$0.021^{+0.08}_{-0.02}$	15
NGC4593	0.009	Sy1	$0.08^{+0.05}_{-0.05}$	0	< 0.01	15

Table 3.1 (cont'd)

Sources (1)	z (2)	Type (3)	Strength (4)	Reference (5)	N_H^X (6)	Reference (7)
NGC526a	0.019	Sy1	$0.26^{+0.06}_{-0.06}$	0	$1.62^{+0.83}_{-0.83}$	15
Mkn231	0.042	Sy1	-0.65	4	$1.46^{+0.30}_{-0.27}$	6
M-6-30-15	0.006	Sy1	$0.17^{+0.04}_{-0.04}$	0	$0.41^{+0.26}_{-0.31}$	15
IC4329a	0.016	Sy1	$0.01^{+0.03}_{-0.03}$	0	$0.11^{+0.04}_{-0.03}$	15
NGC5548	0.017	Sy1	$0.27^{+0.05}_{-0.05}$	0	$0.043^{+0.007}_{-0.010}$	15
H1846-786	0.074	Sy1	$-0.03^{+0.04}_{-0.04}$	0	$6.40^{+4.60}_{-3.00}$	15
Mrk509	0.034	Sy1	$0.11^{+0.04}_{-0.04}$	0	0.01	15
NGC7213	0.006	Sy1	$1.09^{+0.10}_{-0.07}$	0	0.01	15
MCG-2-58-22	0.047	Sy1	$0.26^{+0.04}_{-0.04}$	0	< 0.01	15
NGC1068	0.004	Sy2	-0.38	4	>1000	16
Mrk1066	0.012	Sy2	$-0.28^{+0.27}_{-0.09}$	0	>100	16
NGC1386	0.003	Sy2	$-0.32^{+0.03}_{-0.03}$	0	>100	16
NGC2110	0.008	Sy2	$0.30^{+0.08}_{-0.08}$	0	$2.89^{+0.21}_{-0.29}$	16
NGC2273	0.006	Sy2	$-0.11^{+0.13}_{-0.11}$	0	>1000	16
IR07145-2914	0.006	Sy2	$-0.33^{+0.03}_{-0.03}$	0	>1000	16
MCG-5-23-16	0.008	Sy2	-0.52	4	$2.00^{+0.50}_{-0.500}$	20
NGC3081	0.008	Sy2	$-0.17^{+0.04}_{-0.04}$	0	66^{+18}_{-16}	16
NGC3281	0.011	Sy2	$-0.69^{+0.02}_{-0.02}$	0	79.8^{+19}_{-15}	16
NGC3393	0.013	Sy2	$-0.28^{+0.04}_{-0.04}$	0	>1000	16
NGC4388	0.008	Sy2	$-0.51^{+0.04}_{-0.05}$	0	42^{+6}_{-10}	16
NGC4507	0.012	Sy2	$-0.02^{+0.03}_{-0.03}$	0	$29.20^{+2.30}_{-2.30}$	16
NGC4939	0.010	Sy2	$0.01^{+0.06}_{-0.06}$	0	>1000	16
NGC4941	0.003	Sy2	$0.01^{+0.04}_{-0.04}$	0	45^{+25}_{-14}	16
NGC5005	0.003	Sy2	$0.09^{+0.19}_{-0.22}$	0	>100	16
NGC5135	0.014	Sy2	$-0.45^{+0.10}_{-0.08}$	0	>100	16
NGC5347	0.008	Sy2	$0.01^{+0.04}_{-0.04}$	0	>100	16
Circinus	0.001	Sy2	-0.79	4	430^{+190}_{-110}	16
NGC5506	0.006	Sy2	$-0.53^{+0.02}_{-0.02}$	0	$3.40^{+0.26}_{-0.12}$	16
NGC5643	0.004	Sy2	$-0.35^{+0.04}_{-0.04}$	0	>1000	16
NGC5674	0.025	Sy2	$0.01^{+0.06}_{-0.06}$	0	$7^{+2.8}_{-2.6}$	16
ESO103-G035	0.013	Sy2	$-0.60^{+0.02}_{-0.02}$	0	$13.50^{+3.30}_{-2.30}$	15
NGC7172	0.009	Sy2	$-0.80^{+0.02}_{-0.02}$	0	$8.60^{+0.79}_{-0.33}$	16
IC5135	0.016	Sy2	$-0.36^{+0.06}_{-0.04}$	0	>100	16
NGC7314	0.005	Sy2	$-0.30^{+0.03}_{-0.03}$	0	$0.80^{+0.89}_{-0.09}$	15
2MASX J00070361+1554240	0.114	2MQ	$0.02^{+0.07}_{-0.07}$	0	2.45	17
2MASX J00505570+2933281	0.136	2MQ	$-0.17^{+0.05}_{-0.05}$	0	1.23	17
2MASSi J0108351+214818	0.285	2MQ	$-0.12^{+0.04}_{-0.04}$	0	1.47	17

Table 3.1 (cont'd)

Sources (1)	z (2)	Type (3)	Strength (4)	Reference (5)	N_H^X (6)	Reference (7)
2MASSi J0157210+171248	0.213	2MQ	$-0.21^{+0.20}_{-0.20}$	0	0.70	17
2MASX J02215058+1327409	0.140	2MQ	$-0.14^{+0.08}_{-0.08}$	0	0.70	17
2MASX J02343065+243835	0.310	2MQ	$0.29^{+0.08}_{-0.08}$	0	0.86	17
2MASSi J0348576+125547	0.210	2MQ	$-0.24^{+0.04}_{-0.04}$	0		
2MASSi J0918486+211717	0.149	2MQ	$-0.05^{+0.07}_{-0.06}$	0	< 0.11	21
2MASSi J0955045+170556	0.139	2MQ	$0.14^{+0.09}_{-0.09}$	0	2.06	17
2MASSi J1027249+121920	0.231	2MQ	$-0.16^{+0.05}_{-0.05}$	0	1.46	17
2MASX J10514428+3539304	0.158	2MQ	$-0.21^{+0.09}_{-0.09}$	0	$0.720^{+0.070}_{-0.070}$	21
2MASSi J1258074+232921	0.259	2MQ	$-0.20^{+0.03}_{-0.03}$	0	1.47	17
2MASX J13000533+1632151	0.080	2MQ	$0.07^{+0.05}_{-0.05}$	0	$2.900^{+0.500}_{-0.500}$	21
2MASSi J1307006+233805	0.275	2MQ	$-0.68^{+0.05}_{-0.05}$	0		
2MASX J14025121+2631175	0.187	2MQ	$0.07^{+0.09}_{-0.09}$	0	< 0.04	21
2MASSi J1453315+135358	0.139	2MQ	$-0.73^{+0.04}_{-0.04}$	0		
2MASX J15011320+2329085	0.258	2MQ	$-0.09^{+0.04}_{-0.04}$	0	0.58	17
2MASSi J1516532+190048	0.190	2MQ	$0.24^{+0.04}_{-0.04}$	0	1.23	17
2MASSi J1637002+222114	0.211	2MQ	$-0.01^{+0.07}_{-0.07}$	0	0.70	17
2MASSi J1659397+183436	0.170	2MQ	$0.15^{+0.06}_{-0.06}$	0	2.93	17
2MASSi J1714427+260248	0.163	2MQ	$0.13^{+0.07}_{-0.07}$	0		
2MASSi J2222022+195231	0.366	2MQ	$0.28^{+0.05}_{-0.05}$	0		
2MASXi J222211+195947	0.211	2MQ	$0.27^{+0.06}_{-0.06}$	0		
2MASX J22255423+1958372	0.147	2MQ	$-0.21^{+0.07}_{-0.07}$	0	2.45	17
2MASX J23444953+1221430	0.199	2MQ	$0.21^{+0.10}_{-0.10}$	0	$0.65^{+0.26}_{-0.260}$	21
NGC3998	0.003	LINER	0.80	3	$0.05^{+0.02}_{-0.016}$	19

Note. — Column (1): The sources. Column (2): Redshift. Column (3): The types of AGNs. 'PG': PG quasar; 'RLQ': radio-loud quasar; 'Sy1': Seyfert 1 galaxies; 'Sy2': Seyfert 2 galaxies; 'BALQ': broad absorption-line quasar; 'FRII': FR II radio galaxies; 'LINER': low-ionization nuclear emission-line region; '2MQ': 2MASS quasar. Column(4): The strength of the silicate feature as defined in § 2. Column (5): The references for the silicate data: (0) This work; (1) Siebenmorgen et al. (2005); (2) Hao et al. (2005); (3) Sturm et al. (2005); (4) Roche et al. (1991); (5) Ogle et al. (2006). Column (6): The intrinsic HI column density in the unit of 10^{22}cm^{-2} . Column (7): References for the HI column densities: (6) This work; (7) Donato et al. (2003); (8) Brunner et al. (1997); (9) Porquet et al. (2004); (10) Reeves & Turner (2000); (11) Leighly et al. (1997); (12) Gallagher et al. (2002); (13) Mathur et al. (2000); (14) Dewangan et al. (2003); (15) Turner & Pounds (1989); (16) Risaliti et al. (1999); (17) Wilkes et al. (2002); (18) Wang et al. (1996); (19) Ptak et al. (2004); (20) Gallagher et al. (1999); (21) Wilkes et al. (2005); (22) Worrall et al. (2001); (23) Belsole et al. (2006); (24) Isobe et al. (2002)

The silicate feature strengths were estimated as follows. Narrow emission lines were removed from the spectra and they were then smoothed to a resolution of $0.1 \mu\text{m}$. The continuum was defined by using a spline interpolation between the blue and red ends of the IRS spectral range. We defined (all in rest-frame wavelengths) the blue end as $5\text{--}7.5 \mu\text{m}$, while the red end was defined as $13\text{--}14 \mu\text{m}$ for the 13 objects observed only with the SL module. For six BALQs at higher redshifts, the red end was chosen to be $10.5\text{--}13 \mu\text{m}$. For the remainder of the sample, the red spectral end was defined as $25\text{--}30 \mu\text{m}$. For nine objects with the red end contaminated by silicate emission (Figure 3.1(b)), the continuum at this end was estimated to be below that observed by $<20\%$ at the reddest point, based on the spectra of objects without contamination. For twelve objects with the blue end contaminated by the strong $6\text{--}8 \mu\text{m}$ aromatic feature (Figure 3.1(c)), the continuum in this bandpass was given by two segments between 5 and $5.5 \mu\text{m}$ where the contamination is negligible. The fit was judged to be good when it matched the flux at both ends within the noise and the curvature of the continuum varied gradually from one end to the other over the silicate region. The uncertainty in continuum fitting was obtained by adjusting the flux of the continuum up and down over the fitting spectral range. For the objects with continuum not contaminated by either aromatic or silicate features as shown in Figure 3.1(a), we adjusted the fit until the continuum was just above (for upper error) or below (for lower error) the observed flux over the whole spectral fitting range. To estimate the uncertainty for the objects with red end contaminated by the silicate feature (Figure 3.1(b)), we first fixed the blue end and adjusted the red end continuum up to the red end point that matched the upper-envelope of the underlying continuum plus noise and down by the same amount as an estimate of the errors of the continuum fit. To account for the effects of noise in the blue end, we added another 4% uncertainty (the mean value for objects without aromatic or silicate feature contamination). For the objects with blue end contaminated by the aromatic feature (Figure 3.1(c)), we fixed the red end and adjusted the blue end to get the uncertainty in a similar way where the upper-limit of the underlying continuum is the flux at $7 \mu\text{m}$ (the median wavelength between the peaks of the

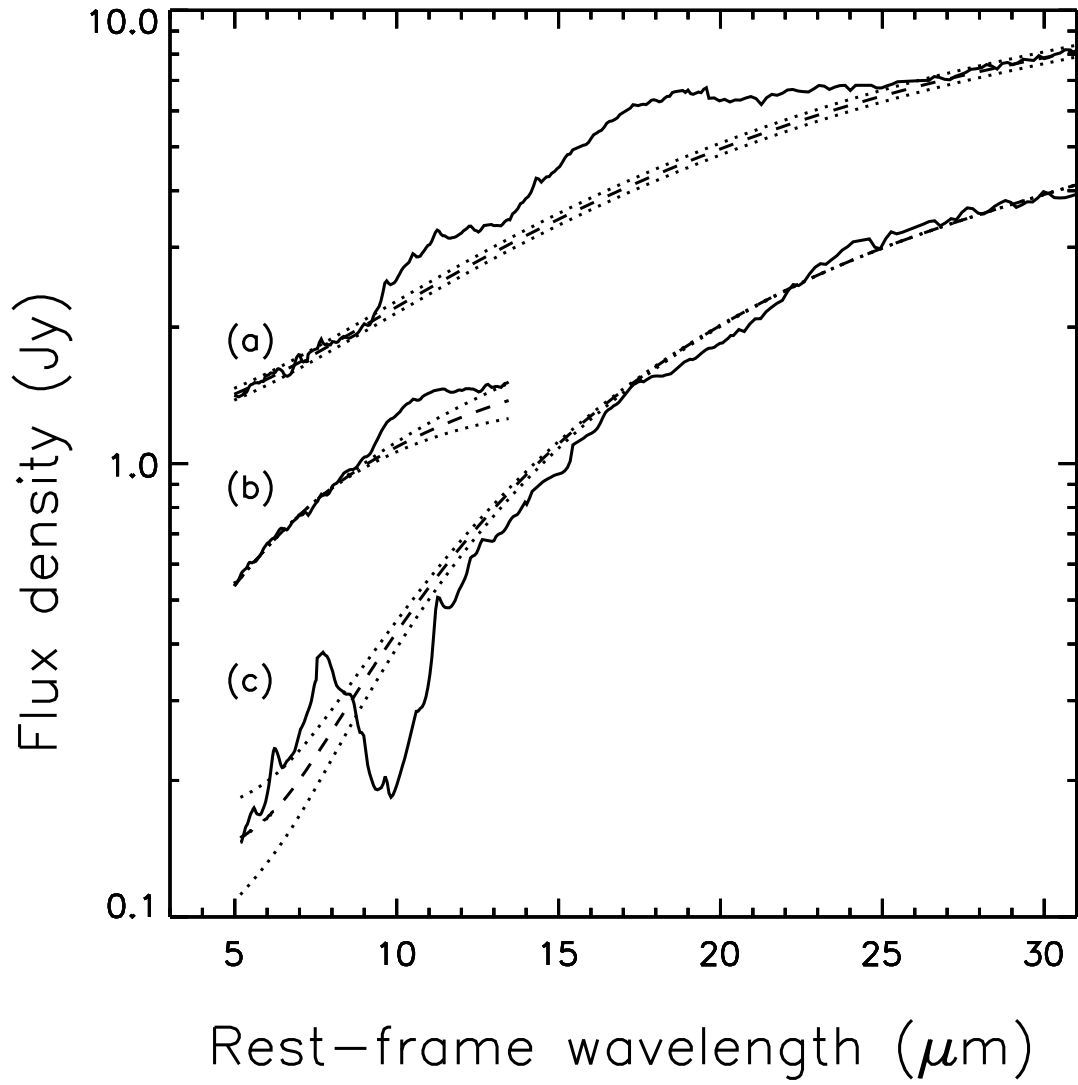


Figure 3.1 IRS spectra of 3 objects with fits. The dashed line is the fitted continuum and the dotted line is the estimated uncertainty in the continuum fitting. The scaling factors for (a) MCG-2-58-22, (b) Fairall9 and (c) NGC4388, are 30, 5 and 1.5, respectively.

6.2 μm and 7.7 μm aromatic features). Another 4% uncertainty was added to this uncertainty to account for the effects of noise in the red end. There are no objects with red end contaminated by the silicate feature and blue end contaminated by the aromatic features.

The strength of the 9.7 μm silicate feature is defined as $(F_f - F_c)/F_c$, where F_f and F_c are the observed flux density and underlying continuum flux density, respectively, at the peak (for emission) or the minimum (for absorption) of the silicate feature. The feature strength in this definition is a direct measure of the optical depth for the silicate absorption. Figure 3.2 shows the IRS spectra presented for the first time in this study in order of HI column density. No ice or hydrocarbon absorption is found in Figure 3.2. Especially at 5-8 μm , where there is no contamination of the silicate feature, the spectra are well described by power laws except for those with aromatic emission. Therefore, once the continuum had been fitted, we could calculate the feature strengths unambiguously.

3.3 Results

Figure 3.3 shows the strength of the 9.7 μm silicate feature as a function of HI column density. The right y-axis of Figure 3.3 shows the IR-absorbing column density estimated from the silicate absorption feature by assuming $\tau_{9.7\mu\text{m}} = \ln(F_c/F_f)$, $A_v/A_{9.7\mu\text{m}}=19$ (Roche & Aitken, 1985) and $A_v/N_H=0.62\times 10^{-21}\text{cm}^{-2}$ (Savage & Mathis, 1979). The silicate feature varies from emission (+) to absorption (-) as the X-ray spectra become more heavily obscured. The trend is also demonstrated by the composite spectra in different bins of HI column as shown in Figure 3.4. Since the silicate feature is broad, the composite spectra are the geometric mean spectra to conserve the global spectral shape (e.g. Vanden Berk et al., 2001). The relationship between HI column and silicate feature behavior is generally consistent with the AGN unification scheme where material surrounding the central SMBH obscures both the X-ray and silicate emissions.

The correlation (black lines in Figure 3.3) is defined by all types of AGN. To

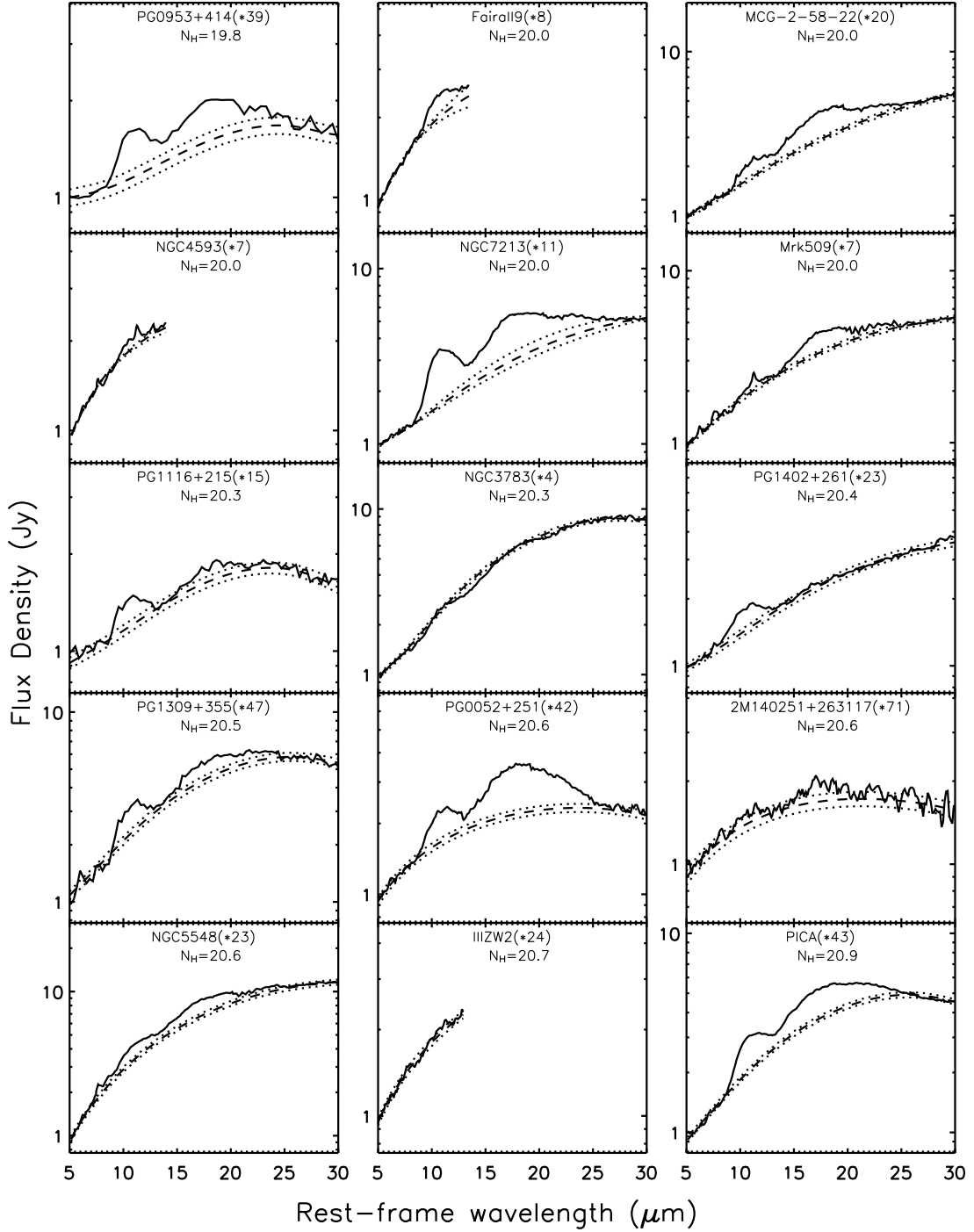


Figure 3.2 The IRS spectra for objects with available X-ray data in order of the HI column density. Narrow emission lines have been removed from the spectra (see text). The dashed lines are the fitted continua and the dotted lines show the estimated uncertainties in the continuum fitting. The scaling factor to normalize the spectra at $5 \mu\text{m}$ and the logarithm of the HI column density in units of cm^{-2} are given for each object.

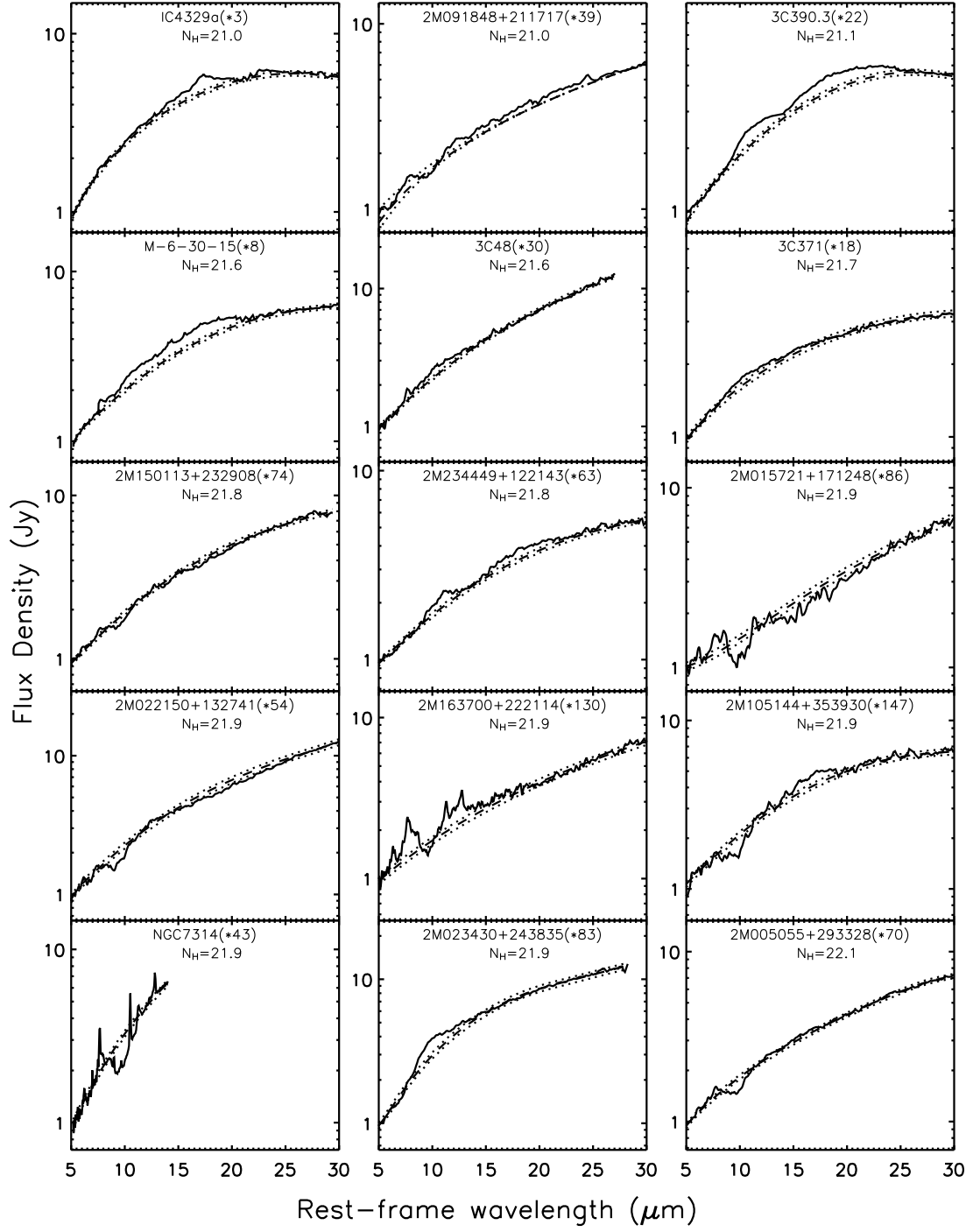


Figure 3.2 Continued

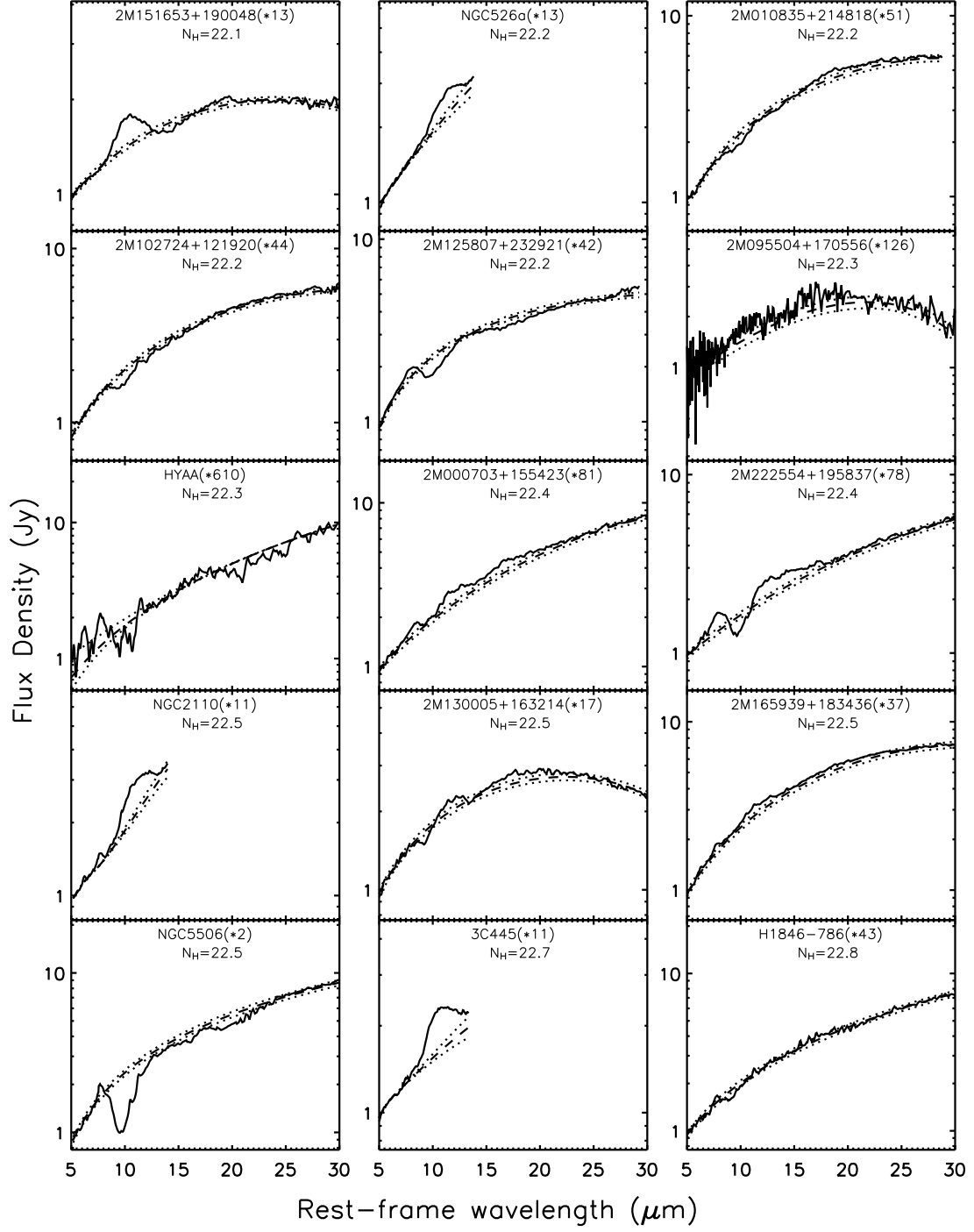


Figure 3.2 Continued

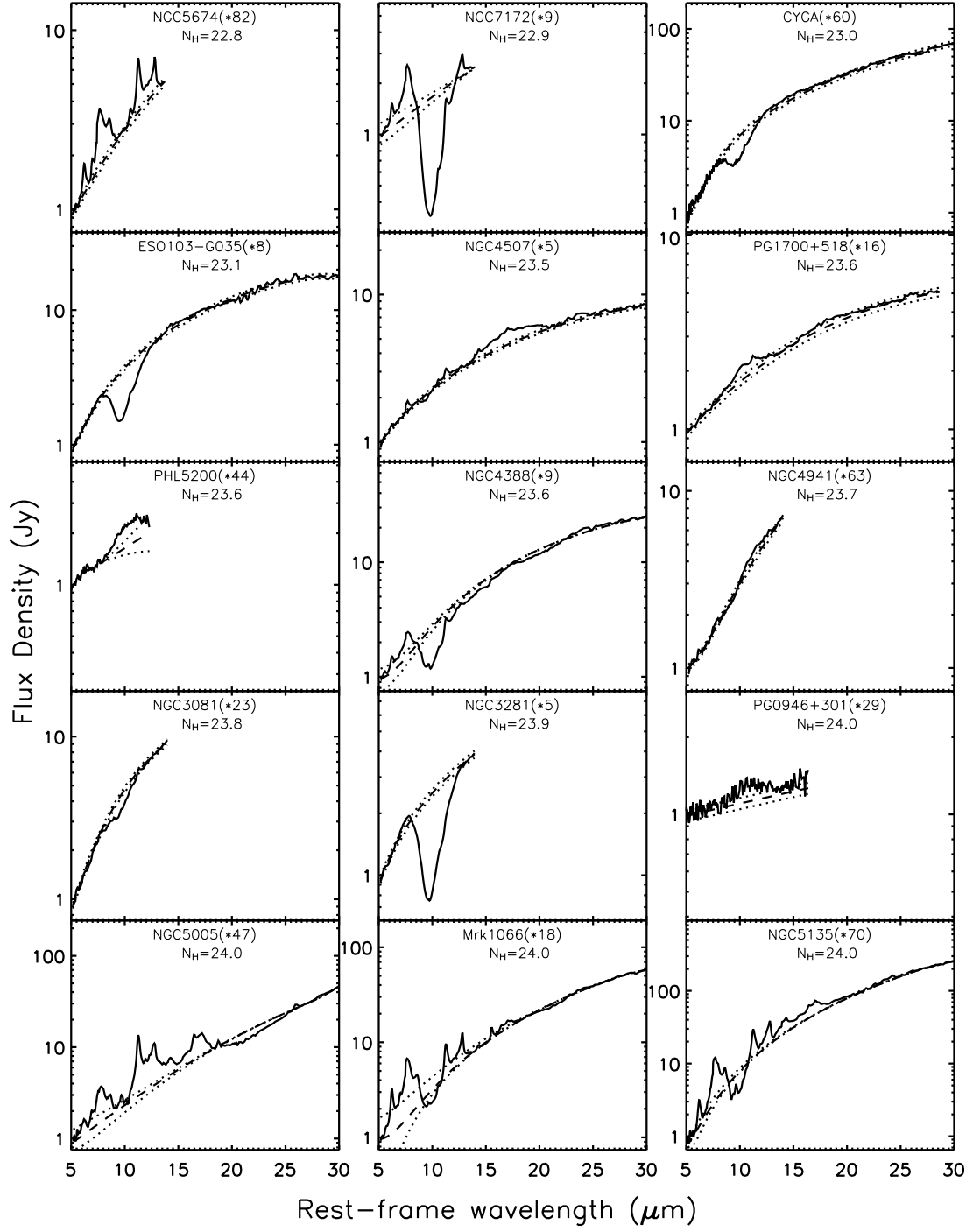


Figure 3.2 Continued

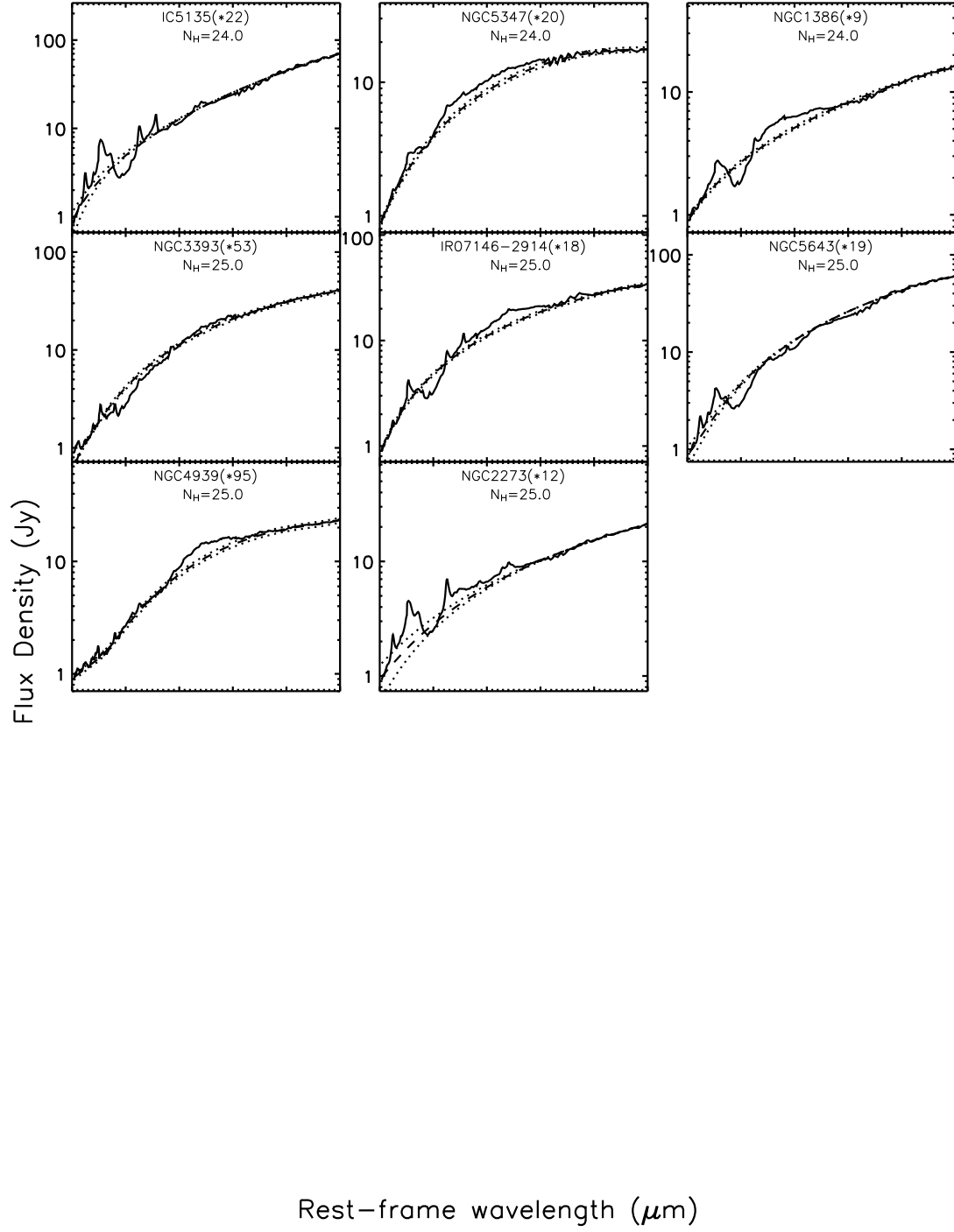


Figure 3.2 Continued

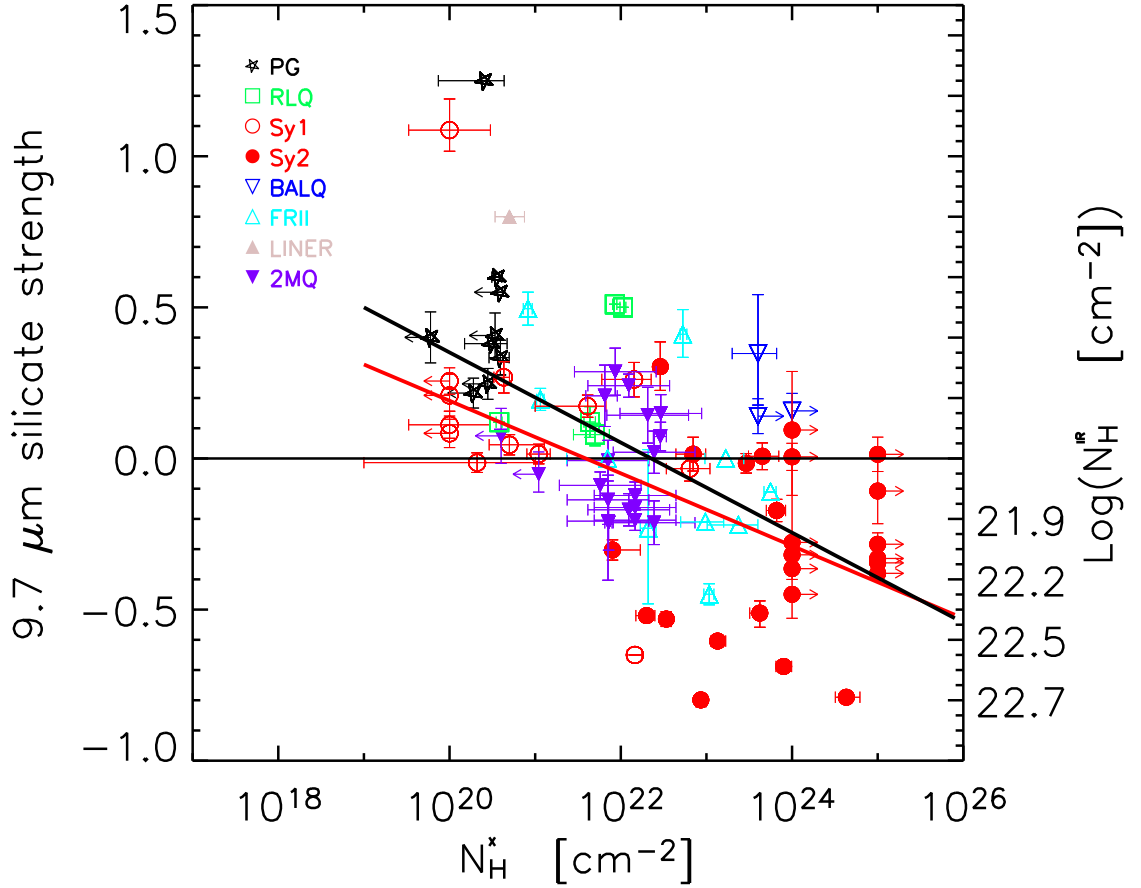


Figure 3.3 The strength of the silicate feature as a function of HI column density. The strength of the silicate feature is defined as $(F_f - F_c)/F_c$, where F_f and F_c are the observed flux density and underlying continuum flux density, respectively, at the peak (for emission) or the minimum (for absorption) of the silicate feature. The black line is the linear fit to all objects while the red line is the fit to Seyfert galaxies. 'PG': PG quasar; 'RLQ': radio-loud quasar; 'Sy1': Seyfert 1 galaxies; 'Sy2': Seyfert 2 galaxies; 'BALQ': broad absorption-line quasar; 'FRII': FR II radio galaxies; 'LINER': low-ionization nuclear emission-line region; '2MQ': 2MASS Quasar.

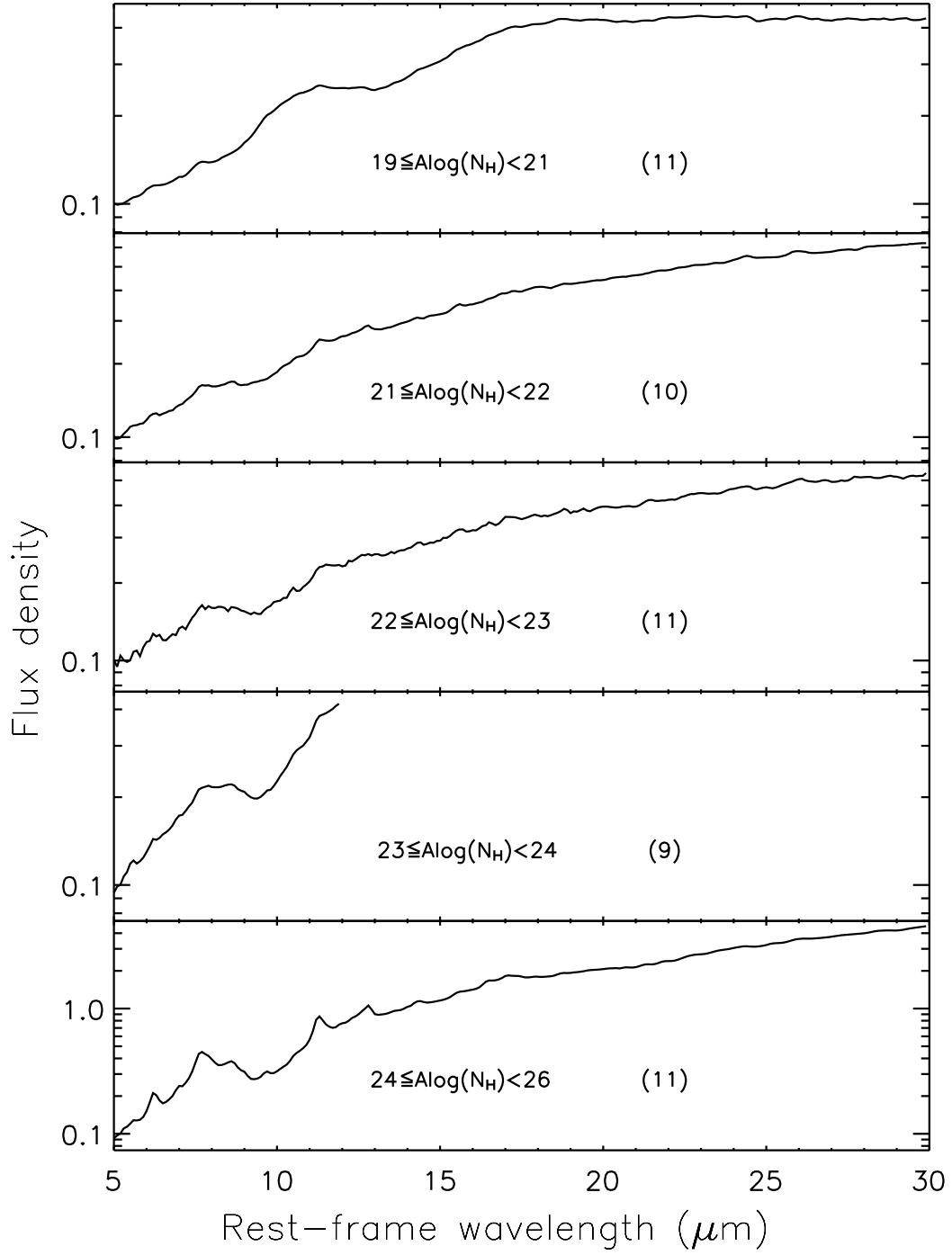


Figure 3.4 The composite spectra of AGNs in different HI column bins. The number in parenthesis is the number of objects used for the composite spectrum in each bin.

Table 3.2. The linear fits to objects with different AGN types

Type (1)	A (2)	B (3)	Number (4)
Seyfert	2.6 ± 0.7	-0.12 ± 0.03	38
2MQ & PG	5.5 ± 1.2	-0.25 ± 0.06	28
FRII & RLQ	3.9 ± 1.6	-0.17 ± 0.07	15
all objects	3.3 ± 0.5	-0.15 ± 0.02	85
Seyfert ¹	4.6 ± 1.3	-0.21 ± 0.06	23
all objects ¹	5.1 ± 0.9	-0.23 ± 0.04	61

Note. — Column(1): The AGN types. See caption to Figure 3. Column(2) and Column(3): Parameters of the linear fit $S = A + B * \log(N_H^X)$ where S is the strength of the silicate feature as defined in § 2 and N_H^X is the HI column density in the unit of cm^{-2} . Both parameters A and B are unitless due to the definition of the silicate strength. Column(4): the total number of objects for each fit.

¹Fits excluding objects without measured HI columns (i.e., upper and lower limits to the HI are excluded).

Table 3.3. Tests of the correlation

Type	Num	K-S Prob.(%)	Mean	Variance
(1)	(2)	(3)	(4)	5
Sy	38	90	1.0	0.85
2MQ & PG	28	2	0.02	0.35
RLQ & FR II	15	10	0.06	0.40

Note. — Column(1): The AGN type. See caption to Figure 3.3. Column(2): the total number of a given AGN type. Column(3): The probability from the K-S test that the given AGN type has the same distribution as a theoretical Monte Carlo distribution produced by the correlation defined by the Seyfert galaxies. Column (4): The significance that the distribution of the given AGN type and the theoretical distribution have the same mean. A value greater than 0.05 indicates the same mean for the two distributions. Column (5): The significance that the distribution of the given AGN type and the theoretical distribution have the same variance. A value greater than 0.05 indicates the same variance for the two distributions.

investigate the behavior for individual AGN types, we unified Seyfert 1 and Seyfert 2 galaxies as one type of AGN (Seyfert galaxies). Similarly, FR II radio galaxies and radio-loud QSOs are classified as radio-loud AGNs while PG and 2MASS QSOs are classified as radio-quiet QSOs. Table 3.2 shows the linear fits to these AGN types where the limits to the HI column density are treated as detections during the fitting. The fits for different AGN types are characterised by large uncertainty and are generally consistent with each other within the uncertainty. Radio-quiet QSOs (2MASS and PG QSOs) exhibit a small (less than two standard deviations) deviation from other two types of AGN. As shown in Figure 3.3, this deviation arises because the PG QSOs with low HI columns have larger silicate strengths.

To quantify the discrepancy between different types of AGN, we examined the probability that the other AGN types follow the Seyfert correlation by producing a Monte Carlo theoretical distribution with 10000 data points using the Seyfert correlation (red line in Figure 3.3) with associated scatter. Table 3.3 shows the result of three tests: 1.) the probability from a K-S test that the given AGN type has the same distribution as the theoretical distribution; 2.) the significance that two distributions have the same mean (indicated by a value greater than 0.05); and 3.) the significance that two distributions have the same variance (indicated by a value greater than 0.05). The high K-S probability for the Seyfert galaxies indicates that the theoretical distribution is a good representative of them (as it should be). As shown in Table 3.3 and Figure 3.3, radio-loud AGNs (radio-loud QSOs and FR II galaxies) are consistent with the Seyfert correlation and radio-quiet QSOs (2MASS and PG QSOs) show slightly higher silicate strengths at low HI column compared to Seyfert galaxies.

Sturm et al. (2006) recently found that six type 2 QSOs in the HI column range of $10^{21.5}$ - 10^{24} cm^{-2} do not show any silicate feature, slightly higher but still consistent with those of the Seyfert galaxies at the same range of HI columns. As shown in Figure 3.3, the three BALQs and the one LINER in this study deviate from the Seyfert correlation significantly. More objects are needed to address whether these two types follow the Seyfert correlation. Given that most PG QSOs have upperlimit

measurements of HI columns, the intrinsic deviation of radio-quiet QSOs from the Seyfert trend should be smaller than we calculate. Although the intrinsic slope of the Seyfert correlation should be smaller due to the lower limit measurement of the HI column for half the Seyfert 2 galaxies, the effect on the comparison is small because it is dominated by the column range where Seyfert galaxies have detected HI columns. In Table 3.2, we also list the linear fits to the Seyferts and the whole sample excluding objects with limit measurements of the HI columns. The comparison between the new slopes shows that the consistency between different AGN types may become even better.

Therefore, except for LINERs and BALQs, the remaining non-Seyfert AGN types follow more or less the Seyfert correlation. The rough agreement among AGN types indicates that the geometry of the circumnuclear material and our viewing angle are the primary factors influencing the relation between the silicate feature and the X-ray attenuation. This correlation is nonetheless curious because, as shown in Figure 3.3, the column required for the observed X-ray obscuration levels is up to $\sim 10^{25} \text{ cm}^{-2}$, two orders of magnitude larger than that required to produce the silicate absorption, $\sim 10^{23} \text{ cm}^{-2}$. This implies that along many lines of sight there must be X-ray absorbing material that is not contributing to the silicate absorption.

The dispersion in the correlation is much larger than the uncertainties in silicate-feature strength and HI column density. The large dispersion appears to be characteristic of all the AGN types with large numbers of objects (Seyfert galaxies, radio-quiet QSOs and radio-loud AGNs). This is consistent with a common mechanism (the circumnuclear geometry) regulating the correlation and dispersion in Figure 3.3. Due to different physical aperture diameters from 500 pc to galaxy-scale in size, the differing amounts of extended emission from star-forming regions may contribute to the scatter. However, such contributions must be small. As shown in Figure 3.2, twelve of 85 objects have strong aromatic features and their silicate features may be contaminated by star-forming regions. However, the dispersion of the correlation is almost the same for the 73 objects without aromatic features. Another possible contribution to the scatter is the gas-to-dust ratio. However, as indicated

by Figure 3.3, the gas-to-dust ratio needs to vary nearly three orders of magnitude to account for the scatter in the correlation. Such large variation is unreasonable given the similar IR SEDs and IR luminosities for objects with similar HI column but different silicate features as shown in Figure 3.2, for example, NGC 4941 versus NGC 3281.

Another characteristic of the correlation is that several Compton-thick AGNs have silicate absorptions that are much weaker than predicted. Again, this implies that additional absorbing material must be present in the Compton-thick sources, but placed so it does not obscure the IR emission.

3.4 Discussion

We now describe a conceptual model to explain the large difference in the absorbing columns for the X-rays and infrared, but that can also account for the correlation in Figure 3.3. The goal is to find a geometry for the circumnuclear material that can explain Figure 3.3 solely in terms of variations in viewing angle. As mentioned in the Introduction, there are three classes of model that are generally successful in fitting the IR SEDs of specific AGN types: 1.) a compact disk (e.g. Pier & Krolik, 1992); 2.) a more extended disk (radius of hundreds of pc) (e.g. Granato et al., 1997); and 3.) a disk with clumps or clouds of material (e.g. Nenkova et al., 2002). We now explore whether the ideas behind these three types of model can be combined to provide a possible explanation for the behavior of the silicate feature. It is beyond the scope of this paper to compute a quantitative model to fit the data. However, by confining our argument to combinations of features in models already shown to fit other aspects of AGN behavior, it is likely that our explanation of the silicate-X-ray correlation will also be compatible with the other observations of AGNs. Overall, our model requires both a component of material similar to the cloudy model (e.g. Nenkova et al., 2002) and a diffuse component with outer radius similar to the compact disk-model (e.g. Pier & Krolik, 1992) and with column density similar to the model of the extended disk (e.g. Granato et al., 1997).

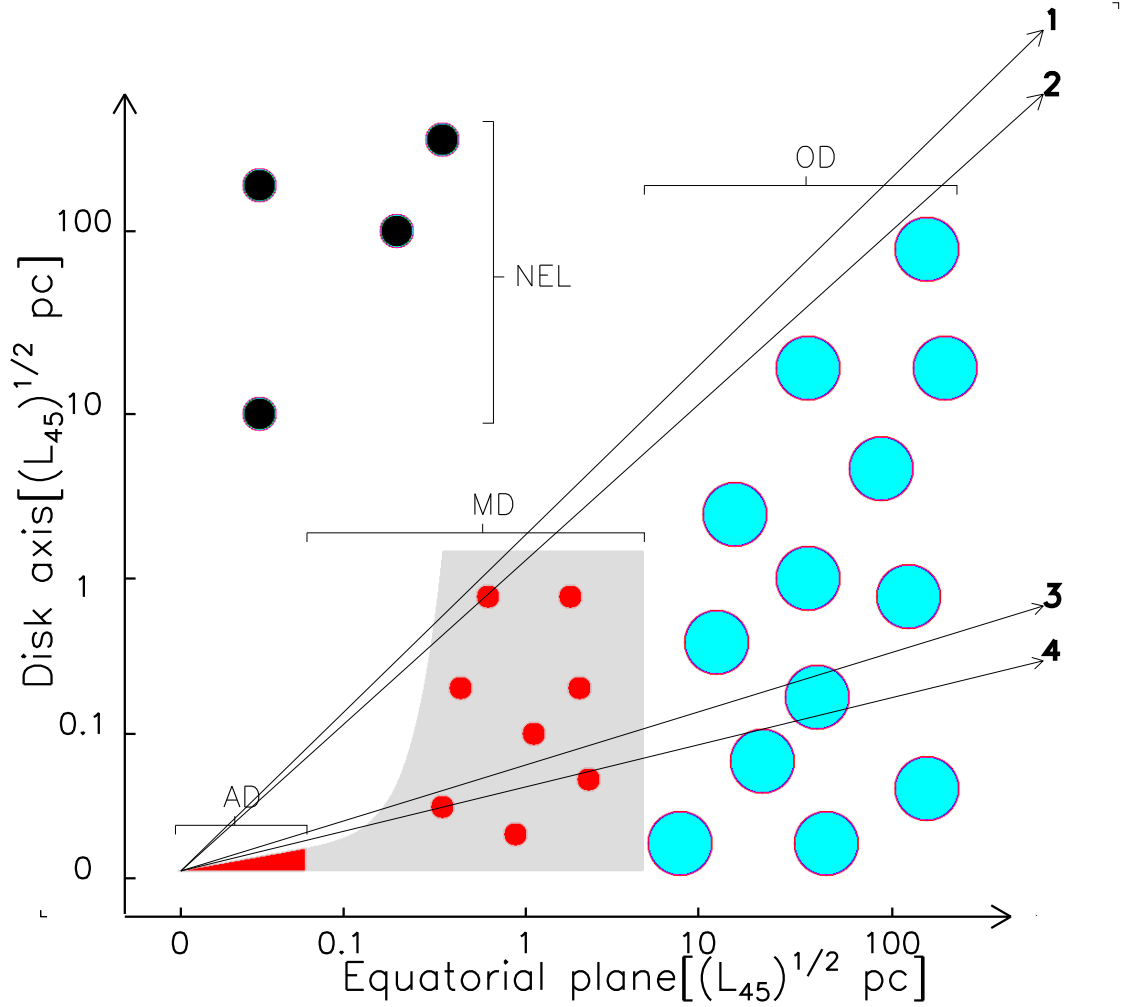


Figure 3.5 The structure of the material surrounding the central blackhole in the first quarter section. The whole structure is symmetric about the disk axis and the equatorial plane. From inside to outside: 1.) the inner accretion disk (AD), which produces X-ray and UV radiation ionizing the narrow-emission-line (NEL) and broad-emission-line clouds, and heating the dust; 2.) the middle disk (MD) with a diffuse component (grey) and with denser embedded clouds – the diffuse component produces the silicate emission while the embedded clouds heavily obscure the central X-ray emission when the line of sight intercepts them; and 3.) the outer disk (OD) with clouds that obscure the silicate and X-ray emission, and are responsible for the far-IR emission. Four lines of sight indicate: 1.) silicate emission with low HI column; 2.) silicate emission with high HI column; 3.) silicate absorption with low HI column; 4.) silicate absorption with high HI column.

In Figure 3.5, we show the hypothetical disk geometry. We include an inner accretion disk (AD), and in the same plane a middle disk (MD) with a diffuse component (grey) joining to the AD. Denser clouds or clumps are embedded in this MD. It merges with a cloudy or clumpy outer disk (OD). The X-ray and UV radiation from the AD heat the dust in the MD and OD to produce IR emission and ionize the broad-emission-line clouds and the narrow-emission-line (NEL in Figure 3.5) clouds, which are not shielded by the diffuse component. Compton-thick X-ray obscuration can arise either in the AD, or in the clouds in the MD. Irregularities in the AD or the passage of clouds through the line of sight may be responsible for the variations in X-ray obscuration observed toward some AGNs (e.g. Elvis et al., 2004; Risaliti et al., 2005). However, for a model with only the central disk and the clouds, there is a large probability of viewing the central X-ray emission directly without any extinction even for an inclined disk (along the equatorial plane). This is inconsistent with Figure 3.3, where the lower-envelope of the data distribution shows a strong trend that the HI column density increases with the depth of the silicate absorption. The diffuse component of the MD is required to obscure the X-ray emission even if the line of sight does not cross any cloud. This component is also the source of the silicate emission. The silicate absorption results from the material in the OD.

We argue that the outer edge of the MD should not extend beyond around 10 pc and the dust within it can have sufficiently high temperature (> 300 K; Laor & Draine, 1993) to produce the silicate emission. Given the maximum silicate absorption of 10^{23}cm^{-2} and the maximum HI column of $>10^{25}\text{cm}^{-2}$, the clouds in the MD should have $N_H > 10^{23}\text{cm}^{-2}$ and produce significant obscuration of the X-ray emission for an intercepting line of sight but not obscure the silicate emission significantly due to a small covering factor. For a given strength of the silicate feature along a line of sight, the large variation in the HI column is caused by the variation in the number or column density of clouds that the line of sight intercepts and the minimum X-ray obscuration is due only to the diffuse component. Based on this concept, as the line of sight varies such that the silicate strength ranges from

0.0 to -0.8 (the minimum value in the sample) as shown in Figure 3.3, the column density of the diffuse component varies from 10^{21} cm^{-2} to 10^{23} cm^{-2} . The evidence for the cloudy OD is that the mid-IR images of NGC 1068 at $10 \mu\text{m}$ (Jaffe et al., 2004) and NGC 4151 (Radomski et al., 2003) at ~ 10 and $\sim 18 \mu\text{m}$ show that the radius of any diffuse component should be smaller than 2 pc and 35 pc, respectively. However, the dust in the OD is relatively cool and emits any reprocessed energy mainly at far-IR wavelengths and thus may be missed for observations at mid-IR wavelengths. Since both the MD and OD are unresolved in the IRS beam, the observed silicate absorption can be provided by several clouds in the OD and the depth of the absorption feature is determined by the average number of clouds along a line of sight. This is because a cloud in the OD is not large enough to cover the whole MD.

3.5 Conclusions

We report observations of $9.7\mu\text{m}$ silicate features in 97 AGNs. The features vary from emission to absorption with increasing HI column density, consistent with unification models. Radio-loud AGN (radio-loud QSOs and FR II galaxies) and radio-quiet QSOs (PG and 2MASS QSOs) lie roughly on the Seyfert-correlation between HI column and silicate feature strength. The behaviors of LINERs and BALQs are not clear due to the small number of objects for these two AGN types. The scatter in the relation is large and several Compton-thick AGNs do not show deep silicate absorption. Qualitatively, the correlation requires a circumnuclear disk geometry with an accretion disk outside of which is a middle disk with high density and with even denser clouds embedded (0.1-10 pc in radius), co-aligned with an outer clumpy disk (10-300 pc in radius). The similarity of the behavior of various types of AGN suggests that this disk geometry may be typical for AGN in general.

CHAPTER 4

Thermal and Non-Thermal Infrared Emission from M87

4.1 Introduction

In this chapter, we study the thermal and non-thermal infrared emission from M87 at 3.6, 4.5, 5.8, 8, 24, 70 and 160 μm . The SED of the thermal IR emission will give insights into the effect of feedback from the jet on the interstellar dust in M87. The nonthermal IR emission will constrain the synchrotron emission model of the radio jets and lobes, which will be useful to reveal how the jet kinetic energy is deposited into the surrounding media. Chapter 4.2 presents the data reduction and analysis. The analysis of the thermal and non-thermal infrared emission is shown in Chapter 4.3. Conclusions are included in Chapter 4.4.

4.2 Data Reduction and Analysis

4.2.1 HST image

We retrieved archived *HST* data (PID 8048, PI J. Biretta) taken with the Wide Field and Planetary Camera 2 (WFPC2). The images were obtained on 2001 November 17 through filters F450W, F606W and F814W. The data were processed through the Post Observation Data Processing System (PODPS) pipeline to remove bias and flat-field artifacts (Biretta et al., 1996). Individual exposures at each wavelength were combined to remove the cosmic-ray events. The outputs of the four chips of WFPC2 were combined and the final image was rotated to put north at the top and east to the left.

To obtain the optical image of the jet and lobe, galaxy light was subtracted in IRAF as in Perlman et al. (2001a). We masked out the optical jet and the Sf lobe as indicated by the 5 GHz radio image. We also masked the region without data

because of the smaller FOV of the PC chip compared to the WFC one. The task ELLIPSE in IRAF was used to fit isophotes of the galaxy image and a model image was constructed with task BMODEL. The optical nonthermal emission was obtained by subtracting the model image from the original image with task IMCALC. We then masked out the globular clusters and chip joining region based on the residual image. The above processes were repeated several times until the final galaxy-subtracted image did not exhibit ring-like structure. In this final image, we replaced each pixel of the masked region except for the jet and lobe with a simulated value based on the average and scatter of residual counts in the non-masked region with the same distance to the galactic center. The final uncertainty includes the fluctuation in the residual image, flat-fielding errors ($\sim 1\%$) and zero-point errors ($\sim 1\%$).

As shown in the right column of Figure 4.1, the optical jet is well detected at all *HST* bands after subtracting the galaxy light. In the region of the radio Sf lobe, there is an elongated feature that becomes more prominent at the longer wavelengths. This feature has morphology, location and position angle similar to the radio component θ seen in the 6 cm image (See Hines et al., 1989). The optical spectrum of this feature has $\alpha \sim 2$ (where $f_\nu \propto \nu^{-\alpha}$), steeper than that of the optical jet ($\alpha \sim 1$, See Perlman et al., 2001a) but flatter than that of galaxy light (~ 2.5). The non-thermal spectrum of this feature indicates it is the optical component of the Sf lobe. The optical counterpart of filament θ has also been detected by previous ground-based observations (Stiavelli et al., 1992; Sparks et al., 1992).

4.2.2 SPITZER DATA

Our MIPS observations (PID 82, PI G. Rieke) were made with the standard small field photometry mode and were reduced with the MIPS instrument team Data Analysis Tool (DAT) version 3.03 (Gordon et al., 2005). At $70\ \mu\text{m}$, extra processing steps beyond those in the DAT were applied to remove known transient effects associated with the $70\ \mu\text{m}$ detectors to achieve the best possible sensitivity. Detector-dependent structures were removed by subtracting column averages from each exposure with the source region masked. In addition, a pixel-dependent time

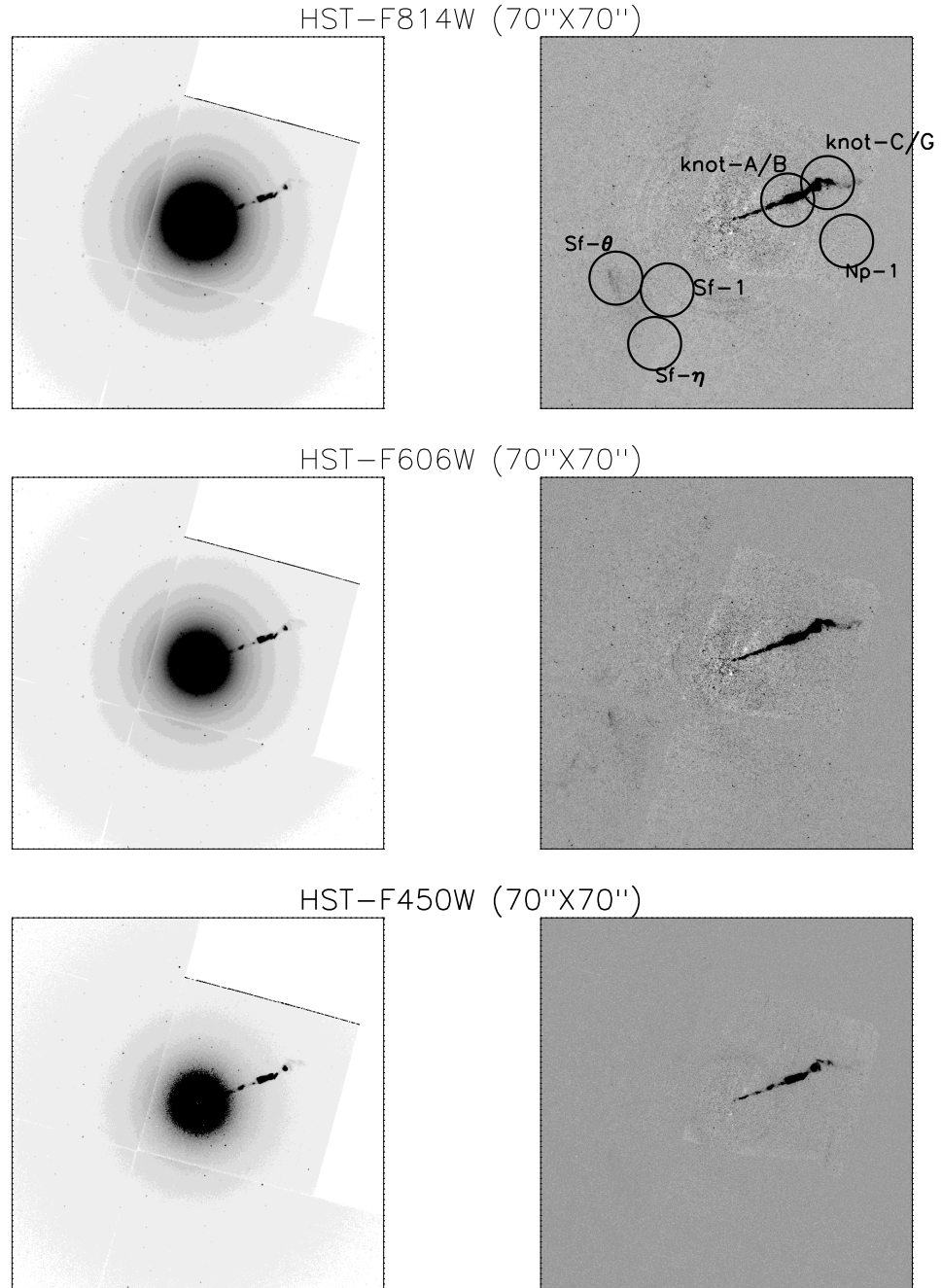


Figure 4.1 Original *HST* images of M87 in the left column and galaxy-light subtracted image in the right column.

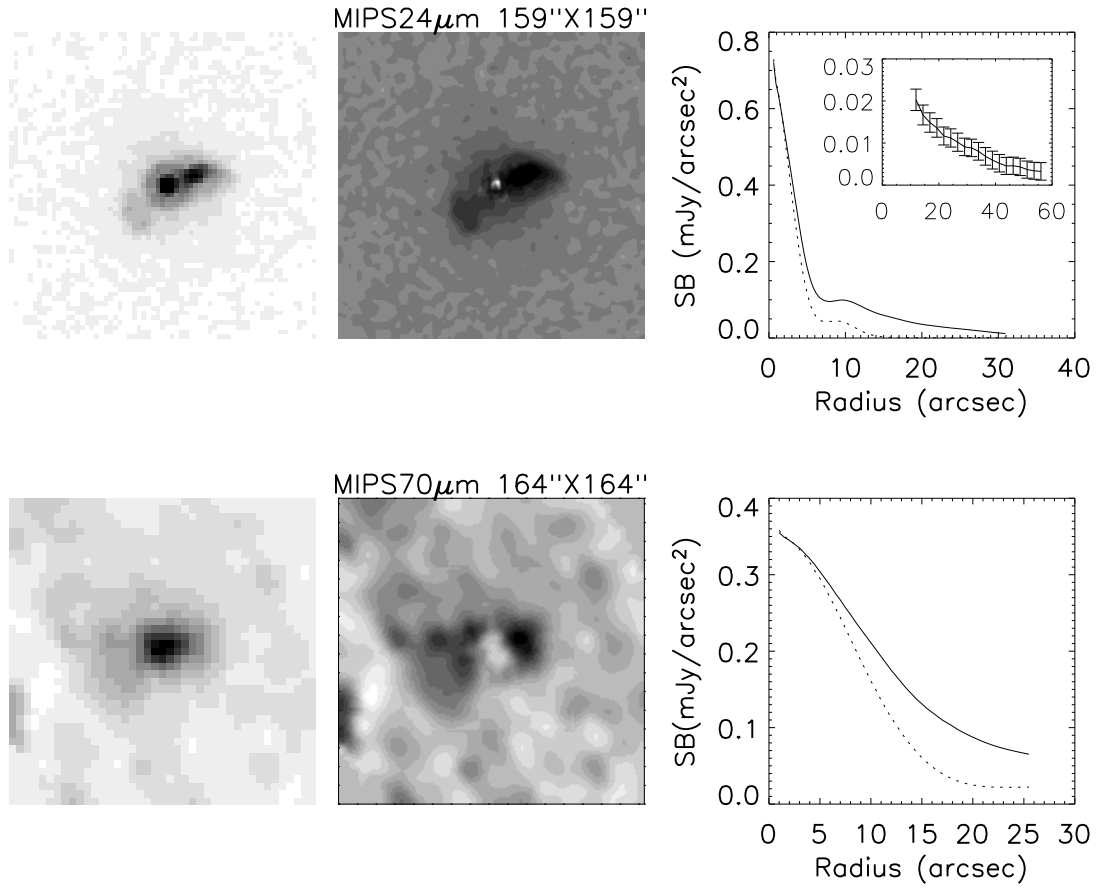


Figure 4.2 Original MIPS images of M87 in the left column. MIPS images of M87 after subtracting the nucleus in the middle column. The radial profile of surface brightness is shown in the right column where the solid line is the profile of the original image and the dotted line is the profile of the PSF at the corresponding wavelength. The subplot at $24\mu\text{m}$ shows the surface brightness of the emission after masking the central lobe region defined by the lowest level contour in Figure 4 of Hines et al. (1989).

filter was applied (with the source region masked) to remove small pixel-dependent residuals. For all the bands, the background was subtracted using the sky level at the edge of each field. The resultant images were resampled by a factor of four and rotated to put north at the top and east to the left. The final MIPS images have fields of view (FOVs) of $7'.5 \times 7'.5$, $6'.5 \times 3'.0$ and $2'.5 \times 6'.0$ at $24\ \mu\text{m}$, $70\ \mu\text{m}$ and $160\ \mu\text{m}$, respectively.

To isolate the output of the jet and lobes at 24 and $70\ \mu\text{m}$, we subtracted the nuclear emission. We used the empirical point spread function (PSF) based on the observed images of stars and provided by the *Spitzer* Science Center (SSC)¹. We aligned the PSF with the centroid of the image and determined the normalization by matching the average surface brightness within a half-FWHM radius. Although the PSF image has a FOV smaller than the image of M87, the contribution is negligible compared to the Poisson noise at regions outside of the PSF coverage. The original and nuclear-subtracted images are shown in Figure 4.2. The uncertainty in the nuclear-subtracted image was estimated by repeating the subtraction with the PSF placed over a 4×4 grid around the centroid of the image. This uncertainty and the Poisson noise were added quadratically to create the final noise image.

IRAC data were taken from the *Spitzer* archive (PID 3228, PI W. Forman). We used the post-basic-calibrated-data (post-BCD) images at a pixel scale of $1''.2$ pixel⁻¹. The resultant images were also rotated to put north at the top and east to the left.

To obtain the non-thermal emission of the jet and lobes at the IRAC bands, the stellar emission was subtracted similarly to the *HST* image. Figure 4.3 shows the original image and residual image of M87 at the four IRAC bands. For some of the faint low-surface-brightness features, we found it impossible to extract reliable measurements at 3.6 and $4.5\ \mu\text{m}$ because of the residuals from subtraction of the stellar emission. With this exception, we obtained reliable measurements for two positions along the jet and four in the lobes at all the *Spitzer* bands out to $24\ \mu\text{m}$, a measurement of the jet and Sf lobe at $70\ \mu\text{m}$, and an integrated measurement of the

¹<http://ssc.spitzer.caltech.edu/mips/psf.html>

nuclear region and surrounding galaxy at $160\mu\text{m}$.

Because of the complexity of the images, we could not apply standard aperture corrections to our photometry. Instead, we used a variety of approaches optimized for each situation. The nuclear fluxes were measured by PSF fitting and calibrated against standard stars measured the same way. To determine spectral slopes, we convolved all the images to the resolution of the lowest resolution image and then used the same photometry approach on all. To obtain flux densities for the jet knots, we used the *HST* F814W image as a template. We first did photometry in the selected aperture on the full-resolution image, and then repeated the photometry on the image convolved with the $24\mu\text{m}$ PSF. A comparison of the results yielded the appropriate aperture correction. We quote all the IRAC photometry at this resolution also for consistency. However, the nonthermal lobes are not well enough detected to use the F814W image in this way, and they are more extended than the knots, so we report photometry for them with no aperture correction. For IRAC measurements of the full M87 galaxy, we applied extended source corrections in accordance with the procedure recommended by the SSC. MIPS photometry of the whole galaxy was corrected in accordance with smoothed STinyTim models of the image, which have been shown to fit the observed PSFs well (Engelbracht et al. in prep., Gordon et al. in prep., Stansberry et al. in prep.). Color corrections are also applied to MIPS photometry for a power law spectrum with an index of 1.0.

The measurements are summarized in Tables 1 - 3. Notes to the tables give details regarding the aperture, extended source and color corrections.

4.2.3 Radio Data

A VLA 5GHz radio map of M87 was obtained at a resolution of $\sim 0.4''$ on 1986 April 25 by Hines et al. (1989), who describe the observation strategy and data reduction.

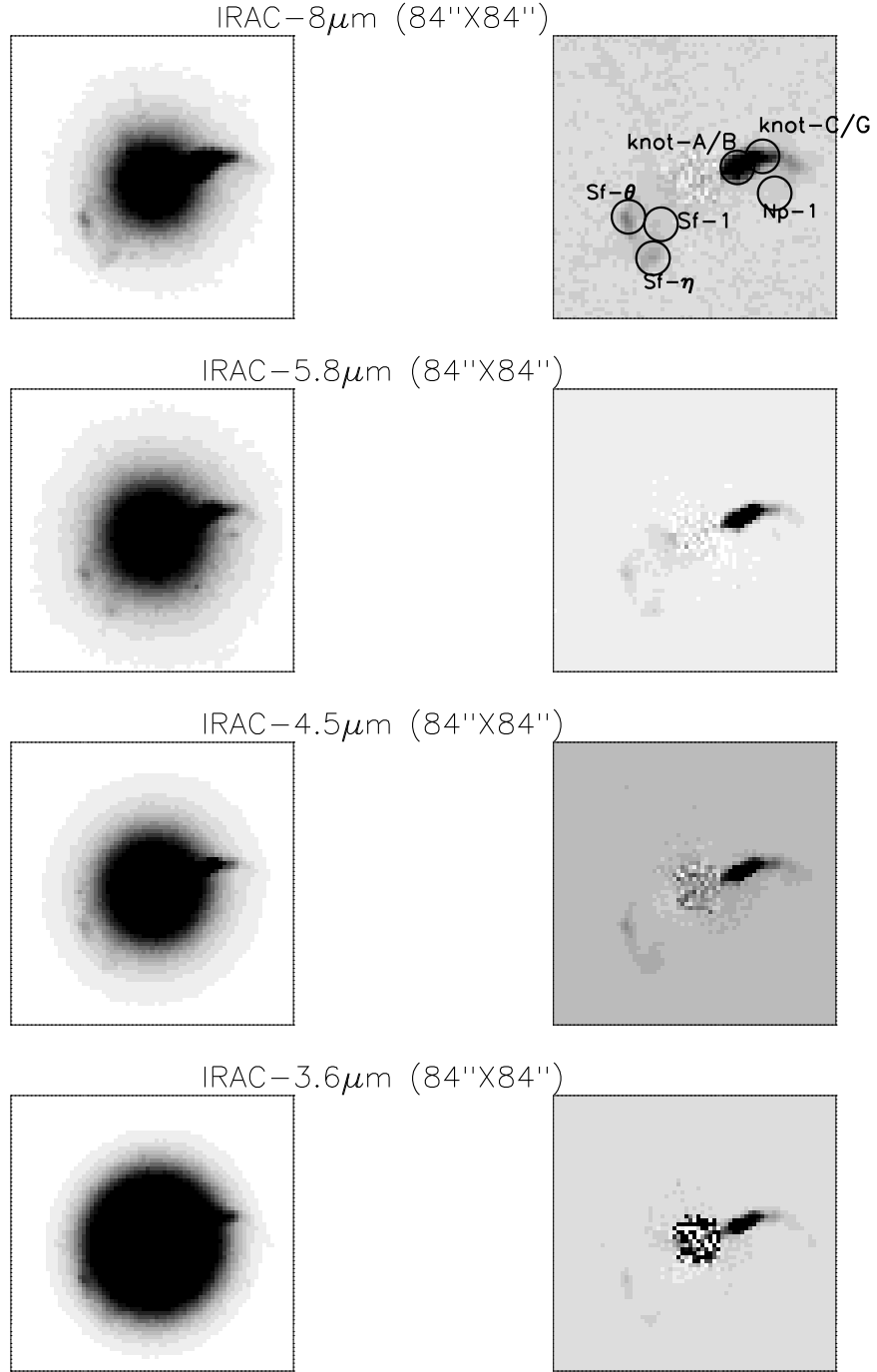


Figure 4.3 Original *IRAC* images in the left column and galaxy-light subtracted images in the right column.

4.2.4 Image Convolution

The images must be convolved to the same resolution as MIPS at $24\mu\text{m}$ to construct the full spectral energy distributions (SEDs). Therefore, we convolved the *HST* and the 6 cm radio data with the MIPS PSF. For the 6 cm image, we subtracted the nuclear emission by masking the central $1''.6 \times 1''.6$ region before convolution. The IRAC images were convolved with kernels that transform the observed IRAC PSFs to the MIPS $24\mu\text{m}$ PSF (Gordon et al., in prep.) The noise images were calculated by error propagation. The centroids of all images were aligned to the center of the 6 cm data at RA(J2000)=12h30m49.42s, DEC(J2000)=12d23m27.97s.

4.3 RESULTS

4.3.1 Infrared Image

Figure 4.4 shows the radio, MIPS $24\mu\text{m}$, IRAC $8\mu\text{m}$ and optical image of M87 with nuclear subtraction at the resolution of MIPS at $24\mu\text{m}$. The stellar emission was also subtracted for the IRAC and optical images. It is obvious that the jet, Np and Sf lobe are all detected at $8\mu\text{m}$ and $24\mu\text{m}$, with morphology similar to the radio emission. The infrared jet extends from the nucleus along a straight line until it bends toward the southeast near the boundary of the Np lobe. The infrared jet peaks at the position of knot-A (although not all knots are resolved), which is the brightest knot in the radio and optical. The brightness profile across the jet indicates the width of the jet is not resolved at $24\mu\text{m}$ but marginally resolved at $8\mu\text{m}$, consistent with the width of the jet of around $1''$ at knot A in the optical image. As illustrated by contours in Figure 4.4, unlike in the radio and optical image where only one flux peak is present in the Sf lobe, there are two flux peaks near the boundary of the Sf lobe in the infrared. The radio filaments (See Hines et al., 1989) corresponding to these two peaks are the filaments θ and η .

Besides the infrared jet and lobes, an infrared halo is clearly visible at $24\mu\text{m}$. The subplot in Figure 4.2 shows the surface brightness of the emission at $24\mu\text{m}$ after masking the central lobe region defined by the lowest level contour in Figure 4

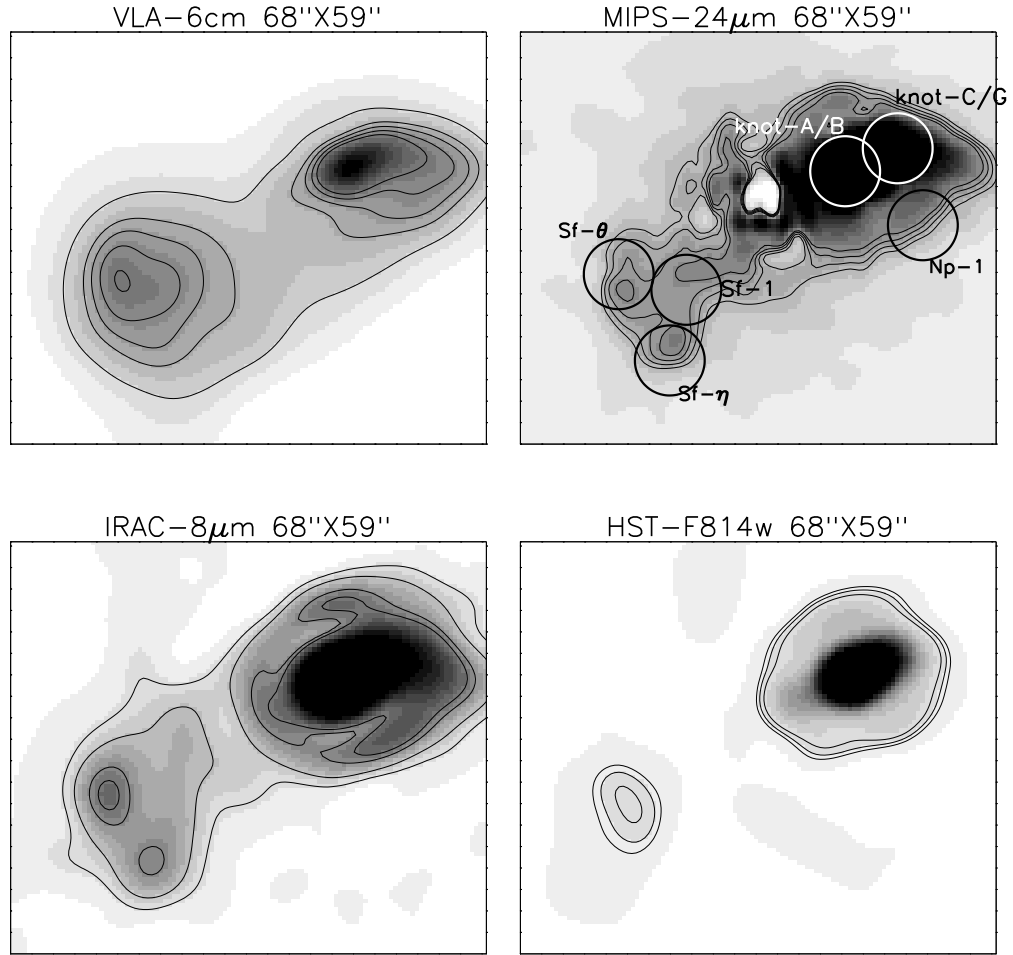


Figure 4.4 The radio, MIPS 24 μ m, IRAC 8 μ m and *HST* optical image of M87 after subtracting the nucleus at the resolution of the MIPS 24 μ m image. The galaxy light is also subtracted for the IRAC and *HST* images. The contours (thin solid lines) are superposed to illustrate two local maxima in the Sf lobe at the infrared wavelength while only one maximum is present in the radio and optical.

of Hines et al. (1989). Unlike the lobe, it has a spherical structure as shown in Figure 4.2, with flux decreasing with increasing distance from the nucleus. Moreover, although the infrared halo is on the same scale as the radio inner region ($1'.5 \times 2'.0$), the morphologies are quite different since the radio inner region is elongated and aligned with the radio lobe (See Owen et al., 2000). The discrepancy in the morphology implies that the emission of the infrared halo arises from a different mechanism. Figure 4.5 shows the map of the spectral index $\alpha_{5GHz}^{24\mu m}$ where the photometry at each grid point at 5 GHz and 24 μm was carried out on the image at the resolution of MIPS at 24 μm and with the nucleus subtracted. The halo has $\alpha_{5GHz}^{24\mu m}$ flatter than the nonthermal emission region, again suggesting a different emission mechanism.

As shown in Figure 4.2, at 70 μm , the jet and Np lobe are detected but are blended; the Sf lobe is also detected. At 160 μm , the jet and lobes are all blended at the *Spitzer* resolution. The infrared halo is not detected at either 70 μm or 160 μm .

4.3.2 Infrared Emission from the Host Galaxy

Table 4.1 shows photometry of M87 within a radius of $30''$, including emission from the nucleus, jet, and most of the Np and Sf lobes. The photometry for the Two Micron All Sky Survey (2MASS) was carried out on the original images without nuclear subtraction. The ISOCAM photometry is from Xilouris et al. (2004); the ISOCAM measurements at shorter wavelengths have been supplanted by the IRAC data, which has a substantially improved ratio of signal to noise. We also include IRAS Faint Source Catalog (FSC) data. Since it was extracted using a point source filter, the effective apertures should be close to the $60''$ used for the other data sources.

To interpret these data, we fitted a stellar SED in the near infrared, taking galaxy colors from Johnson (1966) (because this reference consistently integrates JKL - we applied color corrections as in Carpenter (2001) and Rieke et al., in prep.). The SED was continued to the longer IRAC bands using the measurements of individual K stars in Reach et al. (2005). In normalizing the stellar spectrum,

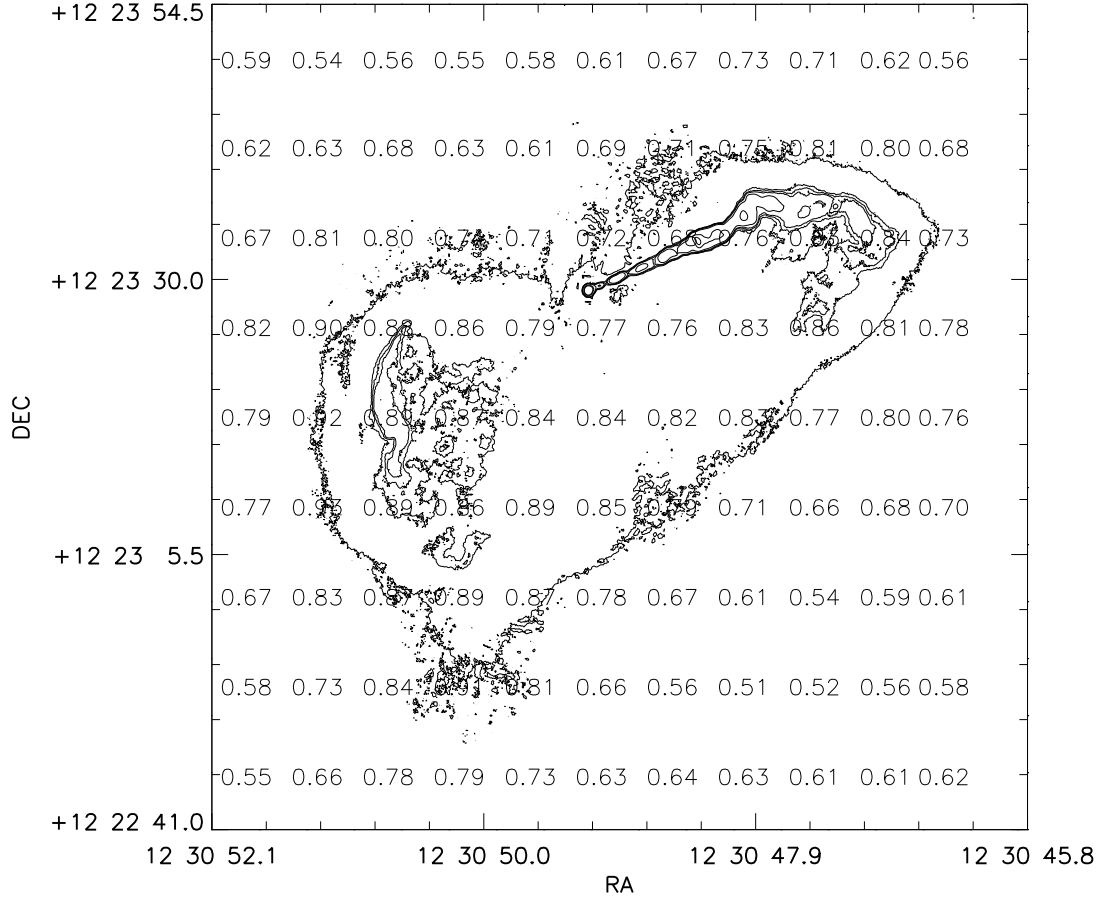


Figure 4.5 The map of the spectral index $\alpha_{5GHz}^{24\mu m}$. The measurements of flux density at 5GHz and 24 μm were made on the image with nuclear subtraction at the resolution of MIPS at 24 μm . The solid contour is the intensity distribution of the original 6 cm image. Contour intervals are [0.11, 0.43, 0.53, 0.64, 1.06, 5.32, 10.64, 173.86] mJy.

Table 4.1. Photometry within the central 60'' diameter region

Wavelength (μm)	Total Flux Density (mJy)	Stellar Component (mJy)	Nonthermal Component (mJy)	Residual (mJy)
1.25	1241 ± 124^1	1122	5	—
2.16	1202 ± 120^1	1110	9	—
3.6	605^2	616	15	—
4.5	375^2	365	19	—
5.8	302^2	225	24	53 ± 15^6
8	189^2	121	33	35 ± 10^6
12	231 ± 37^3	55	49	127 ± 40
15	106 ± 21^4	35	62	9 ± 25
24	171.9 ± 13.4^5	14	99	59 ± 15
60	394 ± 51^3	2	251	141 ± 60
70	455.2 ± 9.2^5	1	293	161 ± 15
160	581.5 ± 10.0^5	0	682	—

Note. — ¹2MASS; ²IRAC, from PID 3228, PI W. Forman. We used extended source corrections of 0.934 at 3.6 μm , 0.97 at 4.5 μm , 0.86 at 5.8 μm and 0.80 at 8 μm ; ³IRAS FSC; ⁴ Xilouris et al. (2004); ⁵MIPS, from PID 82, PI G. Rieke, aperture corrections of 1.09, 1.31 and 1.93 respectively at 24, 70 and 160 μm , color corrections of 1.04, 1.1 and 1.04 respectively at 24, 70 and 160 μm ; ⁶Errors are taken to be 5% of the total flux density in the band.

Table 4.2. Photometry at 70 μm of the nucleus, jet and lobes

Region	RA	DEC	$f_{70\mu\text{m}}$ (Jy)
Nucleus	12 30 49.42	12 23 27.97	228^1
Jet & Np lobe	12 30 48.21	12 23 33.9	70^2
Sf lobe	12 30 50.49	12 23 14.2	57^2

Note. — ¹From PSF fitting; ²Aperture correction factor of 1.3 for a 30''-diameter aperture; Color correction factor of 1.1 for all three fluxes.

we emphasized the IRAC 3.6 and $4.5\mu\text{m}$ points because systematic errors within the IRAC measurements should be smaller than between them and data from other sources. Specifically, the photometry in all four IRAC bands was conducted on the SSC post-BCD images, using the same apertures and sky reference areas.

We fitted two power laws to the nonthermal spectrum, because the nucleus is self-absorbed at frequencies below ~ 2 GHz (e.g. Charlesworth & Spencer, 1982) and hence has a different spectrum from the other components. The nuclear component is fitted to the $10.8\mu\text{m}$ measurement of Perlman et al. (2001b), our measurements at 24 and $70\mu\text{m}$, and those reported by Haas et al. (2004) at 450 and $850\mu\text{m}$. It has $\alpha = 1.15$ and a flux density of 45mJy at $24\mu\text{m}$. The remaining nonthermal emission remains optically thin into the radio, down to 1.4GHz. It has been fitted with a power law with $\alpha = 0.92$ and a flux density of 50mJy at $24\mu\text{m}$. Because the break frequency for the majority of the nonthermal emission is in the optical or UV (Section 4.3.3.3), we continue the power laws toward shorter wavelengths.

Table 4.1 shows the aperture photometry, the stellar and nonthermal spectral components, and the residual flux densities when the modeled SEDs are subtracted from the measurements. This information is also illustrated in Figure 4.6. There is a well detected excess above the model from 6 through $70\mu\text{m}$, which is particularly strongly indicated at 24 and $70\mu\text{m}$. However, the measured values for the nonthermal emission (nucleus, jet, and lobes) at these two wavelengths fall very close to the model, which is dominated by the nonthermal emission. Therefore, it appears that the excess is not associated with the resolved nonthermal sources. The possibility that this emission is associated with the extended nonthermal radio emission can be tested from Figure 5, which shows that the spectrum between 5GHz and $24\mu\text{m}$ becomes *flatter* with increasing distance from the nucleus and jet. This behavior is not expected for extended nonthermal emission, which should either retain the same slope or have a steeper one due to energy losses in the synchrotron electron spectrum.

Sparks et al. (1993) discuss filaments visible in $\text{H}\alpha$. It is plausible that dust in these filaments contributes some of the infrared emission not associated directly

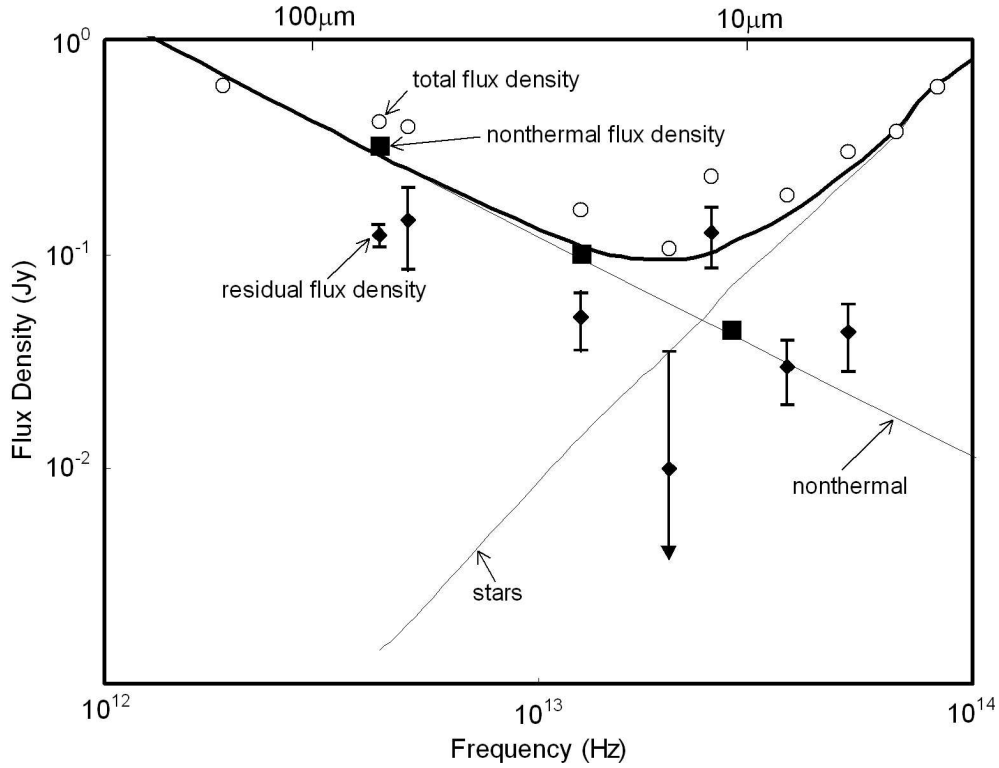


Figure 4.6 Comparison of large aperture photometry with models of the stellar and nonthermal SEDs. The light lines show the models of the power law nonthermal emission and the stellar output, and the heavy line is the sum of the two components. The open circles are the 60 arcsec diameter aperture photometry. The filled boxes show the flux densities for the nucleus, jet, and lobes from this work at 70 and 24 μm , and from Perlman et al. (2001b) (with a correction for low surface brightness components) at 10.8 μm . The diamonds show the residual fluxes after subtracting the model from the totals measured. At 70 μm , we label the points for total, nonthermal, and residual flux density.

with the nonthermal source components. However, the morphology of the $24\mu\text{m}$ image (Figure 4.2) shows it to be more symmetric and more extended than the $\text{H}\alpha$ filaments, which are concentrated in the region occupied by the jet and lobes. Therefore, most of the infrared emission must arise from a different component of the galaxy. The agreement with the pure elliptical isophotes seen in the optical surface brightness (Liu et al., 2005) indicates the dust should be smoothly distributed in the host galaxy.

The overall level of excess emission at $70\mu\text{m}$ is at a normal level for giant elliptical galaxies (e.g. Temi, 2004; Leeuw, 2004), where the dust is heated by the stellar light or collisions with electrons in the hot gas. The overall SED of M87 from the near infrared to $24\mu\text{m}$ is very similar to those of the low-activity (i.e., non-infrared-luminous) brightest cluster galaxies (BCGs) discussed by Egami et al. (2006). The excesses detected weakly in the IRAC 5.8 and $8\mu\text{m}$ bands and in the IRAS FSC at $12\mu\text{m}$ suggest the possibility of weak, extended aromatic emission, which is seen in a number of X-ray-emitting elliptical galaxies by Kaneda et al. (2005) (but see also Bregman et al. (2006)). However, aromatic emission is not seen in the nuclear spectrum (Bressan et al., 2006), which instead shows silicate emission either associated with the AGN or with evolved stars. Therefore, if these features are present they must arise from dust distributed within the galaxy and perhaps heated as in other X-ray-emitting giant ellipticals. In any case, the characteristics of the mid- and far-infrared excess above the compact nonthermal emission from M87 appear to be consistent with expectations for a normal BCG and need have little to do with the nonthermal activity in the nucleus and jet.

4.3.3 Behavior of the Nonthermal Sources

4.3.3.1 SEDs of the Nonthermal Sources

We now consider the extranuclear nonthermal emission. As shown in Figure 4.7, we constructed the SED from the radio to optical wavelengths for two regions in the

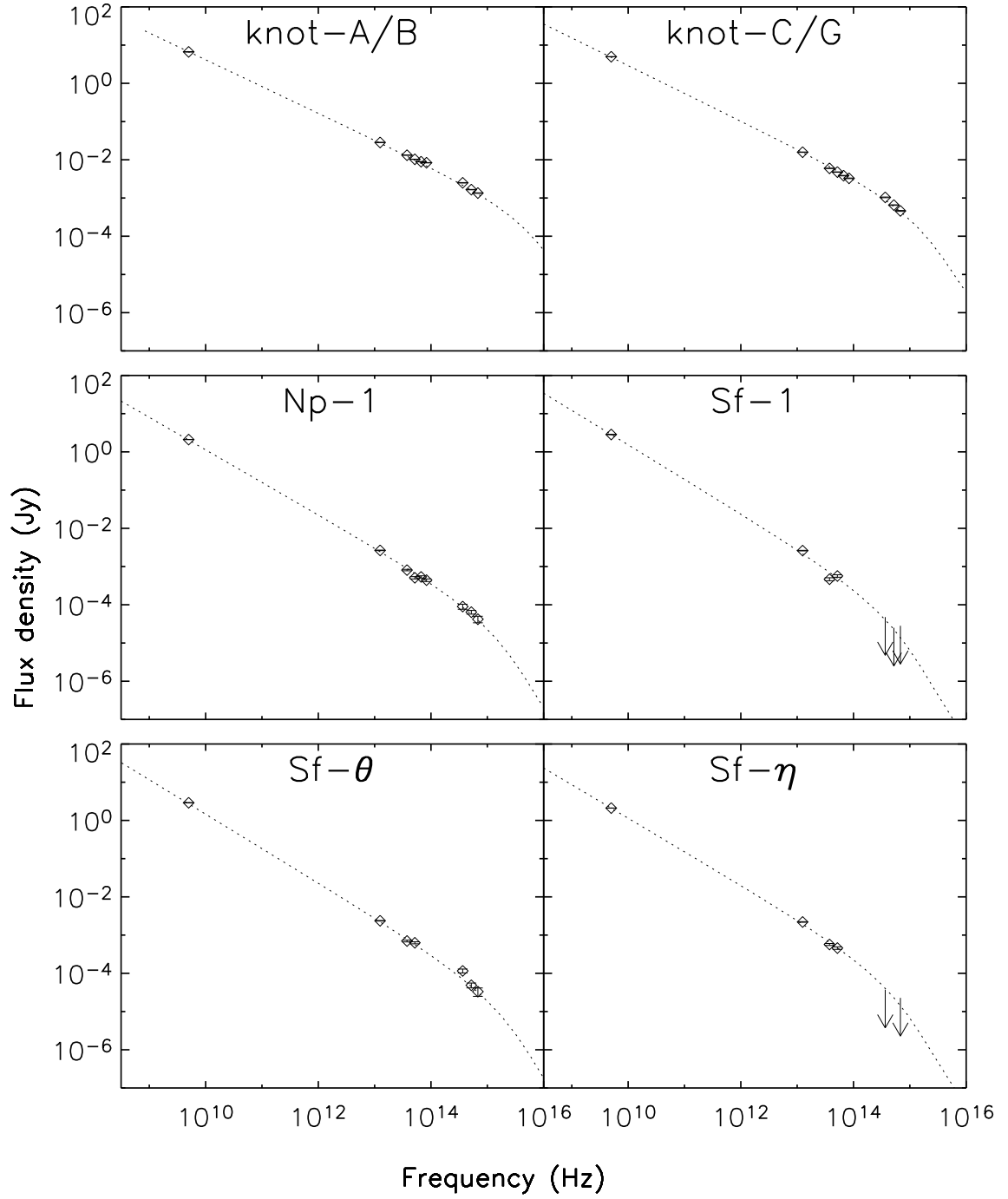


Figure 4.7 SEDs of individual regions in the MIPS 24 μm image (see Figure 4.2). The photometry of the nonthermal features is shown as diamonds, with downward pointing arrows for the upper limits. The lines are the fits of the KP synchrotron emission models.

Table 4.3. Spectral properties of the nucleus, jet and lobes at the resolution of
MIPS at $24\mu\text{m}$

Region	RA	DEC	$f_{24\mu\text{m}}$ (mJy)	$f_{8\mu\text{m}}$ (mJy)	$f_{5.8\mu\text{m}}$ (mJy)	$f_{4.5\mu\text{m}}$ (mJy)	$f_{3.6\mu\text{m}}$ (mJy)	$\alpha_R^{24\mu\text{m}}$	α_R^{opt}	L_{tot}^{syn} (erg)
Nucleus	-	-	50.7 ¹	-	-	-	-	-	-	-
knot-A/B	12 30 48.64	12 23 32.2	32.1 ²	13.19	10.29	8.92	8.36	0.70	0.71	1.81E+42
Knot-C/G	12 30 48.12	12 23 35.4	17.6 ³	5.97	4.77	3.84	3.27	0.74	0.77	6.88E+41
Np-1	12 30 47.88	12 23 24.5	3.22 ⁴	0.81	0.51	0.54	0.44	0.85	0.91	1.03E+41
Sf-1	12 30 50.19	12 23 15.3	3.45 ⁴	0.47	0.57	-	-	0.89	> 0.99	9.29E+40
Sf- θ	12 30 50.85	12 23 17.5	2.93 ⁴	0.70	0.63	-	-	0.91	0.94	1.01E+41
Sf- η	12 30 50.35	12 23 5.2	2.70 ⁴	0.57	0.46	-	-	0.88	> 0.98	7.85E+40

Note. — ¹ Nuclear flux density obtained by fitting PSF to the surface brightness profile; ²An aperture correction factor of 1.76; ³An aperture correction factor of 1.40; ⁴No aperture correction; Color correction factor of 1.04 at $24\mu\text{m}$.

jet (knot-A/B and knot-C/G ², one region (labeled as Np-1) in the Np lobe, and three regions (Sf-1, Sf- θ and Sf- η) in the Sf lobe. Each region is circular with a radius of $5''$. The position of each region and the corresponding $24\mu\text{m}$ flux density are listed in Table 4.3.

Figure 4.7 shows the SEDs of the different regions. The stellar emission is modeled with a blackbody spectrum fitted to the total IRAC $3.6\mu\text{m}$ and total optical emission within each region. Table 4.3 lists the radio-infrared spectral index $\alpha_R^{24\mu\text{m}}$ between 5 GHz and $24\mu\text{m}$ after subtracting the stellar contribution and the radio-optical index α_R^{opt} between 5GHz and the three *HST* bands. In the jet and lobe, it seems that the regions with lower infrared surface brightness have a steeper $\alpha_R^{24\mu\text{m}}$. $\alpha_R^{24\mu\text{m}}$ is also flatter than α_R^{opt} , as expected for synchrotron radiation with a higher rate of electron energy loss at the higher energies. The larger steepening $\Delta\alpha = \alpha_R^{opt} - \alpha_R^{24\mu\text{m}}$ in the lobe (~ 0.03 - 0.1) than the jet (~ 0.01 - 0.03) reveals that the high-energy cutoff of electron energy in the lobe occurs at a lower frequency, as demonstrated by the SED fits below.

²we use composite designations to emphasize that the knots are blended at our resolution.

4.3.3.2 Minimum Pressure Analysis

Assuming the equipartition condition that the particle energy is equal to the magnetic energy, the minimum magnetic field, energy, and pressure of the emitting plasma can be derived from the observed SED, the emitting volume and the filling factor ϕ (Pacholczyk, 1970). The standard minimum pressure analysis assumes a power law distribution of electron energy; the dependence of the physical parameters on the high frequency cut-off is negligible if the spectral index $\alpha > 0.5$, as for M87. This implies that the synchrotron loss at high frequencies does not change the results for M87.

During the calculation, the ratio of proton energy to electron energy is assumed to be unity. The SED is assumed to be a power law with a spectral index equal to $\alpha_R^{24\mu m}$ between 10^8 Hz and the break frequency. A low frequency cut-off of 10^8 Hz was adopted, as the SED of jet and lobe starts to deviate from a power law at 1 GHz (Felten, 1968; Meisenheimer et al., 1996). One order of magnitude variation in the low frequency cutoff results in a factor of ~ 1.2 change in the magnetic field and a factor of ~ 1.4 change in the energy and pressure. The volume is taken to be spherical with a radius of 5 arcsec and the filling factor is assumed to be 0.1. A factor of 10 variation in the filling factor corresponds to a factor of ~ 2 in the magnetic field, energy, and pressure. The filling factor is hard to determine as it depends on the true three dimensional structure of the synchrotron plasma. The value of 0.1 was adopted to balance among various alternatives, such as a whole filled volume or a thin boundary layer of the volume as proposed by some studies (Owen et al., 1989).

The last three columns of Table 4.4 list the minimum magnetic field, energy, and pressure computed with formulae given by Burns et al. (1979). Our results agree well with those of Eilek et al. (2003). Independent support for the derived magnetic field strengths comes from the inverse Compton fluxes measured in Tev gamma rays. Stawarz et al. (2005) analyze the HESS and HEGRA data to derive a lower limit of $300\mu\text{G}$. However, the Tev gamma ray limit cannot be applied individually to the

Table 4.4. The physical parameters from the spectrum fit

Region	α_{INPUT}	$\nu_t(\text{Hz})$	$t_{syn}(\text{yr})$	$Ee_{max}(0.5\text{Mev})$	$B_{minP}(\text{G})$	$E_{minP}(\text{erg})$	$P_{minP}(\text{dyn cm}^{-2})$
(1)	(2)	(3)	(4)	(5)	(6)	(7)	(8)
knot-A/B	0.70	$\geq 5\text{E}15$	$\leq 5\text{E}2$	$\geq 4\text{E}06$	$1.3\text{E}-04$	$3\text{E}54$	$8\text{E}-10$
Knot-C/G	0.73	$\geq 1.4\text{E}15$	$\leq 8\text{E}2$	$\geq 2\text{E}06$	$1.2\text{E}-04$	$2.5\text{E}54$	$6\text{E}-10$
Np-1	0.85	$\sim 1.6\text{E}15$	$\sim 9\text{E}2$	$\sim 2\text{E}06$	$1.0\text{E}-04$	$1.6\text{E}54$	$4\text{E}-10$
Sf-1	0.90	$\sim 6\text{E}14$	$\sim 1.4\text{E}3$	$\sim 1.3\text{E}06$	$1.1\text{E}-04$	$2\text{E}54$	$5\text{E}-10$
Sf- θ	0.90	$\geq 2\text{E}15$	$\leq 7\text{E}2$	$\geq 2\text{E}06$	$1.1\text{E}-04$	$2\text{E}54$	$5\text{E}-10$
Sf- η	0.88	$\sim 6\text{E}14$	$\sim 1.5\text{E}3$	$\sim 1.4\text{E}06$	$1.0\text{E}-04$	$1.6\text{E}54$	$4\text{E}-10$

various regions we have isolated in M87.

4.3.3.3 Model of the Synchrotron Emission

We employ a quantitative model to extract the underlying physical parameters regulating the SED. The Kardashev-Pacholczyk (KP) model (Kardashev, 1962; Pacholczyk, 1970) has been shown to fit the jet behavior well (Perlman et al., 2001a). It describes the synchrotron emission of an ensemble of electrons ejected t seconds ago. Assuming the initial energy distribution of the electrons is a power law $N(E_0, \omega, 0) = N_0 E_0^{-\gamma}$ where ω is the pitch angle, the new energy distribution of electrons at time t due to synchrotron loss is:

$$N(E, \omega, t) = N_0 E^{-\gamma} (1 - c_2 B^2 \sin^2(\omega) E t)^{\gamma-2} \quad (4.1)$$

where $c_2 = 2.37 \times 10^{-3}$ (in cgs units) as defined in Pacholczyk (1970). Integrating over the pitch angle, the intensity of the synchrotron emission from these electrons at frequency ν is:

$$I_\nu = 2\pi s c_3 c_1^{(\gamma-1)/2} N_0 B^{(\gamma+1)/2} \tilde{\nu}_T^{(1-\gamma)/2} \tilde{B}(\tilde{x}_T, \gamma) \quad (4.2)$$

where s is the extension of the source along the line of sight, $c_1 = 6.27 \times 10^{18}$ (in cgs units), $c_3 = 1.87 \times 10^{-23}$ (in cgs units), B is the magnetic field, $\tilde{\nu}_T = c_1 / (c_2^2 B^3 t^2)$. and $\tilde{x}_T = \nu / \tilde{\nu}_T$. Therefore, for a given magnetic field, the shape of the synchrotron

radiation spectrum is described by three physical parameters: the break frequency ($\tilde{\nu}_T$), the initial power-law index of the electron energy distribution (γ) and the normalization (flux at a given frequency).

The dotted line in Figure 4.7 shows the SED model fitted to the photometry excluding upper limits. The results from the SED fits for regions in the jet and lobe are given in Table 4.4. As a check of our calculations, the break frequency in knot-A/B agrees well with previous work; for example, it is intermediate between the values for the individual knots A and B obtained by Waters & Zepf (2005). Our values for the knots are $\geq 1 - 5 \times 10^{15}$ Hz. In the Np and Sf lobes, the turnover of the spectrum occurs in the optical with a break frequency at least a factor of five lower than for knots A/B, except for the Sf- θ region, which has a comparable break frequency to the jet. Stiavelli et al. (1997) obtained a cutoff frequency of 4.3×10^{14} Hz for the feature θ , almost one order of magnitude lower than our value. The discrepancy arises mainly because of the difference in the optical photometry of the feature θ . We believe that the high resolution and high S/N *HST* images should minimize the uncertainties associated with the stellar subtraction. Nonetheless, accurate determination of the break frequencies requires photometry in the UV, which is not used in either study. However, our conclusions in this paper depend only on the break frequencies lying at optical or shorter wavelengths, not on the exact frequencies involved.

The lowerlimit of the current maximum electron energy (Uchiyama et al., 2006) derived from the break frequency

$$E_{max} = 0.28 \left(\frac{1+z}{\delta} \right)^{0.5} (B/10^{-4})^{-0.5} (v_t/10^{14})^{0.5} \text{ Tev} \quad (4.3)$$

is another physical parameter constraining the acceleration model, where z is the redshift and δ is the Doppler factor. For $z=0$ and $\delta=1$, as shown in Table 4.4, a maximum electron energy with Lorentz factor greater than 10^6 prevails in both the jet and lobe regions.

4.3.3.4 *In Situ* Reacceleration in the Lobe

The *Spitzer* data provide improved constraints on the synchrotron spectrum in the Np and Sf lobes, showing that the break frequency occurs in the optical or in the UV for Sf- θ . The corresponding synchrotron age ($t = (c_1/(c_2^2 B^3 \nu_t))^{0.5}$ secs; Pacholczyk, 1970) for the two jet regions and Sf- θ is around 500 yrs while electrons in the Np and Sf lobes are $\sim 1 \times 10^3$ yrs old. The largest distance that electrons can travel in 1000 yrs must be smaller than $ct = 300\text{pc}$ ($4''$) where c is the speed of light. Therefore, *in situ* reacceleration of electrons must occur in the jet (as found previously by, e.g., Perlman et al., 2001a; Eilek et al., 2003; Waters & Zepf, 2005), and in both the Np and Sf lobes. Hines et al. (1989) showed how this process could explain some additional features in the lobes, such as the bright radio filaments.

As shown in Table 4.4, the individual regions in the lobes have a minimum electron energy around 10^{54} erg and thus a conservative estimate of the electron energy in an entire lobe is around 10^{55} erg, considering its probable total volume. Given a synchrotron age of 10^3 yrs, the minimum input energy rate into an entire lobe is around 3×10^{44} erg s $^{-1}$. Assume for the moment that this energy is supplied by supernovae. If each supernova releases an energy of 10^{52} erg, the explosion rate accounting for the observed input energy rate is 1 yr $^{-1}$, much higher than observed in normal galaxies. The gravitational potential as implied by the X-ray luminosity of thermal gas is much lower compared to this reacceleration rate. The most plausible energy source is the jet, especially for the Np lobe where the jet is visible. The minimum jet power is around 3×10^{44} erg s $^{-1}$ (Owen et al., 2000). If the electrons in the lobe are reaccelerated *in situ* by a mechanism driven by the jet, most of the jet power must be converted into the kinematics of electrons in the lobe.

Radial outflow connecting the lobe and outer halo is frequently interpreted as a buoyant bubble originally inflated by jet (Owen et al., 2000); the radio lobe may be inflating the bubble before detaching from the nucleus (Gull & Northover, 1973; Bicknell & Begelman, 1996; Churazov et al., 2001). The rising bubble captures the hot X-ray gas from the ambient medium, creating the X-ray arc as seen in the X-ray

image (Young et al., 2002; Forman et al., 2006). In general, the total energy of jet power is converted to the internal energy of the lobe or to the work to inflate the lobe (e.g. Bicknell et al., 1997). The relative fraction may be determined by the expansion process. The result of this study, that most of the jet power is locked into the kinetic energy of the electrons in the lobe, implies that only a small fraction of the jet power is used to inflate a cavity (radio lobe) in the thermal gas atmosphere. This conclusion appears to be consistent with the X-ray observation that the energy for inflation is much lower than the minimum jet power (See Young et al., 2002). The kinetic energy of the high-energy electrons should be carried away by radiation due to the short synchrotron lifetime, while the radio plasma could live long enough to inflate the lobe if synchrotron radiation is the only energy loss mechanism. As shown in Table 4.3 and Table 4.4, the total synchrotron luminosity of the lobe is much smaller than the energy rate for electron reacceleration. It is possible that most of the low-energy-electron kinetic energy is carried away by bubbles to the outer halo to heat the cooling flow.

4.4 Conclusions

We present *Spitzer* observations of the giant elliptical galaxy M87 in the Virgo cluster. The basic conclusions are:

- (1) The far infrared excess emission above the non-thermal power law is likely to be warm dust distributed throughout the galaxy. Its luminosity is similar to that observed in the far infrared for other, normal giant elliptical galaxies.
- (2) The infrared emission in the jet and two lobes is synchrotron emission with break frequencies in the UV (jet) or optical (lobes). The high break frequency in the lobes indicates that *in situ* reacceleration of electrons occurs there as well as in the jet. The minimum input energy rate to reaccelerate the electrons in the lobe is comparable to the jet power, implying that most of the jet power is converted to electron kinematics in the lobe, not used to inflate the lobe.

CHAPTER 5

Aromatic Features in AGN: Star-Forming Infrared Luminosity Function of AGN Host Galaxies

5.1 Introduction

Although the commonly used star-formation tracers (the total UV, $H\alpha$ and IR emission) may be contaminated severely by the nuclear emission, there are several alternatives to estimate the SFR in AGN, such as the extended UV emission, extended mid-IR emission, and narrow metal emission lines. The extended UV emission can be observed with high-resolution telescopes such as *HST*. However, due to the large brightness contrast between type 1 AGN and the host galaxy in the UV, this method is limited to type 2 AGN, and even for them the scattered nuclear UV emission may be significant (Zakamska et al., 2006). Extended mid-IR emission has been used to estimate the SFR for nearby Seyfert galaxies (e.g. Maiolino et al., 1995). Due to the limited angular resolution of infrared telescopes, it becomes difficult to resolve the AGN from the circumnuclear star formation for objects at $z > 0.05$ ($0.5'' = 500\text{pc}$). Estimating the SFR with narrow metal emission lines is difficult because they are contaminated by the AGN narrow emission line region. In addition, this method suffers from other problems, for example, the $[\text{OII}]\lambda 3727$ flux of PG quasars indicates a very low SFR (Ho, 2005), which is inconsistent with the abundant molecular gas in these objects and possibly a result of under-estimating the amount of extinction of the emission line (Schweitzer et al., 2006).

In this chapter, we study the general behavior of star formation in AGN host galaxies by employing the aromatic features. Chapter 5.2 describes the sample, the data reduction, the extraction of the features at 7.7 and $11.3\ \mu\text{m}$ and the determination of the associated uncertainties. In Chapter 5.3, we provide evidence for the star-formation excitation of the aromatic feature in these objects. In Chapter 5.4,

we estimate the conversion factor from the aromatic flux to the total IR flux. Chapter 5.5 discusses the origin of AGN far-IR emission. In Chapter 5.6, we construct the luminosity function of the SFR in AGN host galaxies and discuss its implication for AGN activity. Chapter 5.7 presents our conclusions.

5.2 DATA AND ANALYSIS

5.2.1 Sample

The sample in this paper is composed of objects derived from three parent samples selected by different techniques: optically-selected Palomar-Green (PG) quasars (Schmidt & Green, 1983); the Two-Micron All Sky Survey (2MASS) quasars (Cutri et al., 2001); and 3CR radio galaxies and quasars (Spinrad et al., 1985). PG quasars are selected at B band to have blue $U-B$ color, a dominant starlike appearance, and broad emission lines. 2MASS quasars represent a much redder near-IR-to-optical quasar population compared to PG quasars but have similar K_s -band luminosity (Smith et al., 2002). Unlike PG quasars, the 2MASS and 3CR samples include objects with narrow, intermediate and broad emission lines.

Besides IRS spectra observed in our own programs (Program-ID 49, PI F. Low; Program-ID 82, PI G. Rieke; Program-ID 3624, PI R. Antonucci; Program-ID 20142, PI P. Ogle), we searched for archived spectra for objects in the three parent samples. Our sample is listed in Table 5.1. Fig. 5.1 compares the final three subsamples with their corresponding parent samples. For the PG parent sample from Schmidt & Green (1983), we exclude a non-quasar object PG 0119+229 and correct the redshift of PG 1352+011 to be 1.121 according to Boroson & Green (1992). As shown in Fig. 5.1, we have included the whole PG parent sample at $z < 0.5$. The quasar PG 2349-014 is not included in the original PG parent sample and this is why our PG subsample has one more object in the second redshift bin. For the 2MASS and 3CR subsamples at $z < 0.5$ and $z < 1.0$, respectively, about one third of the objects are included in this study. The subplots show that our 2MASS and 3CR subsamples are strongly biased toward high flux density at the wavelength where their parent

Table 5.1. AGN with associated physical parameters

source (1)	Redshift (2)	F(7.7 μ m) (3)	EW(7.7 μ m) (4)	F(11.3 μ m) (5)	EW(11.3 μ m) (6)	L_{SFIR} (7)	$L_{5-6\mu m}$ (8)	$S_{\text{CO}}\Delta V$ (9)	Ref (10)
PG0003+158	0.450			< 0.13			1.2×10^{11}		
PG0003+199	0.025	< 1.39		0.29 ± 0.06	0.01	$(8.8 \pm 4.03) \times 10^{08}$	3.3×10^{09}		
PG0007+106	0.089	< 1.39		0.51 ± 0.06	0.03	$(3.2 \pm 1.32) \times 10^{10}$	1.9×10^{10}	< 3.00	1
PG0026+129	0.142	< 0.36		< 0.12		$< 4.5 \times 10^{10}$	3.0×10^{10}		
PG0043+039	0.385	< 0.36		< 0.08		$< 5.1 \times 10^{11}$	1.0×10^{11}		
PG0049+171	0.064	< 0.50		< 0.05		$< 3.1 \times 10^{09}$	2.1×10^{09}		
PG0050+124	0.061	8.28 ± 5.61	0.05	2.77 ± 0.25	0.02	$(9.3 \pm 3.82) \times 10^{10}$	4.3×10^{10}	18.00	2
PG0052+251	0.155	< 1.74		0.55 ± 0.12	0.05	$(1.3 \pm 0.62) \times 10^{11}$	3.2×10^{10}	2.00	3
PG0157+001	0.163	6.71 ± 2.44	0.25	2.44 ± 0.16	0.09	$(8.9 \pm 3.61) \times 10^{11}$	5.7×10^{10}	8.10	
PG0804+761	0.100	< 1.75		< 0.19		$< 3.8 \times 10^{10}$	5.6×10^{10}	2.00	2
PG0838+770	0.131	1.46 ± 0.60	0.17	< 0.23		$(6.1 \pm 3.09) \times 10^{10}$	1.2×10^{10}	3.40	1
PG0844+349	0.064	1.56 ± 0.60	0.09	0.38 ± 0.07	0.03	$(1.0 \pm 0.44) \times 10^{10}$	6.5×10^{09}	< 1.50	2
PG0921+525	0.035	< 0.59		< 0.05		$< 8.6 \times 10^{08}$	2.2×10^{09}		
PG0923+201	0.190	< 0.35		< 0.29		$< 9.0 \times 10^{10}$	5.9×10^{10}		
PG0923+129	0.029	9.73 ± 2.28	0.28	2.42 ± 0.13	0.08	$(1.3 \pm 0.51) \times 10^{10}$	1.6×10^{09}		
PG0934+013	0.050	2.86 ± 0.60	0.26	0.74 ± 0.05	0.08	$(1.2 \pm 0.48) \times 10^{10}$	1.8×10^{09}		
PG0946+301	1.216	< 0.47		< 0.11		$< 1.8 \times 10^{13}$	1.7×10^{12}		
PG0947+396	0.205	< 0.38		< 0.18		$< 1.2 \times 10^{11}$	5.0×10^{10}		
PG0953+414	0.234	< 1.39		< 0.20		$< 3.8 \times 10^{11}$	7.8×10^{10}		
PG1001+054	0.160	< 0.38		0.17 ± 0.03	0.03	$(3.8 \pm 1.66) \times 10^{10}$	2.7×10^{10}		
PG1004+130	0.240	< 0.58		0.20 ± 0.05	0.02	$(1.3 \pm 0.62) \times 10^{11}$	6.2×10^{10}		
PG1011-040	0.058	< 0.56		0.50 ± 0.04	0.03	$(1.1 \pm 0.44) \times 10^{10}$	3.6×10^{09}		
PG1012+008	0.186	< 0.61		< 0.09		$< 8.2 \times 10^{10}$	3.6×10^{10}		
PG1022+519	0.044	4.22 ± 0.74	0.44	1.32 ± 0.08	0.19	$(1.8 \pm 0.73) \times 10^{10}$	1.4×10^{09}		

Table 5.1 (cont'd)

source (1)	Redshift (2)	F(7.7 μ m) (3)	EW(7.7 μ m) (4)	F(11.3 μ m) (5)	EW(11.3 μ m) (6)	L_{SFIR} (7)	$L_{5-6\mu\text{m}}$ (8)	$S_{\text{CO}}\Delta V$ (9)	Ref (10)
PG1048+342	0.167	< 0.33		< 0.04		$< 2.1 \times 10^{10}$	1.3×10^{10}		
PG1048-090	0.344	< 0.33		< 0.06		$< 2.8 \times 10^{11}$	5.4×10^{10}		
PG1049-005	0.359	1.17 ± 0.38	0.07	0.17 ± 0.07	0.01	$(3.4 \pm 1.93) \times 10^{11}$	2.2×10^{11}		
PG1100+772	0.311	< 1.04		0.29 ± 0.08	0.04	$(4.1 \pm 1.99) \times 10^{11}$	1.0×10^{11}		
PG1103-006	0.423	< 0.18		< 0.09		$< 3.6 \times 10^{11}$	1.3×10^{11}		
PG1114+445	0.143	< 0.40		< 0.11		$< 5.2 \times 10^{10}$	4.4×10^{10}		
PG1115+407	0.154	2.55 ± 0.33	0.28	0.46 ± 0.03	0.08	$(1.1 \pm 0.46) \times 10^{11}$	2.1×10^{10}		
PG1116+215	0.176	< 3.32		< 0.25		$< 2.3 \times 10^{11}$	1.1×10^{11}		
PG1119+120	0.050	2.26 ± 0.89	0.06	0.80 ± 0.09	0.03	$(1.3 \pm 0.53) \times 10^{10}$	5.0×10^{09}	4.50	1
PG1121+422	0.225	< 0.35		< 0.09		$< 1.2 \times 10^{11}$	3.0×10^{10}		
PG1126-041	0.060	< 1.23		1.35 ± 0.36	0.04	$(3.6 \pm 1.75) \times 10^{10}$	1.6×10^{10}	< 2.60	1
PG1149-110	0.049	< 0.64		< 0.10		$< 3.5 \times 10^{09}$	2.2×10^{09}		
PG1151+117	0.176	< 3.30		< 0.48		$< 5.2 \times 10^{11}$	1.9×10^{10}		
PG1202+281	0.165	1.41 ± 0.48	0.14	0.37 ± 0.05	0.04	$(1.0 \pm 0.44) \times 10^{11}$	2.5×10^{10}	< 2.40	1
PG1211+143	0.080	< 1.82		< 0.15		$< 1.9 \times 10^{10}$	2.8×10^{10}	< 1.50	2
PG1216+069	0.331	< 0.34		< 0.05		$< 1.9 \times 10^{11}$	8.9×10^{10}		
PG1226+023	0.158	< 2.16		< 0.16		$< 1.0 \times 10^{11}$	3.7×10^{11}		
PG1229+204	0.063	< 0.54		0.38 ± 0.12	0.02	$(9.8 \pm 4.94) \times 10^{09}$	7.0×10^{09}	2.40	2
PG1244+026	0.048	1.76 ± 0.86	0.14	0.51 ± 0.04	0.04	$(7.0 \pm 2.86) \times 10^{09}$	1.8×10^{09}		
PG1259+593	0.477	< 0.16		< 0.04		$< 3.8 \times 10^{11}$	2.7×10^{11}		
PG1302-102	0.278	< 0.51		< 0.14		$< 3.7 \times 10^{11}$	1.0×10^{11}		
PG1307+085	0.155	< 3.47		< 0.43		$< 3.2 \times 10^{11}$	2.6×10^{10}		
PG1309+355	0.184	< 3.17		< 0.36		$< 3.9 \times 10^{11}$	4.4×10^{10}	< 0.61	3
PG1310-108	0.034	2.40 ± 0.86	0.11	0.18 ± 0.03	0.01	$(1.0 \pm 0.44) \times 10^{09}$	1.3×10^{09}		

Table 5.1 (cont'd)

source (1)	Redshift (2)	F(7.7 μ m) (3)	EW(7.7 μ m) (4)	F(11.3 μ m) (5)	EW(11.3 μ m) (6)	L_{SFIR} (7)	$L_{5-6\mu m}$ (8)	$S_{\text{CO}}\Delta V$ (9)	Ref (10)
PG1322+659	0.168	0.72 \pm 0.30	0.07	0.20 \pm 0.02	0.03	(5.3 \pm 2.20) $\times 10^{10}$	2.9 $\times 10^{10}$		
PG1341+258	0.087	0.45 \pm 0.21	0.06	0.11 \pm 0.02	0.02	(5.3 \pm 2.39) $\times 10^{09}$	4.7 $\times 10^{09}$		
PG1351+236	0.055	7.54 \pm 1.05	0.87	2.75 \pm 0.12	0.44	(6.7 \pm 2.71) $\times 10^{10}$	1.6 $\times 10^{09}$		
PG1351+640	0.088	3.12 \pm 6.54	0.09	1.29 \pm 0.15	0.03	(9.3 \pm 3.89) $\times 10^{10}$	2.2 $\times 10^{10}$	4.00	2
PG1352+183	0.152	<14.14		< 2.60		<2.4 $\times 10^{12}$	1.7 $\times 10^{10}$		
PG1354+213	0.300	< 0.27		< 0.06		<1.8 $\times 10^{11}$	4.2 $\times 10^{10}$		
PG1402+261	0.164	< 1.59		< 0.22		<1.6 $\times 10^{11}$	6.8 $\times 10^{10}$	< 2.00	1
PG1404+226	0.098	0.88 \pm 0.37	0.14	0.25 \pm 0.02	0.05	(1.7 \pm 0.71) $\times 10^{10}$	5.1 $\times 10^{09}$		2
PG1411+442	0.089			0.31 \pm 0.04	0.01	(1.8 \pm 0.74) $\times 10^{10}$		< 1.80	2
PG1415+451	0.113	1.67 \pm 0.30	0.14	0.86 \pm 0.06	0.10	(1.1 \pm 0.43) $\times 10^{11}$	1.3 $\times 10^{10}$	3.30	1
PG1416-129	0.129	< 0.56		< 0.15		<5.8 $\times 10^{10}$	8.5 $\times 10^{09}$		
PG1425+267	0.366	< 0.45		< 0.06		<3.1 $\times 10^{11}$	1.1 $\times 10^{11}$		
PG1426+015	0.086	1.19 \pm 0.64	0.03	0.31 \pm 0.06	0.01	(1.7 \pm 0.73) $\times 10^{10}$	2.4 $\times 10^{10}$	3.60	2
PG1427+480	0.221	< 0.28		< 0.03		<3.4 $\times 10^{10}$	2.5 $\times 10^{10}$		
PG1435-067	0.126	< 0.44		< 0.19		<4.3 $\times 10^{10}$	1.7 $\times 10^{10}$		
PG1440+356	0.079	6.74 \pm 2.89	0.20	2.27 \pm 0.13	0.10	(1.3 \pm 0.53) $\times 10^{11}$	2.0 $\times 10^{10}$	9.00	2
PG1444+407	0.267	0.38 \pm 0.28	0.03	< 0.15		(7.8 \pm 6.19) $\times 10^{10}$	8.5 $\times 10^{10}$	0.71	3
PG1448+273	0.065	1.98 \pm 0.59	0.11	0.94 \pm 0.06	0.07	(3.0 \pm 1.22) $\times 10^{10}$	5.7 $\times 10^{09}$		
PG1501+106	0.036	< 1.70		< 0.38		<7.9 $\times 10^{09}$	4.2 $\times 10^{09}$		
PG1512+370	0.370	< 0.22		< 0.07		<3.1 $\times 10^{11}$	8.8 $\times 10^{10}$		
PG1519+226	0.137	0.59 \pm 0.21	0.04	0.21 \pm 0.02	0.02	(3.3 \pm 1.37) $\times 10^{10}$	2.7 $\times 10^{10}$		
PG1534+580	0.029	1.45 \pm 0.72	0.05	0.44 \pm 0.08	0.02	(2.0 \pm 0.88) $\times 10^{09}$	1.5 $\times 10^{09}$		
PG1535+547	0.038	0.62 \pm 0.22	0.02	0.08 \pm 0.03	0.01	(5.6 \pm 2.87) $\times 10^{08}$	3.1 $\times 10^{09}$		
PG1543+489	0.399	< 0.34		< 0.26		<6.3 $\times 10^{11}$	2.4 $\times 10^{11}$		

Table 5.1 (cont'd)

source (1)	Redshift (2)	F(7.7 μ m) (3)	EW(7.7 μ m) (4)	F(11.3 μ m) (5)	EW(11.3 μ m) (6)	L_{SFIR} (7)	$L_{5-6\mu m}$ (8)	$S_{\text{CO}}\Delta V$ (9)	Ref (10)
PG1545+210	0.264	< 1.75		< 0.17		$< 4.1 \times 10^{11}$	5.8×10^{10}	< 0.96	3
PG1552+085	0.119	< 0.30		0.11 ± 0.02	0.02	$(1.1 \pm 0.46) \times 10^{10}$	1.0×10^{10}		
PG1612+261	0.130	< 0.46		0.38 ± 0.22	0.03	$(5.8 \pm 4.17) \times 10^{10}$	2.1×10^{10}		
PG1613+658	0.129	3.02 ± 1.87	0.08	0.77 ± 0.09	0.03	$(1.3 \pm 0.53) \times 10^{11}$	5.5×10^{10}	8.50	1
PG1617+175	0.112	< 0.45		< 0.48		$< 3.2 \times 10^{10}$	1.9×10^{10}		
PG1626+554	0.133	< 0.47		< 0.09		$< 3.2 \times 10^{10}$	1.3×10^{10}		
PG1634+706	1.334	< 0.52		< 0.11		$< 2.4 \times 10^{13}$	9.4×10^{09}		
PG1700+518	0.292	< 5.70		< 0.20		$< 6.5 \times 10^{11}$	3.2×10^{11}		
PG1704+608	0.371	< 1.04		< 0.11		$< 6.5 \times 10^{11}$	2.6×10^{11}		
PG2112+059	0.466	< 0.24		0.27 ± 0.05	0.02	$(1.2 \pm 0.52) \times 10^{12}$	4.8×10^{11}		
PG2130+099	0.062	4.20 ± 1.29	0.06	0.55 ± 0.21	0.01	$(1.5 \pm 0.83) \times 10^{10}$	2.1×10^{10}	4.30	2
PG2209+184	0.070	1.32 ± 0.37	0.20	0.29 ± 0.03	0.06	$(9.1 \pm 3.74) \times 10^{09}$	3.0×10^{09}		
PG2214+139	0.065	< 0.81		< 0.28		$< 1.7 \times 10^{10}$	1.6×10^{10}	1.60	2
PG2233+134	0.325	< 1.44		< 0.15		$< 6.6 \times 10^{11}$	9.4×10^{10}		
PG2251+113	0.325	< 0.55		< 0.26		$< 6.3 \times 10^{11}$	1.5×10^{11}		
PG2304+042	0.042	< 0.46		< 0.05		$< 5.6 \times 10^{09}$	8.8×10^{08}		
PG2308+098	0.433	< 0.27		< 0.06		$< 5.4 \times 10^{11}$	1.4×10^{11}		
PG2349-014	0.174	< 0.47		0.41 ± 0.10	0.05	$(1.3 \pm 0.61) \times 10^{11}$	4.6×10^{10}	3.20	3
2MASSJ000703.61+155423.8	0.114	3.00 ± 0.71	0.32	1.00 ± 0.10	0.14	$(1.3 \pm 0.52) \times 10^{11}$	9.7×10^{09}		
2MASSJ005055.70+293328.1	0.136	1.76 ± 0.34	0.19	0.33 ± 0.09	0.05	$(5.6 \pm 2.71) \times 10^{10}$	1.5×10^{10}		
2MASSJ010835.16+214818.6	0.285	< 1.25		< 0.21		$< 6.6 \times 10^{11}$	1.1×10^{11}		
2MASSJ015721.05+171248.4	0.213	2.02 ± 0.46	0.33	0.58 ± 0.12	0.16	$(3.5 \pm 1.56) \times 10^{11}$	3.0×10^{10}		
2MASSJ022150.60+132741.0	0.140	< 3.31		< 0.39		$< 2.1 \times 10^{11}$	2.5×10^{10}		
2MASSJ023430.64+243835.5	0.310	< 1.16		< 0.34		$< 1.3 \times 10^{12}$	6.4×10^{10}		

Table 5.1 (cont'd)

source (1)	Redshift (2)	F(7.7 μ m) (3)	EW(7.7 μ m) (4)	F(11.3 μ m) (5)	EW(11.3 μ m) (6)	L_{SFIR} (7)	$L_{5-6\mu\text{m}}$ (8)	$S_{\text{CO}}\Delta V$ (9)	Ref (10)
2MASSJ034857.64+125547.3	0.210	< 1.56		< 0.33		$< 5.2 \times 10^{11}$	2.3×10^{11}		
2MASSJ091848.63+211717.1	0.149	< 1.27		0.45 ± 0.25	0.04	$(1.0 \pm 0.69) \times 10^{11}$	3.2×10^{10}		
2MASSJ095504.56+170556.1	0.139	< 1.10		< 0.28		$< 1.4 \times 10^{11}$	9.5×10^9		
2MASSJ102724.95+121920.4	0.231	< 1.49		< 0.36		$< 7.1 \times 10^{11}$	7.0×10^{10}		
2MASSJ105144.25+353930.7	0.158	< 0.99		< 0.24		$< 1.7 \times 10^{11}$	1.0×10^{10}		
2MASSJ125807.46+232921.5	0.259	1.54 ± 0.78	0.09	< 0.16		$(3.9 \pm 2.29) \times 10^{11}$	9.4×10^{10}		
2MASSJ130005.35+163214.8	0.080	< 4.82		< 1.05		$< 1.7 \times 10^{11}$	2.2×10^{10}		
2MASSJ130700.66+233805.0	0.275	9.27 ± 1.58	0.57	< 0.27		$(3.9 \pm 1.33) \times 10^{12}$	2.2×10^{11}		
2MASSJ140251.22+263117.5	0.187	< 1.46		< 0.58		$< 4.4 \times 10^{11}$	2.6×10^{10}		
2MASSJ145331.51+135358.7	0.139	10.31 ± 2.81	0.51	1.10 ± 0.70	0.16	$(2.3 \pm 1.76) \times 10^{11}$	4.0×10^{10}		
2MASSJ150113.21+232908.3	0.258	< 1.31		0.19 ± 0.08	0.03	$(1.4 \pm 0.82) \times 10^{11}$	5.0×10^{10}		
2MASSJ151653.24+190048.4	0.190	< 2.22		< 0.57		$< 7.2 \times 10^{11}$	1.6×10^{11}		
2MASSJ163700.22+222114.0	0.211	2.81 ± 0.61	0.60	0.51 ± 0.04	0.15	$(2.7 \pm 1.10) \times 10^{11}$	2.0×10^{10}		
2MASSJ165939.77+183436.9	0.170	3.43 ± 1.21	0.17	0.65 ± 0.16	0.04	$(2.2 \pm 1.01) \times 10^{11}$	4.7×10^{10}		
2MASSJ171442.77+260248.5	0.163	1.19 ± 0.34	0.20	0.32 ± 0.07	0.08	$(8.0 \pm 3.60) \times 10^{10}$	1.7×10^{10}		
2MASSJ222202.22+195231.5	0.366	< 0.97		< 0.09		$< 5.0 \times 10^{11}$	2.7×10^{11}		
2MASSJ222221.12+195947.4	0.211	< 1.05		< 0.14		$< 1.8 \times 10^{11}$	4.3×10^{10}		
2MASSJ222554.27+195837.0	0.147	1.97 ± 0.33	0.22	< 0.21		$(1.2 \pm 0.40) \times 10^{11}$	1.6×10^{10}		
2MASSJ234449.57+122143.4	0.199	< 1.25		< 0.15		$< 1.8 \times 10^{11}$	3.5×10^{10}		
3C6.1	0.840			< 0.05		$< 2.5 \times 10^{12}$			
3C15	0.073	< 0.52		< 0.03		$< 2.4 \times 10^9$	1.0×10^9		
3C20	0.174	< 1.20		< 0.24		$< 2.1 \times 10^{11}$	4.2×10^9		
3C22	0.936			< 0.03		$< 1.5 \times 10^{12}$			
3C28	0.195	< 0.30		< 0.06		$< 5.3 \times 10^{10}$	8.6×10^8		

Table 5.1 (cont'd)

source (1)	Redshift (2)	F(7.7 μ m) (3)	EW(7.7 μ m) (4)	F(11.3 μ m) (5)	EW(11.3 μ m) (6)	L_{SFIR} (7)	$L_{5-6\mu\text{m}}$ (8)	$S_{\text{CO}}\Delta V$ (9)	Ref (10)
3C29	0.045	< 0.75		< 0.02		<6.6 $\times 10^8$	2.3 $\times 10^8$		
3C33	0.059	< 0.60		< 0.15		<9.1 $\times 10^9$	2.7 $\times 10^9$		
3C33.1	0.180	< 1.62		< 0.39		<4.0 $\times 10^{11}$	1.2 $\times 10^{10}$		
3C47	0.425	< 0.28		< 0.06		<4.1 $\times 10^{11}$	1.1 $\times 10^{11}$		
3C48	0.367	< 4.55		< 0.53		<4.0 $\times 10^{12}$	2.5 $\times 10^{11}$	2.00	4
3C55	0.734	< 0.18		< 0.07		<1.7 $\times 10^{12}$	8.9 $\times 10^{10}$		
3C61.1	0.187	< 0.23		< 0.05		<4.2 $\times 10^{10}$	8.3 $\times 10^8$		
3C65	1.176	< 0.42		< 0.08		<1.2 $\times 10^{13}$	8.1 $\times 10^9$		
3C75	0.023	< 0.33		< 0.01		<7.6 $\times 10^7$	2.6 $\times 10^7$		
3C76.1	0.032	< 0.43		< 0.05		<6.3 $\times 10^8$	9.4 $\times 10^7$		
3C79	0.255	< 1.02		< 0.17		<3.9 $\times 10^{11}$	3.0 $\times 10^{10}$		
3C83.1	0.025	< 0.36		0.16 ± 0.02	0.09	(4.4 ± 1.84) $\times 10^8$	4.6 $\times 10^8$		
3C84	0.017			4.11 ± 1.19	0.02	(7.1 ± 3.53) $\times 10^9$	1.6 $\times 10^9$		
3C109	0.305	< 1.75		< 0.26		<1.1 $\times 10^{12}$	2.2 $\times 10^{11}$		
3C123	0.217	< 0.61		< 0.05		<5.6 $\times 10^{10}$	1.3 $\times 10^9$		
3C129	0.020	< 0.36		0.07 ± 0.01	0.06	(1.3 ± 0.56) $\times 10^8$	1.2 $\times 10^8$		
3C138	0.759			< 0.03		<1.0 $\times 10^{12}$			
3C147	0.545			< 0.05		<6.6 $\times 10^{11}$			
3C153	0.276	< 0.40		< 0.04		<8.2 $\times 10^{10}$	4.7 $\times 10^8$		
3C172	0.519	< 0.17		< 0.05		<5.8 $\times 10^{11}$	5.5 $\times 10^9$		
3C173.1	0.292	< 0.31		< 0.03		<6.6 $\times 10^{10}$	1.6 $\times 10^9$		
3C175	0.770	< 0.17		< 0.03		<1.0 $\times 10^{12}$	2.8 $\times 10^{11}$		
3C184	0.994			< 0.06		<5.7 $\times 10^{12}$			
3C192	0.059	< 0.43		< 0.05		<2.8 $\times 10^9$	2.1 $\times 10^8$		

Table 5.1 (cont'd)

source (1)	Redshift (2)	F(7.7 μ m) (3)	EW(7.7 μ m) (4)	F(11.3 μ m) (5)	EW(11.3 μ m) (6)	L_{SFIR} (7)	$L_{5-6\mu\text{m}}$ (8)	$S_{\text{CO}}\Delta V$ (9)	Ref (10)
3C196	0.871	< 0.14		< 0.04		<2.1 $\times 10^{12}$	3.3 $\times 10^{11}$		
3C200	0.458			< 0.09		<9.4 $\times 10^{11}$			
3C216	0.670	< 0.28		< 0.12		<2.3 $\times 10^{12}$	2.5 $\times 10^{11}$		
3C219	0.174	< 0.30		< 0.10		<5.9 $\times 10^{10}$	6.0 $\times 10^9$		
3C220.1	0.610	< 0.29		< 0.10		<1.8 $\times 10^{12}$	1.7 $\times 10^{10}$		
3C220.3	0.680	< 1.05		< 0.03		<6.9 $\times 10^{11}$	1.6 $\times 10^{10}$		
3C234	0.184	< 0.90		< 0.24		<2.4 $\times 10^{11}$	1.2 $\times 10^{11}$		
3C244.1	0.428	< 0.21		< 0.04		<3.3 $\times 10^{11}$	2.5 $\times 10^{10}$		
3C249.1	0.311	< 1.04		0.29 \pm 0.10	0.04	(4.1 \pm 2.16) $\times 10^{11}$	1.0 $\times 10^{11}$		
3C263	0.646	< 0.14		< 0.07		<9.4 $\times 10^{11}$	3.6 $\times 10^{11}$		
3C263.1	0.824	< 0.10		< 0.16		<1.2 $\times 10^{12}$	1.6 $\times 10^{10}$		
3C265	0.811	0.62 \pm 0.23	0.24	< 0.30		(3.4 \pm 1.62) $\times 10^{12}$	2.6 $\times 10^{11}$		
3C268.1	0.970	< 0.15		< 0.08		<3.2 $\times 10^{12}$	2.2 $\times 10^{10}$		
3C270	0.007			0.60 \pm 0.04	0.09	(1.4 \pm 0.56) $\times 10^{08}$	5.4 $\times 10^{07}$		
3C272	0.944			< 0.02		<1.1 $\times 10^{12}$			
3C272.1	0.003			1.70 \pm 0.12	0.33	(2.0 \pm 0.04) $\times 10^{09}$	3.0 $\times 10^{07}$		
3C273	0.158	< 2.16		< 0.16		<1.0 $\times 10^{11}$	3.7 $\times 10^{11}$		
3C274	0.004			< 0.97		<2.3 $\times 10^{08}$	4.3 $\times 10^{07}$	< 11.7	5
3C274.1	0.422	< 0.19		< 0.08		<3.7 $\times 10^{11}$	3.0 $\times 10^{09}$		
3C275.1	0.555	< 0.15		0.09 \pm 0.02	0.09	(5.1 \pm 2.29) $\times 10^{11}$	5.2 $\times 10^{10}$		
3C280	0.996	< 0.09		< 0.09		<1.9 $\times 10^{12}$	2.3 $\times 10^{11}$		
3C292	0.710			< 0.09		<3.4 $\times 10^{12}$			
3C293	0.045	3.96 \pm 0.70	0.62	1.27 \pm 0.10	0.41	(1.7 \pm 0.71) $\times 10^{10}$	9.2 $\times 10^{08}$		
3C295	0.464	< 0.13		< 0.24		<3.1 $\times 10^{11}$	3.5 $\times 10^{09}$		

Table 5.1 (cont'd)

source (1)	Redshift (2)	F(7.7 μ m) (3)	EW(7.7 μ m) (4)	F(11.3 μ m) (5)	EW(11.3 μ m) (6)	L_{SFIR} (7)	$L_{5-6\mu\text{m}}$ (8)	$S_{\text{CO}}\Delta V$ (9)	Ref (10)
3C298	1.436	< 0.30		< 0.07		<1.7 $\times 10^{13}$	1.2 $\times 10^{12}$		
3C300	0.270	< 0.34		< 0.06		<1.2 $\times 10^{11}$	1.5 $\times 10^{09}$		
3C303.1	0.267	< 0.38		0.09 \pm 0.02	0.18	(6.9 \pm 3.21) $\times 10^{10}$	5.3 $\times 10^{09}$		
3C309.1	0.905	< 0.11		< 0.03		<1.9 $\times 10^{12}$	3.3 $\times 10^{11}$		
3C310	0.053	< 0.30		< 0.03		<1.3 $\times 10^{09}$	1.5 $\times 10^{08}$		
3C315	0.108	< 0.44		0.17 \pm 0.02	0.50	(1.4 \pm 0.61) $\times 10^{10}$	5.4 $\times 10^{08}$		
3C318	1.574	< 0.51		< 0.07		<2.3 $\times 10^{13}$	2.8 $\times 10^{11}$		
3C319	0.192	< 0.23		< 0.08		<5.6 $\times 10^{10}$			
3C321	0.096	6.51 \pm 1.04	0.49	< 0.28		(1.7 \pm 0.57) $\times 10^{11}$	6.1 $\times 10^{09}$	< 4.70	5
3C323.1	0.264	< 1.75		< 0.17		<4.1 $\times 10^{11}$	5.8 $\times 10^{10}$		
3C325	1.135	< 0.10		< 0.04		<3.3 $\times 10^{12}$	9.3 $\times 10^{10}$		
3C326	0.089	< 0.62		< 0.11		<1.7 $\times 10^{10}$	3.2 $\times 10^{08}$		
3C330	0.550	0.25 \pm 0.07	0.29	< 0.02		(3.8 \pm 1.54) $\times 10^{11}$	2.8 $\times 10^{10}$		
3C334	0.555	0.58 \pm 0.21	0.17	< 0.03		(1.1 \pm 0.50) $\times 10^{12}$	1.5 $\times 10^{11}$		
3C336	0.927			< 0.08		<6.6 $\times 10^{12}$			
3C337	0.635			< 0.05		<1.2 $\times 10^{12}$			
3C340	0.775			< 0.03		<1.1 $\times 10^{12}$			
3C343	0.988			< 0.04		<3.2 $\times 10^{12}$			
3C343.1	0.750			< 0.02		<7.2 $\times 10^{11}$			
3C348	0.154	< 0.81		< 0.19		<1.1 $\times 10^{11}$	8.3 $\times 10^{08}$		
3C351	0.371	< 1.04		< 0.11		<6.5 $\times 10^{11}$	2.6 $\times 10^{11}$		
3C352	0.806			< 0.05		<2.3 $\times 10^{12}$			
3C356	1.079	< 0.17		< 0.06		<5.2 $\times 10^{12}$	8.0 $\times 10^{10}$		
3C371	0.051	< 2.12		< 0.13		<5.1 $\times 10^{09}$	8.6 $\times 10^{09}$		

Table 5.1 (cont'd)

source	Redshift	F(7.7 μ m)	EW(7.7 μ m)	F(11.3 μ m)	EW(11.3 μ m)	L_{SFIR}	$L_{5-6\mu\text{m}}$	$S_{\text{CO}}\Delta V$	Ref
(1)	(2)	(3)	(4)	(5)	(6)	(7)	(8)	(9)	(10)
3C380	0.692	< 0.17		< 0.09		<1.3 $\times 10^{12}$	3.5 $\times 10^{11}$		
3C381	0.160	< 0.48		< 0.05		<3.0 $\times 10^{10}$	1.5 $\times 10^{10}$		
3C382	0.057	< 0.97		< 0.12		<6.3 $\times 10^{09}$	1.7 $\times 10^{10}$		
3C386	0.016			< 0.04		<1.4 $\times 10^{08}$	9.0 $\times 10^{07}$		
3C388	0.091	< 0.36		< 0.06		<8.8 $\times 10^{09}$	5.9 $\times 10^{08}$		
3C390.3	0.056	< 0.63		< 0.16		<7.9 $\times 10^{09}$	8.3 $\times 10^{09}$	< 10.3	5
3C401	0.201	< 0.27		< 0.03		<2.9 $\times 10^{10}$	1.1 $\times 10^{09}$		
3C403.1	0.055	< 0.25		< 0.02		<7.1 $\times 10^{08}$	1.7 $\times 10^{08}$		
3C405	0.056	< 3.28		< 0.55		<3.3 $\times 10^{10}$	3.5 $\times 10^{09}$	< 1.90	5
3C427.1	0.572	< 0.22		< 0.03		<5.6 $\times 10^{11}$	3.4 $\times 10^{09}$		
3C433	0.101	< 0.83		< 0.22		<4.9 $\times 10^{10}$	2.0 $\times 10^{10}$		
3C436	0.214	< 0.40		< 0.05		<5.4 $\times 10^{10}$	1.1 $\times 10^{09}$		
3C438	0.290	< 0.35		< 0.04		<9.3 $\times 10^{10}$	1.5 $\times 10^{09}$		
3C441	0.708			< 0.06		<1.9 $\times 10^{12}$			
3C445	0.056	< 1.48		< 0.30		<1.7 $\times 10^{10}$	1.7 $\times 10^{10}$		
3C452	0.081	< 0.50		< 0.07		<7.9 $\times 10^{09}$	2.7 $\times 10^{09}$		
3C465	0.030	< 0.86		< 0.21		<2.6 $\times 10^{09}$	3.5 $\times 10^{08}$		

Note. — Column (1): Sources. Column (2): Redshift. Column (3): The observed-frame 7.7 μ m aromatic flux in the unit of 10^{-13} erg s $^{-1}$ cm $^{-2}$. Column (4): The rest-frame EW of 7.7 μ m PAH in the unit of μ m. Column (5): The observed-frame 11.3 μ m aromatic flux in the unit of 10^{-13} erg s $^{-1}$ cm $^{-2}$. Column (6): The rest-frame EW of 11.3 μ m PAH in the unit of μ m. Column (7): The star-forming IR luminosity in the unit of L_{\odot} . Column (8): The mid-IR luminosity in the unit of L_{\odot} integrated from 5 to 6 μ m. A factor of 22.6 can be applied to convert it to the total IR luminosity (3-1000 μ m) based on the quasar template of Elvis et al. (1994). Column (9): The CO flux in the unit of Jy km s $^{-1}$. Column (10): Reference for column (9).

REFERENCES: (1)Evans et al. (2001); (2)Scoville et al. (2003); (3)Casoli & Loinard (2001); (4)Scoville et al. (1993); (5)Evans et al. (2005)

samples are selected.

5.2.2 Data Reduction

The spectra were obtained with the IRS using the standard staring mode. The intermediate products of the *Spitzer* Science Center (SSC) pipeline S13.0.1, S13.2.0 and S15.3.0 were processed within the SMART software package (Higdon et al., 2004). For a detailed description of the data reduction, see Shi et al. (2006b), Hines et al. (2006) and Bouwman et al. (2006).

The slit widths of the short-low (SL) and long-low (LL) modules are $3''.6$ and $10''.5$, respectively. In order to measure the star formation from the entire galaxy, we need to evaluate the extended IR emission outside of the IRS SL slit. The SL slit width is several hundreds of parsecs for 3C 272.1 and 3C 274, 2-10 kpc for sixty-one objects ($z < 0.17$) and > 10 kpc for the remaining objects. For 3C 272.1, the MIPS image shows extended IR emission from the host galaxy and that this emission is thermal based on the extrapolation from radio data. The extended IR emission of 3C 274 is dominated by non-thermal emission (Shi et al., 2007a) and is not related to star formation. For objects with physical slit widths between ~ 2 kpc and 10 kpc, a total of seventeen objects show excess IR fluxes in the LL modules compared to the SL modules. However, the flux difference between the SL and LL modules can be caused by different slit-loss due to pointing errors, not necessarily by extended IR emission outside the SL module slit. For 14 out of these 17 objects, we obtained archived MIPS $24\ \mu\text{m}$ images and measured the FWHMs of the radial brightness profiles. All of them show FWHMs smaller than 3 pixels (the PSF has a FWHM of 2.4 pixels), implying that the excess IR fluxes in the LL modules are not due to extended IR emission from the host galaxies. For the remaining three objects without MIPS $24\ \mu\text{m}$ images, we use 2MASS K-band images and find that the excess flux of LL relative to SL for one object (PG 2304+042) may be due to extended IR emission. For objects with slit widths larger than 10 kpc, we simply assume that the IRS slit contains all the IR emission from the galaxy and that the mismatch between the SL and LL spectra is due to variable slit-loss. Therefore,

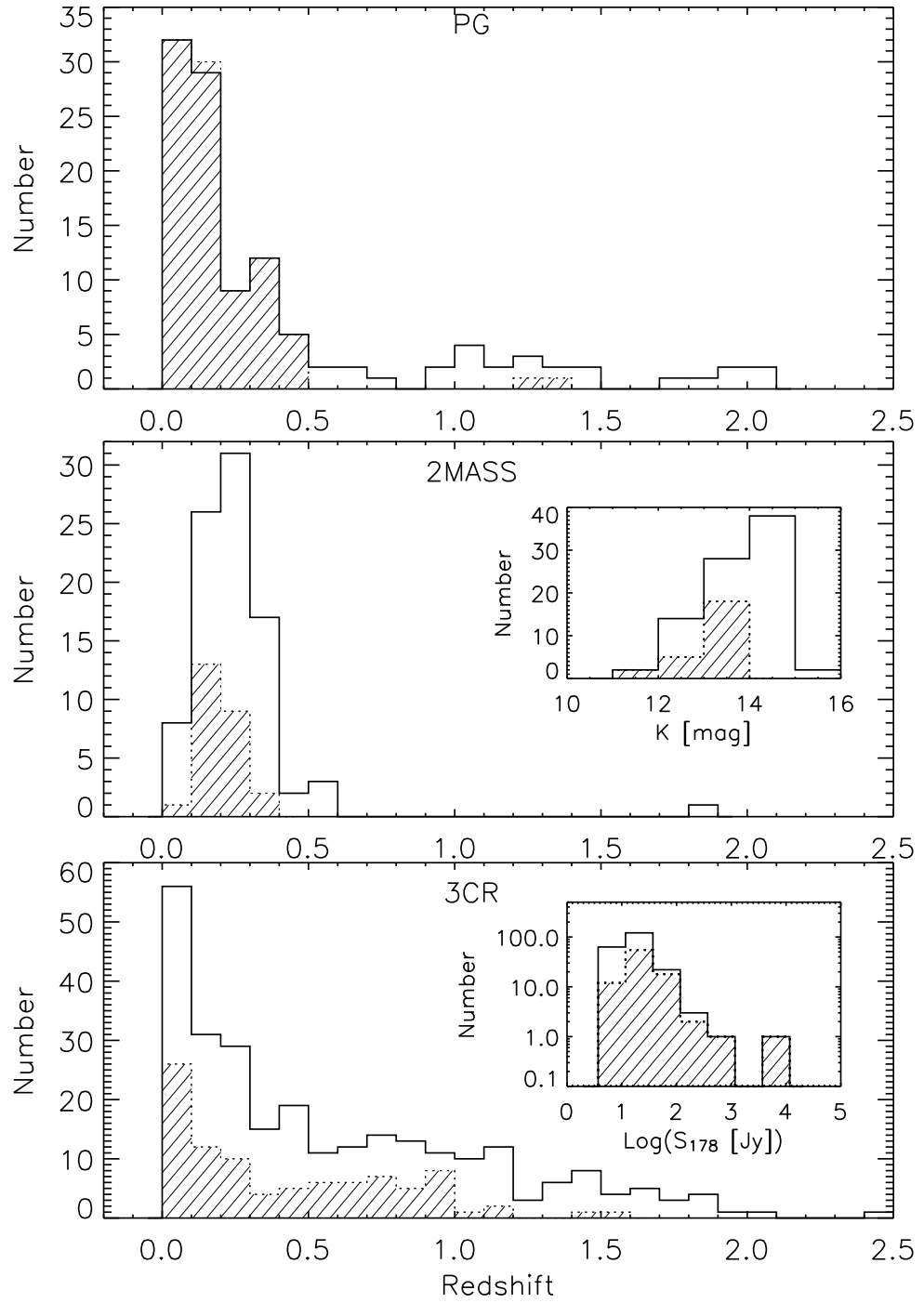


Figure 5.1 The redshift distribution of the three subsamples in this study (shaded area) compared to the corresponding parent samples for the PG, 2MASS and 3CR objects. The insert plots show the flux distribution of the subsample (shaded area) and the corresponding parent sample for the 3CR and 2MASS objects.

except for 3C 272.1, 3C274 and PG 2304+042, we rescale the SL spectra so that the SL and LL spectra have the same flux density at $14.2 \mu\text{m}$.

5.2.3 The Extraction of Aromatic Features

The $7.7 \mu\text{m}$ feature resides at the blue end of the silicate feature. The level of contamination by the silicate feature on the aromatic flux measurement depends on several factors, including the strength of the silicate feature, the shape of its blue wing and the shortest wavelength that the blue wing extends to. As shown in Hao et al. (2005) or our Figure 5.3, all these factors vary in different sources, resulting in deviations from the line profile for a normal galaxy interstellar medium. To account for these variations, we fit the blue wing of the silicate feature with a Doppler profile:

$$f_{\lambda} = \frac{f_{\lambda_0}}{(\lambda - \lambda_0)^2 + (\alpha_L)^2} \exp(-((\lambda - \lambda_0)/\alpha_D)^2) \quad (5.1)$$

where λ_0 can be interpreted as the central wavelength of the silicate feature, and the combination of α_D and α_L control the shape of the blue wing and the starting wavelength where the silicate feature arises. The profile has no physical meaning and is adopted only for practical purposes. As shown in Figure 5.2, it can fit the $7.7 \mu\text{m}$ feature well.

The procedure to extract the $7.7 \mu\text{m}$ aromatic feature is as follows. The spectra are first rebinned to a resolution of $0.1 \mu\text{m}$ to remove multiple points at the same wavelength, using the SMART software. The continua underlying the $7.7 \mu\text{m}$ aromatic features and silicate features are defined as power laws over three spectral windows, $5.2\text{-}5.5 \mu\text{m}$, $5.5\text{-}5.8 \mu\text{m}$ and $6.7\text{-}7.0 \mu\text{m}$. These spectral regions are selected to avoid the possible ice feature at $6.0 \mu\text{m}$ and aromatic features at $6.2 \mu\text{m}$. We then fit the continua-subtracted spectra simultaneously with two aromatic features at 7.7 and $8.6 \mu\text{m}$ and the silicate feature. The shapes of the aromatic features are assumed to be Drude profiles. Due to the low EW of aromatic features in AGNs, the FWHMs of the 7.7 and $8.6 \mu\text{m}$ features are fixed at 0.6 and $0.3 \mu\text{m}$, respectively. The height of the $8.6 \mu\text{m}$ feature is also fixed to be one-third of that of the $7.7 \mu\text{m}$ feature. This relative height is similar to those of two average spectra of HII-like

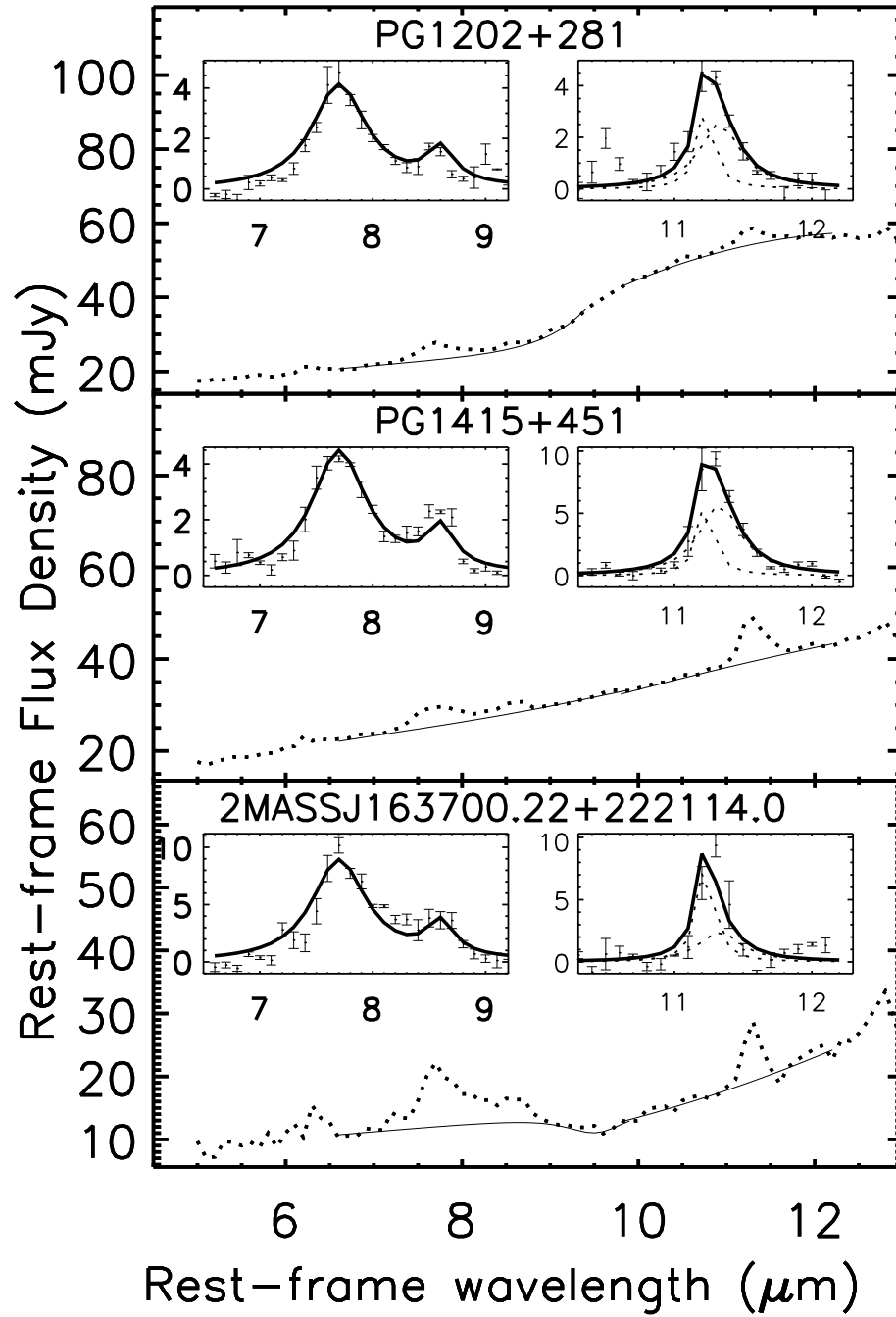


Figure 5.2 Examples of the extraction of the 7.7 and 11.3 μm aromatic features in the spectra with silicate emission, no silicate feature and silicate absorption, respectively. The dotted lines are the IRS spectra while the solid lines are the continua. The subplots show the Drude profiles of the two features where the 11.3 μm feature is fitted with two Drude profiles (dotted lines).

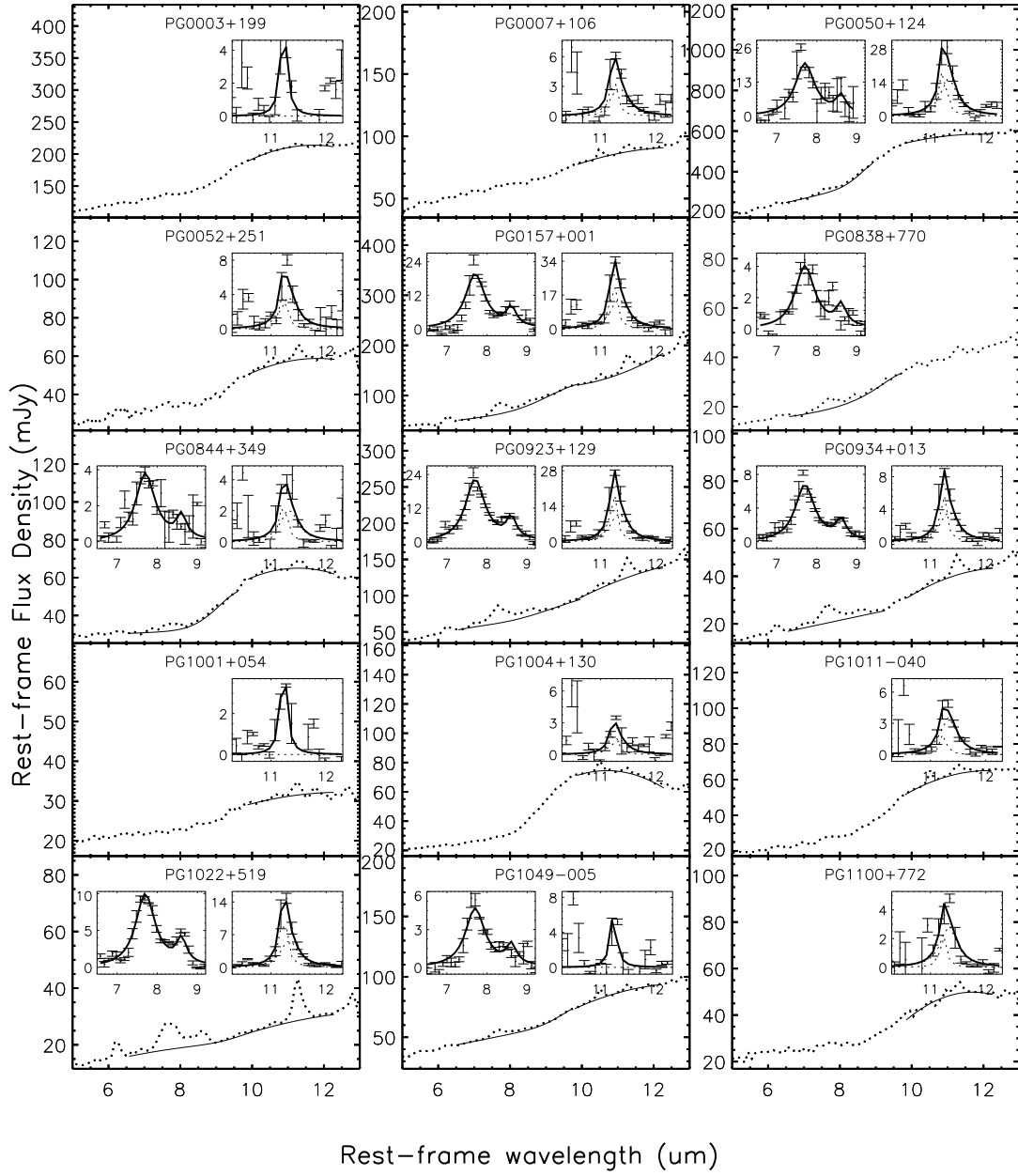


Figure 5.3 IRS spectra of AGN with detected aromatic features. The solid line is the derived continuum for the 7.7 μm and/or 11.3 μm aromatic features. The subplots show the Drude profiles of the two features.

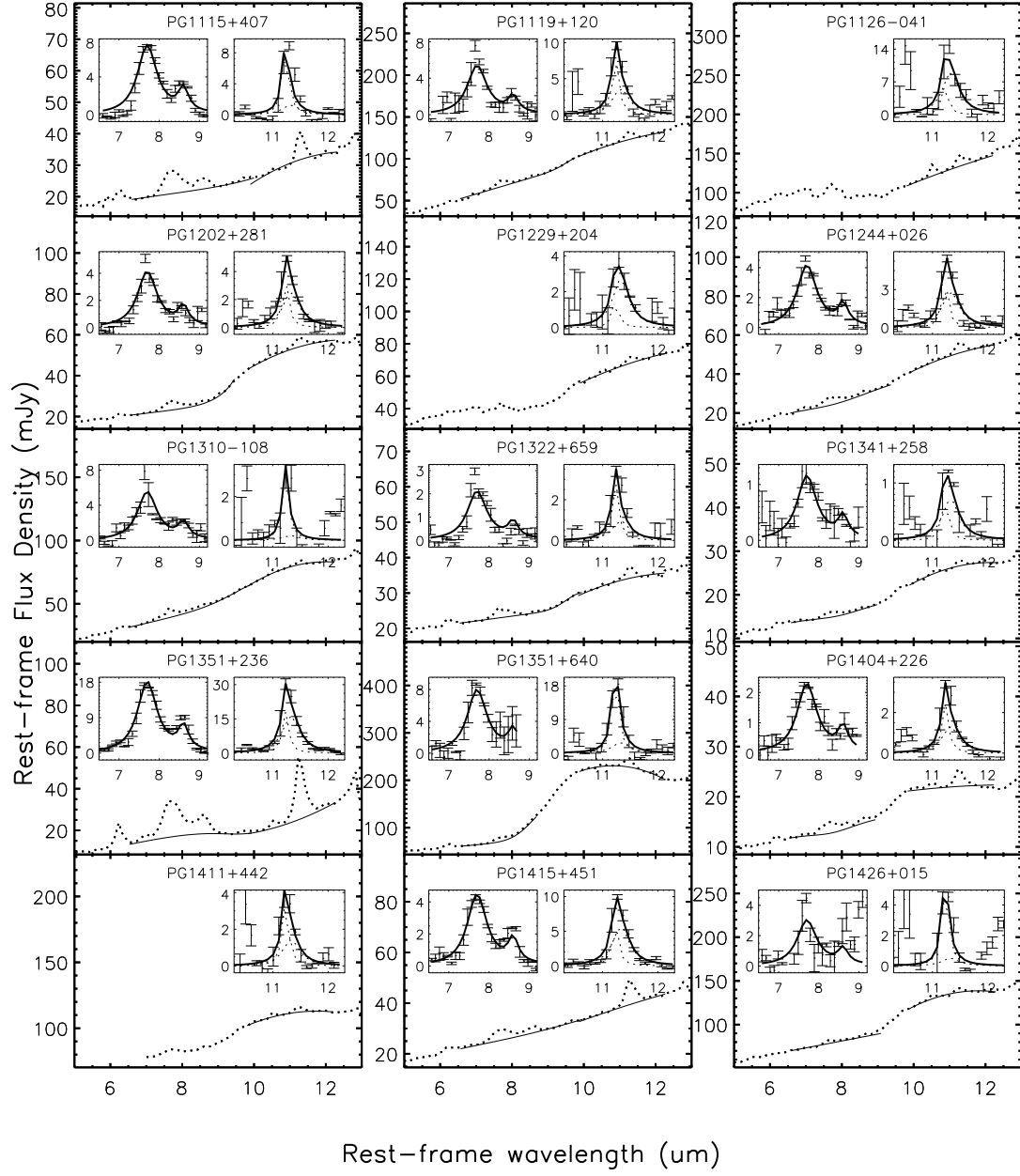


Figure 5.3 Continued.

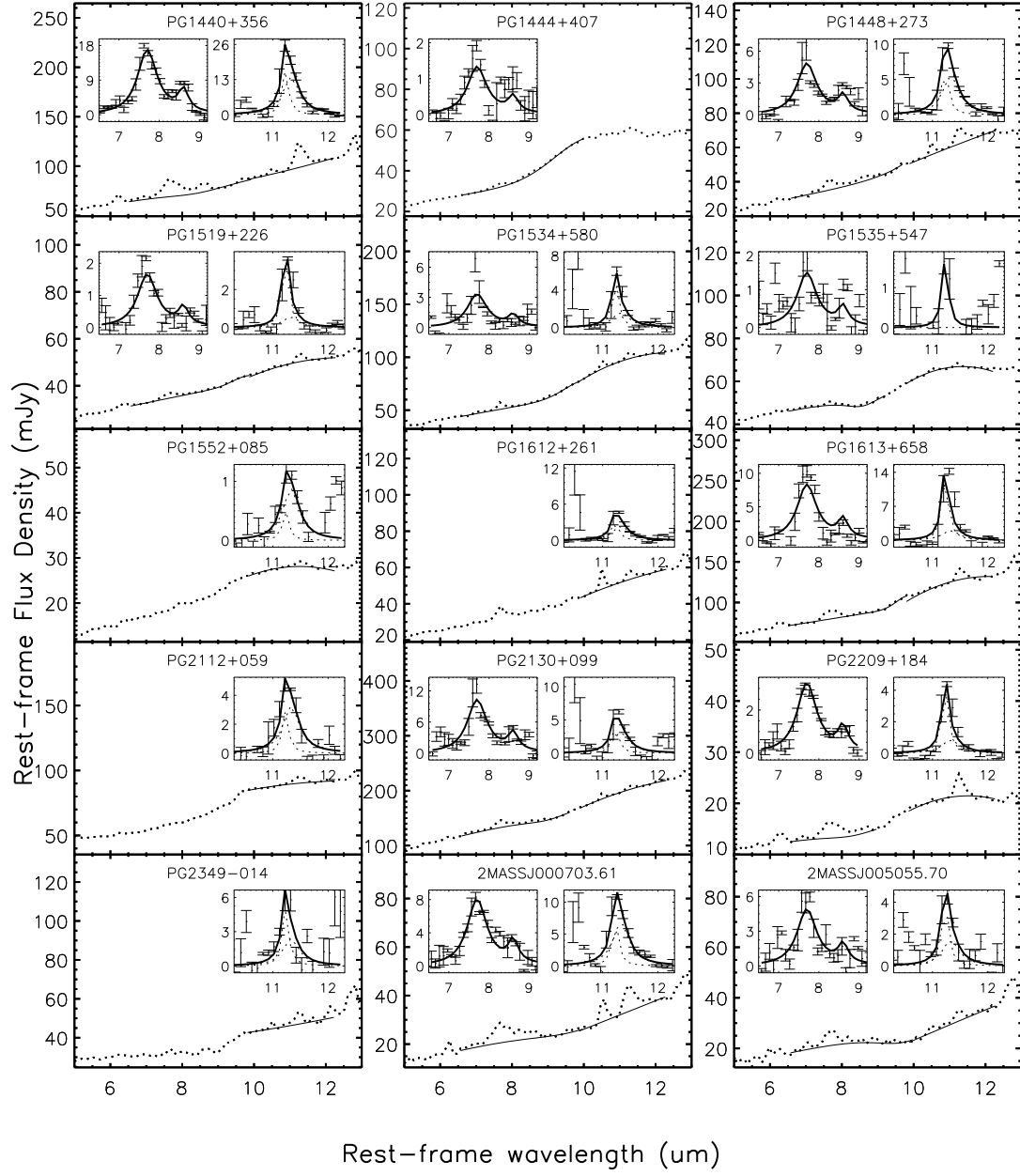


Figure 5.3 Continued.

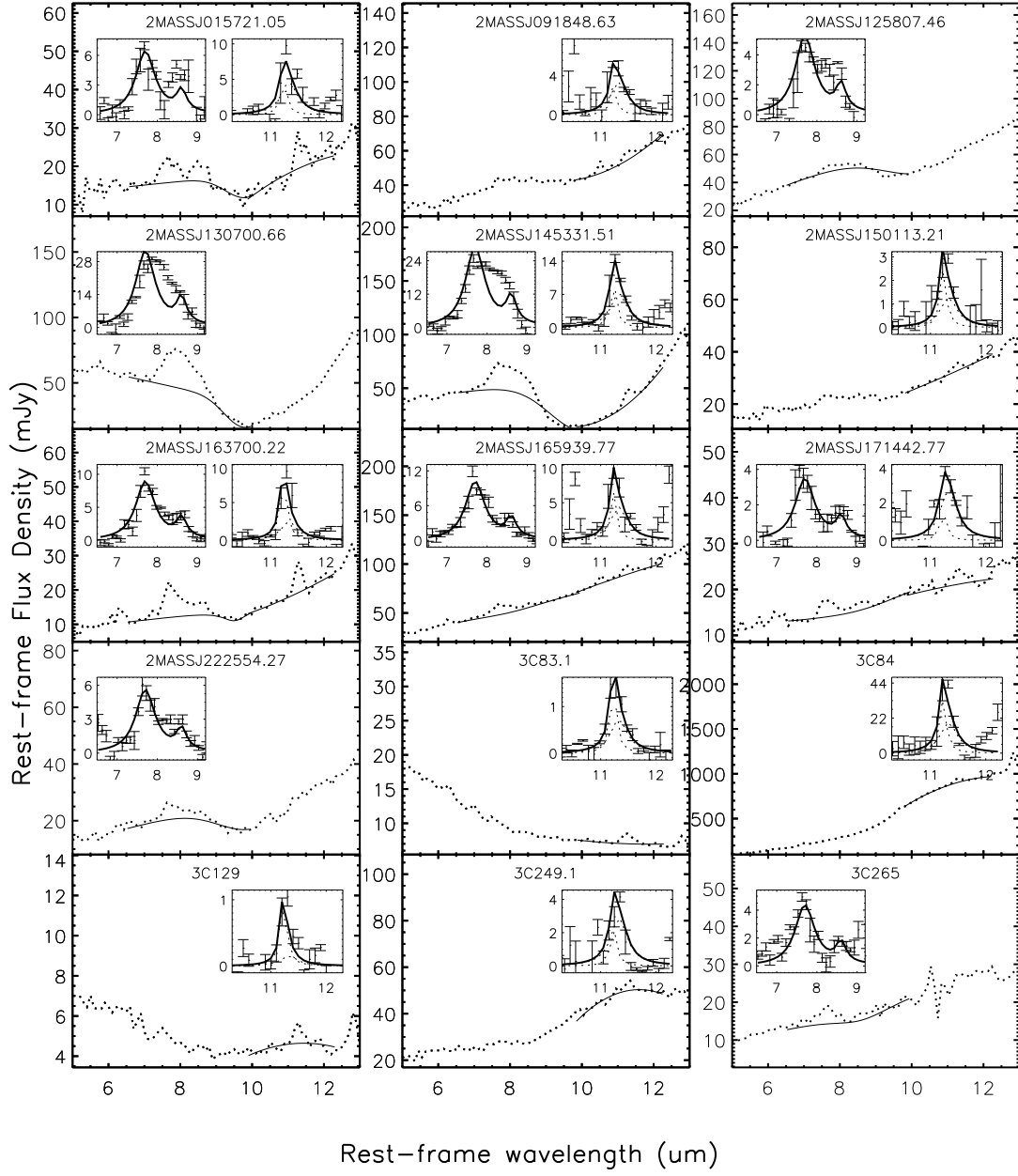


Figure 5.3 Continued.

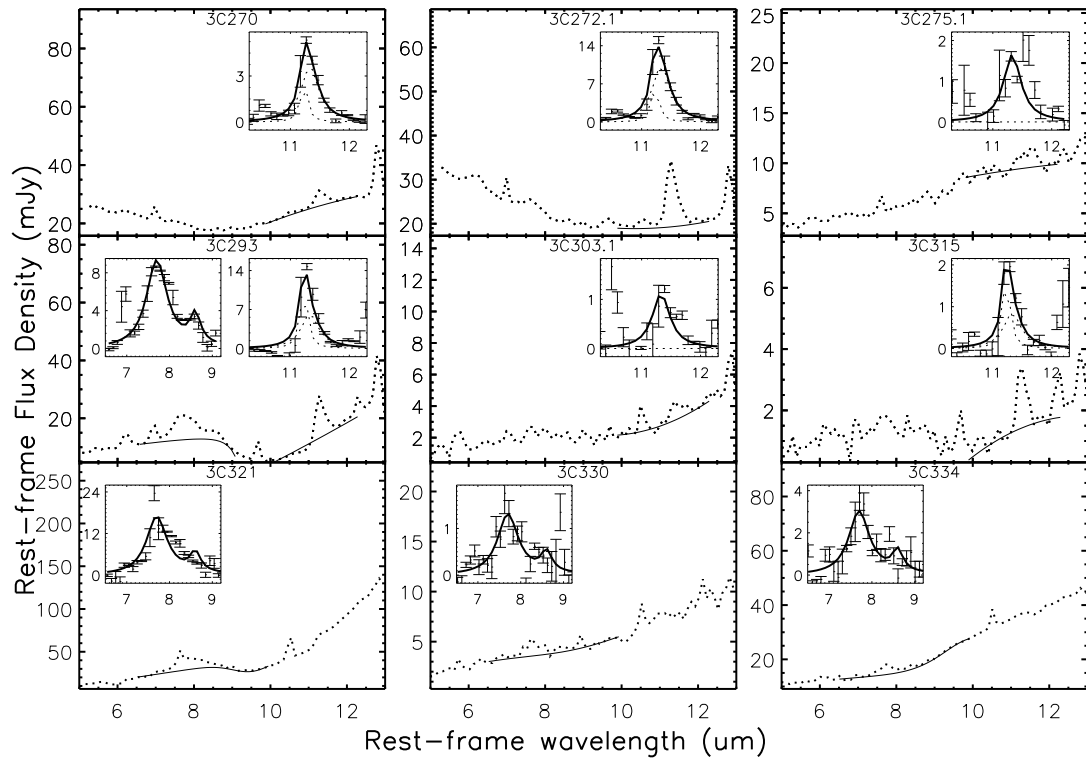


Figure 5.3 Continued.

nearby galaxies obtained by Smith et al. (2007). For the silicate feature, we fit only the blue wing with a Doppler profile. The starting wavelength of the spectral range for the fit is fixed at $6.5\mu\text{m}$. We vary the red end from 9 to $12\mu\text{m}$ to have the best fit judged by visual inspection. For most of the sources, the measured aromatic flux depends little on the selected red end wavelength. The feature is considered detected if the height of the $7.7\mu\text{m}$ feature is five times greater than the mean noise in the continuum.

For the $11.3\mu\text{m}$ feature, the silicate feature behaves like a continuum and the slope of the underlying silicate profile varies smoothly across the aromatic feature. Therefore, we are able to determine the silicate profile simply with a quadratic interpolation. The $11.3\mu\text{m}$ feature is fitted with two Drude profiles centered at 11.23 and $11.33\mu\text{m}$ with fixed FWHMs of 0.135 and $0.363\mu\text{m}$, respectively. The combination of these two Drude profiles fits well the $11.3\mu\text{m}$ features of nearby galaxies, as demonstrated with high S/N IRS spectra by Smith et al. (2007). After the spectrum is rebinned to a resolution of $0.1\mu\text{m}$, the continuum (plus silicate feature) shape is defined by using a quadratic interpolation over the four continuum spectral regions, $9.7\text{--}10.0$, $10.0\text{--}10.3\mu\text{m}$, $10.7\text{--}11.0\mu\text{m}$ and $11.7\text{--}12.1\mu\text{m}$. We then fix the continuum shape, the FWHM and the center wavelength of the two Drude profiles, but adjust the normalization of the continuum and the strength of Drude profiles to fit the spectra in the range including the continuum and the feature ($9.7\text{--}10.3\mu\text{m}$ and $10.7\text{--}12.1\mu\text{m}$). The feature is considered detected if the height of the combination of the two Drude profiles is five times greater than the mean noise in the continuum. If the feature is not detected, the upper limit is calculated by assuming the same relative strength of the two Drude profiles as given by the fit and taking five times the mean noise for the total height of the two profiles. We visually inspected each detected feature and found that the $11.3\mu\text{m}$ features of eleven objects may not be real due to larger noise around the feature relative to the mean noise in the continuum. For fifteen objects, the continuum was also fitted with an alternative quadratic interpolation, due to a large change in the slope of the silicate profile around the $11.3\mu\text{m}$ feature. However, the difference in the

feature strength is smaller than a factor of 1.5, showing that the continuum fitting procedure does not affect our results strongly.

To test the robustness of our procedures against strong continua, power-law continua with different strengths are added to the star-forming templates from Dale et al. (2001) and Dale & Helou (2002). The 7.7 and 11.3 μm aromatic features are extracted using the above procedures and the flux variations are smaller than 1% for the EW range from the original value ($\sim 1\mu\text{m}$) to 0.01 μm .

5.2.4 Uncertainty of the Aromatic Flux

We have evaluated each step in extracting the features to estimate the final uncertainty of the aromatic flux. To estimate the uncertainty due to the rebinned spectral resolution, the fluxes are re-measured with rebinned resolutions from 0.08 to 0.12 μm for features observed with SL module (resolution of $\sim 0.1\mu\text{m}$). For the objects at $z > 0.24$, where the 11.3 μm feature is observed with LL module (resolution of $\sim 0.28\mu\text{m}$), we compare the measured flux for rebinned resolutions ranging from 0.1 to 0.3 μm . Comparing these measurements to the feature flux obtained at a rebinned resolution of 0.1 μm , we find that the differences are always below 10%.

To estimate the uncertainty caused by the photon noise and the fit of the continuum and silicate feature, we produce a noiseless spectrum for each detected aromatic feature. The simulated noiseless spectrum for the 7.7 μm feature is the measured power-law continuum plus the measured Doppler profile of the silicate feature plus two Drude profiles of the measured 7.7 and 8.6 μm features. The spectrum for 11.3 μm is the quadratically interpolated continuum and silicate profile plus two measured Drude profiles. We then perturb this noiseless spectrum 100 times to produce noisy spectra with mean S/N equal to the observed S/N. The aromatic features are then extracted from these simulated spectra in the same way and the 1- σ uncertainty is obtained as the difference between the original flux and those from the simulated spectra. The uncertainty in this step is typically <15% for the 11.3 μm feature and <30% for the 7.7 μm feature.

Due to the contamination by the silicate feature, we are unable to fit the 7.7 μm

feature with multiple Drude profiles. To compute the uncertainty in the assumed profile with a fixed FWHM for the $7.7\ \mu\text{m}$ feature, we have used the code (PAH-FIT.pro) written by Smith et al. (2007) to measure accurate fluxes for the $7.7\ \mu\text{m}$ aromatic complexes of the four composite spectra of nearby galaxies in Smith et al. (2007). We then re-construct the $7.7\ \mu\text{m}$ profile with the fitted parameters and measure the flux with a single Drude profile with a FWHM of $0.6\ \mu\text{m}$. The difference in fitted feature strengths is around 10%, which is adopted as the uncertainty due to the $7.7\ \mu\text{m}$ aromatic profile. No uncertainty is applied for the assumed profile of the $11.3\ \mu\text{m}$ feature. The above uncertainties are added quadratically to give the final error of the measured aromatic flux. Table 5.1 lists the measured fluxes, uncertainties and EWs for both aromatic features.

5.3 EXCITATION MECHANISM OF AROMATIC FEATURES IN AGNS

As shown in § 1, the low EW of the aromatic features and the spatial extension of the aromatic emission in active galaxies suggest that these features are most likely predominantly excited by star formation. With the significant number of detections of aromatic features in this study, we can test this hypothesis.

5.3.1 The Profile of Aromatic Features in AGN

5.3.1.1 The Composite Spectra

To study the profile of the aromatic features in AGN, we have produced the composite spectra for several groups of objects. The composite spectrum is computed following the procedure described in Vanden Berk et al. (2001). All the observed spectra are shifted to the rest-frame and then rebinned to a common spectral resolution ($0.1\ \mu\text{m}$) within SMART. After they are ordered by redshift, the first spectrum is rescaled randomly. The following individual spectrum is rescaled to have the same mean flux density in a common spectral region of the mean spectra of all lower redshift spectra. The common spectral region is defined to be $5.0\text{-}6.0\ \mu\text{m}$ where there is little influence from the silicate or aromatic features. The final composite

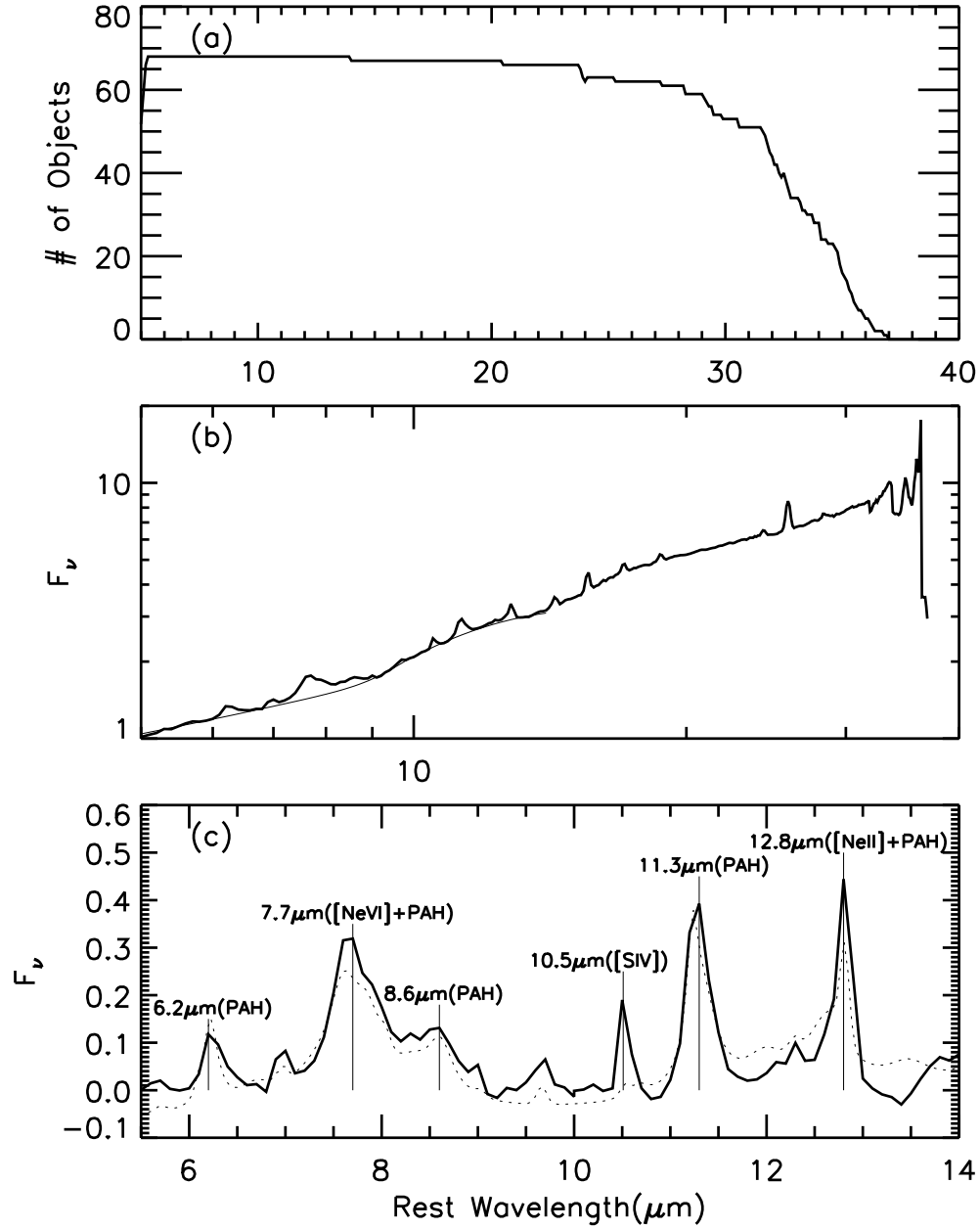


Figure 5.4 (a) The number of objects in each wavelength bin of the composite spectrum. (b) The arithmetic mean spectrum (the heavy solid line) of AGN with one of the 7.7 and $11.3 \mu\text{m}$ aromatic features detected and the fitted continuum (the light solid line). (c) The continuum-subtracted spectrum (the heavy solid line) superposed with the composite spectrum (the dotted line) of the HII-like galaxies from Smith et al. (2007).

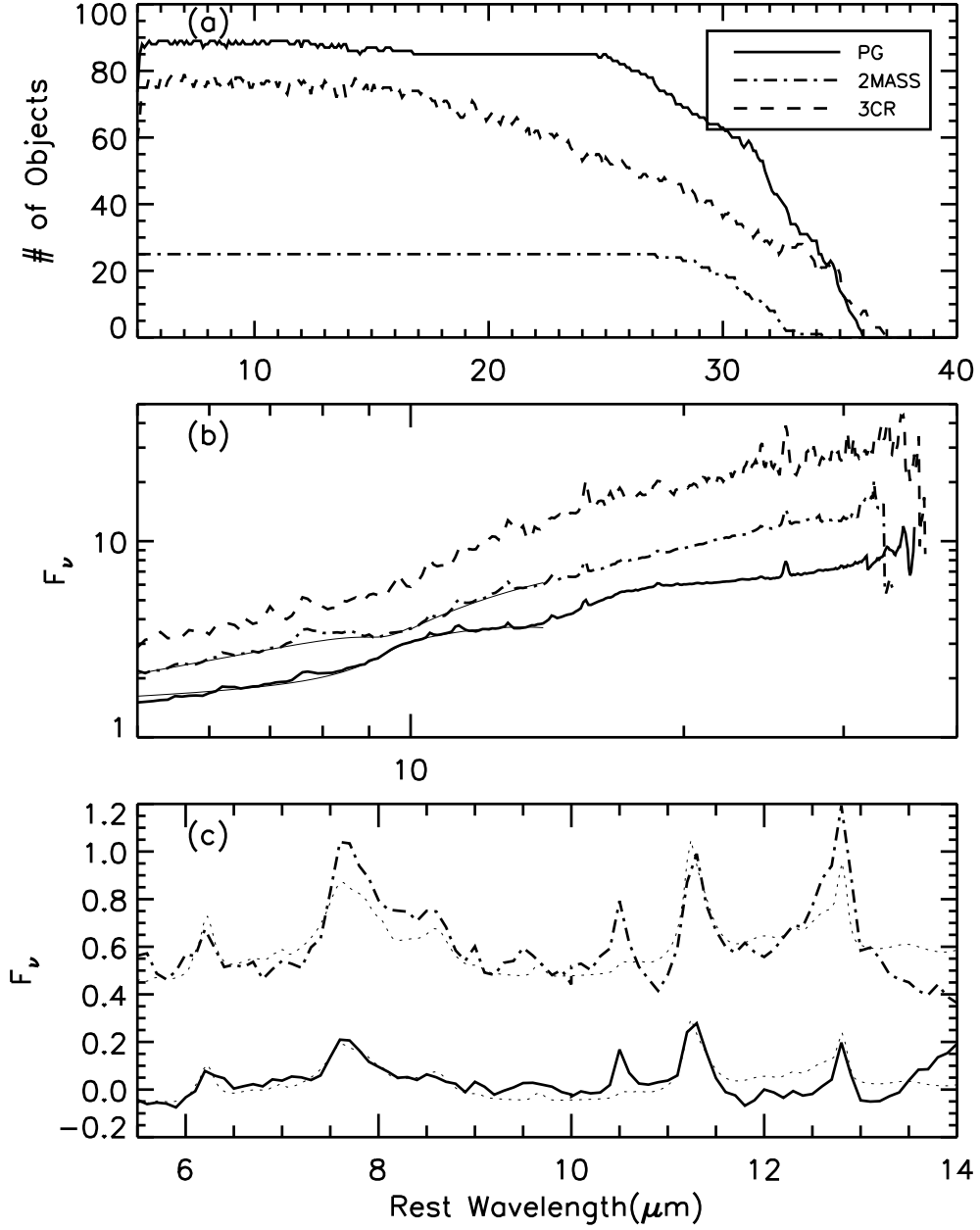


Figure 5.5 (a) The number of objects in each wavelength bin of the composite spectra of PG, 2MASS and 3CR AGN, respectively. (b) The arithmetic mean spectra and the fitted continua (the light solid lines). (c) The continuum-subtracted spectra of PG and 2MASS AGN, superposed with the composite spectra (the dotted lines) of the HII-like galaxies from Smith et al. (2007).

spectrum is the arithmetic mean of all rescaled spectra. Unlike in Vanden Berk et al. (2001), we have not produced the median spectrum since the average one shows much higher S/N. As implied by the compositing procedure, the aromatic features of individual observed spectra with higher EW have larger weight in the feature of the final composite spectrum.

The first arithmetic mean spectrum is the one of AGN with at least one of the 7.7 and 11.3 μm features detected. Fig. 5.4(a) plots the number of objects used in each wavelength bin. As shown in Fig. 5.4(b), the overall spectrum shows a power-law-like continuum with weak silicate features. We determined the continuum between 5.0 and 10.0 μm using the procedure for extracting the 7.7 μm feature but do not constrain the strength of the 8.6 μm aromatic feature. The continuum between 9.5 and 14.0 μm is defined to be a quadratic interpolation over the mean flux densities of four spectral regions (10.0-10.3, 10.8-11.0, 13.0-13.2, and 13.4-13.6 μm). As shown in Fig. 5.4(c), broad features are present at 6.2 μm , 7.7 μm , 8.6 μm , 11.3 μm and 12.8 μm , similar to those in star forming galaxies (See Lu et al., 2003; Smith et al., 2007). The dotted curve in Fig. 5.4(c) shows the mean spectrum of two composite spectra of HII-like galaxies from Smith et al. (2007) where the spectrum is shifted and rescaled to match the 11.3 μm feature of the AGN spectrum. There is only a small discrepancy in the shapes and relative strengths of the aromatic features between AGN and HII-like galaxies. A small amount of excess emission at 7.7 and 12.8 μm in the AGN spectrum is most likely due to [NeV]7.65 μm and [NeII]12.8 μm , respectively, as the excess emission shows a narrow FWHM. The result indicates the observed aromatic features in AGN resemble those in star-forming galaxies. The composite spectrum of AGN without either feature detected still does not show detectable aromatic features.

Fig. 5.5 shows the arithmetic mean spectra for PG, 2MASS and 3CR objects, respectively. The silicate emission features are present in the PG spectrum while the 2MASS and 3CR spectra have silicate absorptions. Aromatic features are visible in the PG and 2MASS composite spectra, but not in the 3CR spectrum. As shown in Fig. 5.5(c), the comparison to the HII-like galaxies indicates the 11.3/7.7 μm feature

ratio (~ 0.30) of the PG spectrum is a little higher while the 2MASS spectrum presents a lower ratio (~ 0.22). However, they are within the one- σ range for star-forming galaxies as shown below.

5.3.1.2 The Distribution of the Aromatic Feature Ratio

The above comparisons reveal that the shapes and relative strengths of the aromatic features of the AGN composite spectra are similar to those of HII-like galaxies. Fig. 5.6 compares the distribution of the $11.3/7.7\mu\text{m}$ aromatic ratios between AGN and normal star-forming galaxies from Smith et al. (2007) and Lu et al. (2003). For the sample of Smith et al. (2007), we only include HII-like galaxies but exclude a low-metallicity dwarf galaxy (HoII). No correction is applied to their aromatic fluxes, since they are obtained with multiple Drude profile fitting. The flux of the 7.7 and $11.3\mu\text{m}$ aromatic features quoted in Lu et al. (2003) is the integrated value without continuum subtraction from 7.20 to $8.22\mu\text{m}$ and from 10.86 to $11.40\mu\text{m}$, respectively. We correct their ratios by a factor of 1.08 to account for the difference between their measured fluxes and the Drude-profile fluxes used in this paper. This factor is obtained based on the four composite spectra of nearby galaxies from Smith et al. (2007). In the Lu et al. (2003) sample, one object is excluded since the integrated aromatic flux contains significant hot dust emission.

As shown in Fig. 5.6, the flux ratio of AGN with both features detected has a similar distribution to that of star-forming galaxies. The mean $11.3/7.7$ -aromatic ratio for the AGN is 0.27 ± 0.1 , compared with 0.28 ± 0.11 and 0.26 ± 0.07 for the spiral galaxies of Lu et al. (2003) and Smith et al. (2007), respectively. The Kolmogorov-Smirnov (K-S) test indicates a probability of 99% and 40% that our AGN sample is the same as the star-forming galaxies of Lu et al. (2003) and Smith et al. (2007), respectively.

Variations of the aromatic flux ratio have been observed among regions covering a wide range of physical and chemical properties (e.g. Roelfsema et al., 1996; Vermeij et al., 2002). On the other hand, studies of the aromatic features in the same environment show that the flux ratio is insensitive to the intensity of the radiation

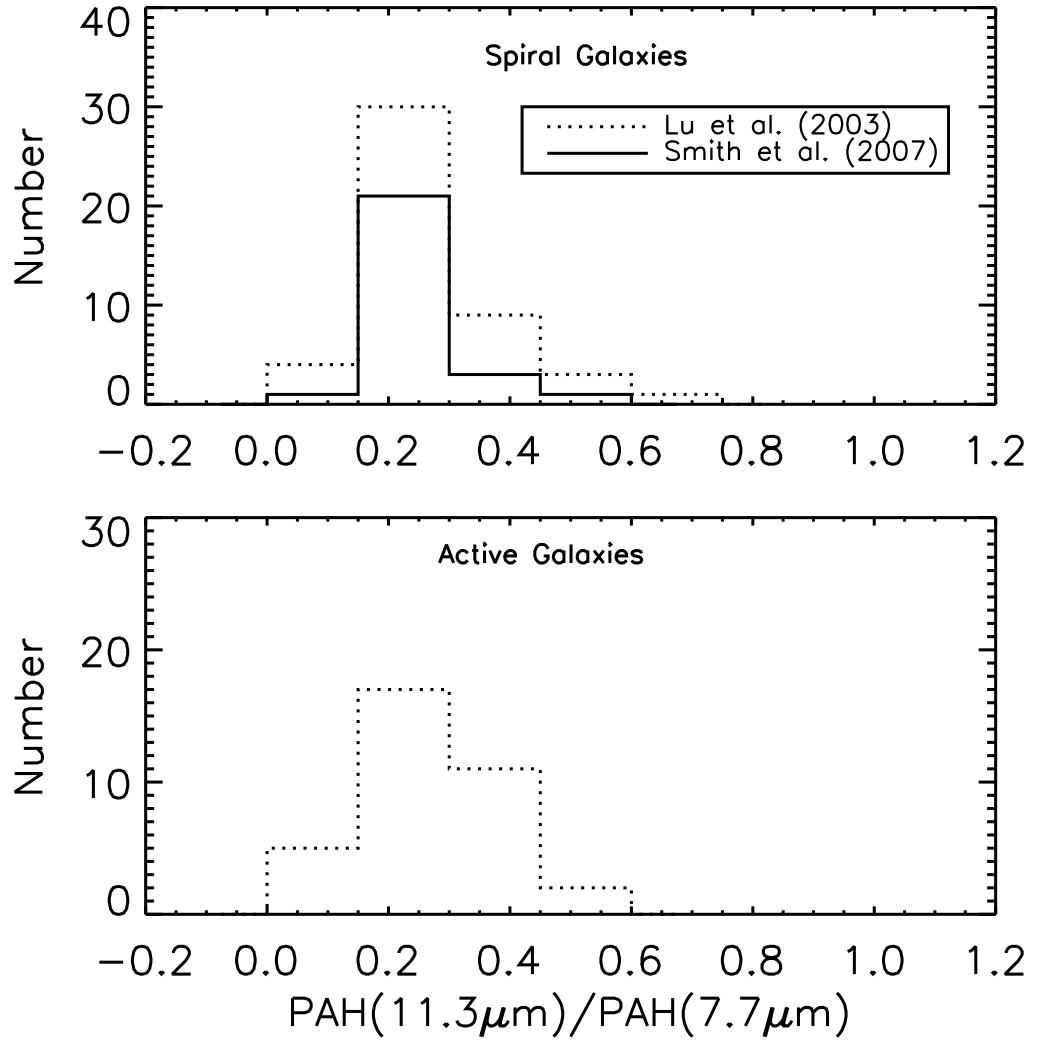


Figure 5.6 The ratio of the 11.3 μm aromatic flux to the 7.7 μm flux. The upper plot is the ratio for normal spiral galaxies from Lu et al. (2003) and Smith et al. (2007) while the lower plot is for active galaxies in this paper.

field (Uchida et al., 2000; Chan et al., 2001). Among different galaxies, there is no systematic difference in the aromatic flux ratio with the intensity of the radiation field, as seen by Lu et al. (2003) where the spiral galaxies studied have total IR luminosity spanning from 10^9 to $10^{11} L_{\odot}$. This may arise because various aromatic regions are averaged out over the entire galaxy. The similar distribution of the ratio between AGN and spiral galaxies as shown in Fig. 5.6 implies that the features observed in AGN are excited under conditions similar to those averaged over normal star forming galaxies. Smith et al. (2007) have found that 20% of galaxies with low-luminosity active nuclei show a weak $7.7 \mu\text{m}$ feature relative to the strength of the $11.3 \mu\text{m}$ feature. The origin of this deviation is not well understood. However, if it is the nuclear radiation that accounts for this peculiar ratio, the similar feature ratio between our sample and star-forming galaxies indicates the aromatic feature output in our sample is dominated by star formation, not by the active nuclei. For objects with only one detected feature, the distribution of the limits on $F_{7.7\mu\text{m}}/F_{11.3\mu\text{m}}$ is still consistent with that of star-forming galaxies.

5.3.2 The Global IR SED

The global IR SED of AGN is affected by many factors. However, if the aromatic feature originates from star-forming regions, the composite spectrum of the subsample with a higher fraction of aromatic emission in the mid-IR emission should show a higher fraction of far-IR emission.

Fig. 5.7 compares the composite spectra from 5 to $200 \mu\text{m}$ for high- $L(\text{PAH})/L(\text{MIR})$ and low- $L(\text{PAH})/L(\text{MIR})$ objects, where $L(\text{MIR})$ is the total mid-IR luminosity between 5.0 and $6.0 \mu\text{m}$ and $L(\text{PAH})$ is the $11.3 \mu\text{m}$ aromatic luminosity or the $7.7 \mu\text{m}$ aromatic luminosity multiplied by a factor of 0.27 for objects with only the $7.7 \mu\text{m}$ feature detected. We define the dividing value of $L(\text{PAH})/L(\text{MIR})$ for all objects with MIPS $70 \mu\text{m}$ measurements so that the high and low- $L(\text{PAH})/L(\text{MIR})$ subsamples have similar numbers of objects. The objects with upper limit measurements for the aromatic fluxes are also included for the low- $L(\text{PAH})/L(\text{MIR})$ subsample while only feature-detected objects are included

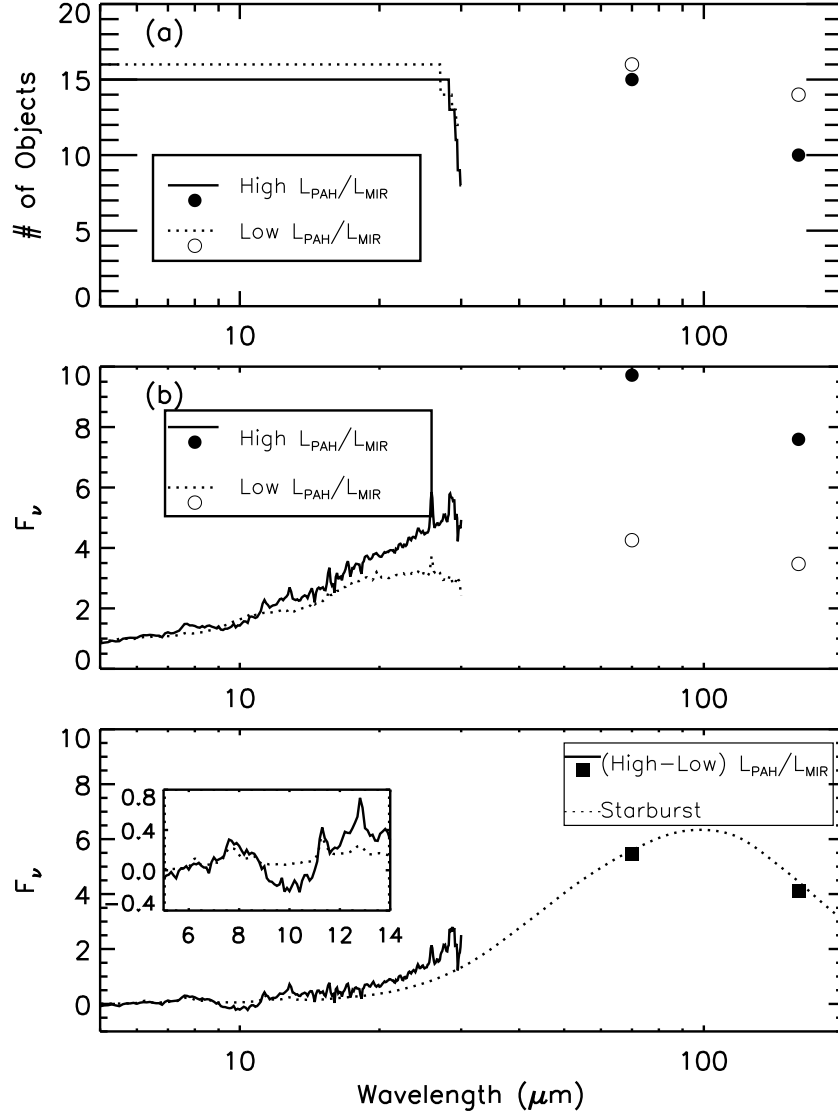


Figure 5.7 (a) The number of objects in each wavelength bin of the composite spectra of the high- $L(\text{PAH})/L(\text{MIR})$ subsample (solid line plus filled circles) and the low- $L(\text{PAH})/L(\text{MIR})$ subsample (dotted line plus open circles), where $L(\text{MIR})$ is the total mid-IR luminosity between 5.0 and 6.0 μm and $L(\text{PAH})$ is the 11.3 μm aromatic luminosity or the 7.7 μm aromatic luminosity multiplied by a factor of 0.27 for objects with only the 7.7 μm feature detected. (b) The geometric mean spectra of the two subsamples. (c) The spectrum of high- $L(\text{PAH})/L(\text{MIR})$ minus low- $L(\text{PAH})/L(\text{MIR})$ objects superposed on the starburst template with $L_{8-1000\mu\text{m}}=2.0\times 10^{11} L_\odot$ from Dale et al. (2001) and Dale & Helou (2002).

for the high- $L(\text{PAH})/L(\text{MIR})$ subsample. We have produced geometric mean composite spectra, which conserve the global continuum shape (See Vanden Berk et al., 2001). For each subsample, the IRS spectra are redshifted and rebinned to a common spectral resolution ($0.1\mu\text{m}$). The MIPS fluxes are K-corrected by assuming $\alpha=1$ and $\alpha=0.0$ ($f_\nu \propto \nu^{-\alpha}$), respectively, based on the IR SED of the AGN in Haas et al. (2003) and Shi et al. (2005). Then each spectrum is normalized by the mean flux density in the wavelength range between 5.0 and $6.0\mu\text{m}$. The final composite spectrum is defined as $(\prod_i^n f_{\lambda,i})^{1/n}$ where λ is the wavelength of a wavelength bin and n is the total number of spectra in this bin.

Fig. 5.7(a) plots the number of objects in each wavelength bin. As shown in Fig. 5.7(b), given that the two composite spectra have similar weak silicate features, obscuration does not account for the difference in the shape of the SEDs. The high- $L(\text{PAH})/L(\text{MIR})$ subsample has relatively larger IR emission toward wavelengths longer than $15\mu\text{m}$. $f(70\mu\text{m})/f(5-6\mu\text{m})$ and $f(160\mu\text{m})/f(5-6\mu\text{m})$ are redder by a factor of 2.5 compared to the values for the low- $L(\text{PAH})/L(\text{MIR})$ subsample. The redder far-IR color is consistent with the star-formation origin of the aromatic features in these active galaxies.

The spectrum of the high- $L(\text{PAH})/L(\text{MIR})$ minus the low- $L(\text{PAH})/L(\text{MIR})$ composite spectra is plotted in Fig. 5.7(c). We match this residual spectrum with star-forming templates from Dale & Helou (2002) and find that the template with $L_{\text{IR}}(8-1000\mu\text{m})=2.0\times 10^{11}L_\odot$ presents the most consistent $70/160\mu\text{m}$ color. After scaling this template to the $70\mu\text{m}$ photometry of the residual spectrum, the subplot shows a good match for the 7.7 and $11.3\mu\text{m}$ aromatic features, although there is some discrepancy for the $[\text{NeII}]12.8\mu\text{m}$ line. This match provides further evidence for the star-formation origin of the aromatic features in these AGN.

5.3.3 Molecular Gas

Fig. 5.8 shows the mass of CO-derived molecular hydrogen gas versus the aromatic-based star-forming IR (SFIR) luminosity (triangles). The aromatic-based SFIR luminosity is calculated in § 4. The mass of hydrogen gas is calculated using

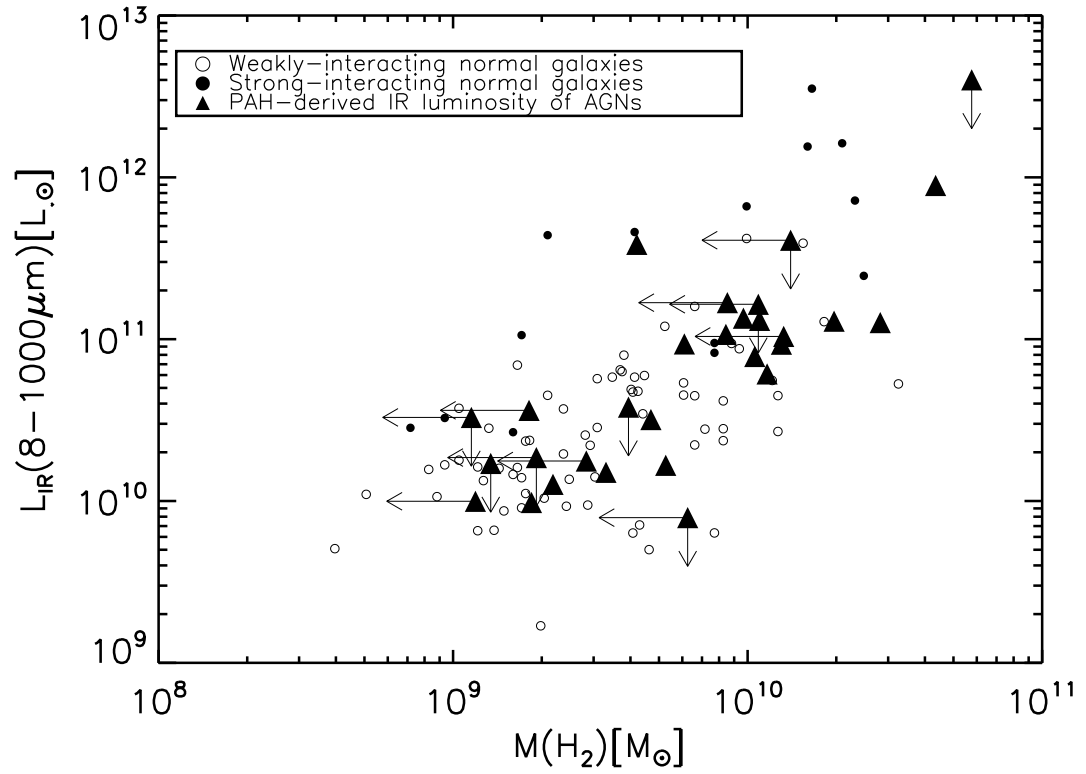


Figure 5.8 The plot of the mass of CO-derived molecular hydrogen gas versus the aromatic-based total IR luminosity (triangles) for AGN. Open and filled circles indicate weakly-interacting normal galaxies and strongly interacting normal galaxies from Solomon & Sage (1988), respectively.

$M_{\text{H}_2} = 1.174 \times 10^4 (S_{\text{CO}} \Delta V) D_L^2 / (1 + z)$, where $S_{\text{CO}} \Delta V$ is the CO flux in Jy km s^{-1} and D_L is the luminosity distance in Mpc. The circles in Fig. 5.8 are the normal galaxies from Solomon & Sage (1988), where open circles are for weakly-interacting normal galaxies and filled circles for strongly interacting ones. The total IR luminosity $L_{\text{IR}}(8\text{-}1000\mu\text{m})$ of the Solomon & Sage (1988) sample is computed from *IRAS* four-band photometry using the relation of Sanders & Mirabel (1996). The difference between the relation of Sanders & Mirabel (1996) and the star-forming templates used to derive the aromatic-based SFIR luminosity is typically less than 5%. All physical parameters were corrected to our adopted cosmological model. Fig. 5.8 shows that the behavior of the aromatic-based SFIR luminosity follows that of normal galaxies well. The relationship between the CO luminosity and SFIR luminosity is consistent with the star-formation excitation of the aromatic feature in our AGN.

As shown above, the profile of aromatic features, the global IR SED of AGN and the gas content in their host galaxies are all consistent with the predominantly star-formation excitation of the aromatic features in active galaxies. This conclusion confirms previous arguments based largely on spatially resolved spectra of nearby active galaxies (e.g. Cutri et al., 1984; Desert & Dennefeld, 1988; Voit, 1992; Laurent et al., 2000; Le Floc'h et al., 2001).

5.4 The Conversion Factor from Aromatic Flux to the SFR

Before proceeding with a quantitative study of the current star formation around AGN based on the measured flux of the aromatic features, we need to know how well the aromatic features trace the ongoing star-formation activity. For Galactic HII regions, the variation of PAH/far-IR(40-500 μm) is up to two orders of magnitude from ultra-compact to extended optically visible examples (Peeters et al., 2004). However, integrated over the whole disk of spiral galaxies, the aromatic features correlate well with $\text{H}\alpha$ (Roussel et al., 2001). This behavior may result from the galaxy-scale quantity averaging out the local physical properties involved in indi-

vidual regions, such as the escape efficiency of ionizing photons from HII regions (e.g. Roussel et al., 2001). The situation becomes complicated in the circumnuclear regions where the EW of the observed aromatic feature is low, as in embedded HII regions (Roussel et al., 2001; Haas et al., 2002; Peeters et al., 2004). The reason for this is unclear; it may be caused by obscuration, PAH destruction, a decrease in ionizing photons as a result of the increasing compactness of the HII regions, or the additional mid-IR emission from highly embedded active nuclei. However, a direct attempt to correlate the aromatic feature to far-IR luminosity for star-forming galaxies shows that the variation of PAH/far-IR is about a factor of 2-3 (Peeters et al., 2004; Spoon et al., 2004; Wu et al., 2005). Spoon et al. (2004) obtained $L(6.2\mu\text{mPAH})/L(\text{IR})=0.003\pm0.001$ from 70 normal and starburst galaxies. Taking a typical value of $L(7.7\mu\text{mPAH})/L(6.2\mu\text{mPAH})=3.5$ (Smith et al., 2007), this measurement is equivalent to $L(7.7\mu\text{mPAH})/L(\text{IR})=0.01\pm0.0035$. The aperture mismatch between the IR flux and the aromatic flux contributes to a part of the scatter. Lutz et al. (2003) derived $L(7.7\mu\text{mPAH})/L(8-1000\mu\text{m})=0.033\pm0.017$ (assuming a Drude profile with $0.6\mu\text{m}$ FWHM for the $7.7\mu\text{m}$ feature) from 10 starburst galaxies. This ratio allows for the aperture differences, although the two quantities are still not well matched. Based on IRS spectra of nearby galaxies, Smith et al. (2007) employed a robust method of extracting aromatic features. The aperture-matched mean values with $1-\sigma$ uncertainties of $L(7.7\mu\text{mPAH})/L(3-1100\mu\text{m})$ and $L(11.3\mu\text{mPAH})/L(3-1100\mu\text{m})$ are $0.052(1\pm40\%)$ and $0.012(1\pm30\%)$, respectively, for 26 HII-like normal galaxies excluding one dwarf galaxy (Ho II) with an extreme low ratio probably caused by metallicity effects (See Smith et al., 2007). A part of the scatter in the ratio of $L(\text{PAH})/L(\text{totIR})$ may arise from a general luminosity dependence. As shown in Figure 3 of Schweitzer et al. (2006), $L(7.7\mu\text{mPAH})/\nu L_\nu(60\mu\text{m})$ decreases from 0.06 for starburst galaxies at $\nu L_\nu(60\mu\text{m})=1.5\times10^{10} L_\odot$ to 0.015 for starburst-dominated ULIRGs at $\nu L_\nu(60\mu\text{m})=10^{12} L_\odot$.

To compute the luminosity-dependent values, we have used the star-forming templates from Dale et al. (2001) and Dale & Helou (2002). Each SED template is optimized for a very narrow luminosity range ($\frac{\Delta L}{L} \sim 0.1-0.4$) where the luminosity

is converted from the α index using the relation given by Marcillac et al. (2006). Aromatic fluxes for all the templates are measured using the same procedures as for AGN. As demonstrated in § 2.3, the aromatic fluxes obtained by our procedure do not change with the EW, implying that there is no systematic difference in the measurements of the aromatic fluxes between the star-forming templates and AGN. The conversion factor for the $7.7 \mu\text{m}$ feature varies from 0.041 at a SFIR luminosity of $10^9 L_\odot$ to 0.0095 at a luminosity of $3.3 \times 10^{12} L_\odot$ and the $11.3 \mu\text{m}$ feature varies from 0.012 to 0.004 over the same luminosity range. These values agree well with the observational ones. To derive the conversion factor for each object, we adopt the template that gives the closest aromatic flux at the redshift of this object. The uncertainties are assumed to be the observed ones (40% and 30% for $L(7.7\mu\text{mPAH})/L(8-1000\mu\text{m})$ and $L(11.3\mu\text{mPAH})/L(8-1000\mu\text{m})$, respectively), although there is only a 10% difference between conversion factors for SED templates in two adjacent luminosity ranges. The final uncertainty of the aromatic-derived SFIR luminosity includes that of the conversion factor and the measurement uncertainty of the aromatic flux. If this final uncertainty is larger than the measured aromatic flux, the 3σ upper limit is adopted. Table 5.1 lists the SFIR luminosity calculated in the above way. For objects with both features detected, we adopted the value from the $11.3 \mu\text{m}$ feature since it generally has smaller uncertainty. The value from the detected feature is listed if only one feature is detected. For objects with neither feature detected, the lower value for the two upper limits is listed.

As discussed in § 2.2, PG 2304+042 and 3C 272.1 have thermal IR emission outside the IRS slit. This extended emission is converted to the total IR luminosity by multiplying by a factor of 12.0 based on the star-forming template with $L_{\text{IR}}(8-1000\mu\text{m})=10^{11} L_\odot$ from Dale & Helou (2002), and is close to the observed value (Chary & Elbaz, 2001).

Non-star-formation sources, such as planetary nebulae and diffuse stellar radiation, can excite low-level IR emission and aromatic features. Aromatic features have been observed in a fraction of elliptical galaxies (Bressan et al., 2006) and some of them may originate from star formation regions while others may be excited by an

old stellar population. In five normal elliptical galaxies observed by Kaneda et al. (2005), the 11.3 μm aromatic luminosity is between 10^5 and $8 \times 10^6 L_\odot$ (the possible problem in this work with stellar light subtraction should not affect the 11.3 μm flux much; Bregman et al., 2006). To be sure we are measuring recent star formation, we adopt a limiting aromatic luminosity of $3 \times 10^7 L_\odot$ above which the old stellar population contribution should be smaller than 25%. The corresponding aromatic-derived total IR luminosity at this limit is $3 \times 10^9 L_\odot$. Therefore, a total of twenty-two objects including eight PAH-detected ones are excluded.

5.5 Origin of the Far-IR emission of AGN

Fig. 5.9 shows the star-formation contribution to the MIPS rest-frame 24, 70 and 160 μm emission versus the integrated mid-IR luminosity between 5.0 and 6.0 μm . The *IRAS* or *ISO* 25 μm fluxes are plotted for objects without MIPS 24 μm flux measurements. For objects without MIPS 70 μm flux measurements, we estimate one by interpolating between the detected *IRAS* or *ISO* 60 and 100 μm fluxes. The MIPS fluxes are K-corrected by assuming $\alpha=1$ for 24 and 70 μm photometry, and $\alpha=0.0$ for 160 μm photometry ($f_\nu \propto \nu^{-\alpha}$), based on the IR SED of AGN in Haas et al. (2003) and Shi et al. (2005). The total PAH-derived SFIR luminosities are converted to the star-formation emission at the three MIPS bands using the luminosity-dependent conversion factors derived from the star-forming templates from Dale et al. (2001) and Dale & Helou (2002).

At 24 μm , Fig. 5.9 indicates most of the objects are dominated by AGN emission. At 70 and 160 μm , the far-IR emission of an individual AGN can be dominated by either AGN power or star formation. To quantify the star-formation fraction at the three MIPS bands and its possible dependence on the AGN luminosity, we have employed the code written by Kelly (2007) that incorporates the upperlimit measurements. As listed in Table 5.2, the average star-formation fractions for the whole sample at MIPS 24, 70 and 160 μm are 4%, 26% and 28%, respectively, at the median mid-IR luminosity ($2.6 \times 10^{10} L_\odot$) of the sample. As indicated by Table 5.2,

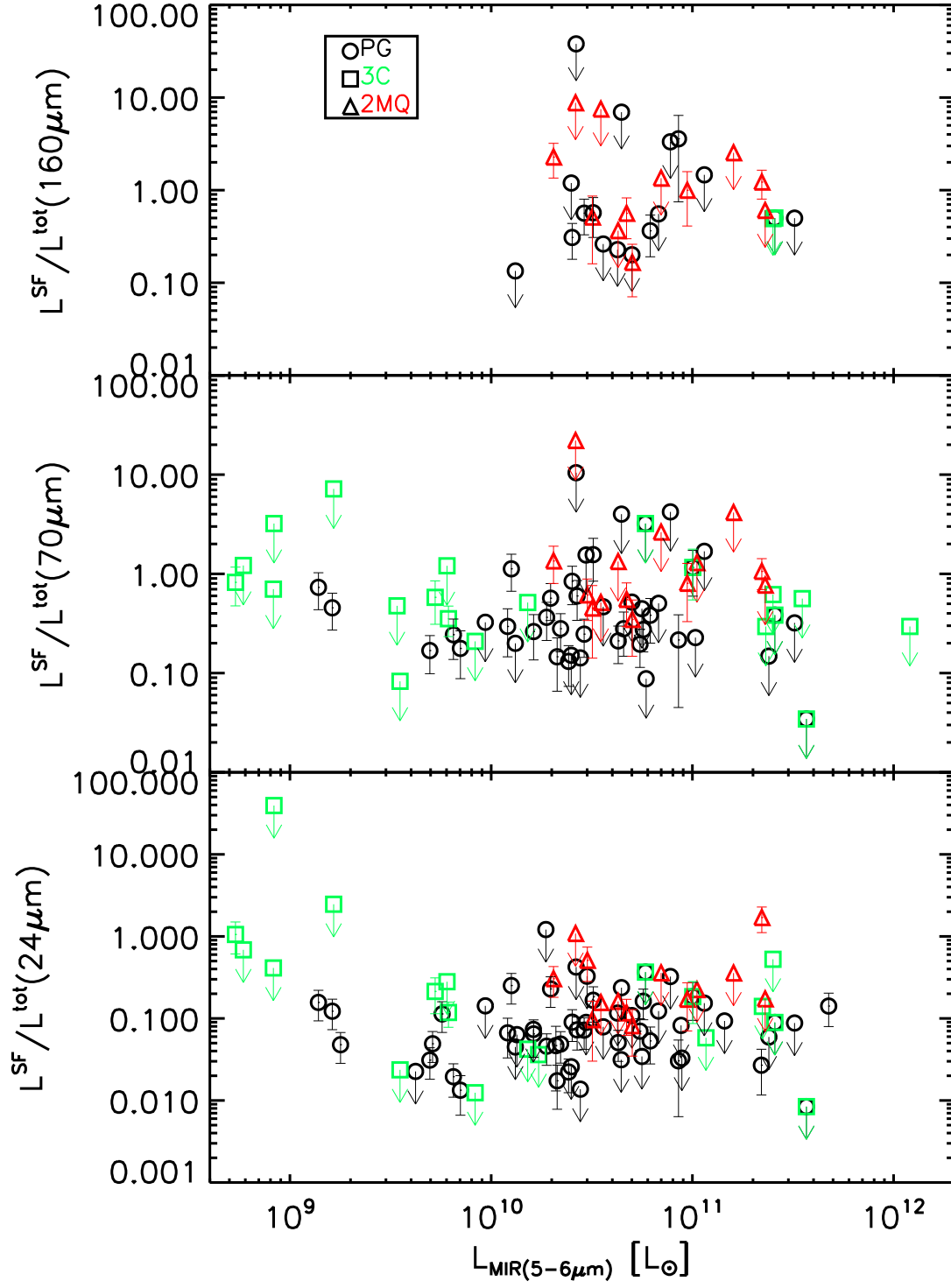


Figure 5.9 The star-formation fraction at 24, 70 and 160 μm versus the mid-IR (5-6 μm) luminosity for the PG, 3C and 2MASS objects, respectively.

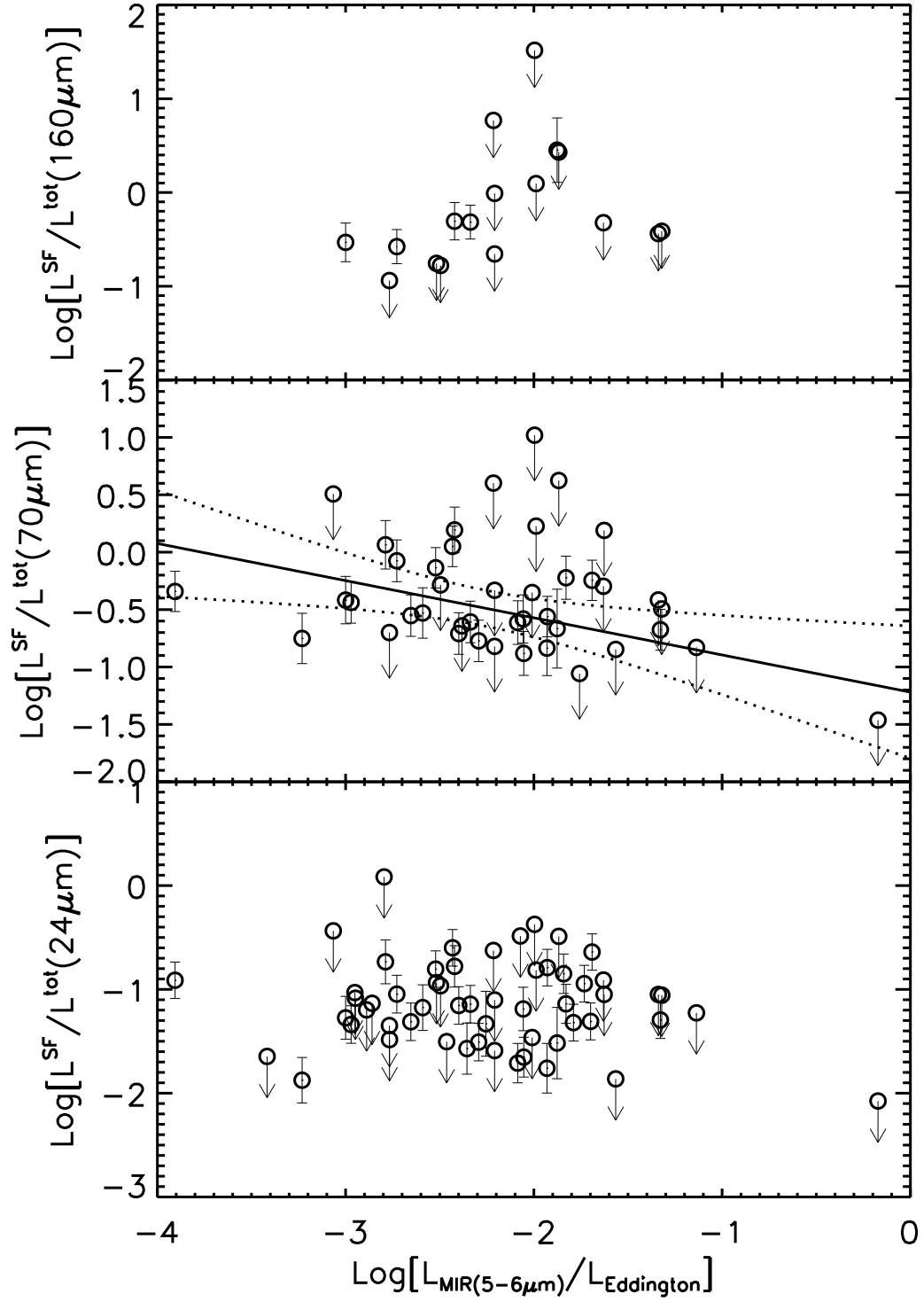


Figure 5.10 The star-formation fraction at 24, 70 and 160 μm versus the ratio of mid-IR (5-6 μm) luminosity and the Eddington luminosity for PG quasars. The solid line is the regression line and the two dotted lines are 2σ confidence bounds.

these ratios depend on luminosity, with a lower relative star-formation contribution at higher AGN mid-IR luminosity. The diverse nature of far-IR emission is consistent with the large scatter of the correlation between the far-IR emission and AGN power indicators (e.g. Shi et al., 2005; Cleary et al., 2006; Tadhunter et al., 2007). There will also be some scatter due to the range of redshifts. However, since the redshifts of our PG and 2MASS samples are similar and modest, the effect should be small.

Table 5.2 also includes the result for PG and 2MASS objects at the MIPS 24 and 70 μm bands, where there are enough detected data points. The average star-formation contributions at MIPS 70 μm for PG and 2MASS are 24% and 51% at median mid-IR luminosities of $3.0 \times 10^{10} L_{\odot}$ and $3.5 \times 10^{10} L_{\odot}$, respectively. The fraction for the PG quasars is lower than that (>30%) obtained by Schweitzer et al. (2006), who also employ the aromatic feature to evaluate the role of star formation. Contributions to the discrepancy include a difference in the conversion factors from the aromatic fluxes to the SFIR fluxes and the relatively large uncertainties in their 7.7 μm fluxes caused by silicate features, whereas our result is mainly based on 11.3 μm features.

Compared to the whole sample, PG objects show relatively stronger luminosity-dependence of the star-formation fractions at 24 and 70 μm , with decreasing fractions at higher mid-IR luminosities. However, the 2MASS objects do not have such a relation and most of the 3CR results are upperlimits. Thus the relation for the whole sample is mainly produced by the PG sample. As shown in Fig. 5.10 and Table 5.3, the star-formation fractions for the PG objects also decrease as the ratios of the mid-IR continuum luminosities and the Eddington luminosities decrease, where the blackhole masses of PG objects are obtained from Vestergaard & Peterson (2006) and Kaspi et al. (2000). The anti-correlations indicate these two relations are not caused by the selection effect that the detectable aromatic features in objects with higher mid-IR continuum emissions have larger fluxes.

Table 5.2. The Star Formation Fraction at Three MIPS Bands as a Function of the mid-IR Luminosity

MIPS band	α	β	Correlation
All(MIPS 24 μm)	0.6 ± 1.3	-0.18 ± 0.13	-0.22 ± 0.15
All(MIPS 70 μm)	1.2 ± 1.0	-0.17 ± 0.10	-0.32 ± 0.17
All(MIPS 160 μm)	2.3 ± 5.5	-0.27 ± 0.51	-0.15 ± 0.29
PG(MIPS 24 μm)	0.2 ± 1.3	-0.15 ± 0.13	-0.22 ± 0.19
PG(MIPS 70 μm)	2.4 ± 1.6	-0.29 ± 0.15	-0.43 ± 0.19
2MASS(MIPS 24 μm)	0.1 ± 12.3	-0.11 ± 1.15	0.01 ± 0.43
2MASS(MIPS 70 μm)	1.2 ± 6.9	-0.14 ± 0.65	-0.05 ± 0.48

Note. — $\text{Log}(\text{Frac}_{SF}^{\text{MIPS}}) = \alpha + \beta \times \text{Log}(L_{MIR})$

5.6 STAR-FORMING IR LUMINOSITY FUNCTION OF QUASAR HOST GALAXIES

5.6.1 Methodology

The main challenge in deducing the SFIR luminosity function (LF) for our sample is that the flux limit of the aromatic feature is not well defined and many objects have only upper limits in these measurements. Therefore, we obtained the SFIR LF by converting the well-defined LF at other wavelengths using the fractional bivariate LF (Elvis et al., 1978). The formula can be written as

$$\Phi_{M_{\text{SFIR}}} = \sum_{M_{\lambda}} \Phi_{M_{\lambda}} F(M_{\lambda}, M_{\text{SFIR}}) \quad (5.2)$$

where $\Phi_{M_{\text{SFIR}}}$ is the SFIR LF and $\Phi_{M_{\lambda}}$ is the LF at λ -band where each parent sample is selected (radio for 3CR objects, B -band for PG objects and K -band for 2MASS objects). The fractional bivariate LF $F(M_{\lambda}, M_{\text{SFIR}})$ indicates the fraction of objects with magnitude M_{λ} at λ -band having SFIR luminosity of M_{SFIR} . We calculate $F(M_{\lambda}, M_{\text{SFIR}}) \Delta M_{\lambda} \Delta M_{\text{SFIR}}$ by dividing the number n_1 of objects with λ -band magnitude in the interval $M_{\lambda} \pm \Delta M_{\lambda}/2$ and the SFIR luminosity in the interval

Table 5.3. The Star Formation Fraction at Three MIPS Bands as a Function of the Eddington ratio

MIPS band	α	β	Correlation
PG(MIPS 24 μm)	-1.6 ± 0.3	-0.10 ± 0.12	-0.18 ± 0.21
PG(MIPS 70 μm)	-1.3 ± 0.3	-0.32 ± 0.12	-0.60 ± 0.17

Note. — $\text{Log}(\text{Frac}_{SF}^{\text{MIPS}}) = \alpha + \beta \times \text{Log}(L_{MIR}/L_{Edd})$

$M_{\text{SFIR}} \pm \Delta M_{\text{SFIR}}/2$ by the number n_2 of objects with λ -band magnitude in the interval $M_\lambda \pm \Delta M_\lambda/2$ that could have had detected aromatic features if they had SFIR luminosities of M_{SFIR} . n_1 is the observed number. Any object with λ -band magnitude in the interval $M_\lambda \pm \Delta M_\lambda/2$ will be counted into n_2 , if it has a limiting SFIR luminosity lower than M_{SFIR} . The limiting SFIR luminosity is defined as the minimum star formation rate to detect the aromatic feature (see § 2.3) plus any extended IR emission.

For PG quasars, Φ_{M_λ} is the B -band LF at $0.0 < z < 0.5$ from Table 9 of Schmidt & Green (1983), where the median redshift of 0.25 is adopted to convert the apparent magnitude to the absolute magnitude and the K-correction is the same as described in Schmidt & Green (1983). This B -band LF has data coverage for M_B from -21.4 mag to -26.4 mag. A double-exponential model (for the formula, see Le Floc'h et al., 2005) fits the B -band LF well and it is used to derive the Φ_{M_B} for any given M_B between -21.0 and -26.5 for our PG subsample. The SFIR luminosity of this PG subsample spans the range from 3.1×10^9 to $2.4 \times 10^{12} L_\odot$. To construct the fractional bivariate LF ($F(M_B, M_{\text{SFIR}})$), the entire ranges of M_B and SFIR luminosity are each divided into four intervals. The final fractional bivariate LF ($F(M_B, M_{\text{SFIR}})$) along with Poissonian uncertainties is listed in Table 5.4.

For 2MASS objects, the LF at K band from Cutri et al. (2001) is adopted as Φ_{M_λ} . A two-exponential model does not fit the data well and thus we interpolate the measured data points to get the space density at a given K -band magnitude.

Table 5.4. Fractional Bivariate Luminosity Function for PG quasars

$\text{Log}(L_{totIR}^{PAH}[L_{\odot}])$	$M_B(\text{mag})$			
	-25.83	-24.57	-23.31	-22.05
10.06	0/0 \pm 1.00	0/0 \pm 1.00	3/6 \pm 0.35	8/12 \pm 0.30
10.75	0/0 \pm 1.00	2/2 \pm 1.00	7/19 \pm 0.16	5/14 \pm 0.19
11.43	1/3 \pm 0.38	2/8 \pm 0.20	3/26 \pm 0.07	1/15 \pm 0.07
12.11	1/14 \pm 0.07	1/17 \pm 0.06	0/26 \pm 0.00	0/15 \pm 0.00

Table 5.5. Fractional Bivariate Luminosity Function for 2MASS quasars

$\text{Log}(L_{totIR}^{PAH}[L_{\odot}])$	$\text{Log}(L_K [L_{\odot}])$		
	10.88	11.26	11.64
11.06	4/5 \pm 0.54	3/2 \pm 1.37	0/0 \pm 1.00
11.70	1/9 \pm 0.12	2/8 \pm 0.20	0/0 \pm 1.00
12.33	0/10 \pm 0.00	1/12 \pm 0.09	0/2 \pm 0.00

Table 5.5 lists the final fractional bivariate LF ($F(M_B, M_{\text{SFIR}})$) for 2MASS objects.

For 3CR objects, $\Phi_{M_{\lambda}}$ is the LF at 151 MHz from Willott et al. (2001), where the LF is obtained based on the 3CRR, 6CE and 7CRS samples. We use the analytic LF of model C for a cosmological model of $\Omega_m=0$, $\Omega_{\lambda}=0$ and $H_0=50 \text{ kms}^{-1}\text{Mpc}^{-1}$, because the LF for this cosmological model is close to that for our cosmological model except for the H_0 value. (Willott et al., 2001). We convert to our cosmological model by setting $\Phi_1(L_1, z)dV_1 = \Phi_2(L_2, z)dV_2$ (Peacock, 1985). The radio luminosity at 151 MHz for our 3CR subsample is calculated and K-corrected using the flux density and spectral index at 178 MHz from Spinrad et al. (1985). Again, we limit our 3CR subsample to the redshift range between 0.0 and 0.5 to match the PG and 2MASS redshift ranges. The final fractional bivariate LF ($F(M_{151\text{MHz}}, M_{\text{SFIR}})$) with Poissonian uncertainties is listed in Table 5.6.

Table 5.6. Fractional Bivariate Luminosity Function for 3CR radio galaxies and quasars

$\text{Log}(L_{\text{totIR}}^{PAH}[L_{\odot}])$	$\text{Log}(L_{151\text{MHz}}[\text{W Hz}^{-1}\text{sr}^{-1}])$		
	25.13	26.23	27.32
10.54	$4/9 \pm 0.27$	$1/3 \pm 0.38$	$0/1 \pm 0.00$
12.01	$0/10 \pm 0.00$	$1/21 \pm 0.05$	$0/9 \pm 0.00$

5.6.2 Star-forming IR Luminosity Function of Active Galaxies

5.6.2.1 Comparison to Field Galaxies

The most important result from the fractional bivariate LFs in Table 5.4, Table 5.5 and Table 5.6 is that objects with a large range of nuclear activity have a non-zero probability of having a high SFIR luminosity. The form of the fractional bivariate LF implies that SFIR LF of AGN host galaxies is much flatter than the LF of the AGN themselves.

Fig. 5.11 shows the results for the SFIR LF for the PG, 2MASS and 3CR subsamples. Each subsample has a brightness limit at the wavelength where it is selected. We set $M_B < -21$ for the PG subsample and $M_K < -25.5$ for the 2MASS subsample and $L_{151\text{MHz}} > 2 \times 10^{24} \text{ W Hz}^{-1} \text{ Sr}^{-1}$ for the 3CR subsample. The dotted line shows the re-normalized IR LF of local field galaxies from Le Floc'h et al. (2005) based on the *IRAS* and *ISO* results; it agrees well with previous studies of the IR LF of field galaxies (See Rieke & Lebofsky, 1986; Sanders et al., 2003). In Fig. 5.11, the SFIR LFs of the three subsamples are much flatter than the re-normalized LFs of field galaxies.

We need to be sure that the flatter LFs are not just a result of the difficulty in measuring the SFR around a bright quasar. We first use Monte-Carlo simulations to test the robustness of the methodology used to derive the SFIR LF of AGNs. The following steps are taken to construct a sample that mimics the PG subsample:

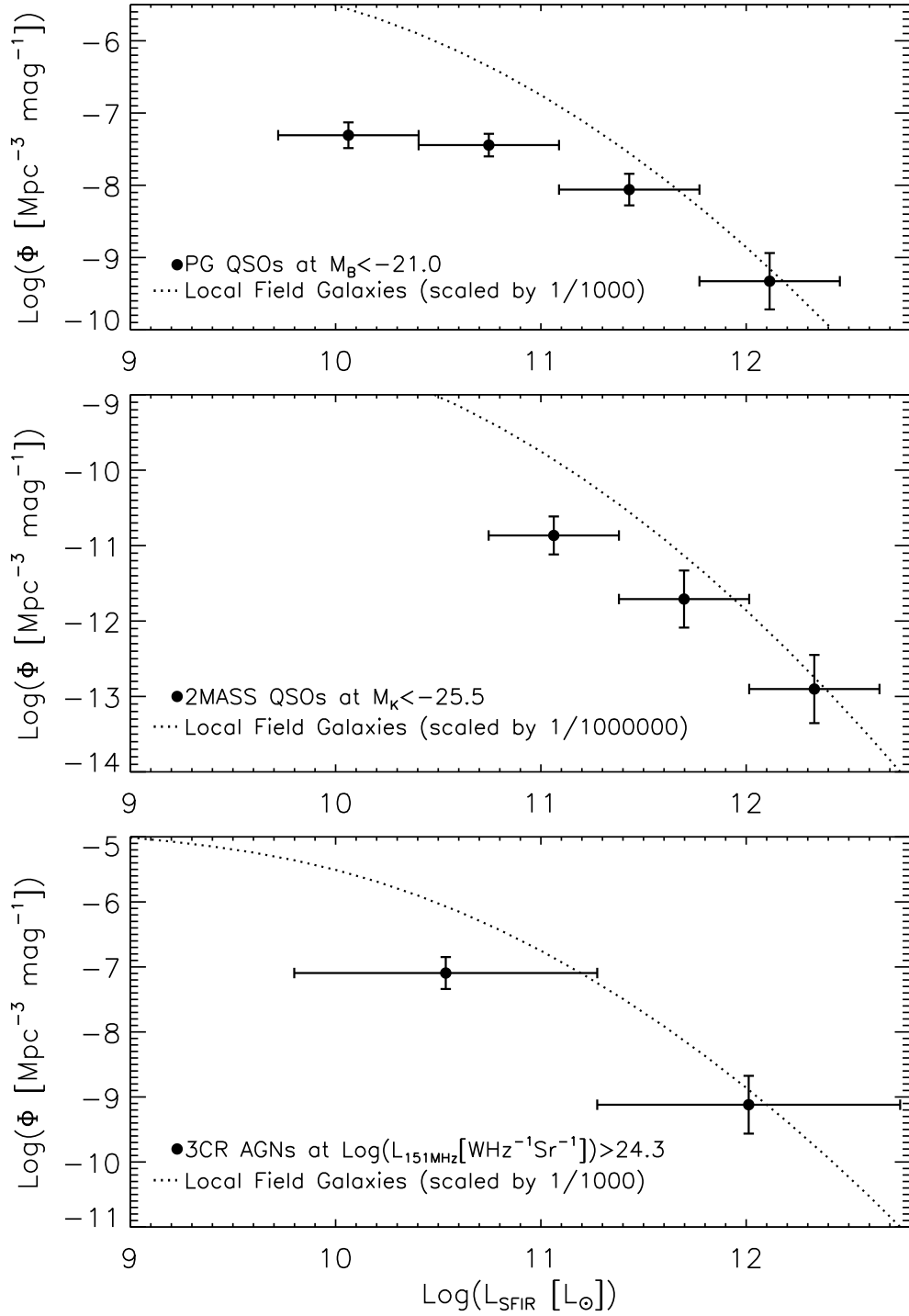


Figure 5.11 Star-forming infrared luminosity functions for the PG, 2MASS and 3CR AGN. The dotted line is the re-normalized luminosity function of local field galaxies from Le Floch et al. (2005).

(1) a total of $N_{obj}(>10000)$ objects is created over the redshift range between 0.001 and 0.5; (2) the comoving number density is constant over the redshift range; (3) a B -band luminosity within the range of the PG subsample is assigned to each object randomly but the relative distribution is the same as the PG B -band LF; (4) similarly, each object has a randomly assigned IR luminosity with relative distribution defined by the SFIR LF of the PG subsample. In this case, the IR flux is not correlated with the B -band flux; (5) a well-defined flux limit is applied in the B -band while the IR flux limit is randomly distributed over the whole range of the SFIR fluxes of the PG subsample. After producing the above set of objects, the fractional bivariate LF is calculated based on those objects detected in the B -band. The final derived SFIR LF using the fractional bivariate LF follows the pre-defined SFIR LF within the Poisson noise. The same result is obtained for the simulation in which the IR flux is tightly correlated with the B -band flux.

Unlike the PG subsample, which is complete, the 2MASS and 3CR subsamples only contain one-third of their parent samples at $z < 0.5$. To test for the effects of the sample incompleteness, we use only one third of the objects brighter than the B -band limiting flux created in the above simulations, with these objects having the brightest apparent B -band magnitude. Again, the derived SFIR LF is consistent with pre-defined SFIR LF within the Poisson noise. We also test using the one-third of the objects with the most luminous absolute B -band luminosity. The shape of the derived IR LF does not change but the normalization becomes smaller. The same result is obtained if the B -band flux correlates with the IR flux. Thus, for all three subsamples, the Monte Carlo code demonstrates the robustness of our methodology to derive the SFIR LF of AGNs

Because AGNs have strong mid-IR continua, aromatic features are detected only in host galaxies with intense star formation. We can now use the Monte-Carlo simulation to demonstrate that this selection effect cannot account for the large difference in the SFIR LF between the field galaxy and PG quasars. In the simulation, we assume the SFIR LF of PG quasars actually follows that of field galaxies. For each PG object, we obtain the IR LF of field galaxies at the redshift of this object by

assuming that the local field galaxy IR LF from Le Floch et al. (2005) evolves with redshift as $L^*(z) = L^*(0)(1+z)^{3.2}$ and $\Phi^*(z) = \Phi^*(0)(1+z)^{0.7}$. We then randomly assign a SFIR luminosity to this PG object with a relative probability that follows the LF of field galaxies at this redshift. The range of the simulated SFIR luminosities is from 3.1×10^9 to $2.4 \times 10^{12} L_\odot$, consistent with the observed range for the PG quasars. Also, we assume that the total probability in this luminosity range is equal to 1. In this case, all simulated IR luminosities are above the low luminosity cut ($3 \times 10^9 L_\odot$), and thus bias the results toward the high luminosity end. Combining the simulated SFIR luminosity and the observed uncertainty or upper limit for each PG object, we can calculate the detection fraction for the aromatic features. After one thousand simulations, we find (despite the bias toward high luminosity) that the detection fraction is only $(28 \pm 3)\%$, much smaller than the observed value (48%). This large difference indicates that our result is not simply due to the selection toward high levels of SFR caused by the AGN emission.

We further measure the probability of producing the observed curvature of the SFIR LF if the PG quasar sample actually has a field galaxy SFIR LF. In each simulation, all PG objects are assigned randomly SFIR luminosities as described above. Using the simulated luminosities and the observed uncertainties or upper-limits, a SFIR LF is constructed using the same procedure including the number of luminosity bins as the observed LF. All data points produced in a total of ten thousand simulations are rebinned to the same bins as for the observed PG LF. In four luminosity bins, the fractions of simulated non-zero number densities are 100%, 100%, 64% and 6% from low to high luminosity. All simulated number densities are then rescaled by a factor to match the composite number density in the first luminosity bin to the observed one. This composite number density is assumed to be the median value of all simulated number densities (including zero value) in the first bin, indicating a probability of 50%. We then calculate the probability for an observed luminosity bin as the fraction of simulated number densities larger than the lower 1-sigma bound of the observed number density in this bin. The probability in each bin from low to high luminosity is 99.0%, 1.0%, 2.5% and 4.0%, respectively. This

result provides further evidence that the flatter SFLF of the PG quasars is robust against selection effects.

We have noticed that our AGN host SFLFs are constructed under an assumption that the SFR of AGN host galaxies does not depend on the nuclear brightness. According to Equation 5.2, the incompleteness of the LF of AGN brightness itself at low luminosity end can flatten artificially the slope of AGN host SFLFs, if the SFRs of AGN hosts are actually proportional to the nuclear brightness. However, such incompleteness is required to be significantly large to produce the whole flattening of AGN host SFLFs relative to that of field galaxies. Therefore, we are still confident about our result that SFLFs of AGN hosts are flatter than that of field galaxies, although the level of flattening requires future detection of aromatic features for a complete AGN sample.

We also noticed that the normalization of the 2MASS K-band luminosity function from Cutri et al. (2001) may be underestimated significantly. Such underestimate may not affect the slope of the 2MASS SFLF, if the normalization is underestimated uniformly over the whole range of the 2MASS K-band luminosity. However, we are discussing with Roc M. Cutri to see if we can further evaluate their 2MASS K-band luminosity function, which should give the accurate normalization for our 2MASS SFLF.

5.6.2.2 Dependence on AGN Luminosity

Fig. 5.12 shows the SFIR LF of PG quasars as a function of the B -band luminosity. The two solid lines are Schechter-function fits for PG quasars at $M_B < -21$ and $M_B < -23$, respectively. The fitting parameters are given in Table 5.7. There is a trend that the SFIR LF of PG quasars becomes flatter for the brighter PG objects. We suggest that the higher SFR for brighter PG quasars is not a selection effect because the B -band luminosity of normal infrared galaxies is not well correlated with IR luminosity and LIRGs rarely have $M_B < -23$ (See Rieke & Lebofsky, 1986). The trend seen in Fig. 5.12 is not likely to be due to evolution with redshift, as the mean redshifts for the faint and bright subsamples are nearly the same from faint

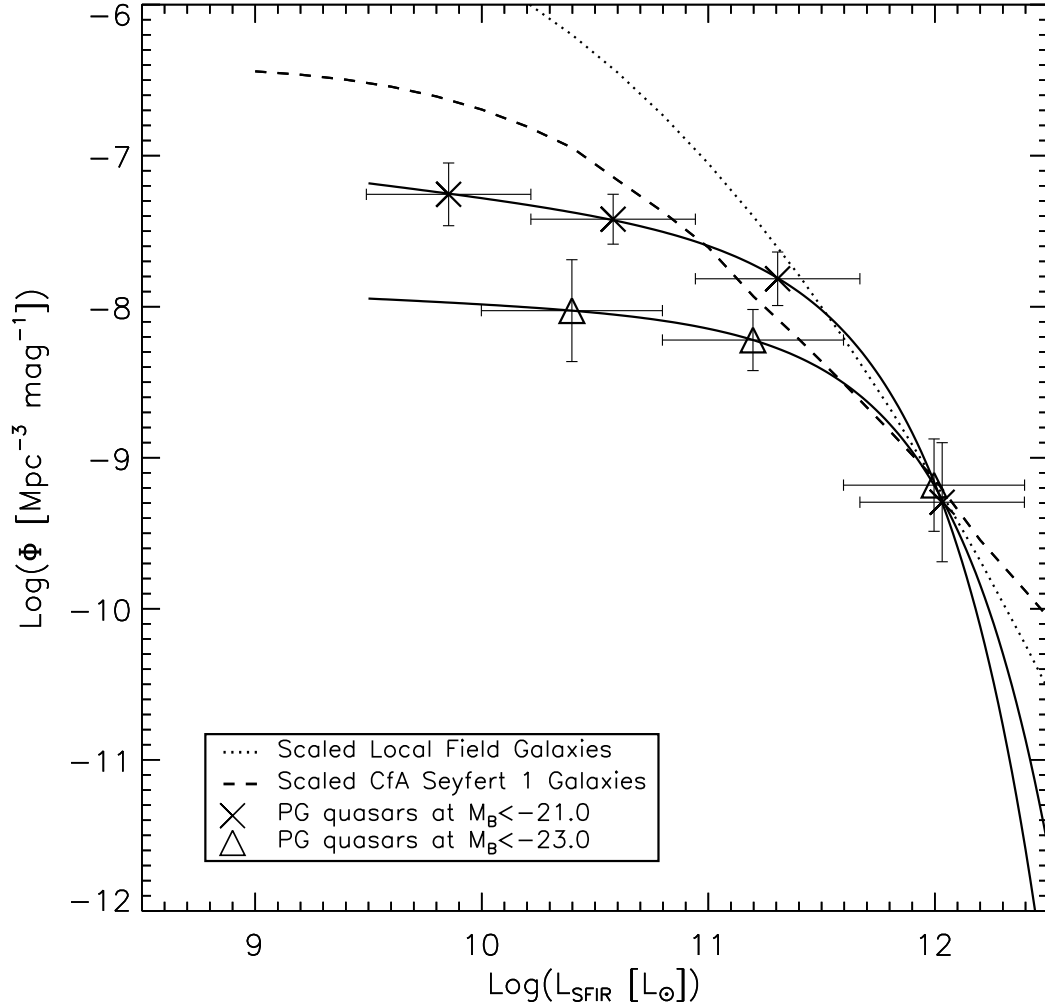


Figure 5.12 Star-forming infrared luminosity functions of PG quasars as a function of quasar brightness. The dashed line is the re-normalized luminosity function of star formation in CfA Seyfert 1 galaxies from Maiolino et al. (1995). The dotted line is the re-normalized luminosity function of local field galaxies from Le Floc'h et al. (2005). The solid lines are Schechter-function fits to the two PG subsamples.

to bright, 0.18 ± 0.30 and 0.24 ± 0.11 respectively.

In Fig. 5.12, the dashed line is the LF of extended star formation in CfA Seyfert 1 galaxies from Maiolino et al. (1995). The extended IR emission of Seyfert galaxies was obtained by subtracting the nuclear emission from IRAS 12 μm photometry (See Maiolino et al., 1995). We converted the 10 μm luminosity to the total IR luminosity using the IR SED template from Dale et al. (2001) and Dale & Helou (2002). Similarly to converting the aromatic flux to the total IR luminosity, the conversion factor from 10 μm to the total IR luminosity depends on the total IR luminosity. The omission of nuclear star formation (within $2''$) in the study of Maiolino et al. (1995) may affect the LF of total star formation in their Seyfert galaxies. However, if nuclear star formation is correlated with the extended star formation as found by Buchanan et al. (2006), the shape of the LF for the total star formation in Seyfert galaxies should not change. As shown in Fig. 5.12, the SFIR LF of Seyfert 1 galaxies is steeper than the LF of PG quasars. There is also a suggestion that the LF for the lower-luminosity PG quasars is steeper than for the higher-luminosity ones. Seyfert galaxies have a higher SFR and flatter LF on average than field galaxies (see Fig. 5.12 and Maiolino et al., 1995). It appears that star formation is correlated with the level of nuclear activity over the full range from normal galaxies to quasars.

To test the trend of the SFIR LF of active galaxies as a function of AGN luminosity, we extended the Monte-Carlo simulations described in § 6.2.1 to test the difference between PG quasars with $M_B < -21$ and PG quasars with $M_B < -23$. In this simulation, we assume that the SFIR LF of PG quasars with $M_B < -23$ actually follows that of PG quasars with $M_B < -21$. For a PG quasar with $M_B < -23$, we obtain the SFIR LF of PG quasars with $M_B < -21$ at the redshift of this object by assuming the SFIR LF of PG quasars at $M_B < -21$ evolving with redshift as $L^*(z) = L^*(z_1)(\frac{1+z}{1+z_1})^{3.2}$ and $\Phi^*(z) = \Phi^*(z_1)(\frac{1+z}{1+z_1})^{0.7}$, where z_1 is the mean redshift (0.2) of PG quasars with $M_B < -21$. Based on this LF, a random SFIR luminosity is assigned to a PG quasar with $M_B < -23$. The luminosity range is between 3.1×10^9 and 2.4×10^{12} , consistent with the observed range for PG quasars with $M_B < -21$.

Table 5.7. Best-fitting parameters to star-forming IR LF of PG quasars

Object	$\text{Log}(\phi^* [\text{Mpc}^{-3} \text{ mag}^{-1}])$	$\text{Log}(L^* [L_\odot])$	α
$\text{PG}(M_B < -21)$	-7.88 ± 0.29	11.45 ± 0.17	-1.18 ± 0.24
$\text{PG}(M_B < -23)$	-8.37 ± 0.35	11.49 ± 0.42	-0.28 ± 1.49

Note. — The formula of luminosity function is a Schechter function:
 $\Phi(L)dL = \Phi^* \left(\frac{L}{L^*}\right)^\alpha \exp\left(-\frac{L}{L^*}\right) \frac{dL}{L^*}.$

The total probability in this luminosity range is equal to 1. Using the observed uncertainties or upper limits, we predict the detection fraction of the aromatic feature for PG quasars at $M_B < -23$ of $17 \pm 5\%$, smaller than the observed fraction of 28%. This result supports our conclusion that the SFIR luminosity increases with increasing AGN luminosity.

5.6.2.3 Comparison Between Different Subsamples

As shown in Fig. 5.11, the behavior of star formation is different around AGN selected by different techniques. Since the SFIR LF of AGN host galaxies is a function of AGN luminosity as found in the last section, the effect of the nuclear brightness needs to be removed. The 2MASS K -band photometry for all PG objects was obtained from the 2MASS Point Source Catalog. We calculated $B - K$ for all PG objects and found that $\langle B - K \rangle = 3.0 \pm 0.6$ and is not a function of absolute K -band magnitude. All PG objects with $M_B < -22.5$ are selected to form a comparison sample for the 2MASS objects with $M_K < -25.5$. For the 3CR subsample, it is difficult to select a PG sample with the same level of nuclear activity. This is because PG objects are selected by thermal emission while 3CR objects are selected because of their non-thermal emission and there is no good correlation between the radio emission and the thermal mid-IR emission (Ogle et al., 2006). Instead, we compare the whole PG subsample at $M_B < -21$ to the whole 3CR subsample at $L_{151\text{MHz}} > 2 \times 10^{24} \text{ W Hz}^{-1} \text{ Sr}^{-1}$.

Fig. 5.13 shows the cumulative fractional luminosity function $F(>L) = \sum_{L=L_0}^{\infty} f(L)$ for PG versus 2MASS and PG versus 3CR. To avoid biases due to evolution, the comparison includes objects with $z < 0.5$. The fractional luminosity function $f(L)$ is defined similarly to the fractional bivariate LF (See Elvis et al., 1978; Golombek et al., 1988). As shown in Fig. 5.13, there is an apparent sequence in terms of the level of SFR that progresses from 3CR to PG to 2MASS objects that generally show the highest SFRs. The median star-forming IR luminosities of 3CR, PG and 2MASS objects are 6×10^9 , 3.0×10^{10} and $1 \times 10^{11} L_{\odot}$, respectively. Different AGN selection techniques appear to identify objects with different levels of star forming activity in their host galaxies.

5.6.3 Implications for Nuclear Activity

The flatter SFIR LF of AGN host galaxies indicates enhanced star-forming activity relative to local field galaxies. Previous studies illustrate the presence of significant post-starburst stellar populations in quasar host galaxies. For example, the optical and near-IR broadband SEDs of AGN indicate the presence of young stellar populations with an age of about a Gyr in the host galaxies, independent of morphological type (Jahnke et al., 2004), consistent with previous studies (Kotilainen & Ward, 1994; Schade et al., 2000; Ronnback et al., 1996). In addition, Kauffmann et al. (2003) found a trend of younger mean stellar population for higher-luminosity AGN based on a very large sample. None of these studies found evidence for intense ongoing massive star formation, except for a few objects (see Jahnke et al., 2004). We emphasize that the techniques employed in the above studies are unable to detect OB stars or suffer from strong degeneracy between the current star-formation and the star-formation history. Therefore, these studies do not contradict our result. Searches for massive star formation through UV spectroscopy or spatially-resolved observations for star-formation tracers (such as recombination lines and IR emission) indicate the presence of massive star formation in Seyfert galaxies (Maiolino et al., 1995; Heckman et al., 1997) and in quasars (Cresci et al., 2004). All of these studies focus on the central region of the galaxy, implying that the star formation in

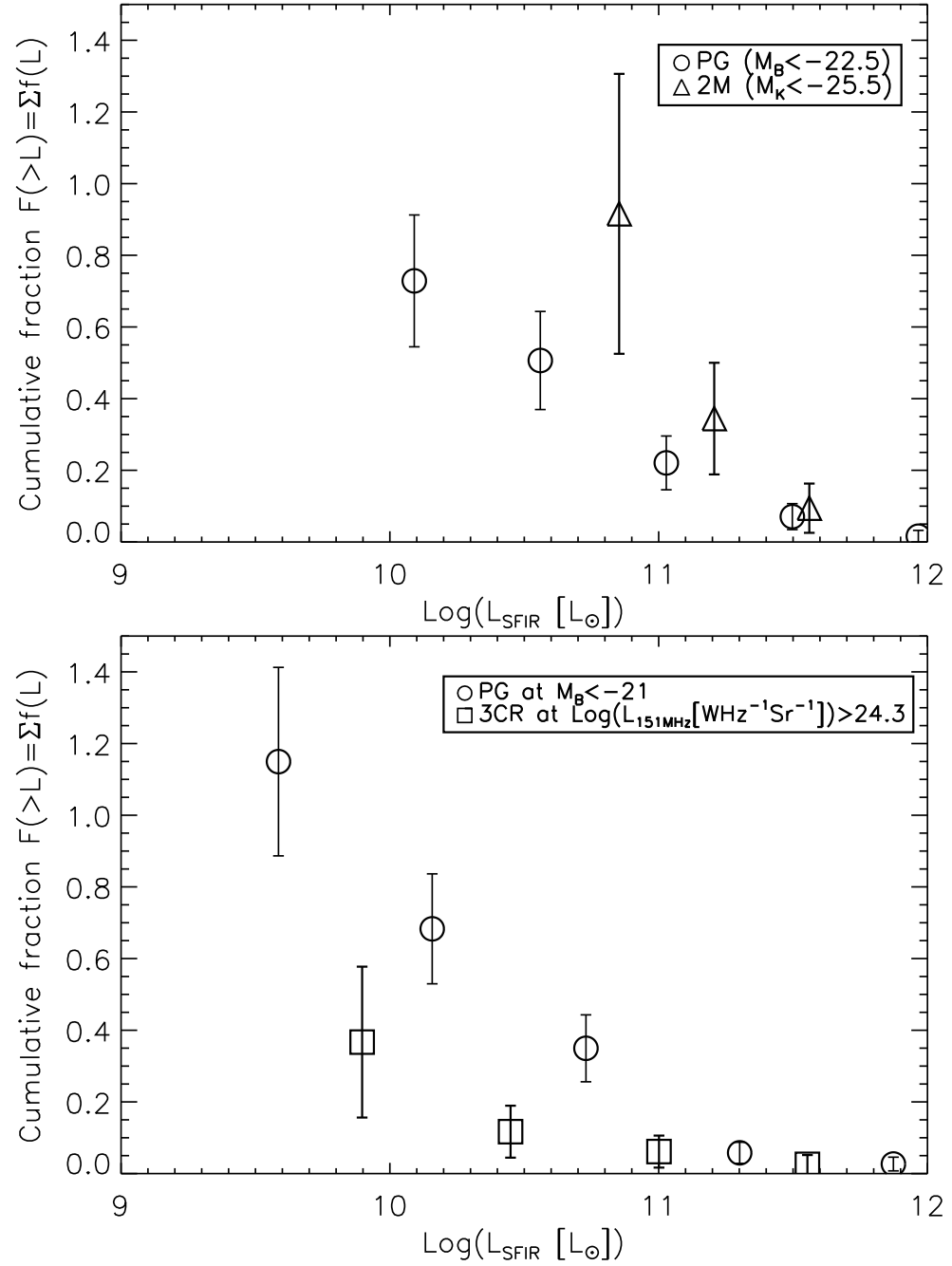


Figure 5.13 Cumulative fraction luminosity functions $F(>L) = \sum_{L=L_0}^{\infty} f(L)$ for the PG objects versus 2MASS objects (upper plot) and the PG objects versus 3CR objects (lower plot), where $f(L)$ is the fractional luminosity function (See text).

quasars is circumnuclear. This is consistent with the lack of spectroscopic evidence for on-going star formation at distances from the nuclei of ~ 15 kpc (Nolan et al., 2001).

The flatter SFIR LF of AGN host galaxies relative to field galaxies also implies that nuclear activity tends to be triggered in galaxies with enhanced star formation. Based on Fig. 5.11, we can calculate the probability of triggering a PG quasar in field galaxies at a given SFR; for example, the probability of triggering nuclear activity at $L_{SFIR}=1.25\times 10^{12} L_{\odot}$ is a factor of 50 higher than that at $L_{SFIR}=1\times 10^{10} L_{\odot}$. This indicates an environment with intense star formation offers preferential conditions for nuclear activity, such as the abundant inflowing material driven by star formation (Granato et al., 2004). On the other hand, it implies that over much of the life of an AGN, its feedback does not quench the star formation, but instead may enhance the host galaxy star formation as demonstrated in some numerical simulations (Silk, 2005). Our result that more luminous AGNs are more likely to reside in host galaxies with more intense star formation provides further evidence that feedback from the two physical processes (star formation and nuclear activity) can enhance both processes. Numerical simulations have predicted the evolution of the SFR and SMBH accretion rate along the merging process (Granato et al., 2004; Springel et al., 2005). They conclude that the evolution of star formation almost follows the SMBH accretion rate, although the former starts to decline a little earlier. A more quantitative and careful comparison between the simulations and our observations will improve our understanding of when and how feedback plays a role in galaxy evolution and SMBH growth.

Although PG, 2MASS and 3CR AGN have flatter SFIR LFs compared to field galaxies, they show differences in the distribution of SFRs, as indicated by the cumulative fractional LFs in Fig. 5.13. Fig. 5.8 shows that the SFR of AGN host galaxies correlates with the amount of molecular gas in the host galaxy, which suggests that different AGN selection methods prefer host galaxies with different levels of gas reservoir. It is interesting that PG and 2MASS quasars have different levels of SFR. Both samples are selected through thermal emission. There is no obscuration along

the line of sight for PG objects while the red IR-optical color of 2MASS objects is attributed to the obscuration of nuclear radiation by dust in the circumnuclear regions or host galaxies (e.g. Smith et al., 2002; Marble et al., 2003). According to the AGN unification model (Antonucci, 1993), 2MASS objects are reddened counterparts of PG objects. The different levels of star formation in 2MASS and PG objects suggest that star formation affects our view of the AGN phenomenon, which is not expected under the unification model. This is not a selection effect that 2MASS objects need to have a larger SFR to have comparable the K -band luminosity to PG quasars, as K -band fluxes in 2MASS objects are dominated by hot dust or starlight, not by star formation. A similar correlation has been observed in Seyfert galaxies, that Seyfert 2 objects have larger star formation rates than Seyfert 1s (e.g. Edelson et al., 1987; Maiolino et al., 1995). Observations and numerical simulations show that the feedback produced by nuclear star formation can heat the circumnuclear material and thus increase its scale height (Maiolino et al., 1999; Ohsuga & Umemura, 1999; Wada & Norman, 2002; Watabe & Umemura, 2005). Such behavior could produce the link between star formation activity and AGN properties.

5.7 CONCLUSIONS

We present *Spitzer* IRS observations of three AGN samples including PG quasars, 2MASS quasars and 3CR radio-loud AGNs. The PG sample includes all PG quasars at $z < 0.5$ while one third of the 2MASS and 3CR parent samples are used in this study. The main results are the following:

1. The aromatic features at 7.7 and 11.3 μm are detected against the strong mid-IR continuum of the AGN. The excitation mechanism for the aromatic features is predominantly star formation.
2. The contribution of star formation to the far-IR emission of individual AGN is diverse; the average contribution is around 25% at 70 and 160 μm . For the PG objects, this contribution shows anti-correlations with the mid-IR luminosity and the ratio of the mid-IR continuum and the Eddington luminosity.

3. The star-forming IR luminosity functions of AGNs are flatter than that of field galaxies, implying the feedback from star formation and nuclear activity can enhance both processes.

4. The star-forming IR luminosity function of AGNs is correlated with the level of nuclear activity over the whole range from normal galaxies to bright quasars, with higher star formation rates for more intense nuclear activity. The 2MASS, PG and 3CR AGNs have distributions of star formation that follow the progression (from high to low SFR) of 2MASS-PG-3CR, implying that various AGN survey techniques select host galaxies with different levels of star forming activity.

CHAPTER 6

Morphology of *Spitzer* 24 μ m-Detected Galaxies in the UDF: the Links between the Star Formation and Galaxy Morphology

6.1 Introduction

In this Chapter, we measure the concentration and asymmetry indices from the *HST* images to quantify the morphologies of a sample of high-redshift LIRGs in the UDF, of a comparison sample of MIPS-non-detected galaxies in the UDF, and of a local sample of LIRGs. These comparisons enable us to gain new insight into the following questions: How do the intensely star-forming galaxies at $z \sim 1$ relate to other galaxies at the same epoch? How are star formation and galaxy morphologies coupled to drive galaxy evolution?

In Chapter 6.2, we summarize the observations, data reduction, and band merging. In Chapter 6.3, we describe the selection of the samples and the measurement of the structural parameters. In Chapter 6.4, we present the morphological characteristics of the galaxies. In Chapter 6.5, we discuss the implications for high-redshift galaxy evolution based on the results from the preceding section. In Chapter 6.6, we present our conclusions. We use AB magnitudes throughout this chapter, where $m_{AB} = 23.9 - 2.5 \log(f_\nu / 1 \mu\text{Jy})$. We denote magnitudes from the *HST* ACS passbands F435W, F606W, F775W, and F850LP as B_{435} , V_{606} , i_{775} , and z_{850} , respectively.

6.2 The Data

6.2.1 *Spitzer* Data

Our 24 μ m MIPS (Rieke et al., 2004) observations of the UDF are part of a scan map covering a larger area centered on the Chandra Deep Field South (CDFS; Gi-

acconi et al., 2002). The images were processed with the MIPS instrument team Data Analysis Tool (DAT; Gordon et al., 2005). Descriptions of 24 μm source detection and photometry are given by Papovich et al. (2004). Table 6.1 lists the sources detected at 24 μm with unambiguous optical counterparts that are the primary subject of this paper. The CDFS was also observed under GTO time with the Infrared Array Camera (IRAC) (Fazio et al., 2004) at 3.6, 4.5, 5.8 and 8.0 μm . Source detection and photometry were done with SExtractor (Bertin & Arnouts, 1996) following similar procedures as in Huang et al. (2004).

6.2.2 *HST* Data

The UDF is a public *HST* survey to image a single Advanced Camera for Surveys (ACS) wide field camera (WFC) field (11.5 arcmin²) in 4 broad-band filters (F435W; F606W; F775W; F850LP) (Beckwith et al., 2005). The WFC has a resolution of $\sim 0.12''$, corresponding to 540 pc at $z=0.3$ and 1 kpc at $z=1.0$. For our analysis we use the reduced UDF data v1.0 made public by the Space Telescope Science Institute (STScI) on 09 March 2004. The z -band-based catalog is used for optical identification of MIPS sources. A total of 7016 objects detected at z -band gives a source density of 0.169 arcsec⁻². The 10- σ limiting magnitudes at B -band, V -band, i -band and z -band are 28.7, 29.0, 29.0 and 28.4, respectively, in an aperture of 0.2 arcsec², corresponding to 10- σ surface brightness of 27.82, 28.12, 28.12 and 27.52 arcsec⁻², respectively.

We also use Near-Infrared Camera and Multi-Object Spectrometer (NICMOS) UDF Treasury Observations for the photometry data for our photo- z code. NICMOS UDF Observations use camera 3 with a resolution of 0.2''/pixel (1.6 kpc at $z=1$). Due to the small field of NICMOS camera, the NICMOS UDF only covers a subsection (5.76 arcmin²) of the optical UDF. The data reduction and photometry are given by Thompson et al. (2005). The catalog contains 1293 objects, giving a source density of 0.0624 arcsec⁻². The 5- σ limiting AB magnitude is 27.7 at 1.1 and 1.6 μm in a 0.6'' diameter aperture, corresponding to a surface brightness of 27.01 arcsec⁻².

Table 6.1. LIRGs in the UDF with unambiguous optical counterpart

MIPS	RA	DEC	ACS	Sep(")	redshift	f_{24} (mJy)	m_z	A	C	Type	X-ray	z Source
(1)	(2)	(3)	(4)	(5)	(6)	(7)	(8)	(9)	(10)	(11)	(12)	(13)
4641	03 32 35.963	-27 48 50.33	566.	0.16	1.31	0.06±0.012	21.56	0.21	3.54	IM	1.31;XID-100	Spec
4644	03 32 37.512	-27 48 38.67	706.	0.41	0.67	0.11±0.013	20.87	0.47	2.51	L/IA		Spec
4645	03 32 37.172	-27 48 33.74	944.	0.21	0.85	0.17±0.015	23.57	0.49	3.19	L/IA		Spec
4649	03 32 41.078	-27 48 53.07	391.	0.09	0.68	0.14±0.012	20.21	0.31	3.41	L		Spec
5088	03 32 35.564	-27 46 27.35	5628.	1.32	1.08	0.20±0.018	21.12	0.49	2.46	L/IA		36689;21.7
5092	03 32 34.863	-27 46 41.52	6139.	1.08	1.10	0.17±0.016	22.73	0.41	2.91	L/IA		Spec
5096	03 32 38.491	-27 47 2.39	4286.	0.09	0.92/0.97	0.07±0.011	21.19	0.27	3.80	IM		This work/35195,23.0
5104	03 32 39.865	-27 47 15.04	3739.	0.25	1.10	0.16±0.013	21.47	0.27	2.35	L		Spec
5106	03 32 36.931	-27 47 26.74	3285.	0.57	1.34/0.98	0.14±0.012	23.24	0.41	4.15	E/IA		This work/34336,23.68
5114	03 32 38.767	-27 47 32.24	3062.	0.16	0.46	0.76±0.027	20.88	0.27	3.06	L	0.46;XID-567	Spec
5115	03 32 37.618	-27 47 43.43	2505.	0.74	1.17/1.06	0.09±0.012	22.11	0.29	3.36	L		This work/33813,22.85
5117	03 32 39.075	-27 46 1.84	6645.	0.12	1.22	0.26±0.016	20.97	0.07	2.90	L	1.22;XID-28	Spec
5121	03 32 40.777	-27 46 16.01	5300.	0.32	0.55	0.14±0.013	20.15	0.27	2.44	L		This work
5628	03 32 43.227	-27 47 56.48	1802.	0.54	0.67	0.16±0.015	20.68	0.20	3.14	L		Spec
5630	03 32 42.275	-27 47 45.99	2344.	0.16	1.00	0.22±0.015	21.25	0.42	1.79	L/IA		Spec
5768	03 32 31.419	-27 47 25.04	3246.	0.82	0.67	0.12±0.010	21.02	0.46	2.72	L/IA		Spec
5828	03 32 39.217	-27 45 32.16	6930.	0.63	1.04	0.16±0.013	21.84	0.47	3.09	L/IA		Spec
13901	03 32 44.198	-27 47 32.70	2874.	0.86	0.74	0.24±0.020	21.42	0.31	3.24	L		Spec
15236	03 32 36.533	-27 46 30.66	5761.	1.69	0.71	0.28±0.015	21.21	0.58	2.54	L/IA	0.77;XID-511	36462;21.4
15942	03 32 44.851	-27 47 27.62	2686.	0.15	0.44	0.77±0.044	18.42	0.25	3.11	L		Spec
15943	03 32 45.103	-27 47 24.24	3382.	0.24	0.44	0.51±0.042	20.41	0.38	2.99	L/IA	0.44;XID-646	Spec

Note. — Column (1): The MIPS ID of the LIRGs in the UDF. Column(2): RA of MIPS source. Column(3): DEC of MIPS source. Column(4): ACS ID of optical counterpart of MIPS source. Column(5): The separation in arcsec between ACS source and MIPS source. Column(6): The redshift. Column(7): 24 μ m flux. Column(8): z -band magnitude. Column(9): Asymmetry. Column(10): Concentration. Column(11): The galaxy type of MIPS source based on CA system. 'IM': Intermediate-type. 'L': Late-type. 'IA': Interacting. 'E': Early-type. Column 12: The photometric redshift and the catalog number of X-ray counterparts of MIPS sources based on the CDFS 1 MS catalog by W. Zheng et al. (2004). Column 13: Where redshifts are from COMBO-17, the corresponding catalog number along with the magnitude at R band is listed; 'This work' indicates that the redshift is computed based on our photo- z code (Pérez-González et al., 2005). 'Spec' means the spectroscopic redshift from Vanzella et al. (2005) and Le Fèvre et al. (2004).

6.2.3 Results and Band Merging

We identified 52 sources with $24\ \mu\text{m}$ flux density greater than 0.06 mJy (at which level the completeness is $\sim 50\%$ in the UDF (Papovich et al., 2004)). We searched for ACS counterparts on the z -band image of the UDF within a $2.5''$ -radius circular region surrounding each $24\mu\text{m}$ source. The choice of this search radius is motivated by the large FWHM of the MIPS $24\ \mu\text{m}$ PSF ($\sim 6''$) and the positional accuracy at $24\ \mu\text{m}$ ($\sim 0.5''$ rms). $2.5''$ (10 kpc at $z=0.3$ and 20 kpc at $z=1.0$) is large enough to account for the possible physical shift between the locations of infrared emission and the optical emission observed in local interacting galaxies (e.g. Le Floch et al., 2002).

Multiple optical sources are present in the search circle for 41 of 52 MIPS sources. The IRAC images were used to identify the most probable optical counterpart for these 41 MIPS sources. In the UDF, there are a total of 312 objects in the IRAC $4.5\ \mu\text{m}$ catalog with flux density greater than $1.6\ \mu\text{Jy}$ at 50% completeness. 23 of the 41 MIPS sources have such an IRAC counterpart within a $1.0''$ radius. The probability of random spatial superposition of IRAC sources in a $1.0''$ -radius circular region is 2.3 %, which indicates a high probability that the IRAC counterparts are physically related to the MIPS sources. We also visually inspected the IRAC image of each source to check if there is nearby IRAC source which might contaminate the $24\ \mu\text{m}$ emission. MIPS-15950, which is contaminated in this way, is excluded. The search radius to match optical counterparts for IRAC sources is $1.5''$, motivated by similar reasons to those for the MIPS sources. 15 of 22 IRAC sources have only one optical source within the search radius, which should be the optical counterpart of the corresponding MIPS source. For the remaining 25 MIPS sources with possible multiple optical counterparts, if an optical object is brighter than other optical objects within the same search circle by 4 magnitudes, this optical object was taken to be the optical counterpart of the MIPS source. This association is justified because IR-luminous galaxies tend to be associated with optically bright galaxies (Mann et al., 1997). On the other hand, the probability of random spatial superposition is

an order of magnitude larger for 4-magnitude fainter objects. Based on the above series of steps for deconfusion of multiple objects in the $24\ \mu\text{m}$ beam, 16 of 52 MIPS sources may still have multiple optical counterparts. We do not use these 16 sources in our analysis to avoid their affecting the distribution of the morphologies of the MIPS-detected sources. Our final sample therefore consists of 35 MIPS-detected galaxies that have unambiguous identifications with ACS images.

An alternative method for evaluating interactions, "pairs statistics", would be strongly affected by the handling of sources with multiple possible counterparts. However, the CA analysis employed here measures the structure of the central image and hence to first order is independent of such effects. As a test, we recomputed the classification parameters including the objects with multiple identifications and using the brightest object as the optical counterpart. We found that the basic results were unchanged; the mean asymmetry of the MIPS-detected objects got slightly smaller but by only 0.03.

Eighteen of our sample of 35 MIPS sources have spectroscopic redshifts based on the VLT/FORS2 spectroscopy catalog (Vanzella et al., 2005) and VIMOS VLT Deep Survey (VVDS) v1.0 catalog (Le Fèvre et al., 2004). For the remaining 17 sources, we use photometric redshifts. The publicly available COMBO-17 survey of the CDFS provides photometric redshifts by means of 17-band photometry (Wolf et al., 2004). The typical photometric redshift accuracy is $\delta z/(1+z) < 0.02$ for galaxies with $m_R < 22$ and reaches 0.1 at $m_R \sim 24$, allowing the rest-frame absolute magnitude to be accurate within 0.1 for $m_R < 22$ and 0.5 mag for $m_R \sim 24$. We searched for COMBO-17 counterparts for each ACS source within a radius of 0.45 arcsec. Given a total of 63,501 COMBO-17 objects in a field of view $31.5' \times 30'$, the probability of random spatial superposition in a $0.45''$ -radius circular region is only 1.1%. We visually inspected the ACS image of each source to assure we matched the right COMBO-17 counterpart. Seven MIPS sources have X-ray emission based on the X-ray 1 MS catalog (Giacconi et al., 2002) and photometric redshifts given by W. Zheng et al. (2004). For the ACS counterpart of any MIPS source without redshifts from these sources, we used our own photo-z code (see Pérez-González et

al., 2005) based on ACS, NICMOS and IRAC observations. We also used our code to compute the redshift for any ACS source with a COMBO-17 counterpart with $m_R > 22$. The main advantage of this photo- z code is it uses photometry over a longer wavelength baseline (including the $1.6 \mu\text{m}$ bump) to obtain redshifts for galaxies up to $z \sim 3$, with accuracy of $\delta z / (1 + z) < 0.1$. We inspected the fitting individually to assure our code gave a robust measurement of redshifts. Except for MIPS-5106, sources with multiple redshifts have consistent measurements of redshift. For this source, we use our redshift measurement since the $1.6 \mu\text{m}$ stellar bump is obviously detected at the IRAC bands in the SED.

The K-corrections for the optical four-band data are computed using codes based on the template spectra of galaxies in the Sloan Digital Sky Survey (SDSS; Blanton et al., 2003).

We used the ACS image that is closest to rest-frame B band to compute the structural parameters for the galaxies. Therefore the maximum redshift in our study is 1.4, beyond which the observed z -band is shorter than the rest-frame B -band. The advantages of classification using rest-frame optical bands and the importance of morphological K-corrections are discussed further in Windhorst et al. (2002) and Papovich et al. (2003).

To obtain accurate total far-infrared luminosities, it is necessary to have photometry over the whole range of infrared wavelengths. In this study, however it is enough to have a coarse estimate of the total infrared luminosity. We used the template spectra of starburst galaxies (with the current SFR much larger than the past-averaged SFR) published by Lagache et al. (2004) to get the 8-1000 μm total infrared luminosity from the observed 24 μm flux density. Due to the high sensitivity of MIPS, some MIPS-detected galaxies at low redshift are normal galaxies, not starbursts. For them, we used the appropriate template for galaxies with total IR emission fainter than $10^{10} L_{\odot}$ (where the threshold is computed from the starburst template). The average conversion factor from $\nu L_{\nu}(24 \mu\text{m})$ to total infrared luminosity is 20 with a dispersion of up to 0.2 dex, indicating that our conversion should be accurate typically within a factor 2 or 3 (Papovich & Bell, 2002; Le Floc'h et al.,

2005), which is enough for the analysis in this paper.

6.3 Methodology

6.3.1 Sample Definition

We only computed the structural parameters for 34 of the 35 MIPS sources that have signal-to-noise (S/N) ratios better than 100 and half light radius $r_{50} > 5$ pixels at z band. High signal-to-noise ratio (SNR) and large size are required for robust measures of the asymmetry parameters (Conselice et al., 2000; Bershadsky et al., 2000). The deep exposure in the UDF thus allowed us to compute reliably structural parameters for a high fraction (97%) of MIPS-detected galaxies.

The members of our control sample are defined to be undetected at $24\ \mu\text{m}$ and (1) to lie $5''$ away from all MIPS sources; (2) to have half light radius $r_{50} > 5$ pixels at z band; (3) to have SNR better than 100 at z band; and (4) to have a COMBO-17 photometric redshift smaller than 1.4. The last condition is necessary for K-corrections and requires $m_z < 25$ (Wolf et al., 2004). The final sample is composed of 252 normal galaxies, representing 80% of the galaxies undetected at $24\mu\text{m}$ meeting only the first three requirements.

Our main goal is to investigate the morphologies of high-redshift LIRGs. We identified a galaxy with $L_{IR} > 10^{11}L_{\odot}$ as a LIRG; the final sample of LIRGs has 21 sources. The deep exposure of the UDF allows us to detect their optical counterparts down to low surface brightness, removing potential biases from less-deep classification imagery. The $10\text{-}\sigma$ surface brightness at z -band is $27.52\ \text{arcsec}^{-2}$, which corresponds to a rest-frame B-band surface brightness of 24.5 for a fiducial galaxy at $z=1$. This corresponds well to the typical surface brightness level reached in morphological studies of local galaxies (although at lower physical resolution). It is also close to the central surface brightness of a local low-surface-brightness (LSB) galaxy. In addition, the LIRG sample is sufficiently large for reliable statistics, as can be seen from the results in Table 6.2.

We also created a sample of 5 MIPS-detected but lower luminosity non-LIRGs

and a control sample of 137 MIPS-non-detected galaxies. The sample of MIPS-detected non-LIRGs is composed of galaxies with $L_{IR} < 10^{11} L_{\odot}$ and $M_B < -18.5$. The sample of MIPS-non-detected galaxies is derived from the sample of 252 normal galaxies with the additional constraints that $M_B < -18.5$ and that the redshift be greater than the minimum redshift of the LIRGs. The cut-off magnitude $M_B = -18.5$ is approximately the rest-frame B magnitude of the faintest LIRG.

Figure 6.1 shows the redshift distributions of the three samples and the infrared luminosity at $24 \mu\text{m}$ flux density of 0.06 mJy as a function of redshift. Galaxies of all three samples mainly fall at $z > 0.3$. The sample of LIRGs and MIPS-non-detected galaxies have almost the same redshift distributions while non-LIRGs mainly fall at lower redshift due to the detection limits. In the following analysis, we mainly discuss the morphologies of the LIRGs and comparisons to the MIPS-non-detected galaxies, since the MIPS-detected non-LIRGs have a different redshift range and are few in number.

6.3.2 Quantitative Morphology Classification: Concentration and Asymmetry

Before measuring the concentration and asymmetry value for each galaxy, some image processing was required. We identified and masked contaminating sources in the region of the galaxy using z -band segmentation maps provided with the UDF data release. We replaced the mask region with noise to compute the morphology parameters.

We measured the concentration index using the methodology described in Bershadsky et al. (2000). To study the morphologies in a fixed-size aperture at the physical scale of each galaxy, the dimensionless parameter η as defined by $\eta(r) = I(r) / \langle I(r) \rangle$ (Petrosian, 1976) is used to define the total size of the galaxy, where $I(r)$ is the surface brightness at radius r and $\langle I(r) \rangle$ is the mean surface brightness within radius r . The apparent total magnitudes are then integrated over an aperture equivalent to the total size of the galaxy defined as twice the radius $r(\eta = 0.2)$. Based on the measured curve of growth, the concentration

Table 6.2. The statistics of morphologies of $M_B < -18.5$ galaxies in the UDF and local LIRGs

	0.3<z<0.9			0.9<z<1.4		
	LIRGs	non-LIRGs	Non-detected sample	LIRGs	Non-detected sample	Local LIRGs
Total number	10	5	49	8	88	49
Late-type	90.00±30.00%	80.00±40.00%	77.55±12.58%	75.00±30.62%	80.68± 9.58%	89.80±13.54%
Merging (A>0.35)	40.00±20.00%	20.00±20.00%	16.33± 5.77%	62.50±27.95%	10.23± 3.41%	30.61± 7.90%
Symmetric (A<0.2)	10.00±10.00%	60.00±34.64%	46.94± 9.79%	12.50±12.50%	64.77± 8.58%	42.86± 9.35%
A ¹	0.34±0.03	0.22±0.05	0.22±0.02	0.38±0.03	0.18±0.02	0.26±0.03
C ¹	2.98±0.10	3.09±0.11	2.98±0.08	2.99±0.28	2.88±0.05	2.74±0.08

Note. — ¹Averages with standard errors of the mean. At the 0.3<z<0.9, both LIRG and MIPS-non-detected samples are complete. At the 0.9<z<1.4, both sample are incomplete.

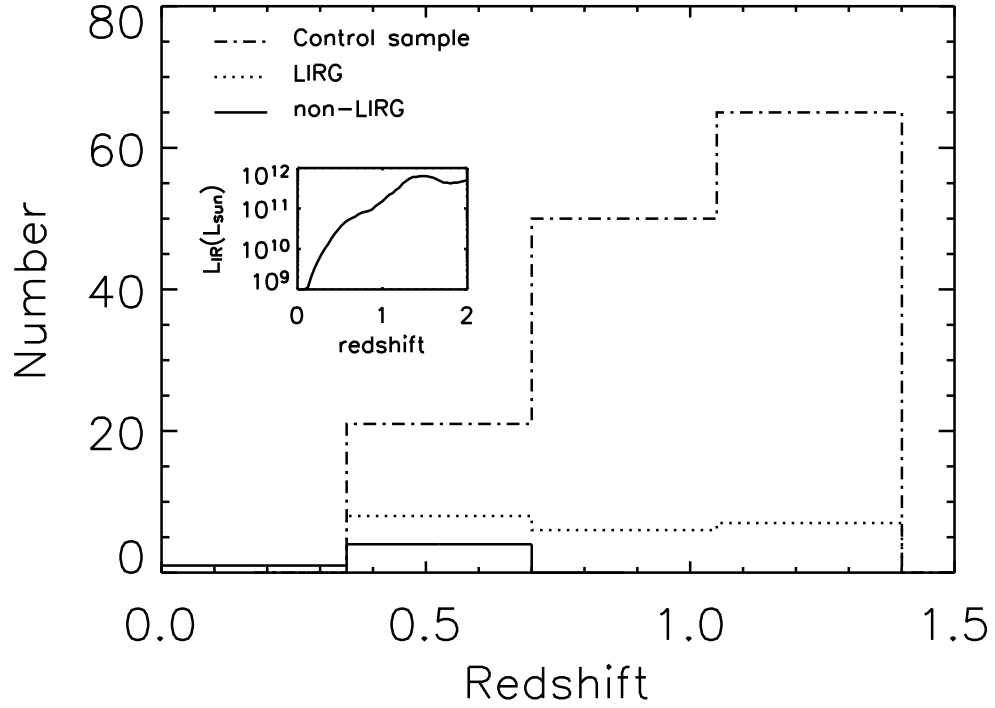


Figure 6.1 The redshift distributions of LIRG ($L_{IR}(8-1000\mu\text{m}) > 10^{11}L_{\odot}$), non-LIRG ($L_{IR}(8-1000\mu\text{m}) < 10^{11}L_{\odot}$) and MIPS-non-detected control samples. The dot-dashed histogram indicates the control sample, the dotted histogram indicates the LIRGs and the solid histogram indicates the non-LIRGs. The control and LIRG samples have almost the same redshift distributions, while non-LIRGs are mainly at low redshift due to the detection limit. The inserted plot shows the IR luminosity at the $24\mu\text{m}$ detection limit (0.06 mJy) as a function of the redshift.

index is defined by

$$C = 5 \log \frac{r_{80}}{r_{20}}, \quad (6.1)$$

where r_{80} and r_{20} are the radii that enclose 80% and 20% of the total light (Kent, 1985), respectively.

The full description of the algorithm to compute the asymmetry index is in Conselice et al. (2000). The asymmetry parameter is defined as:

$$A = \min\left(\frac{\sum |I_0 - I_{180}|}{\sum |I_0|}\right) - \min\left(\frac{\sum |B_0 - B_{180}|}{\sum |I_0|}\right), \quad (6.2)$$

where the sums are over the total size of the galaxy as defined above. In the above equation, the first term represents the asymmetry of the galaxy and the second one corrects the effect of noise on the asymmetry measurement, where I_0 and I_{180} are the intensity of each pixel of the image and of the image rotated by 180° , respectively, and B_0 and B_{180} are the intensity of each pixel of the background region and its 180° -rotated counterpart, respectively. We extracted a 100×100 pixel background region without any contamination and scaled the asymmetry of this region by the relative size of the galaxy to this background region area. The asymmetry minimum was obtained by searching the minimum of asymmetries at rotation centers around the initial galaxy center. See Conselice et al. (2000) for the detailed computation algorithm to locate the rotation center producing the asymmetry minimum.

The uncertainty in the concentration measurement is mainly due to the spatial resolution. Bershadsky et al. (2000) show that the uncertainty of this parameter is around 0.2 for $r_{50} > 5$ pixel. For asymmetry measurements, the noise of the image is the main effect. Conselice et al. (2000) show that asymmetry measurements have errors around 0.02 for $S/N > 500$ and around 0.05 for $100 < S/N < 300$. We tested our programs by computing the concentration and asymmetry parameters of 20 galaxies in Conselice (2003) with asymmetry spanning from 0.01 to 0.4 and concentration from 2.5 to 4.5. The average differences in concentration and asymmetry parameters are 0.2 and 0.02, respectively. For galaxies with SNR better than 100 in our sample, we estimate the typical errors of the concentration and asymmetry indices are around 0.3 and 0.04, respectively, which are adequate for our study.

6.4 RESULTS

6.4.1 Morphologies of a Representative Sample of LIRGs at $0.3 < z < 1.4$

An important aspect of this study is that we can determine morphological properties for a representative sample of high- z LIRGs. In the UDF, 23 of 34 MIPS-detected galaxies at $0.3 < z < 1.4$ with $M_B < -18.5$, $S/N > 100$ and $r_{50} > 5.0$ are LIRGs. Compared with 137 MIPS-non-detected galaxies with the same constraints as above, we find that $\sim 15\%$ of the galaxies with $M_B < -18.5$, $S/N > 100$ and $r_{50} > 5.0$ are LIRGs at $z \sim 1$. This fraction may be underestimated due to the non-detection of LIRGs near $L_{IR} \sim 10^{11} L_\odot$ and also may be overestimated as a result of missing non-LIRGs near $M_B = -18.5$ at high redshift. However, the portion of LIRGs in our sample is similar to those found by others at similar redshift. For example, the fraction of LIRGs at $z > 0.4$ in the Canada France Redshift Survey (CFRS) is about 16% without correction for the non-detection of galaxies near the cut-off limits (Hammer et al., 2005). Another test is to use the infrared and optical luminosity functions. Le Floc'h et al. (2005) recently obtained the infrared luminosity function at $0 < z < 1.2$ based on the MIPS/*Spitzer* 24 μm sources located in the CDFS. Using $L_{IR}^* = 1.9 \times 10^{10} L_\odot$, $\alpha_{IR} = 1.23$ and $\sigma_{IR} = 0.72$ at $1.0 < z < 1.2$, we estimate 70% of the LIRGs at $0.9 < z < 1.4$ are below 0.06 mJy. Using the rest-frame B -band luminosity function of the COMBO-17 survey (Wolf et al., 2003), we estimate 65% of the galaxies with $M_B < -18.5$ are below $m_B = 25$. Correcting the fraction of non-detected galaxies at high redshift, we find that the fraction of LIRGs is almost the same ($\sim 18\%$) as in our study. At $z < 0.9$ where both LIRGs and $M_B < -18.5$ galaxies are detected, we obtain a fraction $\sim 15\%$ of LIRGs for a total of 67 galaxies. We conclude from all these arguments that the fraction of LIRGs for $M_B < -18.5$ is $\sim 15\%$ at $0.3 < z < 1.4$, the same as in our study. This fraction is much larger than that in the local universe, which is 0.5% for galaxies with $L_{\text{tot}} > 10^{10} L_\odot$ (Soifer et al., 1986).

Table 6.1 lists the LIRGs detected in the UDF along with their concentration and asymmetry indices, C and A . MIPS-4641, MIPS-5117 and MIPS-15236 have

X-ray detections (Giacconi et al., 2002) and are classified as type 1 AGN by W. Zheng et al. (2004). These three sources are excluded in our study of morphologies. The other two MIPS sources detected in the X-ray are classified as galaxies by W. Zheng et al. (2004) and are kept in this study.

Table 6.2 lists the statistical results for LIRGs, non-LIRGs and the MIPS-non-detected sample in the intermediate redshift bin $0.3 < z < 0.9$, in the high redshift bin $0.9 < z < 1.4$, and for the local (low redshift) LIRGs. At $0.3 < z < 0.9$, the $24\ \mu\text{m}$ detection limit (0.06 mJy) and the B-band magnitude limit (-18.5) yield complete samples of LIRGs and MIPS-non-detected galaxies, respectively. At $0.9 < z < 1.4$, both the LIRGs and MIPS-non-detected samples are incomplete. We mainly discuss our result based on the complete sample. However, the MIPS-non-detected sample at $0.9 < z < 1.4$ is still dominated by non-LIRGs. Given 9 LIRGs, 88 MIPS-non-detected objects and 70% incompleteness in IR-detection at $0.9 < z < 1.4$, the fraction of LIRGs in 88 MIPS-non-detected objects is $< 25\%$. Therefore, the comparison of morphologies between LIRGs and MIPS-non-detected galaxies at this redshift range is still helpful in our understanding the difference in morphologies between infrared-active galaxies and infrared-inactive galaxies.

Figure 6.2 shows the rest-frame B -band images for LIRGs used for our morphological study. Figure 6.3 plots the galaxies along with our other two high- z samples on the C, A plane. The solid curves show the division of this plane into three regions mainly populated by early-type, intermediate-type and late-type galaxies, based on classifications of local galaxies (c.f. Abraham et al., 1996a,b; Conselice et al., 2000). Figure 6.2 shows that the high-redshift LIRGs are predominantly late-type galaxies (as found previously by Bell et al., 2005a) with asymmetric structures, including long tidal tails and distorted disks. Some of them have very low surface brightness, such as MIPS-5106 with rest-frame B-band surface brightness $\mu_{B0} = 22.4$ within the Petrosian radius.

We define a galaxy with $A > 0.2$ as an asymmetric galaxy in this study. This is motivated by the fact that most ($\sim 90\%$) of local normal galaxies including elliptical galaxies, early-type (Sa-Sb) and late-type spiral galaxies (Sc-Sd), have asymmetry

$A < 0.2$ (Conselice, 2003). As listed in Table 6.2, $90^{+10}_{-30}\%$ of the LIRGs in the UDF are late-type galaxies and $80 \pm 10\%$ of the LIRGs are asymmetric ($A > 0.2$) objects.

The classification of the high- z galaxies using the asymmetry and concentration indices is generally consistent with the conventional visual classifications. Figure 6.2 shows that only two sources, MIPS-5115 and MIPS-13901 are classified visually differently from the results using the structural parameters. In this paper, we make no use of the conventional classifications (other than to place some results in context), basing all of our conclusions on the CA analysis. Thus, the small number of classification discrepancies has no effect on our conclusions.

6.4.2 Comparision of LIRG Morphologies to those of MIPS-non-detected Galaxies

In this Section, we compare the morphologies of LIRGs in the UDF to those of MIPS-non-detected galaxies. Table 6.2 shows that the correlations at high redshift between infrared luminosity and morphology are weak. On average, high- z LIRGs are more asymmetric than the MIPS-non-detected galaxies, characterized by a higher fraction of $A > 0.35$ (merging; Conselice, 2003) galaxies and fewer symmetric objects, defined as $A < 0.2$. However, a number of MIPS-non-detected galaxies show asymmetric structures and/or are currently involved in merging activity. In the following we compare the morphological distributions in terms of the fraction of late-type galaxies and the distribution of asymmetry parameters.

6.4.2.1 Distributions of the Asymmetry and Concentration Parameters

Table 6.2 lists the average asymmetries and the standard deviations of the means. The LIRGs have asymmetry around 0.34, somewhat higher than $A = 0.22$ of the MIPS-non-detected galaxies. The K-S test shows the probabilities that LIRGs and MIPS-non-detected galaxies have the same distribution of asymmetries are 1% and $< 0.1\%$ for the intermediate-redshift and high-redshift bins, respectively. This seems consistent with the suggestion (e.g. Larson & Tinsley, 1978; Sanders & Mirabel, 1996; Barton et al., 2000) that non-symmetric structures, such as tidal distortions,

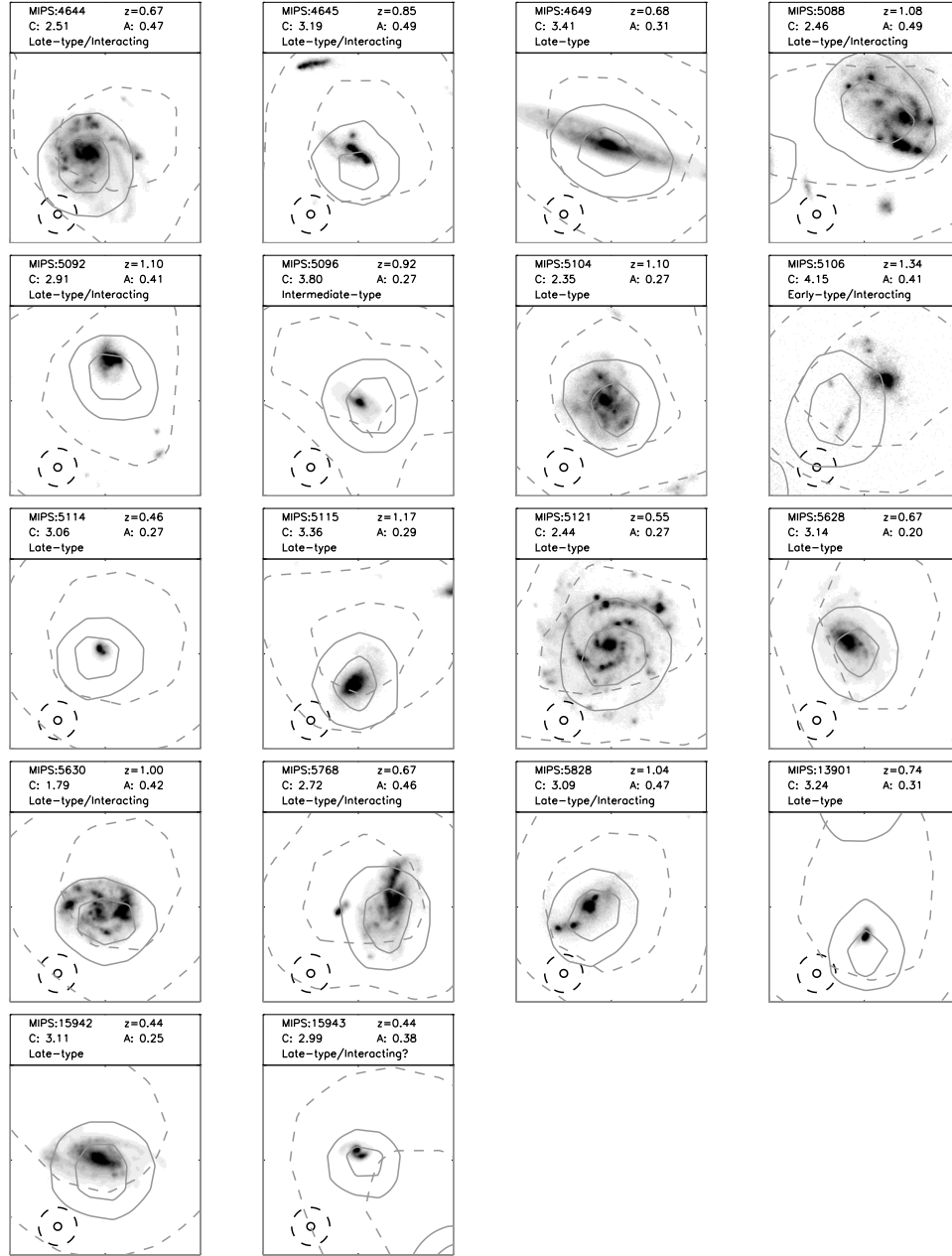


Figure 6.2 The rest-frame B-band images (5×5 arcsec) of non-X-ray LIRGs in the UDF along with the redshifts, structural parameters and the galaxy types based on the *CA* classification scheme. The center of the image is the position of the MIPS source. The light solid and dashed curves show contours at 20% and 50% enclosing flux for IRAC and MIPS, respectively. The heavy solid and dashed circles show the position accuracy for IRAC sources (0.1 arcsec) and MIPS sources (0.5 arcsec).

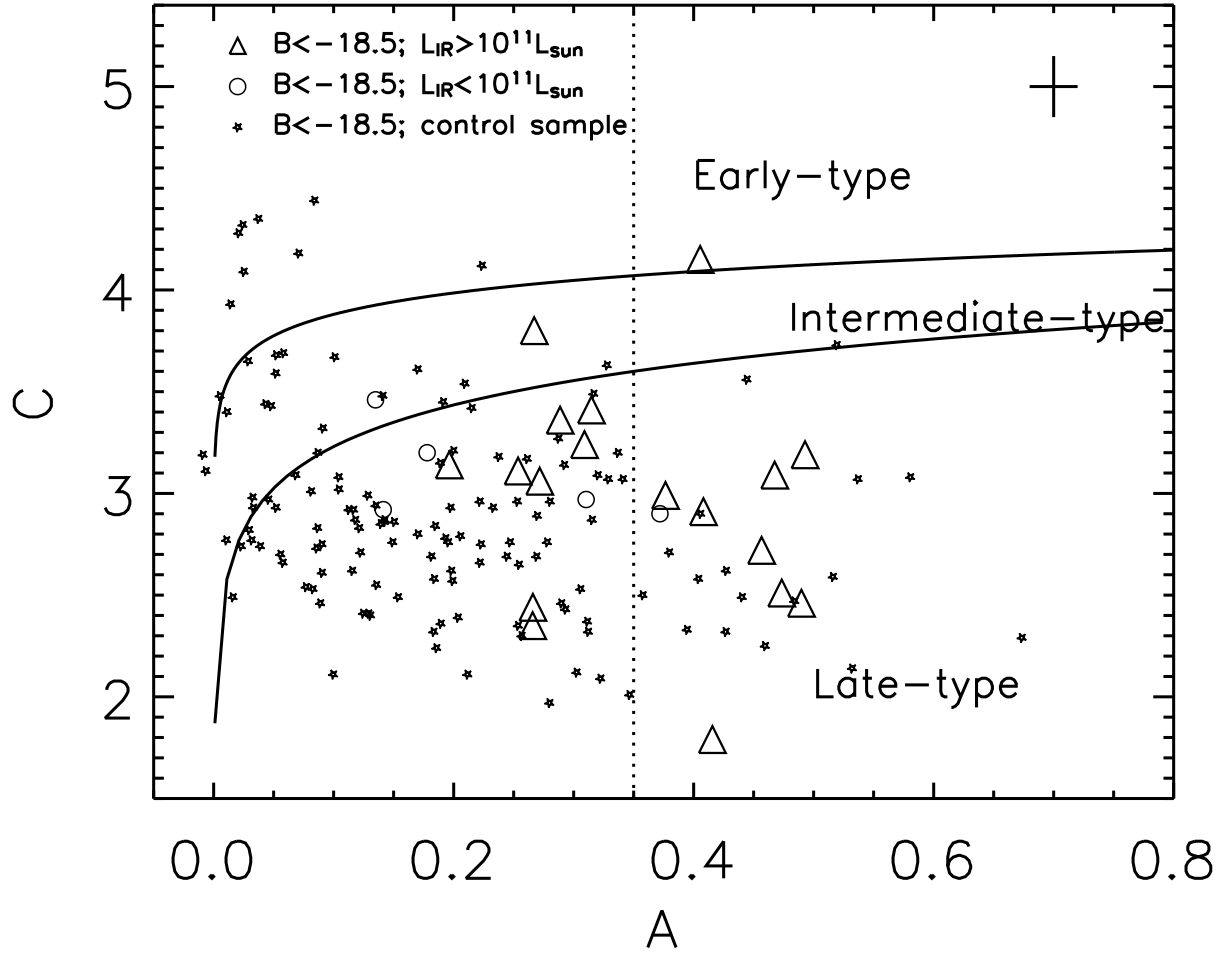


Figure 6.3 The distributions of LIRGs (triangles), non-LIRGs (open circles) and MIPS-non-detected control sample galaxies (stars) in the plane of concentration and asymmetry. The two solid curves divide the plane into three regions populated by early-, intermediate- and late-type galaxies. The dotted line indicates $A = 0.35$, to the right of which galaxies are identified as merging systems. The cross shows typical errors of concentration (0.3) and asymmetry (0.04).

companions, and distorted disks, play an important role in enhancing star formation in galaxies. Figure 6.3 indicates that the MIPS-non-detected galaxies have a wide distribution of morphologies, from classical Hubble types to highly asymmetric, most likely merging systems. The fraction of symmetric ($A < 0.2$) galaxies in this sample is high ($\sim 50\%$). In comparison, the LIRGs virtually lack symmetric objects ($\sim 10\%$).

As listed in Table 6.2, the sample of LIRGs shows a slightly higher fraction of late-type galaxies than the sample of MIPS-non-detected galaxies, although the values are consistent within statistical errors. The classification calibration method in this comparison is based on visually classified local galaxies (Conselice et al., 2000). Alternatively, Cassata et al. (2005) measured the rest-frame B morphology for the K-band selected high-redshift galaxies and used the boundary ($A < 0.2$ and $C > 2.9$) to define the early-type galaxies. Based on their method, we find that the late-type fraction of LIRGs is still a little higher at $0.3 < z < 1.5$, i.e., the $24\mu\text{m}$ -selected sample is biased a little toward late-type galaxies. However, much of this relatively minor difference can be explained by the larger portion of symmetric early- and intermediate-type galaxies in the MIPS-non-detected sample. The differences in morphologies between the late-type galaxies of these two samples are therefore minor.

On the other hand, the galaxies of both samples are more asymmetric than the local Hubble-type galaxies and even slightly more asymmetric than the non-starburst local dwarf irregular galaxies, which have asymmetry of 0.17 ± 0.10 (Conselice, 2003). The K-S test shows that the probability that LIRGs and local irregular galaxies have the same distribution of asymmetry is $< 0.1\%$, while such a probability for MIPS-non-detected galaxies at $0.3 < z < 0.9$ and local irregular galaxies is 27% . Conselice et al. (2000) show that low spatial resolution affects the asymmetry measurement by making the galaxy appear more symmetric. The spatial resolutions are 50 pc/pixel for the local sample of Conselice (2003) and 300 pc/pixel for our galaxies at $z = 0.5$. This reinforces our conclusion that the galaxies in the UDF are more asymmetric than the local galaxies.

Although the two high- z samples show somewhat different levels of asymmetry,

their concentrations are almost the same, characterized by values that are comparable to the local late-type disk-galaxies (Sc-Sd; Conselice, 2003). The K-S test shows that the LIRG sample and the MIPS-non-detected sample have the same distribution of concentration with a probability of 40% and 30% in the intermediate and high redshift bins, respectively. Conselice (2003) argues that the concentration index reveals the past star-formation history of a galaxy because of the correlation of bulge to total light ratios and stellar masses with this index. This behavior implies that the MIPS-non-detected galaxies have similar stellar populations and distributions as the LIRGs except for the LIRGs having a large population of massive young stars due to the presence of a starburst.

6.4.2.2 Merging Galaxies

It is also of interest to determine how many LIRGs are merging. We classify an object as a merger if its asymmetry parameter is greater than 0.35 (Conselice, 2003). The merger as defined here means a major merger, i.e., that the two progenitor galaxies have comparable masses. However, other strong asymmetries may also satisfy this numerical definition. By this definition, the LIRG sample is composed of 40 ± 20 % merging systems, higher than the merging fraction ($\sim 15\%$) of the MIPS-non-detected sample. Although the merging fraction obtained by the asymmetry technique depends on the A value used for merger identification, this conclusion does not change with modest changes in this defining value of A .

Our sample shows 40% of LIRGs at $0.3 < z < 1.4$ are merging systems as identified by the CA method (which emphasizes high levels of morphological disturbance in systems with high surface brightness). This result is probably consistent with but higher than that of Bell et al. (2005a) who found that less than 30% of 1500 star-forming galaxies at redshift $0.65 < z < 0.75$ are strongly interacting based on visual classifications, and that of W. Zheng et al. (2004) who found that 6 ($\sim 17\%$) of 36 distant ($z > 0.4$) LIRGs in the CFRS are obvious ongoing major mergers. W. Zheng et al. (2004) do not count the irregular galaxies (22%), which may have $A > 0.35$, as merging galaxies. Another cause for these differences is that the morphologies

of a merging galaxy at different surface brightness levels show different levels of asymmetry and thus visual identification on a relatively shallow image may misclassify it as a non-merging galaxy.

6.5 Discussion

6.5.1 Continuous Morphological Transformation plus Episodic Starbursts

Our study of morphologies and infrared properties of high-redshift galaxies in the UDF has two basic results. The first one is that LIRGs and MIPS-non-detected galaxies in the UDF are predominantly late-type asymmetric galaxies. The LIRGs are somewhat more asymmetric on average than MIPS-non-detected galaxies and they are characterized by a higher fraction of very asymmetric ($A \geq 0.35$) systems and a lower fraction of symmetric ($A < 0.2$) objects. This result is consistent with the proposal that non-symmetric structures play an important role in enhancing the star formation and hence elevate the infrared luminosities of galaxies. The second result is that there is no one-to-one correlation between the occurrence of high infrared luminosities and disturbed morphologies: highly asymmetric galaxies, including merging systems, do not necessarily have high infrared luminosities.

On average, high- z LIRGs and normal galaxies are both more asymmetric than local irregular types, and their concentration indices are similar to the local late-type disk galaxies. Are the asymmetric normal galaxies and the LIRGs two different populations or are they the same population but in different stages? That is, are the activities of starbursts episodic so that the LIRGs are now in active stages and asymmetric non-LIRGs are similar galaxies that are in quiescent states between-starburst stages?

Based on the statistics at $0.3 < z < 0.9$ listed in table 6.2, 25% of asymmetric galaxies ($A > 0.2$) are LIRGs at $0.3 < z < 0.9$. This fraction is $\sim 10\%$ in the local universe, assuming a merging fraction of 4% (Marzke et al., 1998), a LIRG fraction of 0.5% (Soifer et al., 1986) and an asymmetric galaxy fraction in LIRGs of 74% based on the fraction of close pair and strongly interacting galaxies (Sanders et al., 1988).

One candidate population for asymmetric galaxies without starbursts is interacting galaxies with low metallicity and hence low dust. However, Kobulnicky & Kewley (2004) find that the shift of the luminosity-metallicity relation is smaller than 27% at $z \sim 1.0$ compared to the local trend, based on the nebular emission lines of galaxies ($18.5 < M_B < -21.5$) with $\text{SFR} \sim 0.1\text{--}10 M_\odot \text{yr}^{-1}$. This result is consistent with previous studies (Kobulnicky & Zaritsky, 1999; Carollo & Lilly, 2001). We conclude that both LIRGs and MIPS-non-detected galaxies are not likely to be extremely deficient of dust. Another candidate population for asymmetric non-detected galaxies is interacting galaxies without gas, e.g., interactions between galaxies composed entirely of stars. However, such "dry mergers" appear in general to be uncommon ($\sim 1\%$) (Bell et al., 2005b). Therefore, the similar distributions of concentration index for LIRGs and asymmetric non-MIPS-detected galaxies suggests that these two samples have similar formation histories. The moderately higher asymmetry for the LIRGs could arise from luminous off-nuclear star formation, or from extinction. Thus, the elevated periods of star formation are probably occurring episodically.

In the local universe, starbursts in a given galaxy have a short duration of 0.01 to 0.07 Gyr (Krabbe et al., 1994; Lutz et al., 1996; Alonso-Herrero et al., 2000). Near-IR imaging and spectroscopy in the starburst galaxies M82, IC 342 and NGC 253 indicate several episodes of enhanced star formation (Rieke et al., 1993; Satyapal et al., 1997; Böker et al., 1997; Engelbracht et al., 1998; Förster Schreiber, 2000). The anticorrelation between equivalent width of $\text{H}\alpha$ and galaxy pair spatial separation found by Barton et al. (2000) indicates that the starburst episodes are initiated by a series of close passes. In the early Universe, Lyman Break Galaxies (LBGs) show comparable durations of starburst activity (Papovich et al., 2001; Shapley et al., 2005). Recently, Yan et al. (2004) and Papovich et al. (2005) found that the broadband photometry data for massive galaxies at $z \sim 1\text{--}3$ are better fit by a model star-formation history with recent bursts superimposed on an underlying stellar population compared to simple, monotonically-evolving stellar populations. They conclude that these galaxies have a complicated history with many episodes of star formation. Theoretically, simulations show that in merging galaxies, strong

gas inflow is triggered and nuclear star formation is ignited only after enough gas is accumulated in the center of the galaxies (e.g. Noguchi, 1991; Mihos et al., 1993; Barnes & Hernquist, 1996). During the whole merging process, strong enhancement of the star formation only occurs with a short duration, which supports the proposal for episodic starbursts. A star formation history involving episodic events is also indicated by recent semi-analytic studies (e.g. Somerville et al., 2001; Nagamine et al., 2005).

Given the merging timescale t_{merge} , the fraction f of t_{merge} at which galaxies are actually involved in starbursts, and the timescale for episodic starbursts t_{ESB} , we can estimate the total number of episodes during one merging event $N_{\text{ESB}} = f \times t_{\text{merge}}/t_{\text{ESB}}$. We adopt 0.5 Gyr for the timescale of the greatest merger activity (e.g. Patton et al., 2000). The characteristic timescale of starbursts is estimated at 10-70 Myr as shown above. The fraction f can be computed from the merging fractions of LIRGs and infrared-inactive galaxies as listed in Table 1 and the fraction of LIRGs in a given magnitude-limited sample. We adopt 15% as the fraction of LIRGs as shown in Section 6.4.1 and find $f = 0.15 \times 0.4 / (0.15 \times 0.4 + 0.85 \times 0.16) = 0.3$. Therefore, the average number of episodes during a merging event is around 4 for $t_{\text{ESB}} = 0.04$ Gyr. This indicates that during each merging event, at least one episode of vigorous star formation can be triggered and multiple episodes of such activity are possible.

This conclusion is supported by the studies of nearby galaxies cited above. In addition, simulations by Mihos & Hernquist (1996) show that during merging events, bulgeless disc galaxies can trigger gas inflow even before the occurrence of the actual collision of the galaxies and thus two starburst episodes can occur during the merging event. Recently, Tissera et al. (2002) has shown that in hierarchical clustering scenarios, some merging events can have two episodes of starbursts: one owing to the gas inflow driven as the satellite approaches, and the second one occurring in the collisions of baryonic clumps.

6.5.2 Comparisons to the Local LIRGs

In the last column of Table 2, we present the statistical results for local LIRGs listed in the IRAS Bright Galaxy Sample (Soifer et al., 1987). We extracted the image for each source from the Digitized Sky Survey (DSS) at the POSS2/UKSTU blue band. The table shows that the morphologies of local LIRGs are similar to those of the MIPS-non-detected sample and the LIRGs in the UDF in terms of the fraction of late-type galaxies, of merging galaxies and of symmetric galaxies. The mean asymmetry and concentration of LIRGs in the UDF are slightly higher than those of local LIRGs. The K-S test shows that the probability that the LIRGs at $0.3 < z < 0.9$ and local LIRGs have the same distribution of asymmetry and concentration are 3% and 9%, respectively. That is, the apparent differences are only marginally significant. In the local universe, a very low (4%) fraction of the total population is irregular and interacting galaxies (Marzke et al., 1998). As a result, the morphologies of local LIRGs are quite different from the local normal infrared-inactive galaxies, which is not the case at high-redshift. The small difference in the morphologies between LIRGs and infrared-inactive galaxies in the UDF is due to the fact that, at high redshift, a significant fraction of galaxies are asymmetric systems in which starbursts are much more easily triggered. Locally, LIRGs are exceptional, and an exceptional disturbance is required to trigger their elevated rates of star formation. Based on this trend, we can expect that at higher redshift ($z > 1.5$), the morphologies of LIRGs and non-LIRGs will be even more indistinguishable.

The similarity between the morphologies of local and high- z LIRGs suggests that a certain level of asymmetry is correlated with vigorous star formation, independent of redshift. This situation probably arises because once star formation is initiated, it evolves within a galaxy independent of the galaxy environment (Balogh et al., 2004). Therefore, a similar level of perturbation leads to similar consequences in terms of elevated star formation. At $z \sim 1$, most galaxies appear to have an appropriate level of asymmetry potentially to be transformed into LIRGs by relatively minor mergers. Therefore, the incidence of LIRGs is high, leading to a high density of

star formation. Locally, most galaxies are highly symmetric and only exceptional circumstances, such as an interaction with another massive galaxy, can produce the situations that are a prerequisite for a LIRG. Hence, the incidence of LIRGs is low and so is the density of star formation.

6.6 Conclusions

In this paper, we have investigated the morphologies of 18 high-redshift ($0.3 < z < 1.4$) LIRGs in the UDF down to a rest-frame B-band surface brightness of $\mu_{B0} = 24.5$. They are a representative sample of the LIRGs that dominate the star formation density at $z \sim 1$. We compare their morphologies to those of MIPS-non-detected galaxies at similar redshift and of 49 local LIRGs. We used the concentration and asymmetry indices to quantify the morphologies of all these galaxies. Our main results are:

(1) The fraction of LIRGs for $M_B < -18.5$ galaxies at this redshift range is around 15%, much higher than the 0.5% in the local universe. Their morphologies are dominated by late-type galaxies with asymmetric ($A > 0.2$) structures and include a significant number that appear to be mergers ($40 \pm 20\%$). The morphologies of LIRGs in the UDF are similar to those of local LIRGs but possibly somewhat more asymmetric. Optically luminous MIPS-non-detected galaxies at $z \sim 1$ are nearly as asymmetric as LIRGs, in contrast to the local universe where infrared-inactive galaxies are far more symmetric than local LIRGs.

(2) All of the high- z galaxy types are relatively asymmetric, more so than even local irregular types. Their concentration indices are similar to those of local late-type disk galaxies. We argue that the asymmetric LIRGs and asymmetric MIPS-non-detected galaxies are from the same parent population but in different stages of star formation, which suggests the star formation is episodic. Under this hypothesis, the fraction of the duration of the IR-active phase for asymmetric ($A > 0.2$) galaxies is $\sim 25\%$.

(3) The morphologies of local LIRGs and LIRGs at $z \sim 1$ are similar, suggest-

ing that similar conditions within the galaxy lead to LIRG-levels of star formation. At $z \sim 1$, such conditions are common and LIRGs can develop by relatively minor mergers. Locally, most galaxies are highly symmetric, and only exceptional circumstances such as an interaction with another massive galaxy can create the level of asymmetry associated with LIRG-levels of star formation.

CHAPTER 7

CONCLUSIONS AND FUTURE WORK

7.1 CONCLUSION

7.1.1 Testing the Unification Model

Evidence supporting Unification Model: A crucial ingredient in the unification model is the arrangement of circumnuclear material that obscures the broad-emission-line regions when the AGN is viewed edge-on (Antonucci, 1993). With the goal to understand the structure of this material, we have found that mid-IR obscuration (characterized by the strength of the silicate feature) correlates with the X-ray obscuration (characterized by the HI column density), such that low HI columns correspond to silicate emission while high columns correspond to silicate absorption. This correlation is independent of the type of AGN (Seyfert, radio-loud AGN and radio-quiet QSO). The behavior is generally consistent with unification models. We also found that, along many lines of sight, the amount of X-ray obscuring material is much larger than that for the silicate absorption. A conceptual model (a diffuse+clumpy disk) is proposed to explain the above observations.

As predicted by the unification model for radio-loud AGN, we have shown that radio quasars and some FR II radio galaxies follow a significant correlation between low-frequency (178MHz) radio and the 70 μm emission, two presumably isotropic indicators of nuclear radiation.

Possible Evidence Against the Simple Unification Model: we have found several lines of observational evidence that require corrections to the simple unification model in which our viewing angle is the only factor affecting our view of the AGN phenomenon. Comparison of the SFR between 2MASS and PG quasars with the same level of nuclear radiation reveal that 2MASS host galaxies have higher SFR. A possible explanation for this is that the star formation can heat the circumnuclear

material and thus increase its scale height (Wada & Norman, 2002). As a result, 2MASS quasars have a higher probability to be obscured, consistent with their red IR-optical color caused by the obscuration (Smith et al., 2002).

A significant fraction (1/3) of FR II galaxies show much lower far-IR emission compared to radio quasars at the same radio flux. Two possible explanations are that these galaxies have weaker nuclei, since AGN-dominated far-IR emission can serve as a calorimeter of central power, or that they reside in dense environments boosting their radio emission.

7.1.2 Case Study of AGN Feedback in M87

As found previously, there is an excess in the far infrared over a simple power law interpolation from the radio to the resolved nonthermal features in the mid-infrared and optical. We show that this excess is most likely warm dust in the galaxy itself, and that the properties of this emission component are similar to the far infrared emission of normal giant elliptical galaxies, implying that the ISM in M87 is affected little by the jet. The new observations with *Spitzer* let us determine the spectrum of the jet and surrounding lobes of nonthermal emission. We found that even in the lobes the synchrotron break frequency is in the optical, probably requiring *in situ* particle acceleration not only in the jet but in the lobes as well.

7.1.3 Star Formation of AGN Host Galaxies

To understand the interplay between MBHs and star formation, we have measured aromatic features at 7.7 and 11.3 μm in AGN of three types: PG, 2MASS and 3CR objects. We have provided further evidence that the excitation mechanism for the aromatic features in AGN is predominantly star formation. Based on the aromatic-derived star forming luminosity, we found that the far-IR emission of AGN can be dominated by either star formation or nuclear emission; the average contribution from star formation is around 25% at 70 and 160 μm . The aromatic-derived star-forming luminosity functions (SFLFs) of the three AGN samples are flatter than field

galaxies, implying that the interplay between star formation and nuclear activity enhances both processes. Furthermore, the SFLF of AGNs becomes flatter with an increasing level of nuclear activity over the range from normal galaxies to bright quasars.

7.1.4 Understanding Cosmic SFR Evolution

To explore the possible driving mechanism of dramatic cosmic SFR evolution, we have studied morphologies of a complete sample of LIRGs at $z = 1$ in the Hubble Ultra Deep Field (Shi et al. 2006a). The basic conclusions are: a.) All high- z galaxies are relatively asymmetric. Non-LIRGs are nearly as asymmetric as LIRGs at $z \sim 1$, in contrast to the local universe where infrared-inactive galaxies are far more symmetric than local LIRGs. b.) LIRGs at $z \sim 1$ are as asymmetric as local ones, implying similar conditions within galaxies lead to LIRG levels of star formation. Such conditions may be common at $z \sim 1$ and LIRGs possibly can develop there by relatively minor mergers.

7.2 FUTURE WORK

7.2.1 Revisiting the Role of Major Mergers In Galaxy Evolution

In the cold dark matter universe, structure is believed to form hierarchically. However, the current understanding of the role of the major mergers in galaxy evolution remains ambiguous. The upper panel of Fig. 7.1 summarizes the merging fraction of LIRGs at $z \sim 1$ obtained in different studies. Our UDF result shows a much higher merging fraction than others. Although our study in the UDF is subject to low-number statistics, we suspected that the difference is mainly caused by much shallower observations in other studies. As shown in the lower panel of Fig. 7.1, our initial comparison of the galaxy asymmetry between the GOODS and UDF images for about 50 galaxies confirms that the observation of the GOODS field is not deep enough to reveal the outer low surface brightness features of galaxies. To understand the *true* role of major merging in galaxy evolution, we will carry out a detailed

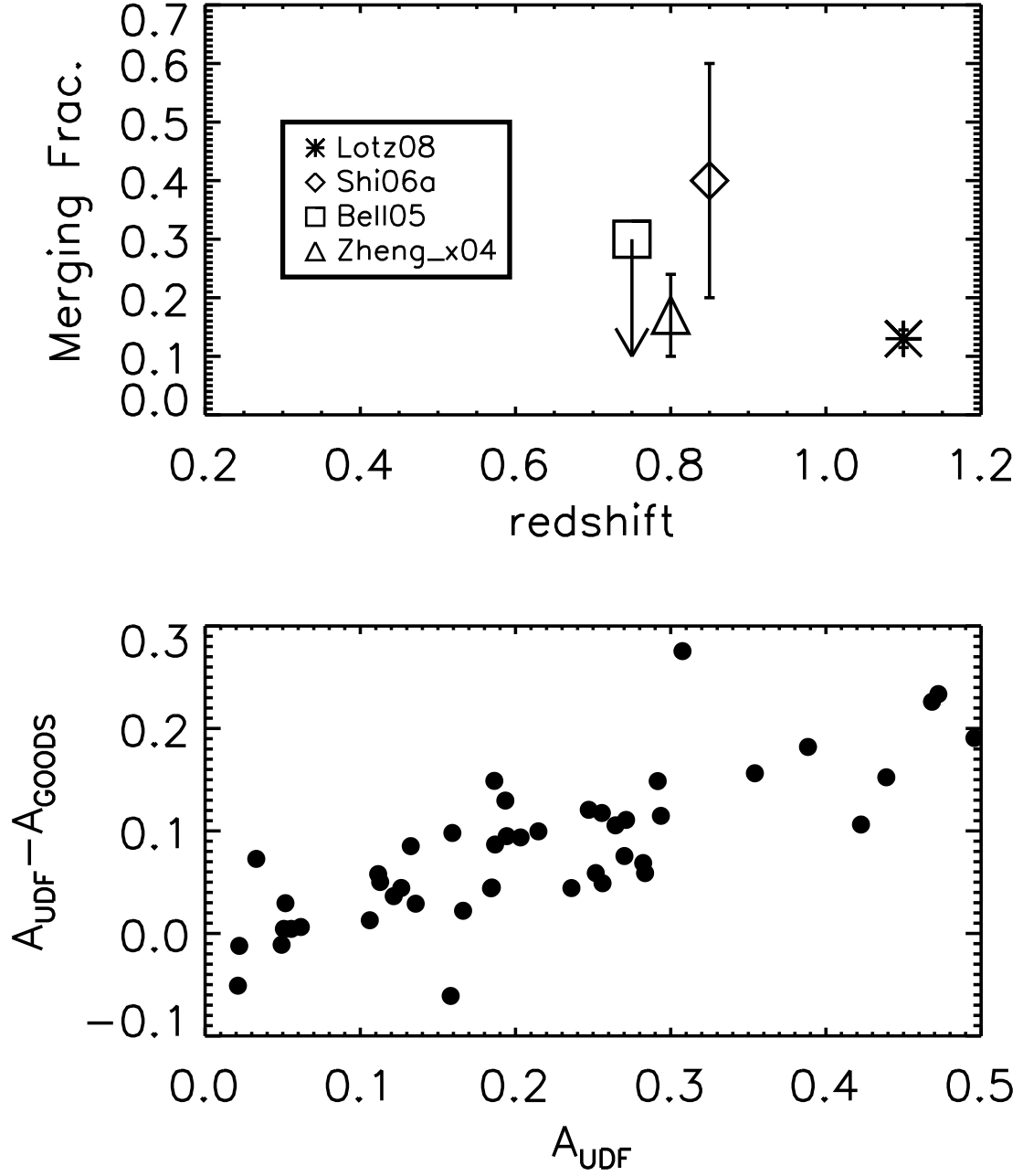


Figure 7.1 Upper panel: The merging fraction of LIRGs in different studies. Lower panel: the difference in asymmetry between UDF and GOODS images for 46 galaxies.

study of galaxy morphologies in the GOODS field, with a plan to correct the current quantitative galaxy classification to better account for the S/N effect.

7.2.2 AGN in Dwarf Host Galaxies

AGN are now recognized as a critical stage of galaxy evolution. The demography of local galaxies suggests that most – perhaps all – massive galaxies host MBHs at their centers and the MBH masses are correlated with the galaxy bulge properties (M - σ) (Kormendy & Richstone, 1995; Magorrian et al., 1998; Gebhardt et al., 2000; Ferrarese & Merritt, 2000), implying the coeval evolution of galaxies and MBHs. As the most abundant population in the universe, dwarf galaxies act as the building blocks of giant galaxies. However, the current understanding of the role of MBHs in *low-mass* galaxy evolution is limited, especially beyond the local universe ($z > 0.1$). To understand the MBH-galaxy interplay in dwarf galaxies, we will carry out a systematic study of ~ 55 AGN in dwarf galaxies found in the X-ray deep fields, including their nuclear properties (accretion disk, BEL region and dusty torus) and host galaxy properties (morphologies, companion environments, metallicity and etc.).

7.2.3 Cosmic Evolution of Star Formation in Quasar Hosts

We have found that local PG quasar hosts have a flatter star formation luminosity function (SFLF) than field galaxies, i.e., the quasars lie in very luminous star forming galaxies more often than would be the case for a random sampling of galaxies without AGN. To characterize the cosmic evolution of star formation in quasar host galaxies, we will measure the aromatic-based SFR of a complete Sloan quasar sample at $0.8 < z < 1.0$. The goals of this project are to: 1.) determine the star-forming environments of high-redshift quasars; 2.) characterize the ULIRG-QSO connections at $z \sim 1$; 3.) study evolution of the dusty torus structure and the role of host galaxy SF in AGN torus properties.

7.2.4 Test the Unification Model with Unusual AGN

Although the unified model (e.g. Antonucci 1993) has achieved tremendous success in explaining the general properties of active galactic nuclei (AGN), there are indications that its axioms may not be universal. AGN with extreme properties relative to the unified model are our best means to refine it and may identify exceptions to the model that would strongly modify our overall view of the subject. We have selected a small sample of extreme AGN from the literature that promise to have this type of impact. They are optically type 1.8/2 objects with little X-ray obscuration.

Why are these objects exceptions to the current unification model? As expected by the current unification model, the HI column densities of 96% of type 2 AGN are larger than 10^{22} cm^{-2} , and they are therefore considered to be X-ray obscured (Risaliti et al. 1999). However, this unusual type of AGN has HI column densities lower than 10^{21} cm^{-2} , corresponding to $A_v \leq 0.62$ (Savage & Mathis 1979), which is inconsistent with their weak or lack of broad hydrogen recombination lines.

We will carry out *Spitzer* and ground-based polarization observations to test various possibilities for this unusual AGN: 1) These objects do not have broad emission line regions; 2) The broad line regions of these objects are dusty; 3) The obscuring material is very patchy.

7.2.5 Prospectives for Future Facilities

The different wavelength coverages, spatial resolutions and sensitivity that future facilities will bring are crucial to the understanding of the interplay between MBHs and galaxies. Here, we list several improvements that future facilities could make:

Herschel: The far-IR and submillimeter emission in the AGN objects can be contributed by both star formation and nuclear activity. The aromatic features obtained by *Spitzer*, far-IR and submillimeter emission obtained by *Herschel* and the most up-to-date normal galaxy templates make it possible to separate accurately the star formation emission from nuclear radiation for a complete sample of local AGN. Such study will help in determining the relative role of star formation vs. nuclear

accretion in galaxy evolution, measuring accurately the contribution of AGN to the cosmic infrared background and testing the unification model to see if an additional parameter (star formation) is required.

EVLA: Radio emission is unaffected by dust obscuration and is well correlated to the star formation rate in normal galaxies. With spatially resolved radio images of local AGN provided by *EVLA*, the level of star formation can be estimated accurately. The measurement of the SFR in local AGN through this technique can be used to calibrate the aromatic-based SFR, which is then adequate to measure the SFR of a large AGN sample at high redshift by *JWST*.

ALMA: *ALMA* will provide spatially-resolved (10-100 pc) images of the molecular gas in local AGN. The morphological and kinetic information of the molecular gas will be crucial to understand the interplay between MBHs and their host galaxies: How is the star formation in AGN hosts triggered? How are the MBHs fed? How does the feedback from one process affect the other?

JWST: With a much higher sensitivity compared to *Spitzer*, *JWST* is able to detect the aromatic features from AGN out to $z \sim 3$. This will provide a complete comparison between the cosmic evolution of star formation in AGN hosts and in normal galaxies. With a much higher spatial resolution (of 300 pc at $z=0.1$ and $\lambda=7\mu\text{m}$), *JWST* can resolve the infrared emission of AGN and their host galaxies. This is critical to estimate the accurate level of star formation in local AGN, and to study the structure of the dusty torus and the properties of dust in the NEL regions. *JWST* will also resolve galaxy morphologies including detecting the fainter galaxy features and accounting for morphological K-corrections at much higher redshift compared to current studies with *HST*.

The above improvements provided by different facilities will complement each other to provide a more complete understanding of MBH growth and galaxy evolution.

REFERENCES

- Abraham, R. G., Valdes, F., Yee, H. K. C., & van den Bergh, S. 1994, *ApJ*, 432, 75
- Abraham, R. G., Tanvir, N. R., Santiago, B. X., Ellis, R. S., Glazebrook, K., & van den Bergh, S. 1996a, *MNRAS*, 279, L47
- Abraham, R. G., van den Bergh, S., Glazebrook, K., Ellis, R. S., Santiago, B. X., Surma, P., & Griffiths, R. E. 1996b, *ApJS*, 107, 1
- Alonso-Herrero, A., Rieke, G. H., Rieke, M. J., & Scoville, N. Z. 2000, *ApJ*, 532, 845
- Alonso-Herrero, A., et al. 2006, *ApJ*, 640, 167
- Antonucci, R. 1993, *ARA&A*, 31, 473
- Armus, L., Heckman, T., & Miley, G. 1987, *AJ*, 94, 831
- Baade, W., & Minkowski, R. 1954, *ApJ*, 119, 215
- Baade, W. 1956, *ApJ*, 123, 550
- Bahcall, J. N., Kirhakos, S., Saxe, D. H., & Schneider, D. P. 1997, *ApJ*, 479, 642
- Ballantyne, D. R., Shi, Y., Rieke, G. H., Donley, J. L., Papovich, C., & Rigby, J. R. 2006, *ApJ*, 653, 1070
- Balogh, M. L., Baldry, I. K., Nichol, R., Miller, C., Bower, R., & Glazebrook, K. 2004, *ApJ*, 615, L101
- Barnes, J. E., & Hernquist, L. 1996, *ApJ*, 471, 115
- Barton, E. J., Geller, M. J., & Kenyon, S. J. 2000, *ApJ*, 530, 660
- Beckwith, S. V., et al. 2005, in preparation

- Bell, E. F., et al. 2005a, ApJ, 625, 23
- Bell, E. F. et al. 2005b, arXiv:astro-ph/0506425
- Belsole, E., Worrall, D. M., & Hardcastle, M. J. 2006, MNRAS, 366, 339
- van den Bergh, S. 1960a, ApJ, 131, 558
- van den Bergh, S. 1960b, ApJ, 131, 215
- Bershady, M. A., Jangren, A., & Conselice, C. J. 2000, AJ, 119, 2645
- Bertin, E., & Arnouts, S. 1996, A&AS, 117, 393
- Bicknell, G. V., & Begelman, M. C. 1996, ApJ, 467, 597
- Bicknell, G. V., Dopita, M. A., & O'Dea, C. P. O. 1997, ApJ, 485, 112
- Biretta, J. A., Burrows, C. J., Holtzman, J. A., et al., 1996, In: Biretta J. A. (ed.)
Wide Field and Planetary Camera 2 Instrument Handbook. STScI, Baltimore
- Biretta, J. A., Sparks, W. B., & Macchetto, F. 1999, ApJ, 520, 621
- Blanton, M. R., et al. 2003, AJ, 125, 2348
- Böhringer, H., et al. 2001, A&A, 365, L181
- Böker, T., Forster-Schreiber, N. M., & Genzel, R. 1997, AJ, 114, 1883
- Boroson, T. A., & Green, R. F. 1992, ApJS, 80, 109
- Bouwman, J., Henning, Th., Hillenbrand L., Silverstone, M., Meyer, M., Carpenter, J., Pascucci, I., Wolf, S., Hines, D. 2006, submitted.
- Bregman, J. D., Bregman, J. N., & Temi, P., Astro-ph/0604369
- Bressan, A., et al. 2006, ApJ, 639, L55
- Brinchmann, J., et al. 1998, ApJ, 499, 112

- Brunner, H., Mueller, C., Friedrich, P., Doerrer, T., Staubert, R., & Riffert, H. 1997, A&A, 326, 885
- Buchanan, C. L., Gallimore, J. F., O’Dea, C. P., Baum, S. A., Axon, D. J., Robinson, A., Elitzur, M., & Elvis, M. 2006, AJ, 132, 401
- Burns, J. O., Owen, F. N., & Rudnick, L. 1979, AJ, 84, 1683
- Canalizo, G., Bennert, N., Jungwiert, B., Stockton, A., Schweizer, F., Lacy, M., & Peng, C. 2007, ApJ, 669, 801
- Carollo, C. M., & Lilly, S. J. 2001, ApJ, 548, L153
- Carpenter, J. 2001, AJ, 121, 2851
- Casoli, F., & Loinard, L. 2001, ASP Conf. Ser. 235: Science with the Atacama Large Millimeter Array, 235, 305
- Cassata, P., et al. 2005, MNRAS, 357, 903
- Chakrabarti, S., Fenner, Y., Hernquist, L., Cox, T. J., & Hopkins, P. F. 2006, ArXiv Astrophysics e-prints, arXiv:astro-ph/0610860
- Chan, K.-W., et al. 2001, ApJ, 546, 273
- Charlesworth, M., & Spencer, R. E. 1982, MNRAS, 200, 933
- Chary, R., & Elbaz, D. 2001, ApJ, 556, 562
- Churazov, E., Brüggen, M., Kaiser, C. R., Böhringer, H., & Forman, W. 2001, ApJ, 554, 261
- Clavel, J., et al. 2000, A&A, 357, 839
- Cleary, K., Lawrence, C. R., Marshall, J. A., Hao, L., & Meier, D. 2006, ArXiv Astrophysics e-prints, arXiv:astro-ph/0612702
- Conselice, C. J., Bershadsky, M. A., & Jangren, A. 2000, ApJ, 529, 886

- Conselice, C. J. 2003, *ApJS*, 147, 1
- Conselice, C. J., Blackburne, J. A., & Papovich, C. 2005, *ApJ*, 620, 564
- Cowie, L. L., Songaila, A., Hu, E. M., & Cohen, J. G. 1996, *AJ*, 112, 839
- Cresci, G., Maiolino, R., Marconi, A., Mannucci, F., & Granato, G. L. 2004, *A&A*, 423, L13
- Cutri, R. M., Rieke, G. H., Tokunaga, A. T., Willner, S. P., & Rudy, R. J. 1984, *ApJ*, 280, 521
- Cutri, R. M., et al. 2001, *ASP Conf. Ser.* 232: The New Era of Wide Field Astronomy, 232, 78
- Cutri, R. M., & McAlary, C. W. 1985, *ApJ*, 296, 90
- Dale, D. A., Helou, G., Contursi, A., Silbermann, N. A., & Kolhatkar, S. 2001, *ApJ*, 549, 215
- Dale, D. A., & Helou, G. 2002, *ApJ*, 576, 159
- Desert, F. X., & Dennefeld, M. 1988, *A&A*, 206, 227
- Dewangan, G. C., Griffiths, R. E., & Schurch, N. J. 2003, *ApJ*, 592, 52
- Di Matteo, T., Springel, V., & Hernquist, L. 2005, *Nature*, 433, 604
- Donato, D., Gliozzi, M., Sambruna, R. M., & Pesce, J. E. 2003, *A&A*, 407, 503
- Donley, J. L., Rieke, G. H., Rigby, J. R., & Pérez-González, P. G. 2005, *ApJ*, 634, 169
- Donley, J. L., Rieke, G. H., Pérez-González, P. G., Rigby, J. R., & Alonso-Herrero, A. 2007, *ApJ*, 660, 167
- Driver, S. P., Windhorst, R. A., & Griffiths, R. E. 1995, *ApJ*, 453, 48

- Driver, S. P., Fernandez-Soto, A., Couch, W. J., Odewahn, S. C., Windhorst, R. A., Phillips, S., Lanzetta, K., & Yahil, A. 1998, *ApJ*, 496, L93
- Edelson, R. A., Malkan, M. A., & Rieke, G. H. 1987, *ApJ*, 321, 233
- Egami, E., et al. 2006, *ApJ*, 647, 922
- Eilek, J., Hardee, P., & Lobanov, A. 2003, *New Ast. Rev.*, 47, 505
- Ellis, R. S., Colless, M., Broadhurst, T., Heyl, J., & Glazebrook, K. 1996, *MNRAS*, 280, 235
- Elmegreen, D. M., Elmegreen, B. G., Rubin, D. S., & Schaffer, M. A. 2005, *ApJ*, 631, 85
- Elvis, M., Maccacaro, T., Wilson, A. S., Ward, M. J., Penston, M. V., Fosbury, R. A. E., & Perola, G. C. 1978, *MNRAS*, 183, 129
- Elvis, M., et al. 1994, *ApJS*, 95, 1
- Elvis, M., Risaliti, G., Nicastro, F., Miller, J. M., Fiore, F., & Puccetti, S. 2004, *ApJ*, 615, L25
- Engelbracht, C. W., Rieke, M. J., Rieke, G. H., Kelly, D. M., & Achtermann, J. M. 1998, *ApJ*, 505, 639
- Evans, A. S., Frayer, D. T., Surace, J. A., & Sanders, D. B. 2001, *AJ*, 121, 3285
- Evans, A. S., Mazzarella, J. M., Surace, J. A., Frayer, D. T., Iwasawa, K., & Sanders, D. B. 2005, *ApJS*, 159, 197
- Fabian, A. C. 1994, *ARA&A*, 32, 277
- Fabian, A. C. 2004, *Coevolution of Black Holes and Galaxies*, 446
- Fadda, D., Flores, H., Hasinger, G., Franceschini, A., Altieri, B., Cesarsky, C. J., Elbaz, D., & Ferrando, P. 2002, *A&A*, 383, 838

- Fan, X., et al. 2004, *AJ*, 128, 515
- Fazio, G. G., et al. 2004, *ApJS*, 154, 10
- Felten, J. E. 1968, *ApJ*, 151, 861
- Ferrarese, L., & Merritt, D. 2000, *ApJ*, 539, L9
- Ferrarese, L. 2002, *ApJ*, 578, 90
- Filippenko, A. V., & Ho, L. C. 2003, *ApJ*, 588, L13
- Forman, W., et al. 2006, *ArXiv Astrophysics e-prints*, arXiv:astro-ph/0604583
- Forster, J. R. 1980, *ApJ*, 238, 54
- Förster Schreiber, N. M. 2000, *New Astronomy Review*, 44, 263
- Gallagher, S. C., Brandt, W. N., Sambruna, R. M., Mathur, S., & Yamasaki, N. 1999, *ApJ*, 519, 549
- Gallagher, S. C., Brandt, W. N., Chartas, G., & Garmire, G. P. 2002, *ApJ*, 567, 37
- Gebhardt, K., et al. 2000, *ApJ*, 539, L13
- Genzel, R., et al. 1998, *ApJ*, 498, 579
- Georgakakis, A., et al. 2008, arXiv0801.2160
- Giacconi, R., et al. 2002, *ApJS*, 139, 369
- Gillett, F. C., Forrest, W. J., & Merrill, K. M. 1973, *ApJ*, 183, 87
- Golombek, D., Miley, G. K., & Neugebauer, G. 1988, *AJ*, 95, 26
- Gordon, K. D., et al. 2005, *PASP*, 117, 503
- Gorjian, V., Cleary, K., Marshall, J., DeMuth, N., Werner, M.W., Lawrence, C. 2006, *ApJ*, in Prep.

- Granato, G. L., & Danese, L. 1994, MNRAS, 268, 235
- Granato, G. L., Danese, L., & Franceschini, A. 1997, ApJ, 486, 147
- Granato, G. L., De Zotti, G., Silva, L., Bressan, A., & Danese, L. 2004, ApJ, 600, 580
- Greene, J. E., & Ho, L. C. 2004, ApJ, 610, 722
- Gull, S. F., & Northover, K. J. E. 1973, Nature, 244, 80
- Haas, M., Klaas, U., & Bianchi, S. 2002, A&A, 385, L23
- Haas, M., et al. 2003, A&A, 402, 87
- Haas, M., et al. 2004, A&A, 424, 531
- Hammer, F., Flores, H., Elbaz, D., Zheng, X. Z., Liang, Y. C., & Cesarsky, C. 2005, A&A, 430, 115
- Hao, L., et al. 2005, ApJ, 625, L75
- Heckman, T. M., Gonzalez-Delgado, R., Leitherer, C., Meurer, G. R., Krolik, J., Wilson, A. S., Koratkar, A., & Kinney, A. 1997, ApJ, 482, 114
- Higdon, S. J. U., et al. 2004, PASP, 116, 975
- Hines, D. C., Eilek, J. A., & Owen, F. N. 1989, ApJ, 347, 713
- Hines, D. C., et al. 2006, ApJ, 638, 1070
- Ho, L. C. 2005, ApJ, 629, 680
- Hopkins, A. M. 2004, ApJ, 615, 209
- Hopkins, P. F., Hernquist, L., Cox, T. J., Di Matteo, T., Robertson, B., & Springel, V. 2006, ApJS, 163, 1
- Houck, J. R., et al. 2004, ApJS, 154, 18

- Huang, J.-S., et al. 2004, ApJS, 154, 44
- Hubble, E. P. 1926, ApJ, 64, 321
- Hubble, E. P. 1936, Yale University Press,
- Hughes, D. H., Dunlop, J. S., & Rawlings, S. 1997, MNRAS, 289, 766
- Isobe, N., Tashiro, M., Makishima, K., Iyomoto, N., Suzuki, M., Murakami, M. M., Mori, M., & Abe, K. 2002, ApJ, 580, L111
- Jaffe, W., et al. 2004, Nature, 429, 47
- Jahnke, K., Kuhlbrodt, B., & Wisotzki, L. 2004, MNRAS, 352, 399
- Jiang, L., et al. 2006, AJ, 132, 2127
- Johnson, H. L. 1966, ApJ, 143, 187
- Junor, W., Biretta, J. A., & Livio, M. 1999, Nature, 401, 891
- Kaneda, H., Onaka, T., & Sakon, I. 2005, ApJ, 632, L83
- Kardashev, N. S. 1962, Soviet Astronomy, 6, 317
- Kaspi, S., Smith, P. S., Netzer, H., Maoz, D., Jannuzi, B. T., & Giveon, U. 2000, ApJ, 533, 631
- Kauffmann, G., et al. 2003, MNRAS, 346, 1055
- Kelly, B. C. 2007, ArXiv e-prints, 705, arXiv:0705.2774
- Kennicutt, R. C. 1998, ARA&A, 36, 189
- Kent, S. M. 1985, ApJS, 59, 115
- Kleinmann, S. G., Hamilton, D., Keel, W. C., Wynn-Williams, C. G., Eales, S. A., Becklin, E. E., & Kuntz, K. D. 1988, ApJ, 328, 161

- Kobulnicky, H. A., & Zaritsky, D. 1999, *ApJ*, 511, 118
- Kobulnicky, H. A., & Kewley, L. J. 2004, *ApJ*, 617, 240
- Kormendy, J., & Richstone, D. 1995, *ARA&A*, 33, 581
- Kotilainen, J. K., & Ward, M. J. 1994, *MNRAS*, 266, 953
- Krabbe, A., Sternberg, A., & Genzel, R. 1994, *ApJ*, 425, 72
- Krolik, J. H., & Begelman, M. C. 1986, *ApJ*, 308, L55
- Lagache, G., et al. 2004, *ApJS*, 154, 112
- Laor, A., & Draine, B. T. 1993, *ApJ*, 402, 441
- Larson, R. B., & Tinsley, B. M. 1978, *ApJ*, 219, 46
- Laurent, O., Mirabel, I. F., Charmandaris, V., Gallais, P., Madden, S. C., Sauvage, M., Vigroux, L., & Cesarsky, C. 2000, *A&A*, 359, 887
- Le Fèvre, O., et al. 2000, *MNRAS*, 311, 565
- Le Fèvre, O., et al. 2004, *A&A*, 428, 1043
- Le Floc'h, E., Mirabel, I. F., Laurent, O., Charmandaris, V., Gallais, P., Sauvage, M., Vigroux, L., & Cesarsky, C. 2001, *A&A*, 367, 487
- Le Floc'h, E., Charmandaris, V., Laurent, O., Mirabel, I. F., Gallais, P., Sauvage, M., Vigroux, L., & Cesarsky, C. 2002, *A&A*, 391, 417
- Le Floc'h, E., et al. 2005, *ApJ*, 632, 169
- Leeuw, L. L., Sansom, A. E., Robson, E. I., Haas, M., & King, N. 2004, *ApJ*, 612, 837
- Leighly, K. M., O'Brien, P. T., Edelson, R., George, I. M., Malkan, M. A., Matsuoka, M., Mushotzky, R. F., & Peterson, B. M. 1997, *ApJ*, 483, 767

- Lilly, S. J., Le Fevre, O., Crampton, D., Hammer, F., & Tresse, L. 1995, *ApJ*, 455, 50
- Liu, Y., Zhou, X., Ma, J., Wu, H., Yang, Y., Li, J., & Chen, J. 2005, *AJ*, 129, 2628
- Lu, N., et al. 2003, *ApJ*, 588, 199
- Lutz, D., et al. 1996, *A&A*, 315, L137
- Lutz, D., Sturm, E., Genzel, R., Spoon, H. W. W., Moorwood, A. F. M., Netzer, H., & Sternberg, A. 2003, *A&A*, 409, 867
- Magorrian, J., et al. 1998, *AJ*, 115, 2285
- Maiolino, R., Ruiz, M., Rieke, G. H., & Keller, L. D. 1995, *ApJ*, 446, 561
- Maiolino, R., Risaliti, G., & Salvati, M. 1999, *A&A*, 341, L35
- Mann, R. G., et al. 1997, *MNRAS*, 289, 482
- Marble, A. R., Hines, D. C., Schmidt, G. D., Smith, P. S., Surace, J. A., Armus, L., Cutri, R. M., & Nelson, B. O. 2003, *ApJ*, 590, 707
- Marcillac, D., Elbaz, D., Chary, R. R., Dickinson, M., Galliano, F., & Morrison, G. 2006, *A&A*, 451, 57
- Marzke, R. O., da Costa, L. N., Pellegrini, P. S., Willmer, C. N. A., & Geller, M. J. 1998, *ApJ*, 503, 617
- Mathur, S., et al. 2000, *ApJ*, 533, L79
- McNamara, B. R., & Nulsen, P. E. J. 2007, *ARA&A*, 45, 117
- Meisenheimer, K., Roeser, H.-J., & Schloetelburg, M. 1996, *A&A*, 307, 61
- Melbourne, J., Koo, D. C., & Le Floch, E. 2005, *ApJ*, 632, L65
- Menanteau, F., Ford, H. C., Motta, V., Benitez, N., Martel, A. R., Blakeslee J. P., & Infante L. 2005, *astro-ph/0509759*

- Merritt, D., Ferrarese, L., & Joseph, C. L. 2001, *Science*, 293, 1116
- Mihos, J. C., Bothun, G. D., & Richstone, D. O. 1993, *ApJ*, 418, 82
- Mihos, J. C., & Hernquist, L. 1996, *ApJ*, 464, 641
- Mills, B. Y. 1952, *Nature*, 170, 1063
- Molendi, S., & Pizzolato, F. 2001, *ApJ*, 560, 194
- Nagamine, K., Cen, R., Hernquist, L., Ostriker, J. P., & Springel, V. 2005, *ApJ*, 618, 23
- Nandra, K., George, I. M., Mushotzky, R. F., Turner, T. J., & Yaqoob, T. 1997, *ApJ*, 477, 602
- Nandra, K., et al. 2007, *ApJ*, 660, L11
- Nenkova, M., Ivezić, Ž., & Elitzur, M. 2002, *ApJ*, 570, L9
- Neumann, M., Meisenheimer, K., Roeser, H.-J., & Stickel, M. 1995, *A&A*, 296, 662
- Noguchi, M. 1991, *MNRAS*, 251, 360
- Nolan, L. A., Dunlop, J. S., Kukula, M. J., Hughes, D. H., Boroson, T., & Jimenez, R. 2001, *MNRAS*, 323, 308
- Ogle, P., Whysong, D., & Antonucci, R. 2006, *ApJ*, 647, 161
- Ohsuga, K., & Umemura, M. 1999, *ApJ*, 521, L13
- Okamura, S., Kodaira, K., & Watanabe, M. 1984, *ApJ*, 280, 7
- Owen, F. N., Eilek, J. A., & Kassim, N. E. 2000, *ApJ*, 543, 611
- Owen, F. N., Hardee, P. E., & Bignell, R. C. 1980, *ApJ*, 239, L11
- Owen, F. N., Hardee, P. E., & Cornwell, T. J. 1989, *ApJ*, 340, 698

- Pacholczyk, A. G. 1970, *Series of Books in Astronomy and Astrophysics*, San Francisco: Freeman, 1970
- Papovich, C., Dickinson, M., & Ferguson, H. C. 2001, *ApJ*, 559, 620
- Papovich, C., & Bell, E. F. 2002, *ApJ*, 579, L1
- Papovich, C., Giavalisco, M., Dickinson, M., Conselice, C. J., & Ferguson, H. C. 2003, *ApJ*, 598, 827
- Papovich, C., et al. 2004, *ApJS*, 154, 70
- Papovich, C., et al. 2005, *astro-ph/0511289*
- Patton, D. R., Carlberg, R. G., Marzke, R. O., Pritchet, C. J., da Costa, L. N., & Pellegrini, P. S. 2000, *ApJ*, 536, 153
- Peacock, J. A. 1985, *MNRAS*, 217, 601
- Peeters, E., Spoon, H. W. W., & Tielens, A. G. G. M. 2004, *ApJ*, 613, 986
- Pérez-González, P. G., et al. 2005, *ApJ*, 630, 82
- Perlman, E. S., Biretta, J. A., Sparks, W. B., Macchetto, F. D., & Leahy, J. P. 2001, *ApJ*, 551, 206
- Perlman, E. S., Sparks, W. B., Radomski, J., Packham, C., Fisher, R. S., Piña, R., & Biretta, J. A. 2001, *ApJ*, 561, L51
- Peterson, B. M. 1993, *PASP*, 105, 247
- Petrosian, V. 1976, *ApJ*, 209, L1
- Pier, E. A., & Krolik, J. H. 1992, *ApJ*, 401, 99
- Pier, E. A., & Krolik, J. H. 1993, *ApJ*, 418, 673
- Pogge, R. W. 1988, *ApJ*, 328, 519

- Polletta, M., Courvoisier, T. J.-L., Hooper, E. J., & Wilkes, B. J. 2000, *A&A*, 362, 75
- Porquet, D., Reeves, J. N., O'Brien, P., & Brinkmann, W. 2004, *A&A*, 422, 85
- Ptak, A., Terashima, Y., Ho, L. C., & Quataert, E. 2004, *ApJ*, 606, 173
- Radomski, J. T., Piña, R. K., Packham, C., Telesco, C. M., De Buizer, J. M., Fisher, R. S., & Robinson, A. 2003, *ApJ*, 587, 117
- Reach, W. T. et al. 2005, *PASP*, 117, 978
- Reeves, J. N., & Turner, M. J. L. 2000, *MNRAS*, 316, 234
- Rieke, G. H., & Low, F. J. 1972, *ApJ*, 176, L95
- Rieke, G. H., & Lebofsky, M. J. 1986, *ApJ*, 304, 326
- Rieke, G. H., Loken, K., Rieke, M. J., & Tamblyn, P. 1993, *ApJ*, 412, 99
- Rieke, G. H., et al. 2004, *ApJS*, 154, 25
- Risaliti, G., Elvis, M., Fabbiano, G., Baldi, A., & Zezas, A. 2005, *ApJ*, 623, L93
- Risaliti, G., Maiolino, R., & Salvati, M. 1999, *ApJ*, 522, 157
- Roberts, M. S., & Haynes, M. P. 1994, *ARA&A*, 32, 115
- Roche, P. F., & Aitken, D. K. 1985, *MNRAS*, 215, 425
- Roche, P. F., Aitken, D. K., Smith, C. H., & Ward, M. J. 1991, *MNRAS*, 248, 606
- Roelfsema, P. R., et al. 1996, *A&A*, 315, L289
- Ronnback, J., van Groningen, E., Wanders, I., & Öömlrndahl, E. 1996, *MNRAS*, 283, 282
- Rottmann, H., Mack, K.-H., Klein, U., & Wielebinski, R. 1996, *A&A*, 309, L19

- Roussel, H., Sauvage, M., Vigroux, L., & Bosma, A. 2001, *A&A*, 372, 427
- Rowan-Robinson, M. 1995, *MNRAS*, 272, 737
- Sandage, A. R. 1961, *The Hubble Atlas of Galaxies* (Washington: Carnegie Inst. Washington)
- Sandage, A., & Tammann, G. A. 1987, *A revised Shapley-Ames Catalog of Bright Galaxies* (Washington: Carnegie Inst. Washington)
- Sandage, A., & Bedke, J. 1994, *Carnegie Atlas of Galaxies* (Washington: Carnegie Inst. Washington)
- Sanders, D. B., Soifer, B. T., Elias, J. H., Madore, B. F., Matthews, K., Neugebauer, G., & Scoville, N. Z. 1988, *ApJ*, 325, 74
- Sanders, D. B., Mazzarella, J. M., Kim, D.-C., Surace, J. A., & Soifer, B. T. 2003, *AJ*, 126, 1607
- Sanders, D. B., & Mirabel, I. F. 1996, *ARA&A*, 34, 749
- Satyapal, S., Watson, D. M., Pipher, J. L., Forrest, W. J., Greenhouse, M. A., Smith, H. A., Fischer, J., & Woodward, C. E. 1997, *ApJ*, 483, 148
- Savage, B. D., & Mathis, J. S. 1979, *ARA&A*, 17, 73
- Schade, D. J., Boyle, B. J., & Letawsky, M. 2000, *MNRAS*, 315, 498
- Schmidt, M., & Green, R. F. 1983, *ApJ*, 269, 352
- Schweitzer, M., et al. 2006, *ApJ*, 649, 79
- Scoville, N. Z., Padin, S., Sanders, D. B., Soifer, B. T., & Yun, M. S. 1993, *ApJ*, 415, L75
- Scoville, N. Z., Frayer, D. T., Schinnerer, E., & Christopher, M. 2003, *ApJ*, 585, L105

- Shankar, F., Salucci, P., Granato, G. L., De Zotti, G., & Danese, L. 2004, MNRAS, 354, 1020
- Shapley, A. E., Steidel, C. C., Erb, D. K., Reddy, N. A., Adelberger, K. L., Pettini, M., Barmby, P., & Huang, J. 2005, ApJ, 626, 698
- Shi, Y., et al. 2005, ApJ, 629, 88
- Shi, Y., Rieke, G. H., et al. 2006a, ApJ, 645, 199
- Shi, Y., et al. 2006b, ApJ, 653, 127
- Shi, Y., Rieke, G. H., et al. 2007a, ApJ, 655, 781
- Shi, Y., Ogle, P., et al. 2007b, ApJ, 669, 841
- Siebenmorgen, R., Haas, M., Krügel, E., & Schulz, B. 2005, A&A, 436, L5
- Silk, J. 2005, MNRAS, 364, 1337
- Smith, P. S., Schmidt, G. D., Hines, D. C., Cutri, R. M., & Nelson, B. O. 2002, ApJ, 569, 23
- Smith, J. D. T., et al. 2007, ApJ, 656, 770
- Smith, R. M., Bicknell, G. V., Hyland, A. R., & Jones, T. J. 1983, ApJ, 266, 69
- Soifer, B. T., et al. 1984, ApJ, 278, L71
- Soifer, B. T., Sanders, D. B., Neugebauer, G., Danielson, G. E., Lonsdale, C. J., Madore, B. F., & Persson, S. E. 1986, ApJ, 303, L41
- Soifer, B. T., Sanders, D. B., Madore, B. F., Neugebauer, G., Danielson, G. E., Elias, J. H., Lonsdale, C. J., & Rice, W. L. 1987, ApJ, 320, 238
- Solomon, P. M., & Sage, L. J. 1988, ApJ, 334, 613
- Soltan, A. 1982, MNRAS, 200, 115

- Somerville, R. S., Primack, J. R., & Faber, S. M. 2001, MNRAS, 320, 504
- Sparks, W. B., Fraix-Burnet, D., Macchetto, F., & Owen, F. N. 1992, Nature, 355, 804
- Sparks, W. B., Ford, H. C., & Kinney, A. L. 1993, ApJ, 413, 531
- Sparks, W. B., Biretta, J. A., & Macchetto, F. 1996, ApJ, 473, 254
- Spinrad, H., Marr, J., Aguilar, L., & Djorgovski, S. 1985, PASP, 97, 932
- Spoon, H. W. W., Moorwood, A. F. M., Lutz, D., Tielens, A. G. G. M., Siebenmorgen, R., & Keane, J. V. 2004, A&A, 414, 873
- Springel, V., Di Matteo, T., & Hernquist, L. 2005, MNRAS, 361, 776
- Sawarz, L., Siemiginowska, A., Ostrowski, M., & Sikora, M. 2005, ApJ, 626, 120
- Steidel, C. C., Adelberger, K. L., Giavalisco, M., Dickinson, M., & Pettini, M. 1999, ApJ, 519, 1
- Stiavelli, M., Biretta, J., Moller, P., & Zeilinger, W. W. 1992, Nature, 355, 802
- Stiavelli, M., Peletier, R. F., & Carollo, C. M. 1997, MNRAS, 285, 181
- Stocke, J. T., Lebofsky, M. J., & Rieke, G. H. 1981, Nature, 294, 319
- Sturm, E., et al. 2005, ApJ, 629, L21
- Sturm, E., Hasinger, G., Lehmann, I., Mainieri, V., Genzel, R., Lehnert, M. D., Lutz, D., & Tacconi, L. J. 2006, ApJ, 642, 81
- Tadhunter, C., et al. 2007, ApJ, 661, L13
- Temi, P., Brighenti, F., Mathews, W. G., & Bregman, J. D. 2004, ApJS, 151, 237
- Thompson, R. I., et al. 2005, AJ, 130, 1

- Tielens, A. G. G. M., Hony, S., van Kerckhoven, C., & Peeters, E. 1999, ESA SP-427: The Universe as Seen by ISO, 579
- Tissera, P. B., Domínguez-Tenreiro, R., Scannapieco, C., & Sáiz, A. 2002, MNRAS, 333, 327
- Tonry, J. L. 1991, ApJ, 373, L1
- Tran, Q. D., et al. 2001, ApJ, 552, 527
- Tristram, K. R. W., et al. 2007, A&A, 474, 837
- Turland, B. D. 1975, MNRAS, 170, 281
- Turner, T. J., & Pounds, K. A. 1989, MNRAS, 240, 833
- Uchida, K. I., Sellgren, K., Werner, M. W., & Houdashelt, M. L. 2000, ApJ, 530, 817
- Uchiyama, Y., et al. 2006, ArXiv Astrophysics e-prints, arXiv:astro-ph/0605530
- Vanden Berk, D. E., et al. 2001, AJ, 122, 549
- Vanzella, E., et al. 2005, A&A, 434, 53
- de Vaucouleurs, G. 1959, Handbuch der Physik, 53, 311
- Valluri, M., Ferrarese, L., Merritt, D., & Joseph, C. L. 2005, ApJ, 628, 137
- Vermeij, R., Peeters, E., Tielens, A. G. G. M., & van der Hulst, J. M. 2002, A&A, 382, 1042
- Verolme, E. K., et al. 2002, MNRAS, 335, 517
- Vestergaard, M., & Peterson, B. M. 2006, ApJ, 641, 689
- Voit, G. M. 1992, MNRAS, 258, 841
- Wada, K., & Norman, C. A. 2002, ApJ, 566, L21

- Wada, K. 2004, *Coevolution of Black Holes and Galaxies*, 186
- Wang, T., Brinkmann, W., & Bergeron, J. 1996, *A&A*, 309, 81
- Watabe, Y., & Umemura, M. 2005, *ApJ*, 618, 649
- Waters, C. Z., & Zepf, S. E. 2005, *ApJ*, 624, 656
- Whysong, D., & Antonucci, R. 2004, *ApJ*, 602, 116
- Wilkes, B. J., Schmidt, G. D., Cutri, R. M., Ghosh, H., Hines, D. C., Nelson, B., & Smith, P. S. 2002, *ApJ*, 564, L65
- Wilkes, B. J., Pounds, K. A., Schmidt, G. D., Smith, P. S., Cutri, R. M., Ghosh, H., Nelson, B., & Hines, D. C. 2005, *ApJ*, 634, 183
- Willott, C. J., Rawlings, S., Blundell, K. M., Lacy, M., & Eales, S. A. 2001, *MNRAS*, 322, 536
- Windhorst, R. A., et al. 2002, *ApJS*, 143, 113
- Wolf, C., Meisenheimer, K., Rix, H.-W., Borch, A., Dye, S., & Kleinheinrich, M. 2003, *A&A*, 401, 73
- Wolf, C., et al. 2004, *A&A*, 421, 913
- Worrall, D. M., Birkinshaw, M., Hardcastle, M. J., & Lawrence, C. R. 2001, *MNRAS*, 326, 1127
- Wu, H., Cao, C., Hao, C.-N., Liu, F.-S., Wang, J.-L., Xia, X.-Y., Deng, Z.-G., & Young, C. K.-S. 2005, *ApJ*, 632, L79
- Xilouris, E. M., Madden, S. C., Galliano, F., Vigroux, L., & Sauvage, M. 2004, *A&A*, 416, 41
- Yan, H., et al. 2004, *ApJ*, 616, 63
- Young, A. J., Wilson, A. S., & Mundell, C. G. 2002, *ApJ*, 579, 560

Yu, Q., & Tremaine, S. 2002, MNRAS, 335, 965

Zakamska, N. L., et al. 2006, AJ, 132, 1496

Zheng, W., et al. 2004, ApJS, 155, 73

Zheng, X. Z., Hammer, F., Flores, H., Assémat, F., & Pelat, D. 2004, A&A, 421, 847